DIAGNOSIS OF REGIONAL MYOCARDIAL ISCHEMIA WITH NEAR-INFRARED SPECTROSCOPIC IMAGING

by

STEPHEN PAUL NIGHSWANDER-REMPEL

A Thesis Submitted to the Faculty of Graduate Studies
In Partial Fulfillment of the Requirements for the Degree of

DOCTOR OF PHILOSOPHY

Individual Interdisciplinary Program
(Departments of Physics & Astronomy,
Human Anatomy & Cell Science,
and Biochemistry & Medical Genetics)

University of Manitoba
Winnipeg, Manitoba

THE UNIVERSITY OF MANITOBA

FACULTY OF GRADUATE STUDIES

*****

COPYRIGHT PERMISSION

Diagnosis of Regional Myocardial Ischemia With Near-Infrared Spectroscopic Imaging

BY

Stephen Paul Nighswander-Rempel

A Thesis/Practicum submitted to the Faculty of Graduate Studies of The University of Manitoba in partial fulfillment of the requirement of the degree

Of

DOCTOR OF PHILOSOPHY

Acknowledgments

The work presented in this thesis involved many other people in various roles, and I would like to recognize their contributions. First, I would like to thank my original supervisor, Dr. Henry Mantsch, for his seemingly inexhaustible faith in me, even when I was overwhelmed by the material; my current supervisor, Dr. Anthony Shaw, for his constant encouragement and help with developing protocols, analysing the experimental data, and reviewing drafts of the thesis; Dr. Valery Kupriyanov, for his support with experimental protocols and reviewing sections of the thesis; and Dr. Judy Anderson and Dr. George Tabisz for their encouragement in the hard times.

I also want to recognize Jennifer Cherkas, Shelley Germscheid, Lori Gregorash, Mark Hewko, Bozena Kuzio, Rachelle Mariash, John Rendell, Amber Stoyko, Allan Turner, and Bo Xiang for their work in various capacities to carry out the details of the experiments. Without their help, I could not possibly have completed this thesis.

I would like to express my gratitude to the National Research Council, the Natural Sciences and Engineering Research Council, and the Manitoba Health Research Council for their financial support of this research project.

Finally, I would like to thank all of my family (including my in-laws) and especially Heidi for their interest, encouragement, support and advice throughout every step of my journey down this road. I am very grateful.

Abstract

This thesis examines the ability of near-infrared spectroscopic imaging (NIRSI) to detect and characterize regional myocardial ischemia with three sets of proof-of-concept experiments. It is hypothesized that NIRSI can not only identify ischemic tissue under surgical conditions, but also quantify the degree of ischemia suffered by the tissue.

In the first study, NIRS images were acquired throughout an ischemia-reperfusion protocol in arrested pig hearts (n=4). Following a period of normal perfusion, the left anterior descending (LAD) artery was completely occluded for 2 hrs. LAD flow was then restored for 10 min, followed by global ischemia for 10 min and a final 10 min period of reperfusion. Regional oxygenation in the LAD perfusion bed (as determined from NIRS images) fell from 80 ± 18% during normal perfusion to 16 ± 10% after 2 hrs LAD occlusion, while oxygenation in perfused regions rose slightly from 65 ± 39% to 77 ± 21%. Reperfusion restored oxygenation in the area at risk (80 ± 8%). Oxygenation in both control and at risk regions fell during global ischemia (18 ± 22% and 8 ± 15%, respectively), and were restored upon reperfusion (88 ± 15% over the whole heart), demonstrating that NIRSI can identify ischemic regions of tissue in arrested hearts.

The second study applied a similar procedure to isolated, beating pig hearts (n=8), with image acquistion triggered by the ECG to ensure that acquisition was consistently in the same phase of the cardiac cycle. The ability of NIRSI to distinguish between degrees of partial ischemia was investigated by reducing LAD flow stepwise to 50%, 20%, and 0% of baseline. Accordingly, oxygenation in the LAD perfusion bed fell from 90 ± 3% during normal perfusion to 85 ± 4%, 78 ± 4%, and 65 ± 4%, respectively. These results demonstrate that NIRSI can not only highlight ischemic regions of tissue, but also, in principle, quantify the severity of ischemia within those regions.

The third study investigated spectroscopic imaging of working pig hearts under conditions mimicking open heart surgery, again triggering image acquisition to the ECG. Following a period of normal perfusion, the LAD was either completely occluded (n=4) or partially occluded (20% flow: n=6, 50% flow: n=4) for 90 min. Hearts were then reperfused for 2 hrs. After 90 min regional ischemia, oxygenation in the LAD perfusion bed fell from 75 ± 4% to 63 ± 6% (complete occlusion), 72 ± 2% to 62 ± 4% (20% flow), and from 74 ± 1% to 68 ± 5% (50% flow). Oxygenation after 90 min of 50% LAD flow was significantly higher than that after 90 min of either 20% flow ($p<0.05$) or complete occlusion ($p<0.05$). Oxygenation during reperfusion was consistently restored to baseline values. These results confirm that NIRSI can identify ischemia under surgical conditions.

A related study was carried out to support quantitative interpretation of the spectroscopic images. That study exploited the relative intensities of near-IR absorption bands of a transition metal complex (Nd-DTPA) added to the tissue perfusate as the basis to estimate the wavelength-dependence of the optical pathlength. Single-point spectroscopy was performed on isolated rat hearts (n=11), and the optical pathlengths at 520, 580, 679, 740, and 870 nm were found to be 41 ± 13%, 49 ± 21%, 90 ± 9%, 94 ± 1%, and 84 ± 1% of the pathlength at 800 nm, respectively.

These results demonstrate that NIRSI can identify ischemic regions of cardiac tissue rapidly and without probes or exogenous contrast agents. Moreover, identification of ischemia by NIRSI is effective on both isolated and *in vivo* hearts, showing promise as a diagnostic tool for use in both research and cardiac surgery.

Contents

Figures

Tables

Abbreviations

Å: Angstrom (10^{-10} metre)

ADP: Adenosine diphosphate

ATP: Adenosine triphosphate

bpm: Beats per minute

Ca^{++}: Calcium ion

CAD: Coronary artery disease

CCD: Charge-coupled device

CoA: Coenzyme A

CP: Creatine phosphate

dHb (dMb): Deoxygenated hemoglobin (myoglobin)

DPF: Differential pathlength factor

DTPA: Diethylene triamine pentaacetic acid

ECG: Electrocardiogram

FAD^+: Flavin adenine dinucleotide (oxidized form)

$FADH_2$: Flavin adenine dinucleotide (reduced form)

FWHM: Full peak width at half maximum

H^+: Hydrogen ion

Hb: Hemoglobin

HbO_2: Oxygenated hemoglobin

HR: Heart rate

Hz: Hertz (1 / second)

ICG: Indocyanine green

K^+: Potassium ion

KHB: Krebs-Henseleit buffer

LAD: Left anterior descending (artery)

LCTF: Liquid crystal tunable filter

LV: Left ventricle

LVEDP: Left ventricular end diastolic pressure

LVSP: Left ventricular systolic pressure

M: Moles / litre

Mb: Myoglobin

MbO_2: Oxygenated myoglobin

mm Hg: Millimetres of mercury

Na^+: Sodium ion

NAD^+: Nicotinamide adenine dinucleotide (oxidized form)

NADH: Nicotinamide adenine dinucleotide (reduced form)

Nd: Neodymium

NIRS: Near-infrared spectroscopy

NIRSI: Near-infrared spectroscopic imaging

nm: Nanometre (10^{-9} metre)

NS: Not significant

PRP: Pressure-rate product

ROI: Region of interest

SR: Sarcoplasmic reticulum

TTC: Triphenyl tetrazolium chloride

1. Introduction

The central role of the heart in keeping the body alive and healthy is so well-recognized that the word "heart" has acquired a new definition as the central part (e.g. "the heart of the matter"). For the heart to keep the body healthy, its own function (i.e. regular contraction) must be maintained, and this requires a steady blood supply. To that end, a network of coronary[1] arteries surround the heart, feeding the tissue with oxygenated blood. A severe restriction to blood flow in the coronary arteries can deprive regions of the heart of needed oxygen, severely impairing its normal function and the health of the individual. This condition is known as "coronary artery disease". Given the high incidence of coronary artery disease in North America, coronary bypass operations aimed at restoring blood flow to those regions of the heart have become routine. As part of such operations, diagnostic tools aimed at monitoring oxygen levels (oxygenation) in the blood and heart tissue would be helpful.

While various cardiac imaging techniques are available to surgeons, none of them are well-suited to monitor oxygenation during surgery. This thesis demonstrates that a new, relatively inexpensive, and easily transportable technology, known as near-infrared spectroscopic imaging, can effectively monitor cardiac blood and tissue oxygenation, opening the door to applications in both research and surgical operations. This chapter

---

[1] From the Latin *corona* (meaning *crown*), the term describes the way the arteries circle the heart. Throughout this thesis, etymologies of terms will be provided, with the understanding that etymologies can provide a glimpse into the history of the field of study. Most of these etymologies were obtained from Stedman (1995).

briefly summarizes the relevant features of coronary artery disease and cardiac imaging techniques, and concludes with an outline of the thesis structure.

1.1. Coronary Artery Disease

Cardiovascular disease, which can culminate in a heart attack or stroke, is a leading cause of death in industrialized countries, accounting for over one third of all deaths in Canada in 1998.(2) Only cancer is comparable in its toll on human life, accounting for almost 30% of Canadian deaths. Coronary artery disease (CAD),[2] characterized by thickening and hardening of the arterial walls and reduction of arterial blood flow, is responsible for most cardiovascular-related deaths. What is particularly sad about this is that CAD is largely preventable. Some major risk factors, including smoking, physical inactivity, and poor nutrition, are matters of choice for most sufferers of CAD. Other risk factors, such as diabetes, high blood pressure, and high cholesterol production, can be countered with the use of medication. Moreover, diagnosis and treatment of CAD place a huge burden on the health care system. The number of surgical interventions in Canada designed to increase the length and quality of life of people with CAD increased steadily from 30,000 in 1990-1991 to over 40,000 in 1995-1996, and cardiovascular diseases were estimated to cost the Canadian government over $2 billion in drugs and hospital and physician care in 1998.(1)

CAD is a complex disease, developing over the course of many years. The initial stages, in which a plaque develops in the arterial wall, comprise a process known as

---

[2] This disease is also referred to as coronary heart disease or ischemic heart disease.

atherosclerosis.[3] Although much remains to be learned about the details of atherosclerotic development, the "response to injury" hypothesis, first proposed by Rudolf Virchow in 1856 and frequently modified and updated since then, has contributed significantly to our current understanding of this process.(215) The basic elements of this hypothesis are as follows. A normal artery wall consists of three layers: an inner layer of endothelial[4] cells, a middle layer of smooth muscle, and an outer layer of connective tissue. Some "injury" to the endothelial layer (which may take any of a variety of forms), caused in part by the risk factors, leads to the attraction and migration of fatty droplets from the bloodstream into the arterial wall. This in turn attracts a type of white blood cell known as monocytes, which consume the fatty droplets. Monocyte penetration attracts more monocytes, and these together with the fatty droplets make up fatty streaks, which may either continue to grow or shrink and disappear.

Fatty streaks are not harmful in and of themselves, and they have been found in people of all ages, including infants. However, if the risk factors persist, then the fatty streak may develop into what is known as a fibrous plaque. Fibrous plaques are characterized by severe structural alterations to the arterial wall interior and hardening of the interior wall surface. As part of the same process, the endothelial layer expands into the arterial lumen,[5] disturbing and restricting blood flow. As the plaque develops further,

---

[3] From the Greek *athērē* (meaning *porridge*) and *sklērōsis* (meaning *hardness*), it describes the appearance and texture of the plaque that develops in the arterial wall.

[4] From the Greek *endon* (meaning *within*) and *thele* (meaning *nipple*), this type of cell was initially known as epithelial cells (using the Greek *epi-*, meaning *upon*) and the name reflects the initial region in which this type of cell was identified.

[5] From the Latin for *light* or *window*, it refers to the interior space of the artery, through which blood flows. The name reflects the empty appearance of small arteries in thin slices viewed through a microscope (Figure 2.2).

muscle cells in the wall die and collagen and cholesterol deposits harden the wall. This itself hinders blood flow, since arterial expansion and contraction normally assist in propelling the blood to the extremities of the body. The physical presence of the plaque also reduces the size of the lumen and may expand enough to close it off completely, preventing movement of blood beyond that point. This atherosclerotic plaque development in a coronary artery is one of the hallmarks of CAD.

When the blood supply to a region of tissue is reduced, that tissue is said to be ischemic.[6] Since poor blood flow results in low oxygen delivery to tissue, CAD may result in impaired cardiac function or a heart attack. Prolonged myocardial[7] ischemia leads to death of heart muscle tissue. Thus, in cases of advanced CAD, intervention is urgently required either to reduce the size of the plaque or to divert blood flow around the plaque, in order to restore oxygen delivery to the tissue. While it may be possible in some cases to reduce the plaque size with a combination of exercise, a proper diet, and medication, coronary artery bypass grafts[8] are often required to restore blood supply adequately.

1.2. Diagnostic Imaging

While bypass grafts have been very successful in extending the lives of people with CAD, graft failure soon after surgery is still a major cause of death.(242) This fact underscores the potential value of a diagnostic imaging tool that can rapidly assess the

---

[6] From the Greek *ischō* (meaning *to keep back*) and *haima* (meaning *blood*)

[7] From the Greek *myo-* (meaning *muscle*) and *kardia* (meaning *heart*), it refers to the heart muscle.

[8] If the plaque in the arterial wall is too restrictive of coronary flow, then that piece of the vessel must be bypassed. In such cases, a piece of an artery (usually taken from the chest or leg (71)) is attached so that blood flows through this vessel to the tissue. This is known as a bypass graft.

success of the bypass procedure during surgery (intraoperatively). A variety of techniques have been adopted to image the heart over the years, including X-ray imaging (radiology),(55) echocardiography (ultrasound),(159) magnetic resonance imaging (MRI),(182) single photon emission computed tomography (SPECT), and positron emission tomography (PET).(195) Although each of these techniques has found a useful niche, none is suitable for intraoperative imaging of blood and tissue oxygenation.

X-ray imaging is the oldest of these techniques and remains the gold standard for determining the viability of the bypass graft intraoperatively.(63,64) However, this technique uses harmful radiation, it involves addition of a dye to the bloodstream, and it is not always available in the operating room.(64) Echocardiography is also widely used for intraoperative assessment of bypass surgery. However, this technique measures only mechanical properties of the heart, such as wall motion.(179) Moreover, it has a limited field of view and it is very operator-dependent.(85) A new technique, using the "SPY" imaging system, visualizes arterial flow using fluorescence of a dye (indocyanine green) added as a bolus to arterial blood. It has been introduced for the intraoperative assessment of graft viability with reasonable success,(210,243) but it too provides no information on blood or tissue oxygenation.

Over the past two decades, magnetic resonance imaging (MRI) has proven capable of monitoring both the coronary vessels and the structure and function of the heart muscle. The BOLD (blood oxygen level dependent) technique has further demonstrated some ability to monitor myocardial blood flow and oxygenation,(270) and MRI has shown excellent utility as a pre-operative diagnostic technique for coronary artery disease.(3) However, the size of the magnet and imaging equipment makes imaging during surgery nearly impossible. The cost of the equipment also makes it inaccessible to many hospitals. Finally, because of its use of magnetic fields, MRI can not be used on patients with pacemakers or other metallic implants. While SPECT and PET show great potential for imaging blood perfusion through cardiac tissue and PET is considered to be the gold standard for determining heart muscle viability,(85) the size and cost of the equipment make both techniques poorly suited to the operating room.

This thesis proposes and explores the use of near-infrared spectroscopic imaging (NIRS imaging or NIRSI) as a new approach to monitor blood and muscle tissue oxygenation. This approach is an extension of near-infrared spectroscopy (NIRS), which has been well-established as a means to monitor local blood and tissue oxygenation.(118,160,232,235) This combination of spectroscopy with imaging has been used previously to monitor tissue viability in skin flap and burn studies with success.(148,158) Moreover, it is substantially less expensive than imaging techniques such as PET, SPECT, or MRI and it can easily be brought into and out of operating theatres. The hypothesis of this thesis is two-fold: first, that NIRSI can identify ischemic regions of cardiac tissue under surgical conditions; and second, that it can quantify the degree of ischemia suffered by the tissue.

1.3. Outline of Thesis

It is necessary to point out here that this study is interdisciplinary, as this has implications to the way in which this thesis is written. Because reviewers of this thesis represent a variety of fields, including physics, chemistry, anatomy, and physiology, it is important that, for the sake of readability, disciplinary terms are avoided whenever lay terminology preserves clarity of meaning. Moreover, when such terms are necessary, they will be defined as they are introduced.

The interdisciplinary nature of this work also means that discussion of some aspects relating to this study, which may be included in a disciplinary thesis, will be excluded here. This includes, for example, in-depth discussions of the quantum mechanics of spectroscopy, cell structure and metabolism, or molecular transport across cell membranes. Instead, this thesis brings together background material from physics, chemistry, and biology, as they are necessary to discuss application of spectroscopic imaging to characterize cardiac ischemia.

This thesis is divided into seven chapters. Following the introduction, the second chapter is a discussion of relevant background material. This includes sections on myocardial structure and function, oxygen transport, and near-infrared spectroscopy. The third chapter discusses the wavelength-dependence of optical pathlength in tissue. This chapter summarizes previous relevant studies and presents a novel investigation of this property.

Chapters 4-6 comprise the central focus of the thesis. The fourth chapter discusses the theory and implementation of NIRS imaging, and presents the first study into the applicability of NIRSI to diagnosis of cardiac ischemia, using a complete, regional ischemia model in arrested pig hearts isolated from the animal body. The fifth chapter presents the subsequent study, in which NIRSI was applied to isolated, beating hearts. That study further evaluated the ability of NIRSI to differentiate between different degrees of partial (and complete) ischemia. The study presented in the sixth chapter mimics actual cardiac surgery, applying spectroscopic imaging to diagnosis of cardiac ischemia in pig hearts under surgical conditions, rather than in isolated hearts. Finally, chapter seven concludes the thesis, summarizing the results and suggesting new avenues along which NIRS imaging might be developed.

2. Review of Literature

The central aim of this thesis is to test the utility of near-infrared spectroscopic imaging (NIRSI) for the detection of regional, myocardial ischemia. In that light, it is necessary to understand normal myocardial structure and function, and how these are impacted by the onset of ischemia; these are discussed in Section 2.1. Moreover, since ischemia impacts oxygen transport (specifically by hemoglobin and myoglobin), the mechanisms of oxygen delivery are of strong relevance; these are reviewed in Section 2.2. Finally, the theoretical considerations underpinning the measured spectra and application of NIRS to blood oxygenation will be presented in Section 2.3.

2.1. Myocardial Ischemia and Infarction

Ischemia is defined as a local reduction in blood supply (or more correctly, hemoglobin supply), and results in reduced oxygen delivery to the tissue (hypoxia). Generally, myocardial ischemia is a result of coronary artery disease, in which atherosclerotic plaque development in one or more coronary arteries restricts blood flow to heart tissue. A flow reduction affecting only a limited tissue volume is known as regional ischemia, whereas a flow reduction to the entire heart is referred to as global ischemia. In either case, blood flow may be completely stopped (total ischemia) or only partially reduced (partial ischemia).

A thorough study of the metabolic, electrophysiological, structural, and functional consequences of myocardial ischemia and hypoxia is available.(207) The present discussion therefore summarizes only those effects most relevant to the studies presented in this thesis.

2.1.1. Normal Structure and Function

2.1.1.1. Structure

Surrounding the atrial and ventricular cavities of the heart are three layers of tissue. The outermost layer is the epicardium[9], a thin layer which covers the heart muscle and the coronary arteries. Lymphatic channels are also included in this layer.(61) The innermost layer of cardiac tissue is the endocardium, composed of a connective tissue skeleton covered by a layer of endothelial[10] cells and providing a structural base for the other two layers. In between these layers, the myocardium (the contractile tissue that drives the circulation) accounts for more than half of the total weight of the heart.(181)(p. 27) As the name implies, this layer is almost entirely muscle, bundled into fibres by collagen and penetrated by capillaries and nervous tissue. The fibres branch and recombine in a network (Figure 2.1), so that during contraction, the ventricular space is compressed to eject the blood into the circulation.(33)

The myocardial fibres are further subdivided into cells (myocytes[11]) that are typically 100 μm long and 8-15 μm wide, and arranged end to end along the fibre. Each

---

[9] From the Greek *epi-* (meaning *upon* or *following*) and *kardia* (meaning *heart*). It is also referred to as the visceral layer of serous pericardium. Similarly, endocardium is derived from the the Greek *endon* (meaning *within*) and *kardia*.

[10] The cells were originally known as epithelial cells (from the Greek *epi*, meaning *upon*, and *thele*, meaning *nipple*). The original term was first used for cells on the surfaces of the nipple and the lips. When these cells were discovered on the interior surfaces of blood vessels and cavities, the prefix *endo-* was applied, forming *endothelium*.

[11] From the Greek *myo-* (meaning *muscle*) and *cyte* (meaning *cell*).

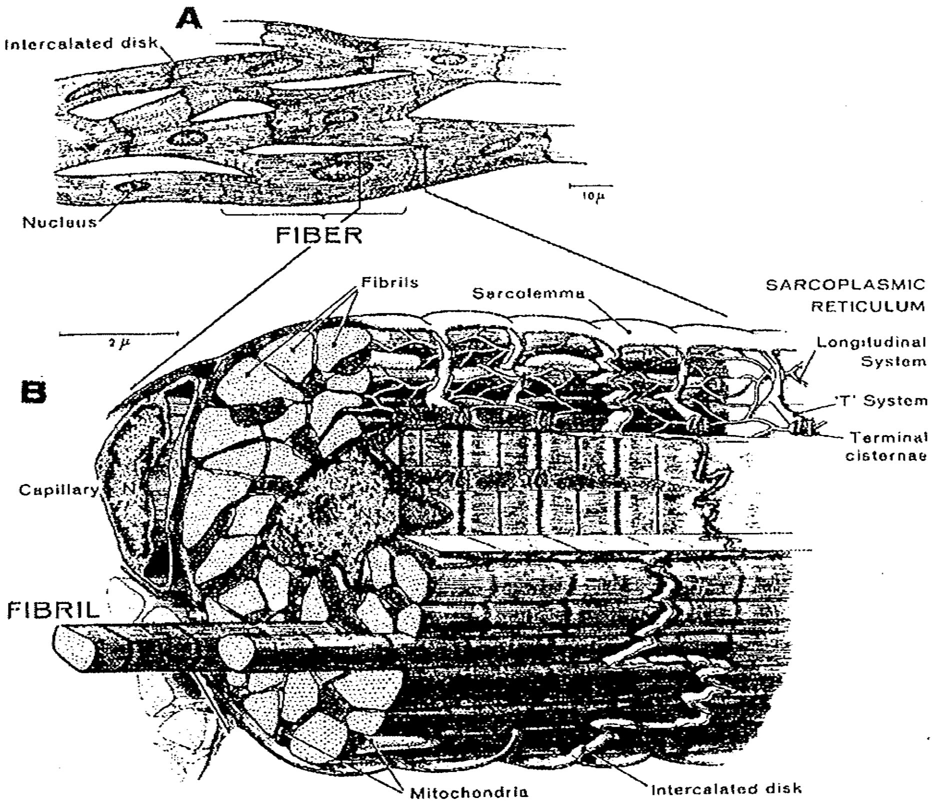

Figure 2.1. Myofibre and myocyte structure. From Braunwald, 1967.

cell is surrounded by a membrane[12]. At the ends of the cells, the membranes form intercalated disks, and between the myocyte membranes is a thin region of extracellular space. Capillaries[13] permeate the myocardium to such an extent that virtually every myocyte is in contact with a capillary (Figure 2.2).(70) Approximately 60% of the myocyte's intracellular volume is composed of myofibrils, which perform the contractile function. Myofibrils consist of thick and thin myofilaments (myosin and actin, respectively) attached to Z-discs, which subdivide each cell lengthwise into sarcomeres (Figure 2.3) Actin filaments are fixed to the Z-discs and myosin filaments lie in between, attached only to the actin.(211).

When muscle contracts, myosin filaments pull themselves along the actin filaments, as the myosin heads detach from and reattach to the actin. This procedure is dependent upon both calcium and adenosine triphosphate (ATP), the energy currency of the cell. Calcium concentrations in the cytosol[14] ($0.1 - 1\ \mu$M) are approximately one thousandth to one ten thousandth of those in the sarcoplasmic reticulum (SR) and extracellular space (Table 2.1). During each contraction, depolarization of the membrane potential allows calcium to enter the cytosol from the SR and extracellular space. Calcium binds to the actin filaments, exposing the receptor site to the myosin head. Binding of myosin to actin increases the myosin ATPase activity, dephosphorylating ATP to ADP. The myosin head then releases the ADP, inducing the head to flex,

---

[12] The cell membrane is often referred to as the plasmalemma or sarcolemma. The latter term comes from the Greek *sarx* (meaning *flesh*) and *lemma* (meaning *husk*). Both prefixes *sarco-* or *myo-* are used to indicate muscle.

[13] From the Latin *capillaris* (meaning *relating to hair*), it describes the fine structure of the vessels.

[14] The cytosol is the intracellular fluid.

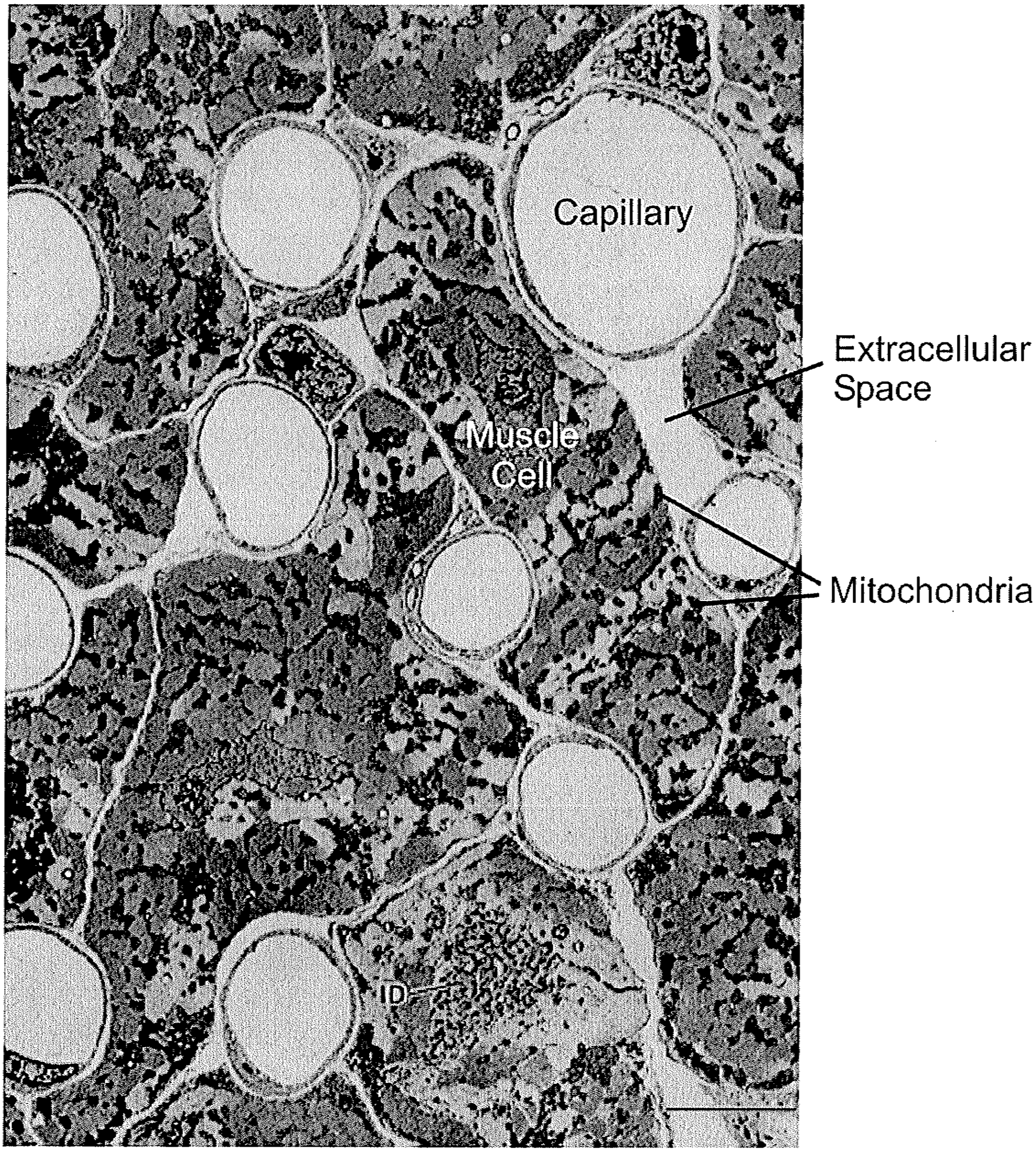

Figure 2.2. Transverse view of myocardium. Each myocyte (muscle cell) is in contact with at least one capillary. Extracellular space is visible between myocyte boundaries. Mitochondria are also visible as black spots within each myocyte. From Forbes, 1989.

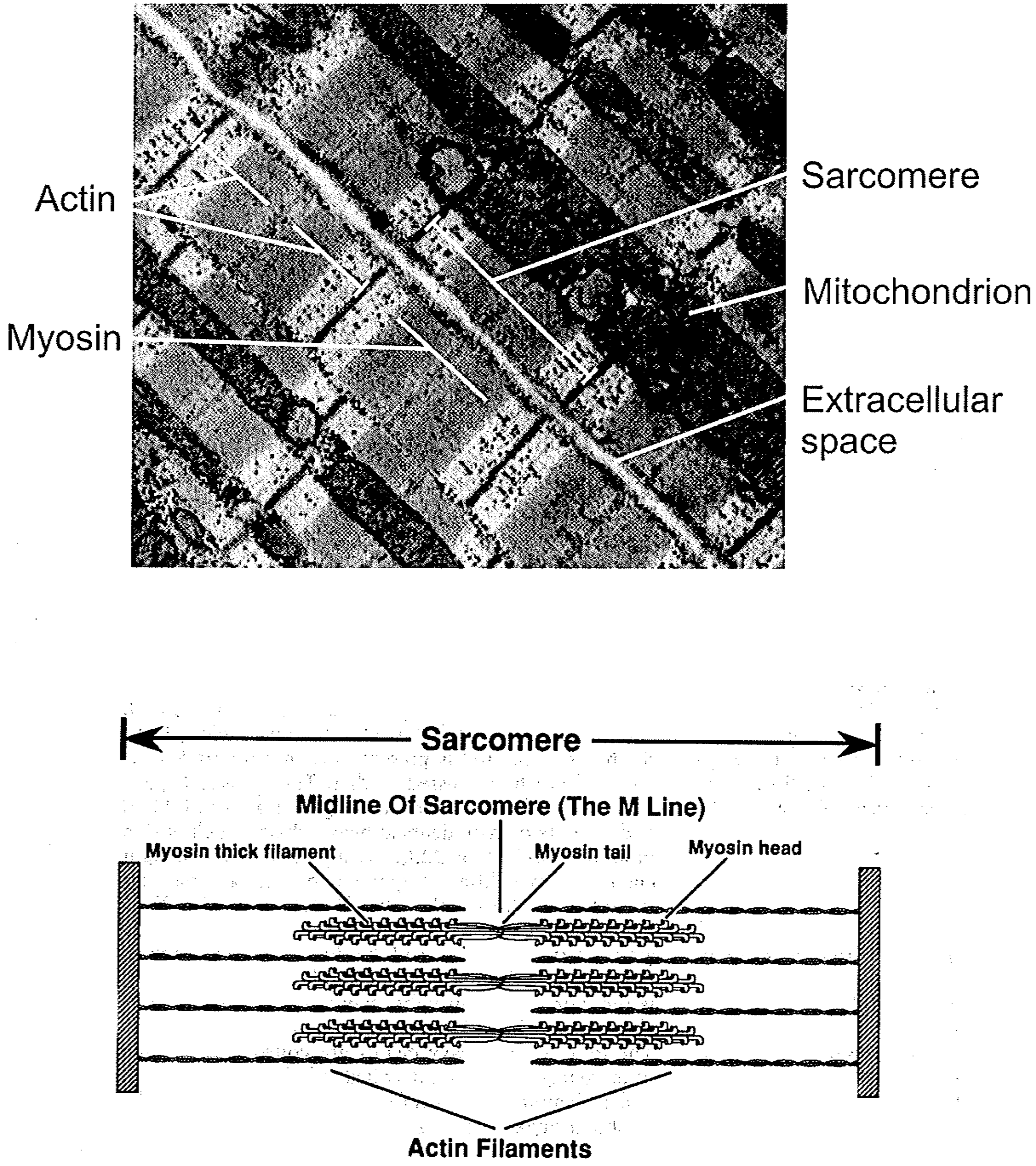

Figure 2.3. (top) Longitudinal view of myocardium, showing myofilaments. From Fawcett, 1969.(67) (bottom) Diagram of myofilaments. From Roberts, 1994.(211) During contraction, myosin heads detach from and reattach to the actin filaments, reducing the length of the sarcomere.

pulling actin filaments closer together and contracting the muscle (systole). Expulsion of calcium from the cytosol through slow calcium channels results in membrane repolarization, reduction of the ATPase activity of myosin, and relaxation of the myosin head (diastole).(91,211)

In addition to the 60% of cellular space occupied by myofibrils, 23% of the intracellular space is composed of mitochondria,(224) and the remaining 17% of cell volume occupied by other organelles and cytoplasm.(13) Since myofibrils perform muscular contraction and mitochondria provide the necessary energy in the form of adenosine triphosphate (ATP), these proportions emphasize both the importance of contractile strength in cardiomyocyte function and the energy demand to maintain the muscle contraction workload.

Table 2.1. Myocardial Ion Concentrations (in mM)

	Intracellular space	Extracellular space
Na^+	10	140
K^+	125	5
Ca^{++}	$10^{-4} - 10^{-3}$	1
Cl^-	20	125

2.1.1.2. Electrolyte levels

Contractile activity is driven in part by oscillating calcium concentration values. Cytosolic calcium levels range from 0.1 μM during diastole to 1 μM or higher in systole.(181)(pp. 127-130) In contrast, extracellular calcium concentrations are on the order of 1000 μM. This steep concentration gradient is maintained by ion transport pumps within the cell membrane, such as the Na^+-Ca^{++} exchanger and the Ca^{++} ATPase[15]. The Ca^{++} ATPase draws energy from ATP to drive calcium from the low-Ca^{++} cytosol into the extracellular space. In contrast, the Na^+-Ca^{++} exchanger does not consume ATP. This exchanger responds to the sodium concentration gradient across the cell membrane to expel one Ca^{++} ion for every three Na^+ ions allowed in.(225) The hydrophobic interior of the cell membrane effectively prevents simple diffusion of ions between the intracellular and extracellular spaces.

The trans-membrane sodium concentration gradient is much less than that of calcium, but myocytes also actively maintain this gradient. Intracellular sodium remains at approximately 10 mM, while extracellular concentrations are sustained near 140 mM (Table 2.1). Although sodium is only 14 times more concentrated in the extracellular space than in the cytosol (while calcium is 1000 times more concentrated), the fact that three Na^+ ions are exchanged for each Ca^{++} increases the relative potential for sodium above that for calcium ($14^3 = 2744 > 1000$) While Na^+-Ca^{++} exchanger activity increases intracellular sodium levels, the Na^+-K^+-ATPase provides a counterbalance. This membrane protein uses the energy of ATP to expel three sodium ions from the cell, while transporting two potassium ions into the cell. Since normal potassium concentrations are higher inside the cell than outside, this pump works against the electrochemical gradient for both sodium and potassium, and therefore requires an external source of energy.

---

[15] The suffix –ase usually indicates an enzyme, which is "a protein that acts as a catalyst to induce chemical changes in other substances".(237) In most cases, the base of the word (ATP in this case) describes what is being acted upon.

2.1.1.3. Glycolysis and Respiration

All work requires energy. In biological tissue, the major energy currency is adenosine triphosphate (ATP). ATP stores energy chemically in phosphate bonds, and dephosphorylation of ATP to adenosine diphosphate (ADP) releases 8000 calories per mole of ATP under standard conditions. Energy is consumed (via dephosphorylation of ATP) both in muscle contraction and in the maintenance of electrolyte concentrations. Therefore, cells must replenish ATP supplies so as to maintain normal cardiac function. When sufficient oxygen is available to meet the needs of cardiac function, ATP is produced primarily in the mitochondria through aerobic[16] respiration. When oxygen supply is low (as during severe ischemia), aerobic respiration can not be sustained. While ATP continues to be produced via anaerobic metabolism under such conditions, this process is much less efficient and can not meet the energy requirements of normal cardiac function. The physiological importance of oxygen lies almost solely in its maintenance of aerobic respiration and ATP synthesis, and thus, it is important to understand the mechanisms by which ATP is produced. Detailed discussions of ATP synthesis from different substrates[17] are available(13,150,175) and only a brief overview will be provided here.

ATP production is a multi-step process governed in part by the processes of phosphorylation (and dephosphorylation) and oxidation/reduction[18] (Figure 2.4).

---

[16] From the Greek *aero* (meaning *air*) and *bios* (meaning *life*), the term reflects the fact that the ancients had not made a distinction between air and oxygen.

[17] From the Latin *substratus* (meaning *to spread under*), in this context it refers to compounds such as glucose, glycogen, or fatty acids which provide the basis from which ATP production may proceed.

[18] Phosphorylation is the endothermic binding of a phosphate compound onto a molecule. Similarly, dephosphorylation releases the phosphate, using the energy in the bond to drive chemical processes. Oxidation and reduction are complementary process in which electrons are transferred. The electron-

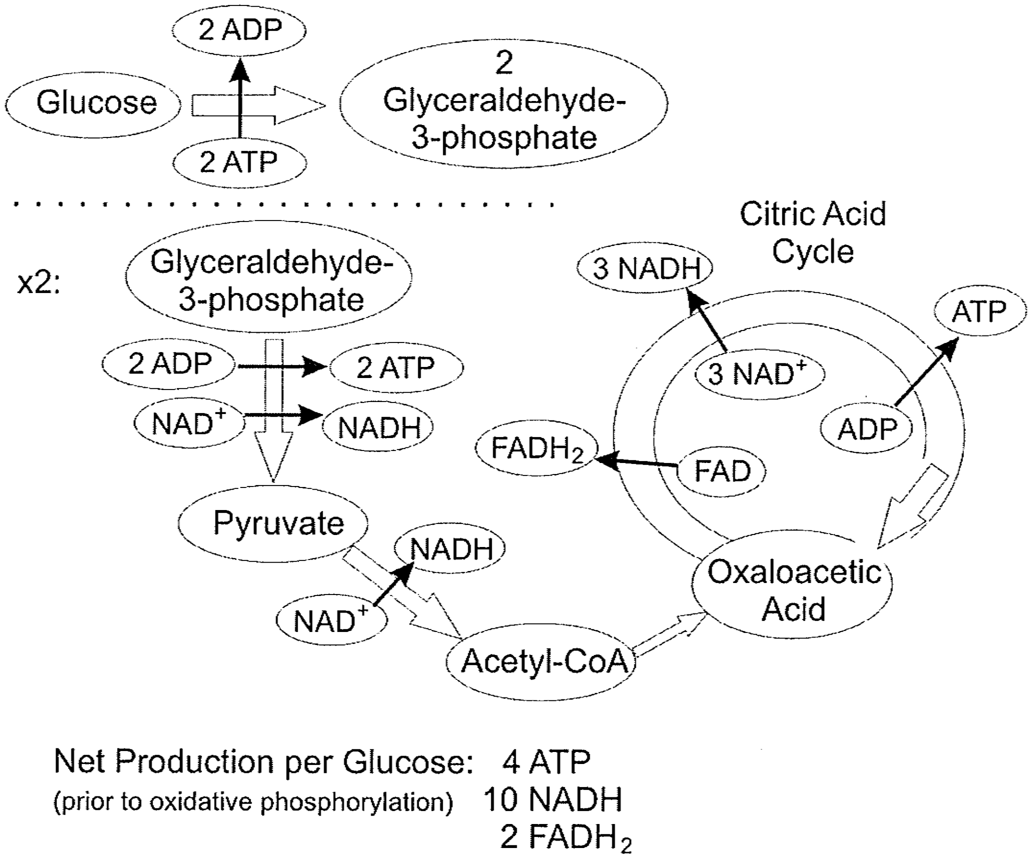

Figure 2.4. Initial steps of aerobic respiration. Two ATP are consumed in the conversion of one glucose molecule to two glyceraldehyde molecules. For each glyceraldehyde, 5 NADH, 1 FADH$_2$, and 3 ATP are created, for a net production of 4 ATP, 10 NADH, and 2 FADH$_2$.

Glycolysis marks the first step in ATP synthesis, converting glucose into pyruvate via several transitions and requiring an initial investment of ATP. During this conversion, two ATP molecules are dephosphorylated in the conversion of glucose to fructose-1,6-biphosphate. This molecule is then cleaved into two molecules of glyceraldehyde-3-phosphate, each of which transforms (reducing NAD$^+$ to NADH) and transforms yet again (phosphorylating one ADP to ATP), yielding a molecule of 3-phosphoglycerate.

---

donor is said to be oxidized, while the recipient is reduced. The term oxidation is used because this process is often associated with binding of oxygen (such as in rusting). The term reduction refers to the reduction in charge experienced by the electron-recipient. Specifically, reduction of nicotinamide adenine dinucleotide (NAD$^+$) and flavin adenine dinucleotide (FAD$^+$) into NADH and FADH$_2$, respectively, as well as the reverse oxidation process, occur repeatedly during aerobic respiration.

Further transformations (phosphorylating another ADP) lead to the creation of pyruvate. Thus, the glycolytic process converts each glucose molecule into two pyruvate molecules, consuming the energy of two ATP but producing four more ATP and two NADH. When blood lactate levels are high, lactate can also be oxidized into pyruvate by the enzyme lactate dehydrogenase (LDH).

Pyruvate moves from the cytosol through the inner mitochondrial membrane and is oxidized to yield an acetyl group, which binds onto coenzyme A (CoA). This process is regulated by the enzyme pyruvate dehydrogenase (PDH). Under normal conditions, acetyl-CoA compound is then used in the citric acid cycle (described below). Conversion of pyruvate into the acetyl group also reduces more NAD^+ to NADH. When the oxygen supply is low, pyruvate is not oxidized but converted to lactate via LDH, oxidizing NADH to NAD^+.

In addition to pyruvate, fatty acids can also contribute significantly to acetyl-CoA synthesis. While glucose is transported down a steep concentration gradient across the cell membrane, fatty acids are actively removed from the blood plasma.(207) In this case, the fatty acid is converted to acyl-CoA in the cytoplasm, consuming two ATP. This compound is transported across the inner mitochondrial membrane, where it is oxidized to acetyl-CoA. Although fatty acids provide many times as much ATP as pyruvate (per mole),(150)(p. 158) metabolism of these fatty acids produce less ATP and more carbon dioxide for each oxygen consumed.(181)(p. 211) The relative contributions of glucose, lactate, and fatty acids to ATP synthesis varies substantially with blood content.(181)(p. 214) For instance, after a high-carbohydrate meal, glucose provides approximately 70%

of the metabolic fuel with lactate making up the difference. On the other hand, in the fasting state, fatty acids can account for over 60% of the oxygen uptake. (82,175)

Use of acetyl-CoA in the production of ATP begins with the citric acid cycle[19]. Acetyl-CoA combines with oxaloacetic acid to form citric acid, which then undergoes a series of reactions, resulting in the formation of another oxaloacetic acid (which can then combine with another acetyl-CoA to repeat the cycle). In the process, one ADP is phosphorylated into ATP, and three NAD^+ and one FAD^+ are reduced to NADH and $FADH_2$. Since two acetyl-CoA are produced for each glucose, 4 ATP, 10 NADH, 2 $FADH_2$, and 6 CO_2 molecules are produced at the end of the citric acid cycle.

NADH and $FADH_2$ stimulate further ATP synthesis via oxidative phosphorylation, the last phase of aerobic respiration. This process involves electron transport between various complexes within the inner mitochondrial membrane (Figure 2.5). First, Complex I oxidizes NADH and Complex II oxidizes $FADH_2$, pumping hydrogen ions (H^+) out from the mitochondrial matrix into the intermembrane space and passing electrons on to coenzyme Q (CoQ), which transports them within the inner mitochondrial membrane to Complex III. In the process, CoQ pumps another H^+ out from the matrix. Complex III[20] transports the electrons to cytochrome c while pumping out a third H^+. Cytochrome c shuttles electrons from Complex III to Complex IV, where the electrons combine with H^+ and oxygen molecules to form water.

---

[19] This cycle is also commonly known as the tricarboxylic acid cycle or the Krebs cycle (named after Sir Hans Krebs, a 20th-century German biochemist working at Oxford).

[20] Complex III consists of two b cytochromes and one cytochrome c_1. Similarly, Complex IV consists of cytochrome a, cytochrome a_3, and two copper atoms. Each of these cytochromes have visible absorbance spectra and are discussed in Chapter 3.

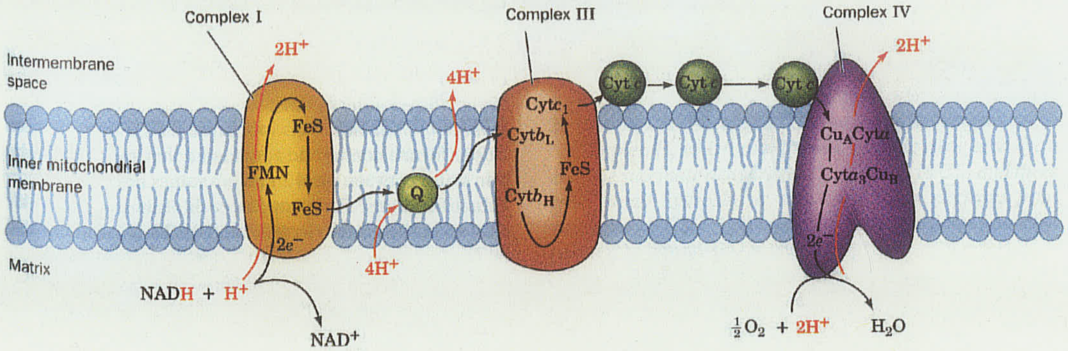

Figure 2.5. Electron Transport Chain. Oxidation of NADH and $FADH_2$ drives electron transport, which expels hydrogen ions and converts oxygen into water. As hydrogen diffuses back through the membrane, ATP is created. From Voet, 1995.

There is a steep electrochemical gradient across the inner mitochondrial membrane and as H^+ diffuses through a membrane hydrogen channel, it reacts with inorganic phosphate (P_i) and ADP to create ATP. Three molecules of ATP are produced for oxidation of each NADH, and two are produced for each $FADH_2$. Thus, 38 ATP are created for each glucose molecule (4 + 3*10 (NADH)+ 2*2 ($FADH_2$)).

When oxygen is unavailable, the electron transport chain stops, leaving the cytochromes in their reduced states. Thus, H^+ is no longer pumped from the matrix and ADP phosphorylation resulting from H^+ diffusion ceases. While anaerobic glycolysis increases significantly to compensate for lost ATP, ischemia also has an inhibitory effect on cardiac glycolysis.(217) These effects can commence within seconds of oxygen deprivation.(187,223)

2.1.2. Effects of Ischemia

Oxygen, supplied by hemoglobin, is necessary for oxidative phosphorylation of ADP into ATP, as described above. The danger of ischemia therefore originates largely (but not entirely) in the restriction of oxygen available to tissue. A severe reduction in coronary flow has many effects and the causative relationships among them are not completely understood. In addition to flow rates, the progression of ischemic injury can differ significantly from that of hypoxic injury in terms of the rate of anaerobic glycolysis, the severity of acidosis, and the maintenance of contractile function.(114,176,217) While (during ischemia) the lack of substrates required for glycolysis is partially responsible for these differences, another significant factor is the largely reduced clearance of metabolic end-products. With little or no flow, potentially dangerous levels of hydrogen ions and lactate can develop in the intra- and extracellular spaces.

2.1.2.1. The First Minute

Severe myocardial ischemia resulting from coronary artery occlusion has a demonstrable impact on the tissue almost immediately. Two direct effects are reductions in both vascular pressure and oxygen supply. While oxygen may continue to be drawn from myoglobin[21] stores and hemoglobin trapped in the tissue, this supply lasts only five to ten seconds.(187,223) The depletion of oxygen then results in immediate cessation of mitochondrial oxidative phosphorylation(264) and hence severely impaired ATP production.

---

[21] Myoglobin is a heme protein with very similar structure and function to hemoglobin, but approximately one fourth the size. While hemoglobin is largely confined to red blood cells, myoglobin is found only in muscle cells.

Although cellular ATP levels do not drop immediately (for reasons outlined below), creatine phosphate[22] (CP) supplies are drastically reduced within seconds of the onset of ischemia. CP, like ATP, stores energy in phosphate bonds, and it is normally present in higher concentrations than ATP.(114) Since ATP does not diffuse freely in the cytosol,(266)(p. 156) CP serves as an energy shuttle, transporting energy from mitochondrial ATP to sites of ATP consumption, according to the following reactions.

$$\text{CP} + \text{ADP} \leftrightarrow \text{ATP} + \text{Creatine} \qquad (2.1)$$

Once ATP is phosphorylated in the mitochondrial matrix and transported through the inner membrane, the enzyme creatine phosphokinase transfers the phosphate from ATP to creatine, releasing more ADP for phosphorylation.(92) (p. 822) The CP then travels to sites of ATP hydrolysis, such as myofibrils or Na^+-K^+-ATPase, where CP phosphorylates ADP into ATP, which in turn drives the metabolic processes.

Since the phosphate bond in CP has a higher free energy (under standard conditions) than that in ATP (9500 calories/mol vs. 8000 cal/mol), equilibrium favours creation of ATP. Thus, during any decrease in oxidative phosphorylation, resulting for instance from ischemia or hypoxia, ATP levels will initially remain steady at the expense of CP. Thus, CP stores are almost completely exhausted within the first minute after severe ischemia.(30,120) ATP levels are maintained, not only by energy transfer from CP to ATP, but also by the rapid increase in anaerobic glycolysis.(137,207)(p. 1894) In fact, after only five minutes of ischemia, intracellular ATP levels in the ischemic region have been shown to fall only to 60-70% of normal levels.(113,174)

---

[22] Creatine phosphate (CP) is also commonly referred to as phosphocreatine (PCr).

Reduced oxidative phosphorylation also results in increased conversion of pyruvate to lactate, so intracellular lactate levels also increase within seconds of the onset of ischemia.(50) This increase in lactate, in addition to the rise in inorganic phosphate and hydrogen ions resulting from dephosphorylation of adenine nucleotides,(45,144) contributes to intracellular acidosis. During hypoxia, continued perfusion washes away these acidotic agents, but during ischemia, they accumulate within the cell.

Some studies indicate a decrease in intracellular K^+ levels within 30 s of onset of myocardial ischemia,(101,258) but other studies demonstrate no significant change in K^+ levels during the first 15 min of cardiac ischemia.(247) Intracellular potassium is normally maintained by the membrane protein Na^+-K^+-ATPase, which requires ATP to import potassium into the cell; it is therefore tempting to attribute any potassium ion loss to Na^+-K^+ ATPase dysfunction. However, potassium levels drop concurrently with the rise in anaerobic glycolysis and before a severe reduction in ATP. Indeed, the function of the pump is unaffected immediately after onset of ischemia.(130) If unchecked, the loss of potassium may lead to a counterbalancing efflux of negative ions such as phosphate and lactate.(131,162) Potassium loss has also been suggested to be therapeutic to the myocardium by reducing the osmotic potential and preventing cellular swelling during the initial stages of ischemia.(115,238)

Perhaps the most critical early effect of ischemia, though, is the impairment of contractile function. It has long been known that contractile function in ischemic regions of the heart decreases within the first 10 seconds after the onset of myocardial ischemia,(94,214) resulting in a visible systolic bulge during severe ischemia,(250) yet its cause is still poorly understood. It is tempting to link reduction of contractility to reduced

ATP levels, but again, ATP levels do not significantly drop until after contractile dysfunction is observed.(123) Although CP levels are found to drop more quickly than ATP levels, contractile dysfunction still precedes CP loss.(123,194) Alternative explanations for reduced contractility have included accumulation of hydrogen ions and lactate and increases in inorganic phosphate levels. Acidotic conditions may indeed contribute to impaired contractility, but contractile dysfunction has also been observed prior to significant decreases in intracellular pH and increases in inorganic phosphate.(109,142) One remaining possibility is that the initial contractile dysfunction is a direct result of the loss of intravascular pressure that follows ischemia.(134)

2.1.2.2. Later Developments

The early effects of ischemia – increases in H^+ and lactate, loss of creatine phosphate and K^+, and impaired contractile function – lead to further complications if perfusion is not restored. Perhaps most significantly, the cessation of oxidative metabolism forces the myocyte to turn to alternative means of ATP generation. A surge of glycolytic activity is observed, and since the supply of glucose and fatty acids is restricted during severe ischemia, intracellular glycogen stores are used to maintain glycolysis. However, this is short-lived during ischemia, since accumulation of H^+ and lactate inhibit the glycolytic pathway. (167,175)

While the impairment of contractile function has obvious harmful effects on the circulation, it also significantly reduces ATP consumption, since myofibrillar contraction accounts for 60-70% of the total ATP consumption during normal perfusion.(181)(p. 260) Nevertheless, anaerobic glycolysis still can not sustain the remaining ATP requirements – especially when inhibited by acidosis – and products of ATP dephosphorylation (ADP and adenosine monophosphate) are further dephosphorylated. Within 15 min of ischemia, ATP levels have been shown to fall by 65% and half of the cellular adenine nucleotide pool is depleted.(111,206)

Besides the myofibrillar ATPase, the major consumers of ATP in the cardiomyocyte are the Na^+-K^+ ATPase, Ca^{++} ATPases in the sarcoplasmic reticulum and cell membrane, and the mitochondrial ATPase.(207)(p. 1894) During ischemia, the mitochondrial ATPase is a major consumer of ATP.(116,216) While it may be expected that during ischemia, Na^+-K^+ ATPase function is reduced due to low energy supply, this protein maintains its function for some time under ischemic conditions. This is most likely a result of the high affinity of the Na^+-K^+ pump for ATP and the low free energy of Na^+-K^+ countertransport.(163) Because of this high affinity for ATP, pump function will not be impaired until ATP levels fall to very low levels. Calcium levels also do not change substantially immediately after onset of hypoxia or ischemia, although they may rise substantially upon reperfusion (see Section 2.1.2.4), depending on the duration of the ischemic episode.(174,196)

Acidosis, resulting from increased glycolytic activity, is an early response to ischemia. Normal intracellular pH is maintained with another membrane protein, the Na^+-H^+ exchanger. This protein allows Na^+ to move down the concentration gradient into the cell, driving H^+ ions out of the cell.(145,194) Increased intracellular H^+ levels cause a greater sodium influx, and intracellular sodium levels have been shown to rise during 30 min periods of ischemia.(194,247)

Later in the course of ischemia, decreased Na^+-K^+ pump function resulting from low ATP levels exacerbates the high intracellular sodium levels.(78) The increased sodium upsets the chemical balance necessary for proper function of the Na^+-Ca^{++} exchanger. Normally, this protein moves Na^+ into the cell (down the gradient), driving one Ca^{++} out for every three Na^+ which enter. However, during ischemia, the calcium gradient overpowers the reduced sodium gradient, and the exchanger begins to export sodium at the cost of importing calcium, although acidosis inhibits Na^+-Ca^{++} exchanger function.(193) Moreover, since ATP levels are low, the Ca^{++} ATPase also can not effectively maintain low cytosolic calcium concentrations.

Thus, intracellular calcium levels have been shown to rise within minutes of ischemia.(128) While the osmotic load is increased early due to CP and ATP hydrolysis[23] (which increases the concentration of ionic phosphate), the increase can be exacerbated by intracellular sodium and calcium concentrations. While an increased osmotic load might be expected to result in intracellular edema,[24] cellular swelling during ischemia has been shown to be mild,(111) perhaps because of the limited extracellular space and water content during total ischemia.(90) Since intracellular calcium regulates myocyte contraction, changes in calcium levels interfere with myocardial function by disrupting myofibrillar contraction and activating various enzymes.

---

[23] From the Greek *hydōr* (meaning *water*) and *lysis* (meaning *dissolution*), it refers to the cleavage of a molecule through which the H and OH parts of the water molecule are taken up.

[24] From the Greek *oidēma* (meaning *a swelling*), it refers to accumulation of water in tissue.

2.1.2.3. Reversible and Irreversible Ischemic Damage

During the first 10 minutes of severe ischemia, most cellular changes are metabolic in nature and the only structural changes are some mild swelling and changes in myofibrillar contraction.(9,86) If ischemia is prolonged, then more severe structural changes begin to take place in the cell. Reduced intracellular pH results in clumping of the chromatin within the nucleus[25].(117) Mitochondria begin to swell and cristae are broken apart. Mitochondrial swelling is enhanced and cellular swelling is also apparent. Nuclear chromatin becomes entirely aggregated into clumps near the periphery, and glycogen stores become depleted.(74)

Nevertheless, if perfusion is restored to cardiac tissue sufficiently early during the course of ischemia, then all of these effects can be reversed and no permanent damage will occur. This is known as reversible ischemic injury. Restoration of flow will remove excess agents of acidosis, contractility will resume (although at reduced levels due to stunning), and electrolytes such as Ca^{++}, Na^{+} and K^{+} will return to normal levels. However, if ischemia is prolonged for an extensive period of time, then cardiac tissue will be damaged sufficiently that reperfusion does not restore normal structure and function. This is referred to as irreversible injury.

Two criteria often used in differentiating reversible from irreversible injury are the integrity of cell membranes (allowing restoration of normal ion concentrations) and the ability of mitochondria to resume ATP production. Mitochondrial dysfunction has been associated with widespread appearance of amorphous matrix densities within the

---

[25] Clumping of nuclear chromatin is known as pyknosis. From the Greek *pyknos* (meaning *dense* or *compact*) and *osis* (meaning *condition*).

mitochondrial space.(49) Development of these densities impairs the ability of mitochondria to create ATP, even if oxygen supply is restored. Similarly, disruption of the cell membrane allows unrestricted movement of particles between the intracellular and extracellular spaces. This prevents the cell from maintaining necessary ion gradients, even upon reperfusion.

A secondary indicator of irreversibility is the observation that irreversibly injured cells typically have lower intracellular ATP concentrations than reversibly injured cells (below 5 μmol/g dry weight as compared to 10 μmol/g dry weight or more).(111,117) As ATP stores are depleted, the cells can no longer sustain normal function. However, ATP concentration alone is not a reliable indicator of irreversible injury.

While the time for which ischemia must be sustained in order for these developments to occur varies with animal species and severity of ischemia, hallmarks of irreversible ischemia have been shown to appear in some rat hearts as early as 30 min after ischemia.(74) After 40 minutes, a much larger proportion of cells are irreversibly injured. Signs of irreversible injury have also been reported between 20 and 60 minutes of ischemia.(42)

It has been suggested that cell membrane disruption is caused by a two-stage process.(81,239) (207)(p. 1909) First, protease activity stimulated by excess Ca^{++} levels degrades the cytoskeleton that connects the cell membrane to Z-disks between the myofibrils. This weakens the cellular structure. Second, accumulation of ions such as Na^{+} and Ca^{++} in the cytosol increases the osmotic load, leading to edema. The increased pressure on the membrane coupled with the weakened structure causes the membrane to burst. Once the membrane is disrupted, ions rapidly move to equilibrate concentrations across the membrane. Loss of K^+ and accumulation of Ca^{++} have disruptive effects on normal metabolic process of the cell, further injuring the cell.(207)(p. 1908)

Another structural consequence of ischemia is myocyte contracture[26], which leads to increases in diastolic ventricular pressure. Suggested causes of this contracture have included calcium overload, reduced ATP levels, and changes in pH. (146,212) However, some evidence indicates that ATP depletion plays a more significant role in contracture development than changes in calcium concentrations.(134)

When myocardial tissue is ischemic for a sufficiently long period, it begins to undergo coagulative necrosis[27]. While necrosis may begin after as little as 30 minutes of ischemia, 6-8 hours of ischemia are usually required for significant amounts of tissue (70-80% of the ischemic tissue) to exhibit necrosis.(212)(p. 1111) During the first few hours following coronary artery occlusion, tissue enzymes are lost from the cytosol, calcium levels continue to increase, and lipid droplets appear in the tissue. Following this phase, white blood cells permeate the area and catabolic activity of exogenous enzymes increases in the tissue. Fibroblast and monocyte levels increase, degrading the myocardial tissue and establishing collagenous infarcts. After one week, the infarct is advanced, and myocardial tissue in the ischemic region is replaced by fibrous tissue. A detailed tabular summary of the progression of myocardial ischemia and infarction is available elsewhere.(181)(p. 459-461)

---

[26] Contracture is defined as static muscle shortening that is irreversible without intervention.

[27] Greek for *death*. Coagulative necrosis is a type of cell death in which the tissue is converted to a dry, homogeneous, fibrous mass.

2.1.2.4. Reperfusion Injury

As mentioned above, if perfusion is restored after a short period (e.g. 15 minutes) of ischemia, then the previously ischemic region (the "area at risk") will eventually recover completely. Some features of reversible ischemia that persist for several minutes following reperfusion include cellular and mitochondrial swelling, margination of nuclear chromatin, myofibrillar relaxation, and reduced glycogen levels.(117) However, after 20 minutes of reperfusion, these conditions return to normal with the possible exception of some swollen mitochondria. Mitochondrial oxidative phosphorylation is quickly restored,(206) but if the adenine nucleotide pool was severely depleted during ischemia, then ATP levels may require up to four days to recover completely.(206,275)

If perfusion is not restored until after 30-60 minutes of ischemia, then the restoration of blood flow may injure the cells further rather than restoring normal function. It is in many cases difficult to determine what injury is due to prolonged ischemia and what is due to reperfusion, and the phrase "reperfusion injury" has been applied to many experimental and clinical conditions, including arrhythmias, cellular degradation, and contractile dysfunction.(207)(p. 1927) Several pathways have been proposed to be involved in the progression of reperfusion injury.(208)

First, cellular acidosis may induce a calcium overload by way of altered Na^+/H^+ and Na^+/Ca^{++} exchange.(90,141,172) Although sodium levels begin to rise after 15 minutes of ischemia, calcium levels have been shown not to be substantially affected even after 30 min ischemia.(247) Upon reperfusion, however, calcium levels increased dramatically.(247) It is likely that during ischemia, intracellular acidosis inhibits Na^+/Ca^{++} exchange function. Upon reperfusion, restored pH and mitochondrial function concurrent with high intracellular Na^+ concentration leads to massive calcium overload, activating proteases and phospholipases.

Another characteristic of reperfusion injury is cellular swelling.(115,256) During ischemia, accumulation of catabolytes (e.g. P_i) and the influx of electrolytes (Ca^{++}, Na^+) increases the osmotic load, and increased phospholipase and protease activity weaken the intracellular structure. Upon reperfusion, water accumulates in the intracellular space. With the weakened structure, membranes can not support the increased pressure and the cells burst. Another potential source of reperfusion injury involves the presence of free radicals including superoxide anion ($\cdot O_2^-$), hydroxyl radical ($\cdot OH$), and hydrogen peroxide (H_2O_2).(82) These reactive oxygen species are created by neutrophils engaged in necrosis, as well as by mitochondria under anaerobic conditions, and several pathways have been proposed to explain their increased concentrations early in reperfusion.(29,207,241) These free radicals can have catabolic effects on fatty acids in the phospholipid membrane and on proteins within the cell.(75,77) They have also been reported to affect ion transport proteins in the cell membrane.(220,260)

2.1.3. Identification of Ischemia and Necrosis

A variety of methods are available for the identification of tissue suffering from ischemia or necrosis. Two were used in the studies presented within this thesis and are introduced here. Studies described herein made use of a regional ischemia model in which a coronary artery (left anterior descending; LAD) was occluded, preventing the flow of blood to tissue downstream. Upon completion of each trial, Evans Blue was added to the perfusate[28] while the LAD artery was occluded, and the heart was imaged (Figure 2.6a). With the occlusion in place, the dye stains tissue that remains perfused, leaving the area at risk (ischemic tissue) unstained. Thus, the region of tissue exhibiting reduced oxygenation during regional ischemia (as revealed by the spectroscopic images) can be compared to the region of tissue left unstained by Evans Blue. The "area at risk" is defined as that region of tissue that suffers ischemia as a consequence of reduced coronary blood flow. Ideally, these regions, defined by spectroscopic imaging and by Evans Blue staining, should correspond exactly.

Tissue suffering from necrosis can be identified by using a different stain, namely triphenyl tetrazolium chloride (TTC), as follows: once the experimental procedure is completed, the heart is cut along the short axis into slices 1 cm thick and the slices are then soaked in TTC. (69) When TTC enters living cells, it is reduced by NADH to form an insoluble red dye. Thus, viable tissue is stained red, but necrotic (dead) tissue which has lost its NADH/NAD$^+$ pool remains unstained (Figure 2.6b). Finally, the area at risk (tissue not stained with Evans Blue) and regions of necrosis (tissue not stained by TTC) can be separately dissected and weighed. This provides a measure of the area at risk and necrotic tissue as proportions of the left ventricular mass. While TTC staining was used in all three imaging studies, Evans Blue was only used for the last two studies.

---

[28] From the Latin *perfusio* (meaning *pouring*), it refers to the fluid that feeds the tissue. In this case, the perfusate is blood. Similarly, perfusion is the convective process by which oxygen is transported to the tissue. Reperfusion is restored perfusion after a period of ischemia.

A. Evans Blue Staining:

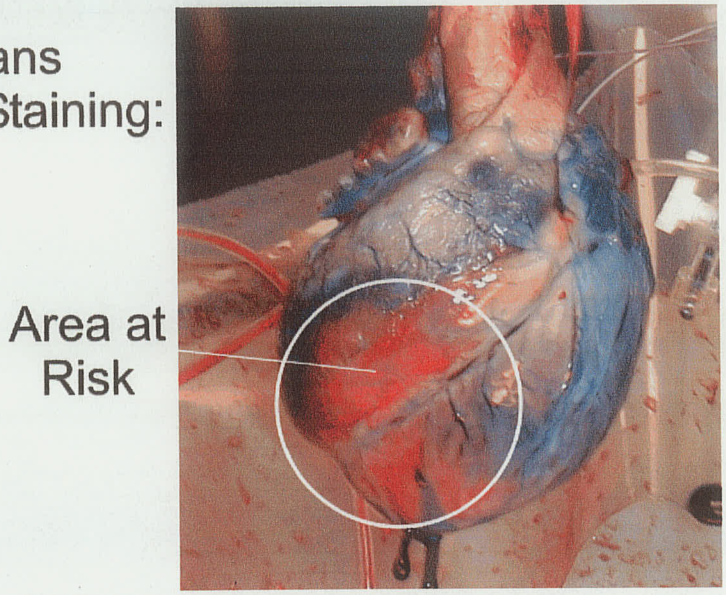

B. TTC Staining:

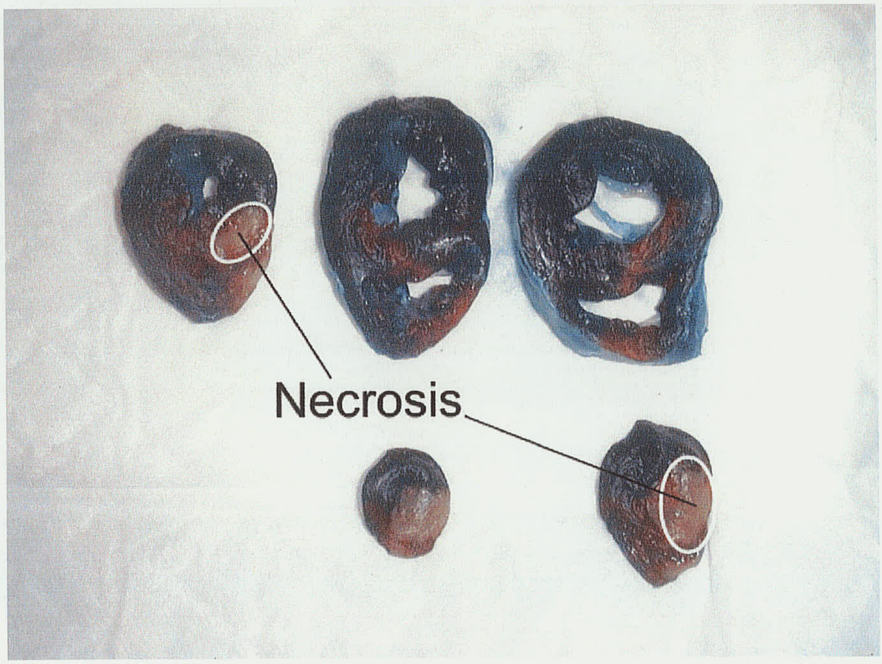

Figure 2.6. Identification of the area at risk and necrotic regions with Evans Blue and TTC staining, respectively. The top image was taken from the Apr. 22 trial of the beating heart study (Chapter 5). The bottom image was taken from the Feb. 08 trial of the *in vivo* study (Chapter 6).

2.2. Oxygen Transport

Appreciation of the effects of ischemia on hemoglobin oxygenation requires an understanding of the mechanisms of normal oxygen transport and oxygen consumption, especially as they pertain to heme proteins. Although it has been known since the time of Galen (approx. 200 AD) that the heart was at the centre of circulation and that the arteries contain blood (instead of air[29]),(95)(p. 8) western science did not understand the pumping function of the heart and its role in blood circulation until 1628, when William Harvey published his *Anatomical Treatise on the Motion of the Heart and Blood in Animals.* (96) Since these historic discoveries, much more has been revealed about the role of oxygen in the nourishment of tissue. The following briefly describes the main features of blood transport, as they are currently understood. Moreover, since the physical principles of fluid mechanics play a critical role in determining oxygen transport, these will also be discussed.

2.2.1. Introduction

Oxygen transport through the body is governed primarily by two physical mechanisms: diffusion and convection. Mass movement of blood through the circulation transports oxygen via convection, whereas oxygen transport into and out of the circulation is governed by diffusion. For instance, in the lungs, oxygen diffuses from areas of high oxygen partial pressure in the alveoli to areas of low oxygen pressure in the

---

[29] The original belief that the vessels in the body carried air has been preserved etymologically, since the word *artery* is a derivative of the Greek *artēria*, meaning *windpipe*.

deoxygenated blood. In peripheral and cardiac tissue, oxygen diffuses from oxygenated blood in capillaries into oxygen-poor tissue.

2.2.1.1. Coronary Vasculature

In order to maintain cardiac function, the heart has its own vascular network (coronary arteries and veins).(227)(p. 609) Since the left and right coronary arteries branch away from the aorta immediately after it leaves the left ventricle (Figure 2.7), cardiac perfusion can be at least partially maintained, even in cases of decreased cardiac performance or low blood volume;(180)(p. 1404) if cardiac output is reduced slightly, oxygen supply to the cardiac muscle is maintained, although possibly at the expense of peripheral tissues.

While the exact branching pattern of the coronary vasculature is variable among hearts (even of the same species), some common elements exist. For instance, the left main artery bifurcates into the left circumflex artery and the left anterior descending (LAD) artery only a few centimetres away from the aorta; almost half of the time, a third branch is also observed.(205) The LAD runs along the anterior side of the heart between the two ventricles, often wrapping around the apex. Usually, two smaller arteries branch away from the LAD (first and second diagonal branches) to perfuse the anterior left ventricle, although more arteries may also be visible. In most cases, the anterior right ventricle is perfused by the right coronary artery.

Thus, occlusion of the LAD proximal to the left main coronary artery has a more significant impact on left ventricular perfusion than right ventricular perfusion. This is made more clear in Figure 2.8. In this figure, Evans Blue dye has been added to the

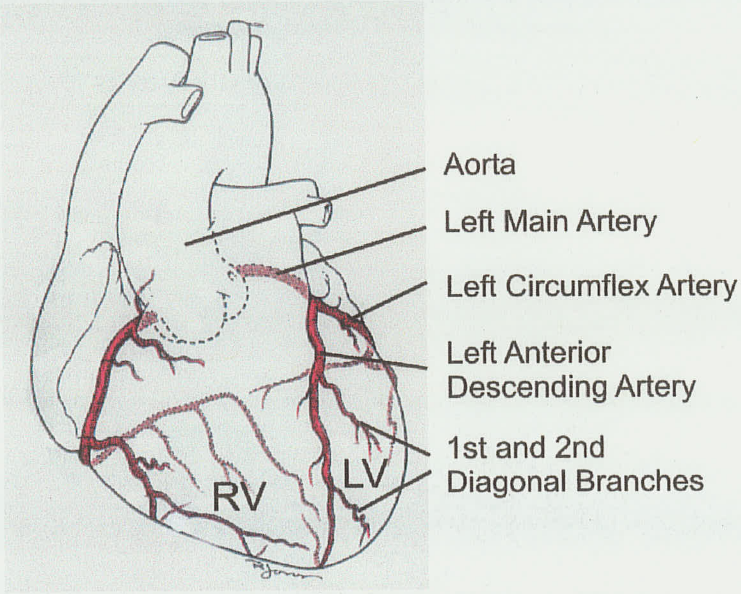

Figure 2.7. Anterior view of the coronary vasculature. The left anterior descending artery perfuses the left ventricle.
LV = Left ventricle, RV = Right ventricle. Adapted from Seeley, 1998.

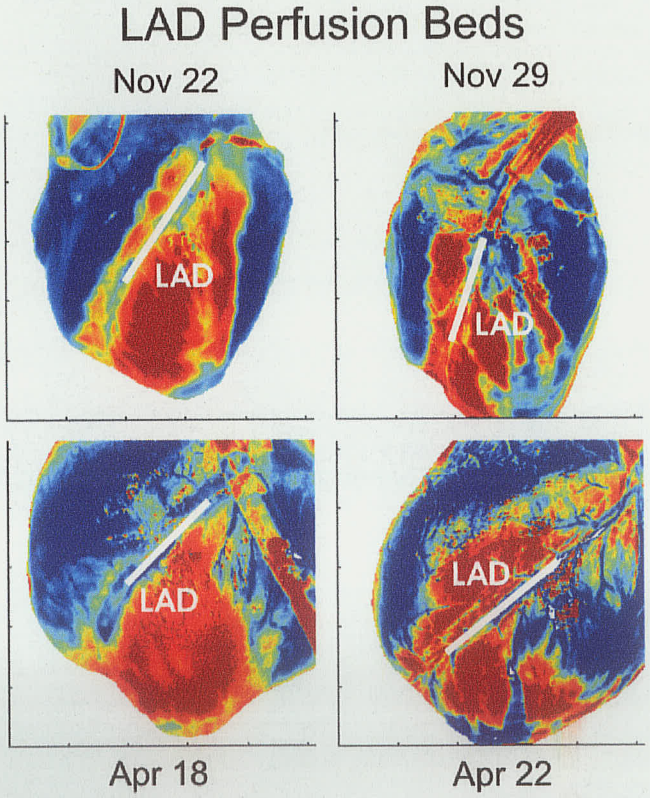

Figure 2.8. Left anterior descending (LAD) artery perfusion beds. The beds are highlighted in red. The position of the LAD artery is shown by the white bar.

perfusate of four individual pig hearts (these hearts were part of a study reported in Chapter 5), for which the LAD had been occluded. Thus, well-perfused tissue is shown in blue and ischemic tissue (in the LAD perfusion bed) is shown in red. While there is some slight variation in the placement of the occlusion along the LAD, it is clear that the size of the LAD perfusion bed (particularly in the right ventricle) is also variable.

2.2.1.2. Oxygen Diffusion into Cardiac Tissue

Oxygen is transported in the bloodstream by hemoglobin. 98% of blood oxygen is bound to hemoglobin in the red blood cells.(227) Oxygen moves into cardiac tissue from the blood through the capillaries, where the vascular walls are thinnest. Capillary diameters can be as narrow as 4-5 μm,(98,265) (although some reports suggest a diameter closer to 8 μm (227)) with walls consisting of a collagen tube covered with a single layer of endothelial cells. This layer provides the most significant resistance to oxygen transport from blood to tissue;(268) the muscle cell walls and the red blood cell walls provide relatively little resistance.(48,98,106) Red blood cells are also typically larger in diameter (8 μm) than capillaries, forcing them to narrowly squeeze through the capillary lumens. This has the effect of increasing the separation distance between the red blood cells and decreasing the available capillary surface area through which oxygen can pass into the tissue.(98,230)

It was recognized early in the 20th century that capillary spacing in heart tissue is fairly regular,(136) and that every cardiomyocyte is in contact with a capillary. Thus, it was initially believed that each capillary perfuses a cylinder of tissue surrounding the vessel and oxygen transport is driven by the difference in oxygen pressure between the vascular space and the myocyte intracellular space (estimated at 1-2 mm Hg). However, these studies failed to account for barriers to oxygen diffusion, such as cellular membranes and capillary wall structure. These factors, along with variability in oxygen diffusion coefficients and the particulate nature of blood, raise the required pressure difference to between 10 and 20 mm Hg,(68,102,268) a range that is more consistent with empirically-determined estimates of the actual oxygen pressure difference.(83,248)

2.2.2. Hemoglobin Structure

Hemoglobin[30] (Hb) is a complex protein composed of four subunits, each made up of one heme compound (the oxygen-binding unit) and one globin protein chain.[31] Many varieties of Hb (with different compositions) have been identified, and Hb A is the variety most common in humans, comprising about 95% of normal adult Hb (36) (p. 4), although Hb found in human fetuses has slightly different structure and chemical properties.(4) Hb also varies among different animal species, and various pathological Hb varieties have been identified.

Hb exhibits four levels of structure. The specific amino acid sequences within the globin chains make up the primary structure of Hb. Hb A contains two different types of globin chains (two each of α and β), which have different primary structures. For instance, α chains begin with the acids valine, leucine, serine, whereas β chains begin

---

[30] From the Greek *haima* (meaning *blood*) and the Latin *globulus* (meaning *globule*), this term was first used by Hoppe-Seyler to describe the pigment of blood in 1864.(103)

[31] The structure of hemoglobin was revealed by X-ray crystallographic studies in the 1950's and 1960's. For their work on the structure of globular proteins, Max Perutz and John Kendrew shared the Nobel Prize for Chemistry in 1962.

with valine, glutamine, and leucine.(4) The β chains also contain more amino acids than α chains (146 for β, 141 for α).

Within each globin chain, the amino acids are arranged in helical sections, separated by amino acids in non-helical formations (the secondary structure); these sections are arranged to form the globular tertiary structure (Figure 2.9a). The helical sections are labelled A, B, C, ..., with each amino acid within the helix assigned a number. For example, the glycine residue[32] in the 22nd position along the globin may be labelled as either residue 22 or residue B3, as it is the third residue in the B helix. The non-helical sections are named by the helical sections at either end (e.g. the non-helical segment between helices C and D is named CD). Approximately 75% of the amino acids are within helices.(261) (p. 20) The quaternary structure of hemoglobin describes the relative positions of the globin chains, which are are held together by salt bridges.[33]

Although the primary structure varies among animal species, Hb variety, and among α and β chains, the secondary, tertiary, and quaternary structures are remarkably similar. Since the oxygen-binding capacity of the hemoglobin and the visible and near-infrared spectra depend largely on the quaternary structure and the heme structure (see Sections 2.2.3 and 2.3.3) rather than the primary structure, variations in these properties between species are minor.

---

[32] All amino acids have a carbon atom bound to an NH_2 group, an H atom, a COOH group, and a group that is unique to the amino acid. This unique group is called the residue. When amino acids are linked together in a polypeptide chain (protein), an H from the NH_2 and an OH from the COOH form water and are removed. The remaining CO from one amino acid binds to the NH from the neighbouring amino acid to form the chain.

[33] Salt bonds, or salt bridges, are interactions between two ionic protein groups of opposite charge.(257) (p. 175)

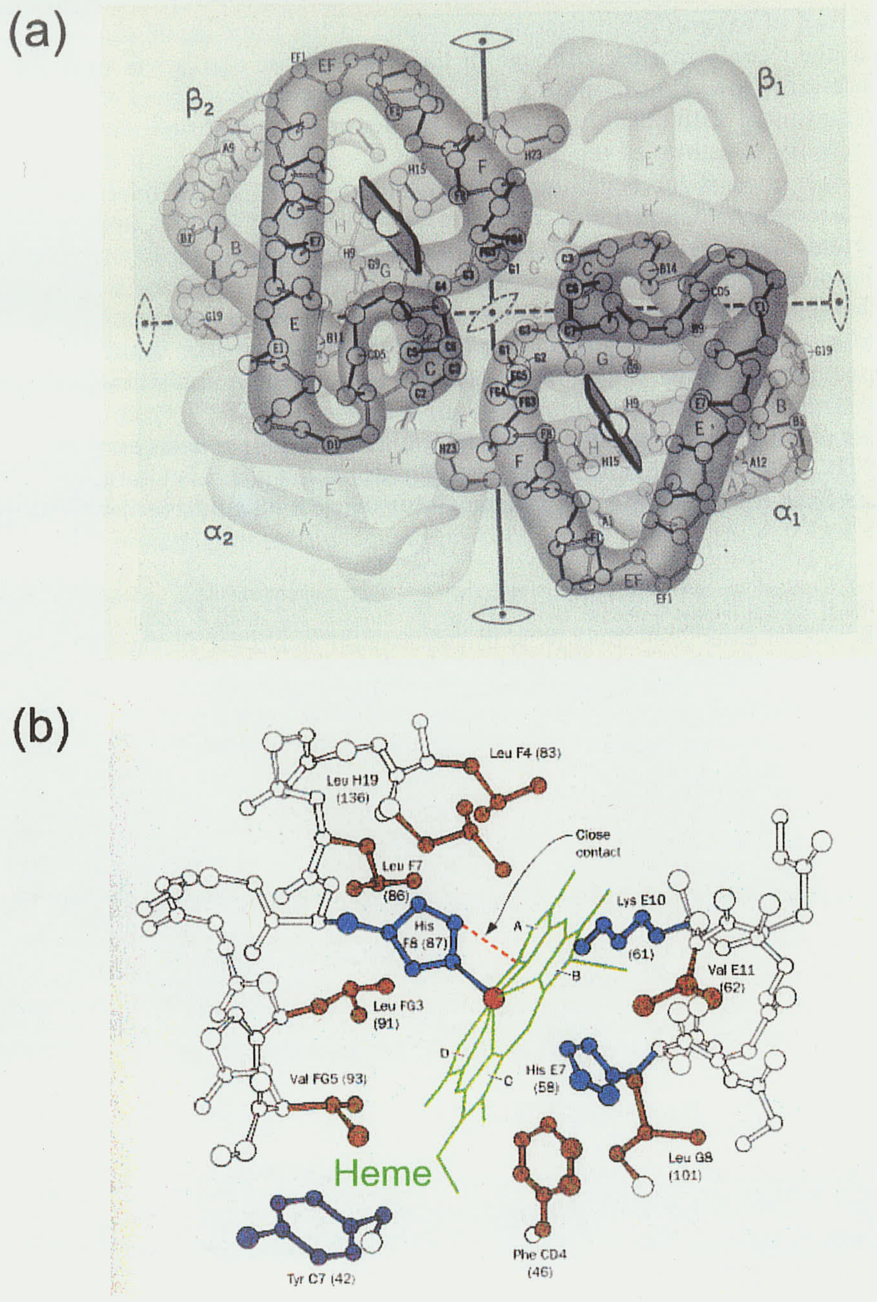

Figure 2.9. Hemoglobin structure. (a) The secondary, tertiary, and quaternary structure, as well as the positions of the hemes relative to the globin chains are depicted. From Weissbluth, 1974 (b) The heme environment. The amino acid residues nearest the heme are coloured, and the bond between the heme iron and the F8 histidine residue is shown. From Voet, 1995.

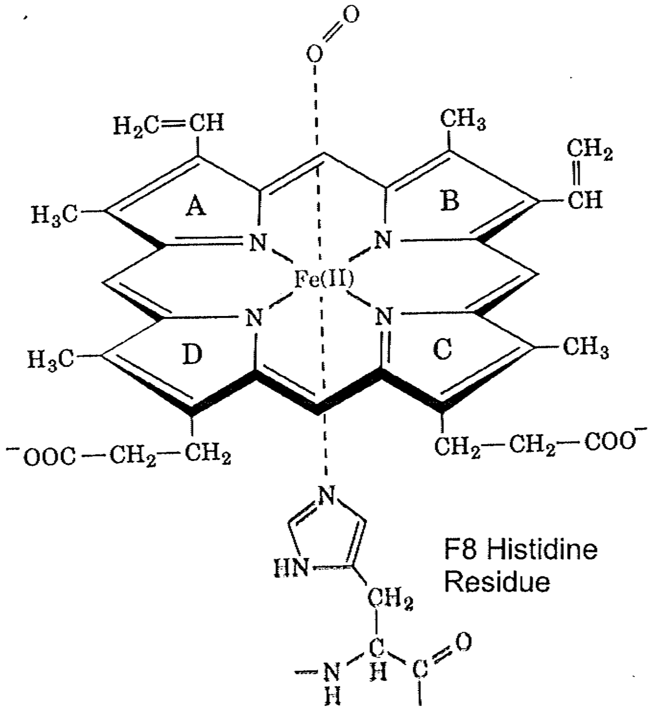

Figure 2.10. Heme Structure. The iron atom (in the ferrous state) at the centre is surrounded by a porphyrin ring to which methyl, vinyl, and propionate side chains are attached. From Voet, 1995 (p. 216).

Attached to each globin chain is a heme group, which is the oxygen-carrying component of hemoglobin (Figure 2.9b). The globins protect the hemes, preventing their autoxidation[34]. Each heme consists of an iron atom in the ferrous state[35], surrounded by a porphyrin ring and side chains around the periphery of the ring. (Figure 2.10). Iron has an octahedral binding structure, meaning that it can share covalent bonds with up to six atoms.[36] Four of its binding sites are occupied by four co-planar nitrogens in the porphyrin ring. The fifth site is occupied by the nitrogen atom of the F8 histidine residue

---

[34] Literally meaning *self-oxidation*, it refers to the formation of a hydroperoxide (OOH) on the compound.(126) (p. 528)

[35] Ferrous iron has a charge of +2. Iron also has a ferric state, which has a charge of +3.

[36] Discussions of binding structures and binding symmetries are available.(10,51)

in the globin chain,[37] and in deoxy-Hb, the sixth binding site remains empty. In this case, the iron is said to have tetragonal binding symmetry and the interaction of the electron orbitals of iron with the surrounding ligands results in the displacement of the iron atom from the plane of the porphyrin ring. The exact value of this displacement lies between 0.4 and 0.8 Å for Hb,(107,154,191,219) but it has been reported to be lower for myoglobin.(229)

When an oxygen molecule binds to the sixth hemoglobin binding site, the iron binding symmetry remains tetragonal, but the interaction with the oxygen molecular orbitals reduces the total spin of the iron, and it is no longer displaced from the porphyrin ring. For deoxy-Hb, the heme iron is in the ferrous state, so deoxy-Hb is a ferrous Hb derivative. However, oxy-Hb is more complicated and the formal description of the oxygen-iron bond has been fiercely debated since two models were proposed in 1964. Pauling(189) proposed that the iron remains ferrous, in order to explain the diamagnetism of oxy-Hb, whereas Weiss(259) proposed an electron transfer from the iron atom to the oxygen molecule (leaving the iron in the ferric state). In complex molecules such as Hb, charge transfer is very difficult to determine exactly,(4)(p.26) but experimental results have tended to favour the Weiss description.[38] Nevertheless, oxy-Hb continues to be classified as a ferrous derivative, since it changes to deoxy-Hb easily and ferric Hb does not bind oxygen.(36,261,274)

Other ferrous derivatives include Hb bound with carbon monoxide or nitric oxide in the 6th position. Among the ferric derivatives, in which the iron atom has only five

---

[37] While the heme-binding histidine is in position 87 in the α chain and position 92 in the β chain, it is the eighth residue in the F helix in both globin chains and is thus labelled F8.

[38] A succinct review of the debate surrounding this issue is available.(168),(204,218,233)

valence electrons, the most common and significant is methemoglobin[39] (metHb). In metHb, the iron atom is oxidized and a water molecule is bound in the 6th position, preventing it from binding oxygen. While metHb is regularly produced in the red blood cells, normal levels are maintained around 1%. A variety of other ferric derivatives exist, but these are not physiologically relevant.(274)

The geometry of the Fe-O_2 bond has also been in debate for several decades, with two models gaining the most discussion. Griffith proposed a coplanar model, in which the two oxygen atoms lie parallel to the porphyrin ring,(89) whereas Pauling suggested a coaxial model, in which the histidine nitrogen, iron, and oxygen atoms are approximately linear.(189) Subsequent analysis and modelling of the electronic orbitals have supported Pauling's model.(62)

The binding of compounds to the heme is influenced by the globin environment of the heme. The heme binding site is not exposed on the outside of the molecule, but is rather surrounded by the globin chain in what is known as the heme pocket. The globin chains nearest the heme iron are the E and F helices (Figure 2.9b).(257) Variations in the quaternary structure of hemoglobin change the oxygen affinity of hemoglobin by changing the ease with which oxygen molecules can reach the binding site.

---

[39] Also known as hemiglobin or ferrihemoglobin. In the latter system of nomenclature, deoxy-Hb is referred to as ferrohemoglobin. Discussions of nomenclature are available.(274) (pp. 11-14),(147) (pp. 208-211)

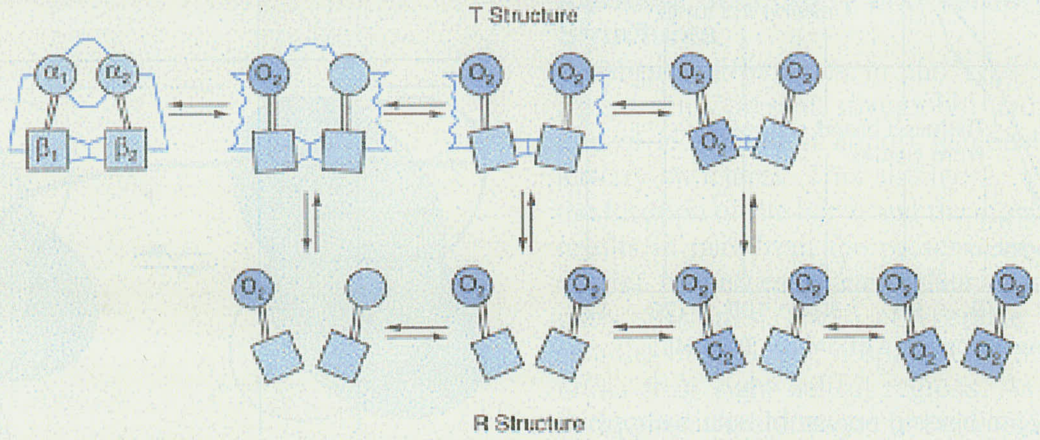

Figure 2.11. Changes in quaternary structure with oxygen binding. From Murray, 1996.(173)

2.2.3. Oxygen Binding

2.2.3.1. Hill Equation

Despite the significant differences in primary structure between the α and β chains (and between globins of porcine and human Hb), the tertiary structures of the chains are remarkably similar. It should be noted that there are two main tertiary conformations – known as the 'T' (tense) and 'R' (relaxed) states. These names reflect the presence or absence, respectively, of additional salt bridges between amino acid residues in the T state. Hemoglobin chains have a lower oxygen affinity in the T state because these bonds stabilize a quaternary structure that restricts oxygen binding. Deoxy-Hb is usually found in this state.

If oxygen binds to one heme, though, some salt bonds weaken. This increases the likelihood that oxygen will bind to the other hemes, and when all four hemes are oxygenated, all of the salt bonds characteristic of the 'T' state are disrupted and replaced by those characterizing the 'R' state of oxy-Hb (Figure 2.11).(173) Because the oxygen affinity of isolated α and β chains is comparable to that of fully oxygenated Hb rather than fully deoxygenated Hb,(35) the oxygen affinity of oxy-Hb is deemed to be its "natural state", and the extra structure inherent in deoxy-Hb reduces the oxygen affinity from this state.

The fact that binding of oxygen to one heme of Hb increases the oxygen affinity of other hemes within that Hb molecule is referred to as cooperativity. To understand the basis for expressing cooperativity in mathematical terms, it is perhaps best to begin with a discussion of myoglobin (Mb), since Mb consists of a single heme and a single globin chain. Thus, myoglobin is either oxygenated (MbO_2) or deoxygenated (dMb), so the equilibrium constant K_M for the transition between these two states can be expressed as

$$K_M = \frac{[MbO_2]}{[dMb][O_2]}, \qquad (2.2)$$

where square brackets indicate concentration. If we define x to be the oxygen partial pressure ($[O_2]$) and y to be the oxygen saturation ($[MbO_2]/([dMb]+[MbO_2])$), then the above equation can be rewritten as

$$y = \frac{K_M x}{1 + K_M x}. \qquad (2.3)$$

Equation 2.3 is known as the Hill equation[40], and there is an unwritten exponent of 1 over the x. This value of 1 is known as the Hill number and reflects the fact that Mb has only one oxygen binding site. Since there are four binding sites in hemoglobin, the analysis is more complex, but results in a similar equation, which can be written as

---

[40] A.V. Hill proposed this equation to describe empirical data relating the equilibrium of Hb with oxygen pressures even before it was known that hemoglobin has four oxygen binding sites.

$$y = \frac{Kx^4}{1 + Kx^4}. \qquad (2.4)$$

This is the Hill equation for Hb. (100) If Hb saturation fit this equation exactly, then Hb would either be completely oxygenated or completely deoxygenated (i.e. Equation 2.4 represents "all or nothing" oxygen binding). Hb would exhibit maximally cooperative oxygen binding and the Hill number would be 4 (seen in the exponent). In truth, although there is a great deal of cooperativity in oxygen binding, it is not maximally cooperative, and the Hill number has been empirically determined to be in the range of 2.7 – 3.0.(68,191)

Plots of the Hill equation (known as oxygen saturation curves) describe the oxygen saturation (So_2) of Hb (or Mb) for a given oxygen pressure[41] (Figure 2.12a).(36) The oxygen saturation curve of Hb has a sigmoidal[42] shape, demostrating the cooperativity of Hb. When oxygen pressures are very low, most of the hemoglobin is deoxygenated and the oxygen affinity is low. At higher oxygen pressures, more Hb molecules have oxygen bound to at least one of their hemes and the overall oxygen affinity increases. When oxygen pressures increase beyond approximately 50 mm Hg, most of the Hb has oxygen bound to all four of its hemes and increases in oxygen pressure do little to saturate the remaining Hb binding sites. In contrast to the oxygen saturation curves, plots of log [y/(1-y)] against log x are known as Hill plots (Figure

---

[41] Numerical values for the oxygen saturation curve (also known as the oxygen dissociation curve) are available.(8,231,249,274)

[42] From the Greek *sigma* (18th letter of the alphabet) and *eidos* (meaning *resemblance*). The shape resembles an old form of the letter, which gave rise to the letter S. This shape is also seen in the form of the integral sign of mathematics, which also took the shape of the letter *S*, standing for "summation".

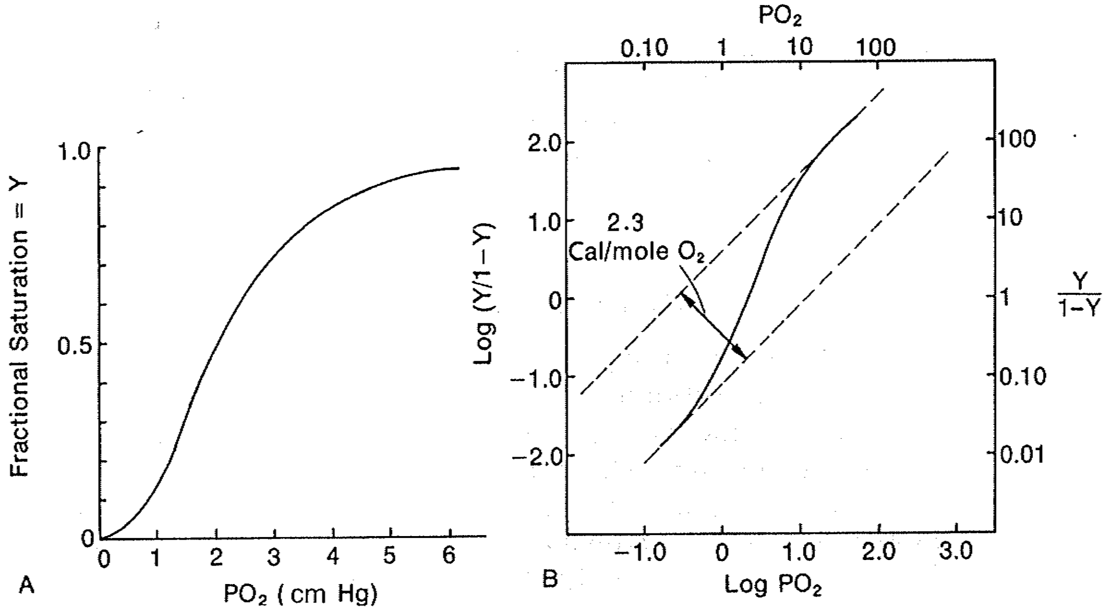

Figure 2.12. (a) Oxygen saturation curve of hemoglobin. (b) Corresponding Hill plot. From Bunn, 1977. N.B. In the original document, the x-axis of part (a) was mislabelled as mm Hg.

2.12b). The slope of the curve in the middle portion (corresponding to physiological oxygen pressures) is equal to the Hill number.

It is interesting to note that the above discussion applies the usual definition of So_2 (Hb) as the percentage of Hb molecules for which all four binding sites are occupied by oxygen.(237) However, since Hb saturation is almost invariably measured using spectroscopic techniques,(24,41) this parameter is in fact rarely measured. Instead, since each heme chromophore will absorb according to whether or not oxygen is bound to its central iron atom (regardless of whether the other hemes in the Hb molecule are oxygenated, see Section 2.3.3), spectroscopic techniques will measure the proportion of hemes that are oxygenated. Since Hb is not maximally cooperative, these results will differ slightly. Thus, the familiar oxygen saturation curves that appear in textbooks do not strictly reflect the usual textbook definition. For the purposes of this thesis, however, the distinction between these definitions is not significant and will be neglected.

2.2.3.2. Bohr and Carbamate Factors

The exact shape and position of the oxygen saturation curve depend upon several factors, including pH and temperature, but it can be described by two parameters – the Hill number, which describes the shape of the curve, and the p_{50}, which is the pressure at which hemoglobin is half-saturated and describes the position of the curve. The dependence of saturation on pH is well-known as the Bohr effect,[43] but the So_2 is dependent on both carbon dioxide levels and pH, as well as 2,3-biphosphoglycerate (BPG)[44] and temperature.

A thorough treatment of the dependence of the oxygen saturation curve on these factors, as well as how they interrelate, is available,(274) and only a brief overview is provided here. Even before the dependence on CO_2 was discovered, it was well-known that the oxygen affinity of hemoglobin decreases with an increase in temperature.(22,104) While the relationship between temperature and oxygen affinity was investigated in succeeding years, most studies described the effect of temperature on oxygen affinity at individual oxygen pressures rather than over the entire So_2 curve. Zwart et al.(276) found that while a change in temperature from 22° C to 42° C moved

---

[43] Named after Christian Bohr, a 19th-century Danish physiologist. The initial discovery of Bohr et al. was actually that the p_{50} is dependent on local carbon dioxide pressures.(27) It was discovered a decade later that the observed effect was due to carbonic acid as a proton donor rather than to carbonic acid itself.(4,43,185)(p.180) While Bohr was famous for his achievements, his son Niels perhaps outstripped him, winning the Nobel prize for physics in 1922 for his work on atomic structure that led to the electron orbital theory discussed in Section 2.3.3.2. His grandson Aage also won the Nobel prize for physics in 1975.

[44] Also known as 2,3-DPG (diphosphoglycerate)

the p_{50} from 10.4 to 32.3 mm Hg, it had no significant effect on the Hill number. Thus, the temperature coefficient (TC, the rate of change of oxygen saturation with temperature), defined as

$$TC = \partial \log p_{O_2} / \partial T \qquad (2.5)$$

is independent of the actual So_2.

Changes in pH, on the other hand, affect both the p_{50} and the Hill number, and the impact is more significant than that due to temperature. The effect on the p_{50} is described by the proton Bohr factor and is defined as

$$\Phi_H = [\partial \log p_{O_2} / \partial pH]_{p_{CO_2}} . \qquad (2.6)$$

Proton Bohr factor values vary with So_2 values, indicating that the saturation curve will be distorted, moving more in response to changes in pH in some parts of the curve than in others. This results in changes to the slope in the Hill plot, and by extension the Hill number.

As the influence of pH on So_2 is known as the proton Bohr factor, the influence of carbon dioxide is known as the carbamate Bohr factor, defined analogously as

$$\Phi_C = [\partial \log p_{O_2} / \partial \log pCO_2]_{pH} . \qquad (2.7)$$

The effect of the carbamate Bohr factor is less significant than that of the proton Bohr factor, but it also affects the Hill number as well as the p_{50}.

The pH and carbon dioxide levels in blood maintain an equilibrium according to the following relation:

$$CO_2 + H_2O \leftrightarrow H_2CO_3 \leftrightarrow H^+ + HCO_3^- . \qquad (2.8)$$

Carbon dioxide (CO_2) and water combine to form carbonic acid, which then dissociates into hydrogen ions and bicarbonate (HCO_3^-). If CO_2 levels increase *in vivo*[45], the system responds by trying to reduce this level. Hydrogen and bicarbonate levels increase as a result. Similarly, if pH decreases (hydrogen ion levels increase), carbon dioxide levels will increase in response.

There are three significant differences between the carbamate and proton Bohr factors. First, the carbamate factor is positive (increased CO_2 results in increased p_{50}) whereas the proton factor is negative (increased pH results in decreased p_{50}). However, since increases in carbon dioxide and decreases in pH both reflect acidosis, they have complementary effects on the saturation curve. Second, the carbamate Bohr factor is much more sensitive to changes in oxygen saturation than the proton Bohr factor, and it has a more significant effect on the Hill number. Finally, the carbamate factor increases monotonically with decreasing oxygen saturation, whereas the proton Bohr factor has a maximum at an So_2 of 70%. Thus, the effect of the carbamate factor on the Hill number is greatest at low So_2, whereas the effect of the proton factor is greatest for moderate So_2.

Finally, BPG was first observed in red blood cells over 50 years ago,(201) but its effect on the oxygen saturation curve was not discovered until 1967.(21,40) As the ratio of BPG to Hb increases from 0.1 to 1.2, the p_{50} increases from 17.2 to 27.0 mm Hg, demonstrating a strong influence of BPG on the oxygen saturation curve (physiological BPG:Hb ratios are approximately 0.9).(4) (p. 2)

All of the molecular influences on oxygen affinity exert their effects by promoting changes in the Hb quaternary structure. Since the sigmoidal nature of the oxygen

---

[45] Latin for *in living (tissue).*

saturation curve was first discovered,(26) the chemical interactions responsible for cooperativity have been studied and are ascribed largely to changes in the quaternary structure.(191,192)

Unlike oxygen, that only binds to the heme, hydrogen ions and carbon dioxide can bind to many locations on the globin chains. When Hb binds these species, its quaternary structure is altered, decreasing the accessibility of the heme to oxygen. BPG acts slightly differently in that it binds only between the β chains, stabilizing the tense state characteristic of deoxy-Hb. Because of this, BPG only affects the oxygen affinity of the tetramer. It has no effect on monomer or dimer chains. Thus, in a pure Hb solution, increasing the BPG to Hb ratio beyond 1 would have no further effect on the oxygen saturation curve. In red blood cells, however, even though BPG can not traverse the cell membrane, it could exert an indirect effect; increasing BPG concentrations continue to affect the pH values which further change the oxygen affinity.(57)

2.2.4. Fluid Mechanics

As mentioned above, there are two main forces which drive oxygen transport – diffusion and convection. Diffusion is the process whereby a substance moves from areas of high concentration to areas of low concentration, and the flux (or rate of flow) can be modelled mathematically by Fick's first law(105)

$$F_i = -D\nabla c_i, \qquad (2.9)$$

where F_i, c_i, are the flux and concentration of the i^{th} constituent and D is the diffusion constant, which reflects the ease with which the constituent moves through the medium.

Convection, on the other hand, is bulk movement, for example as embodied by oxygen transport through the vasculature. Since oxygen is transported by blood, it would be useful to understand arterial blood flow thoroughly, but many factors make precise mathematical modelling of coronary flow very difficult. These include flow pulsatility and turbulence, and the curvature, branching, and tapering of arteries. Reviews of fluid dynamics and the biophysics of arterial flow are available,(56,79,190) and the general nature of these influences is outlined below.

Ultimately, circulatory flow is driven by blood pressure gradients. Pascal's Principle[46] states that if the fluid pressure in a vessel is uniform, then the fluid is motionless throughout the vessel. When the pressure is not uniform, the flow through a vessel (under ideal conditions) is proportional to the pressure difference between the ends of that vessel, according to Poiseuille's Law[47]

$$Q = \frac{\pi \Delta \mathrm{P} r^4}{8\eta l}. \qquad (2.10)$$

Here, Q is the flow, ΔP is the pressure difference between the two ends of the vessel, r is the radius of the vessel, η is the viscosity, and l is the length of the vessel. Since, by Ohm's Law[48], the flow is also inversely proportional to the vascular resistance R,

$$Q = \frac{\Delta P}{R}, \qquad (2.11)$$

the resistance is shown to be proportional to the viscosity and inversely proportional to the fourth power of the radius. In fact, physiological regulation of blood pressure and

---

[46] Named after Blaise Pascal, a 17th-century French mathematician, physicist, and mystic.

[47] Named after Jean L.M. Poiseuille, a 19th-century French physiologist and physicist.

[48] Named after Georg Ohm, a 19th-century German physicist.

flow relies heavily on this relationship between flow and vascular radius. Adrenergic, cholinergic, and metabolic regulators of vascular blood flow act by adjusting the vessel diameter.

Poiseuille's Law is valid for ideal conditions, but application to conditions in the vasculature is much more complicated. For example, local reductions in arterial cross-sectional areas of up to 70% have shown to decrease flow by less than 10%, even though Poiseuille's law would suggest that such a reduction in area should reduce flow by over 90%.(151,170) However, these studies involved only a local reduction in area, mimicking atherosclerotic plaques; Poiseuille's law applies strictly to cases where vascular radius is approximately constant along the entire length of the vessel.

At the heart of blood circulation, though, is cardiac output. Cardiac output is defined as the stroke volume (volume of blood ejected from the left ventricle during each contraction) multiplied by the heart rate, and it is determined by the preload (venous blood pressure), afterload (aortic blood pressure), cardiac muscle contractility, and heart rate. As the heart muscle contracts, ventricular pressure rises to levels above the aortic pressure and blood is ejected. This creates a pulse of high pressure which travels through the vasculature. Elasticity of the large arteries helps to propagate this pressure wave. Thus, the blood pressure remains pulsatile until the capillaries, where it levels out.

Resistance to this pressure wave is provided by both friction against the vascular wall and viscosity in the fluid. The frictional force F is equal to

$$F = \rho v^2, \qquad (2.12)$$

where ρ is the fluid density and v is the fluid velocity of the outer layer.(143) The increased friction near the edge of the vessel lumen results in lower velocity and laminar[49] flow develops.(269) However, branches and curvature increase the probability of turbulence developing within the vasculature.(79) For instance, at an arterial bifurcation, while most of the pressure wave is transmitted along the daughter branches, some is reflected, disrupting the laminar nature of the flow.

The likelihood for turbulence to develop can be quantitatively represented by Reynolds' number[50], *Re*,

$$\mathrm{Re} = \frac{vd\rho}{\eta} \qquad (2.13)$$

where v is the the velocity, d is the diameter, ρ is the density, and η is the viscosity. η/ρ is often expressed as the kinematic viscosity (μ), which represents the ratio of the inertia force (velocity times diameter) to the viscous force (kinematic viscosity). Turbulence typically develops when the Reynolds' number exceeds 2000, which can occur in the ascending aorta.(38,240) Reynolds' number, however, does not take into account the possibility of branches or curves in the vessel.

Another factor in determining resistance to blood flow is the viscosity of the blood. Blood viscosity is highly dependent upon the hematocrit[51] (which reflects the friction between particles in the blood), since the red blood cells constitute approximately 40% of blood volume in humans (Figure 2.13). The influence of blood cells on flow becomes particularly significant in very small arteries and capillaries, where the cell diameter is a significant fraction of the lumen diameter (see Section 2.2.1.2).

---

[49] Laminar flow is orderly flow in which particles maintain the same relative positions to each other in successive cross-sections of the vessel.(56) In this case, flow is higher near the centre of the vessel than near the edge because of the lower resistance.

[50] Named after Osborne Reynolds, an Irish 19th-century mathematician and physicist.

[51] From Greek *haima* (meaning *blood*) and *krinō* (meaning *to separate*), it is the percentage of blood volume occupied by cells.

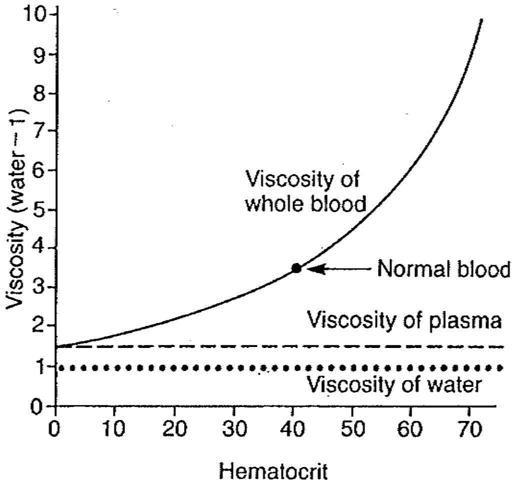

Figure 2.13. Effect of hematocrit on blood viscosity. From Guyton, 1971.

In coronary arteries, blood flow is also restricted by the beating of the heart itself. During muscle contraction (systole), extravascular pressure exceeds blood pressure and closes the vessels completely; as a result, LAD blood velocity falls nearly to zero during systole.(180)

2.3. Near-Infrared Spectroscopy

Near-infrared (near-IR) absorption band spectroscopy[52] (NIRS) is the analysis of matter based on its absorption band in the near-IR region of the spectrum. When light is absorbed by a molecule, its potential energy increases by an amount equal to the energy of the photon. Photons in the visible spectrum (400 – 700 nm) usually promote transitions between different electronic states of atoms and molecules, while energies of mid-IR photons (2500 – 25 000 nm) correspond to transitions between vibrational states with no change in electronic structure.

---

[52] From the Latin *spectrum* (meaning *an image*) and the Greek *skopeō* (meaning *to view*).

Between the visible and the mid-IR lies the near-IR spectral range. Absorption bands in this spectral range generally correspond to transitions in the electronic structure of individual molecules or weak overtones of fundamental vibrational transitions. Although near-IR light was discovered in 1800,[53](99) near-IR spectroscopy received little attention until the first near-IR spectrometers became available in 1954.(183) Over the past several decades, however, near-IR spectroscopy has become well-established as an analytical tool, and the application of NIRS to biomedicine in the late 1970's by Frans Jöbsis opened the floodgates for the development and refinement of this technique in biomedical applications.(118,119) These applications capitalize on the fact that there is only weak absorption band in this region, and this permits longer pathlengths and deeper penetration of the incident light, sufficient to recover physiologically relevant spectral information.

2.3.1. Measurement Techniques

In a traditional spectroscopy experiment, white light is separated into individual wavelengths by means of a prism or diffraction grating. The detected light intensity (after passing through the sample) is measured at each wavelength, and the absorbance A is then defined in terms of the transmitted light intensity I (with the sample in place) and the incident light intensity I_0,

$$A(\lambda) = \log [\, I_0(\lambda) / I(\lambda) \,]. \qquad (2.14)$$

---

[53] Infrared light was discovered by William Herschel, an 18th-century British musician and amateur astronomer and physicist born in Germany. He is also well-known for discovering the planet Uranus.

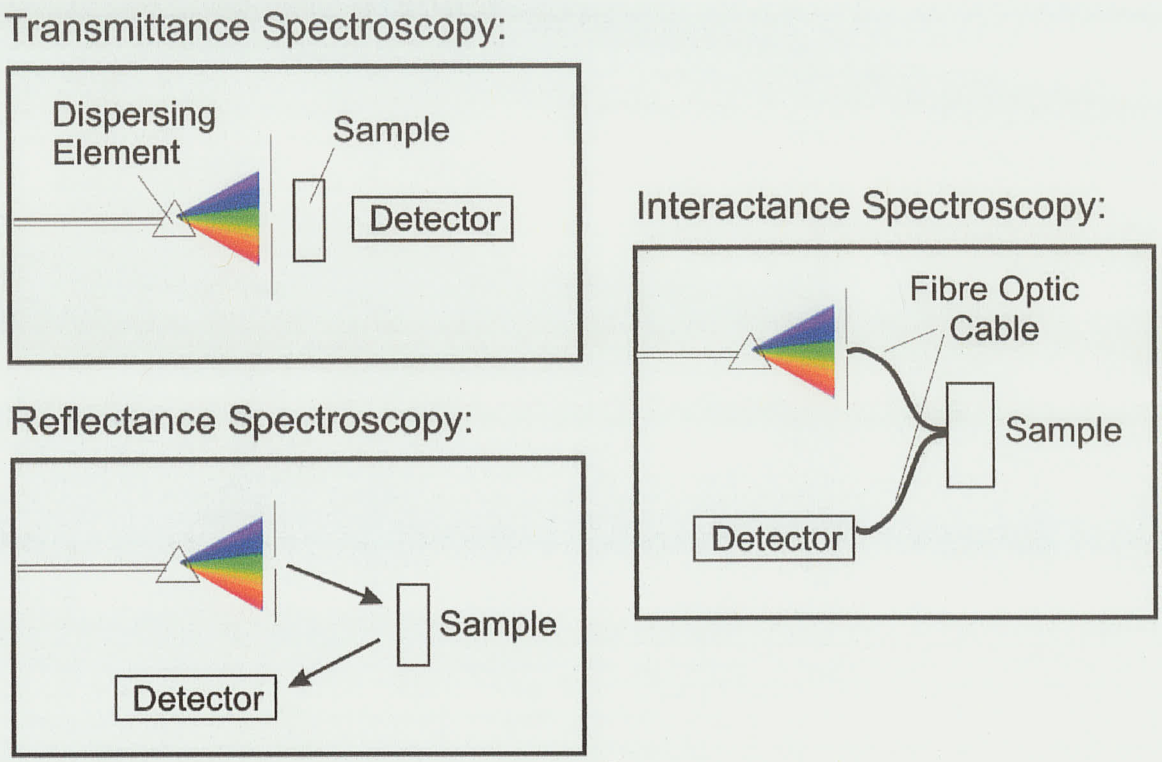

Figure 2.14. Different spectroscopic measurement techniques.

The spectrum of absorbance vs. wavelength is then interpreted to recover information regarding the chemical structure and/or composition of the sample.

Spectroscopic studies are usually carried out either as transmittance or reflectance measurements. In transmittance spectroscopy, the sample is placed between the light source and the detector, which detects light that has been transmitted through the sample (Figure 2.14). In reflectance spectroscopy, the source and the detector are on the same side of the sample and light reflected from the sample is detected. This approach can be advantageous for the analysis of highly scattering samples (such as tissue).

A third experimental technique, known as "interactance" spectroscopy, has also been used. This approach makes use of fibre optic bundles (optodes) that include many individual fibres. One bundle conveys light from the source to the sample, while another gathers light that has interacted with the sample and conveys it to the detector. The probe tip is placed in contact with the tissue, so that detected light is not merely reflected from the surface but rather has travelled through the tissue.

2.3.2. The Beer-Lambert Law

Equation 2.14 is an expression of two laws introduced in the 18th and 19th centuries to describe the transmission of light through absorbing media. Lambert's law[54] states that the intensity of light passing through an absorbing (and non-scattering) substance decreases exponentially with distance.(153)

$$I = I_0\, 10^{-Kl} \qquad (2.15)$$

In this equation, K is the extinction coefficient and l is the thickness of the sample. If the natural base of logarithms is used, then the exponent is the product of the absorption band coefficient μ and the sample thickness. The absorption band coefficient is 2.3 times the extinction coefficient.

Over a century later, August Beer adapted Equation 2.15 to relate the extinction coefficient to the quantity of absorbing substance, based on empirical data regarding absorption band of red light by solutions of inorganic salts.(15) If Lambert's law is reconfigured as

$$\log_{10} [\, I_0(\lambda) / I(\lambda)\,] = K\, l \qquad (2.16)$$

then the absorbance defined in Equation 2.14 can be expressed as

$$A = K\, l = \varepsilon\, c\, l, \qquad (2.17)$$

---

[54] Named after J.H. Lambert (an 18th-century German physicist and mathematician), the law was introduced by P. Bouguer in 1729 and is sometimes called the Lambert-Bouguer law.

where ε is the molar absorptivity[55] (measured in litres $mole^{-1}$ cm^{-1}) and c is the concentration of the chromophore[56] (measured in moles / litre). This is known as Beer's law or the Beer-Lambert law.[57](17) A straightforward extension of this law is the case of multiple absorbers within a sample. The absorbance by each chromophore is proportional to the corresponding concentration, and the total absorbance is simply the sum of each individual absorbance.

$$A = A_1 + A_2 + \ldots = \varepsilon_1 c_1 l + \varepsilon_2 c_2 l + \ldots \qquad (2.18)$$

These relations neglect scattering within the sample. In highly-scattering media such as tissue, detected photons have travelled a distance much longer than the sample thickness. Since the absorbance is proportional to the actual pathlength travelled by photons, the differential pathlength factor (DPF, defined as the ratio of actual pathlength to source-detector separation) is included in the equation.(53,54,66) A final term B is added to account for losses due to geometrical configuration and scattering.(129) Changes in scattering properties of tissue (possibly due to changes in blood volume) can result in shifts of the baseline of acquired spectra.

$$A = \varepsilon_1 c_1 l\, DPF + \varepsilon_2 c_2 l\, DPF + \ldots + B \qquad (2.19)$$

Of course, scattering is also what allows for reflectance and interactance spectroscopy, as light is scattered through the sample back toward the source. While the

---

[55] Previously referred to as the extinction coefficient, the extent to which light of a particular wavelength λ is absorbed by a chromophore is now known as "molar absorptivity". This quantity is governed physically by the energies of corresponding molecular orbitals and the selection rules governing transitions between those orbitals.

[56] Absorbing element within the sample

[57] Although Beer's contribution is fundamentally based on the previous discovery of Bouguer and Lambert, Equation 2.17 is known either as Beer's Law or the Beer-Lambert Law. In order to give credit where credit is due, it will be referred to in this thesis as the Beer-Lambert law.

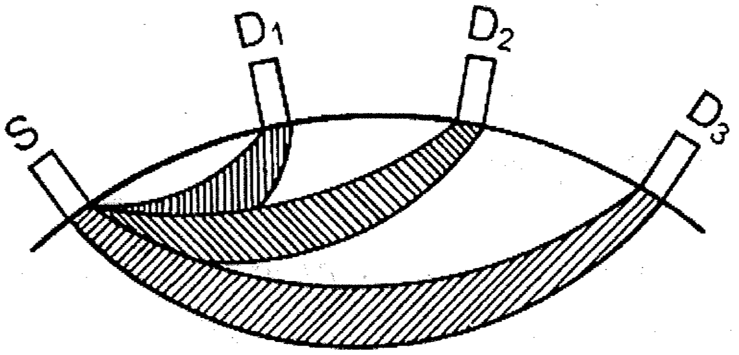

Figure 2.15. Photon paths in tissue. Scattered photons that are detected further from the source are more likely to have penetrated more deeply. From Frackowiak, 2001.(72)

paths travelled by photons, as well as the optical pathlengths, vary substantially for different photons, the mean optical pathlength can be used for spectroscopic determination of absorber concentrations. Monte Carlo simulations have shown that the probability distribution for photons recovered from any particular point "D" is a banana shape (Figure 2.15). The effect of scattering on the mean optical pathlength will be discussed further in Chapter 3.

In cardiac tissue, the most prominent near-infrared-absorbing molecules are hemoglobin, myoglobin, and water. Spectra of oxygenated forms of Hb and Mb are very distinct from spectra of deoxygenated forms (Figure 2.16). However, since the structure of Mb is very similar to that of individual Hb subunits, its spectra are nearly identical to those of Hb.(4,226) While the contribution of Mb to the near-IR signal in previous studies of skeletal muscle has often been deemed insignificant relative to that of Hb,(157,228), the contribution of Mb in heart spectra may be significant, as discussed in Chapters 4 and 5. Oxidized cytochome c oxidase also has a broad, relatively weak

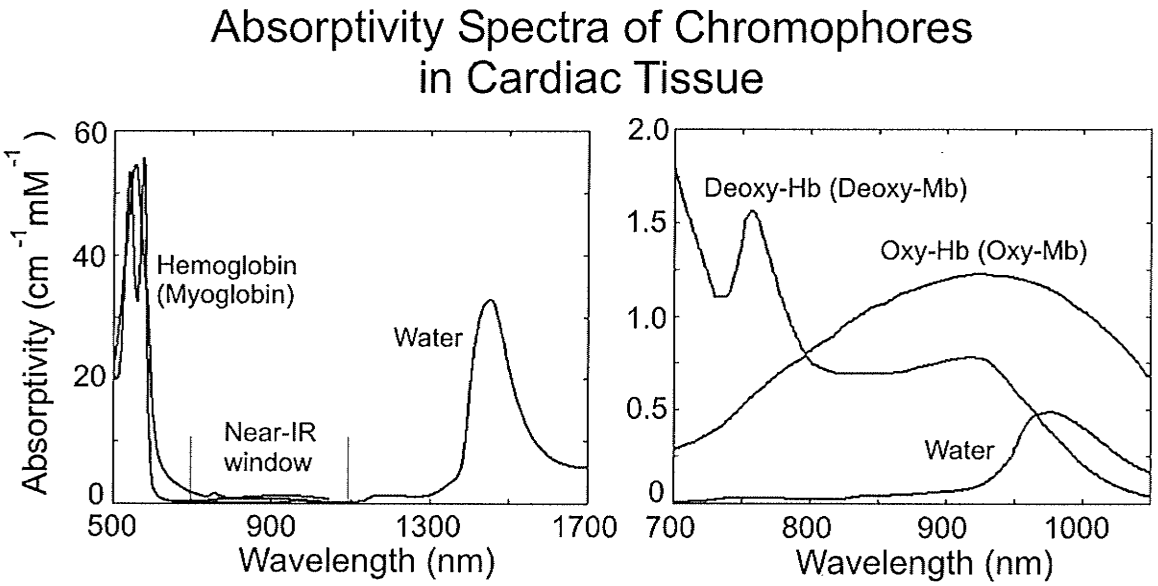

Figure 2.16. Absorptivity spectra of chromophores found in cardiac tissue. The low absorptivity between 700 and 1100 nm (the "therapeutic" near-IR window (118)) is highlighted.

absorption band near 800 nm which disappears upon reduction, but its contribution is extremely small compared to those of Hb, Mb, and water.

Although hemoglobin has strong absorption bands in the visible spectrum and water has strong bands in the infrared, there is a region of low absorption in the near-IR between these bands (Figure 2.16). This is the "near-IR window" discovered by Jöbsis in 1977,(118) and the low absorptivity in this window permits significantly greater transmission of light than is possible in the adjacent visible and mid-IR regions while providing simultaneous access to key absorption bands of dHb/dMb (760 nm), HbO_2/MbO_2 (925 nm), and water (975 nm).

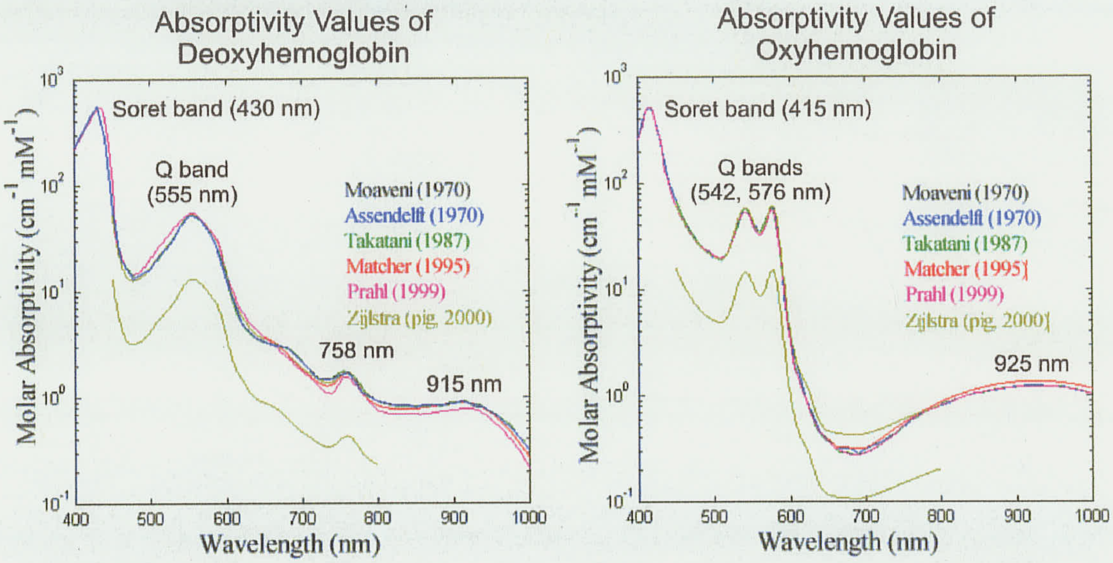

Figure 2.17. Absorptivity spectra of oxygenated and deoxygenated hemoglobin acquired from different sources correspond well with each other. Apparent outliers (Zijlstra data) are reconciled by the factor of 4, converting absorptivity per heme to absorptivity per molecule.

2.3.3. Hemoglobin

2.3.3.1. Visible and Infrared Spectra

Qualitative and quantitative interpretation of spectra measured *in vivo* requires knowledge of the absorptivity spectra for the species of interest. Molar absorptivity values for human oxy-Hb and deoxy-Hb were obtained from the Oregon Medical Laser Center website[58].(199) These data corresponded well with published absorptivity values[59].(161,166,245) Since Prahl (199) reported data with closer point spacing than the

---

[58] The data were from W. B. Gratzer (Med. Res. Council Labs, Holly Hill, London) and N. Kollias (Wellman Laboratories, Harvard Medical School, Boston), and compiled by Scott Prahl. Exact molar absorptivities are dependent upon species (Zijlstra provides absorptivity values for oxygenated and deoxygenated varieties of human, pig, and rat Hb), but the differences are negligible for the studies presented in this thesis.

[59] Published values for pig hemoglobin(274) were offset by a factor of four, but after correction, they also corresponded very well with the others; the factor of four indicates that these absorptivity values were per mM heme (rather than hemoglobin).

other data sets, this set, appended by Matcher's data (161) from 1000 to 1050 nm, was used as the basis for the analyses presented in the following chapters.[60]

The most intense absorption band of deoxy-Hb is the Soret band[61] (also known as the B band) at 430 nm (Figure 2.17). The next most intense band is the Q band at 555 nm; it is approximately one tenth as intense as the Soret band. A shoulder also appears on this band near 587 nm. This strong absorption of blue and green wavelengths gives blood its characteristic red colour. In the near-IR region, the most prominent peak appears near 758 nm,[62] although the absorptivity is approximately one thirtieth the intensity of the Q band. In addition, there is a weak and broad band around 915 nm.

The strongest peak in the spectrum of HbO_2 is again the Soret band, shifted to 415 nm (Figure 2.17). The next most intense is the Q band, which is split into two features with peak positions at 542 and 576 nm. While these peaks have approximately the same intensity (again one tenth that of the Soret band), the longer-wavelength peak is slightly more intense and is designated the α band. The shorter wavelength band is referred to as the β band. HbO_2 has no peak at 760 nm; the only near-IR band is broad and centred at 925 nm.

---

[60] Matcher's data only included absorptivity values up to 1043 nm. Values from 1043 to 1050 nm were extrapolated using a cubic spline fitting algorithm.

[61] This is named after J.L. Soret, who in 1878 discovered the near-ultraviolet absorption bands characteristic of all porphyrins.(274) Among other accomplishments, he also discoved holmium and the chemical composition of ozone. The visible absorbance bands of hemoglobin had been discovered independently about 15 years earlier by Felix Hoppe-Seyler and George Stokes.

[62] The exact location of this peak varies between 756 and 759 nm among the different data sets.

2.3.3.2. Electronic Structure of Heme

Understanding the origins of spectral transitions requires an understanding of the energy levels of the molecules. While the energy of an atom is determined simply by the atomic electronic orbitals that are occupied, in the case of molecules, the electrons occupy molecular orbitals. Within each electronic configuration, the energy of the molecule may be further modulated by transitions between different vibrational modes. Thus, for a particular electronic energy level, a molecule has a series of vibrational energy states, each corresponding to a different potential energy of the molecule as a whole. Similarly, within each vibrational energy state, there is a series of rotational energy states which the molecule may occupy (although these have spectroscopic consequences only for small molecules in the vapour phase). The following sections discuss the molecular orbitals in hemes, in heme ligands, and in other complexes, which give rise to the spectral features described above. For a background on molecular orbital theory, as well as character and symmetry groups and other related issues, the reader is directed elsewhere.(10,51,149)

The visible/near-IR absorption bands of Hb and Mb arise from electronic transitions within the iron-porphyrin[63] complex. In deoxy-Hb, the iron atom is penta-coordinated to the four nitrogen (N) atoms in the porphyrin ring and the nearest nitrogen (N_ε) from the imidazole ring of the proximal histidine residue (F8) (Figure 2.10). In free, atomic iron, the energy levels of the five d atomic orbitals are degenerate. However, when bound to the heme, interactions of the iron atomic orbitals with those of the

---

[63] Protoporphyrin IX, the ring structure found in most hemes, and porphin are both members of the porphyrin family of molecules, all of which share the same basic skeleton of carbon and nitrogen atoms. The difference between porphyrin and porphin is that porphin does not have the side chains (e.g. methyl, vinyl) attached on the periphery. Instead, hydrogen atoms are attached at these locations.(261, p. 131)

porphyrin and imidazole molecular orbitals split these energy levels. Under tetragonal symmetry, the d-orbitals have been shown to split into four distinct energy levels.(107) The planar nature of the imidazole ring adds a rhombic perturbation to the tetragonal symmetry, further splitting the electron orbitals into five distinct energy levels.

Before discussing the specific nature of the transitions that give rise to the oxy-Hb and deoxy-Hb bands, it is worth noting as an aside that near-IR bands are much broader than those in the mid-IR region. This is because the visible/near-IR bands are actually composites of numerous sub-bands representing simultaneous changes in both electronic and vibrational energies. Thus, for a given electronic transition, there will be a number of possible transitions between the vibrational levels, each having slightly different energies. The superposition of these bands has the effect of creating a broad, spectral band rather than a sharp peak. Furthermore, several electronic transitions may appear as a single, broad band.

2.3.3.3. Transitions Responsible for the Bands

In deoxy-Hb, in addition to the four prominent spectral features (the Soret band at 430 nm, the Q band at 555 nm, and two near-IR bands centred at 760 nm and 915 nm), there is a weak band centred at 830 nm that is not well-resolved in experimental spectra (Figure 2.18a). Due to the ubiquity of porphyrin structures in nature, their spectra have been widely studied.(87,152,234,273) Thus, the bands in the visible region have been known for decades to be due to transitions within the porphyrin ring. Specifically, these bands are attributable to transitions from the $a_{1u}(\pi)$ and $a_{2u}(\pi)$ orbitals to the pair of degenerate $e_g{}^*(\pi)$ orbitals under simple molecular orbital theory.(152) The higher-energy

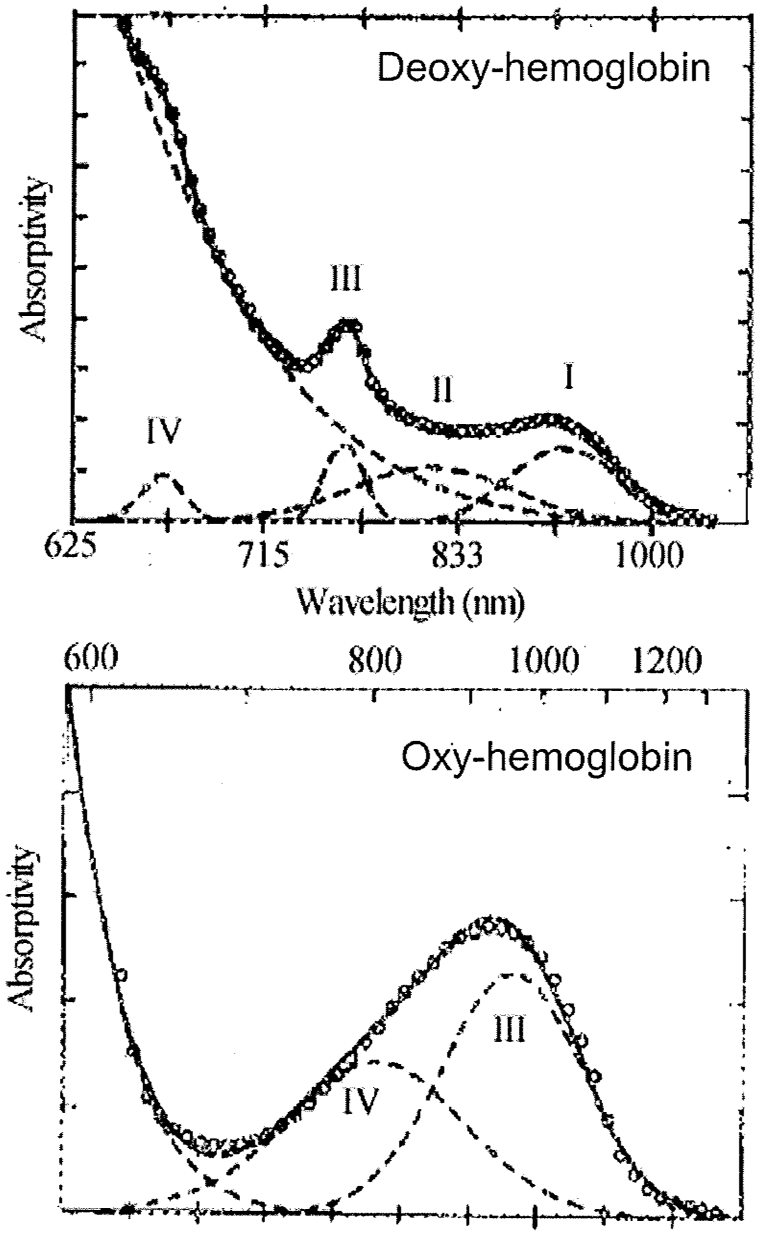

Figure 2.18. Contributions of individual transitions to the overall absorptivity profiles of dHb and HbO_2. The deoxy-Hb profile in the near-IR is the superposition of four bands on the tail of the Q band, while the near-IR oxy-Hb profile is composed of just two bands. From Eaton, 1978.

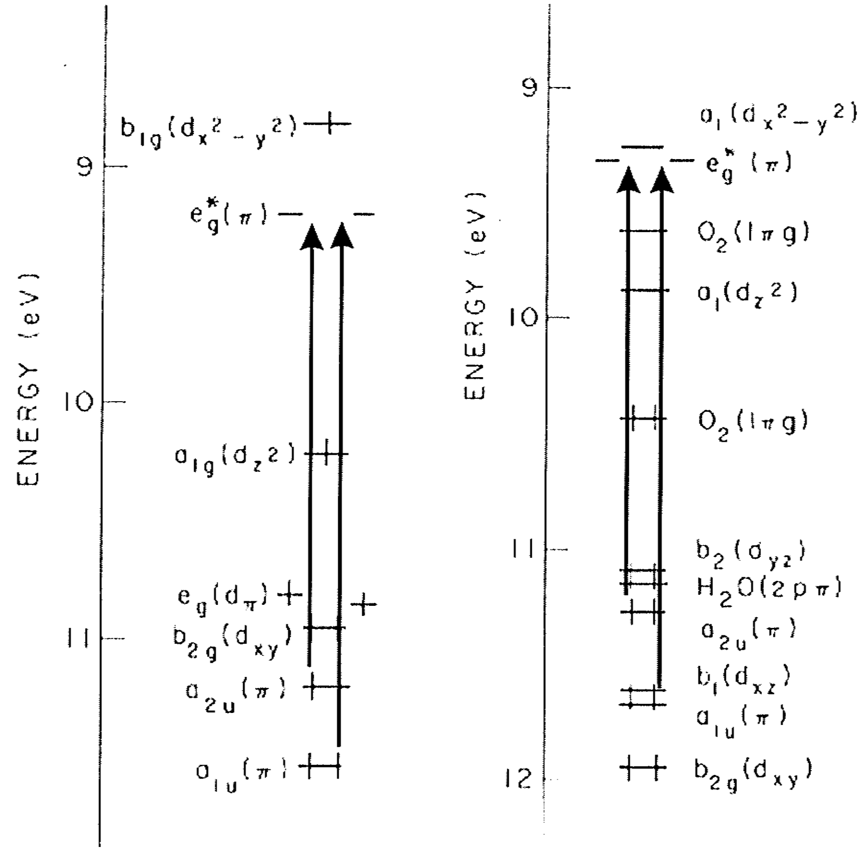

Deoxy-hemoglobin

Oxy-hemoglobin

Figure 2.19. Electronic energy level diagram of heme for deoxy-Hb and oxy-Hb. The Soret and Q bands are due to transitions between the $a(\pi)$ and $e_g(\pi)$ orbitals. From Weissbluth, 1974.

Soret band is mostly due to the $a_{1u} \rightarrow e_g^*$ transition, whereas the Q band is mostly due to the $a_{2u} \rightarrow e_g^*$ transition (Figure 2.19). Due to configuration interaction, though, both bands are assigned as a combination of these transitions.(87) The intensity of the Q band is much lower than that of the Soret band because the transition dipoles of the individual transitions cancel in the former case, whereas they add in the latter case.(273) (p. 385)

In oxy-Hb, the interaction of oxygen removes the degeneracy of the e_g^* orbitals, splitting the Q band into two distinct peaks.(121) Binding of oxygen to heme iron also results in a shift of the Soret band toward the blue; this shift indicates an increase in the separation between the a_{1u} and e_g^* porphyrin π orbitals due to interaction of the oxygen molecular orbitals with the porphyrin orbitals.

The distinctive peak of deoxy-Hb at 760 nm and the broader band at 915 nm have been shown to be accompanied by two less distinctive transitions at 679 and 813 nm (Figure 2.18a).(60) Although the electronic transitions responsible for the visible bands are confined to the porphyrin ring, the infrared bands also involve the *d* orbitals of the central iron. For example, the 915 nm band is predominantly due to a $d_{xz} \rightarrow e_g(\pi)$ transition. This is known as a charge transfer transition, since the electron is transferred from an orbital largely localized on the iron atom to an orbital that is mostly localized in the porphyrin ring. The weak and broad absorption band centred at 813 nm is due to a transition from $d_{xz} \rightarrow d_{z2}$, in which the electron remains largely localized around the iron atom. This band also overlaps with the band at 758 nm due to an a_{2u} $(\pi) \rightarrow d_{yz}$ transition. Finally, there is a very weak band at 679 nm due to an $a_{1u} \rightarrow d_{yz}$ transition.

The only observable near-IR band in the oxy-Hb spectrum arises from two individual transitions (Figure 2.18b).(60) These transitions involve charge transfer from the porphyrin ring to molecular orbitals with significant representation on both the iron atom and the oxygen molecule. There is a low energy component centred at 980 nm, resulting from an a_{2u} (π)$\rightarrow$ d_{xz} + O_2 (π_g*) transition and a higher energy component at 781 nm, resulting from an a_{1u} (π)$\rightarrow$ d_{xz} + O_2 (π_g*) transition. The separation of the vibrational states comprising the Q band also results in narrower bands in the visible region and lower absorbance in the red portion of the spectrum, as compared to deoxy-Hb. Thus the absorbance spectrum of oxy-Hb is less steep between 600 and 700 nm than is that of deoxy-Hb.

2.3.4. Water

In contrast to hemoglobin, the visible and near-IR spectral features of water are not due to electronic transitions; rather, they are overtones of vibrational transitions. Water has strong fundamental symmetric (ν_1) and antisymmetric (ν_3) O-H stretching bands near 3500 cm^{-1} (2860 nm). There is also a bending vibrational band (ν_2) near 1660 cm^{-1}.(31) The overtones and combinations of these bands result in multiple bands in the near-IR and visible regions.

Prahl has compiled a host of references to studies of the optical properties of water, dating back to 1929.(198) All of the data sets since 1970 report essentially identical absorptivity spectra for water.(93,133,135,184,197) The only significant discrepancy is in the region between 400 and 500 nm, but in this region, the absorbance values are so low that noise is likely the cause of this discrepancy (Figure 2.20). Since

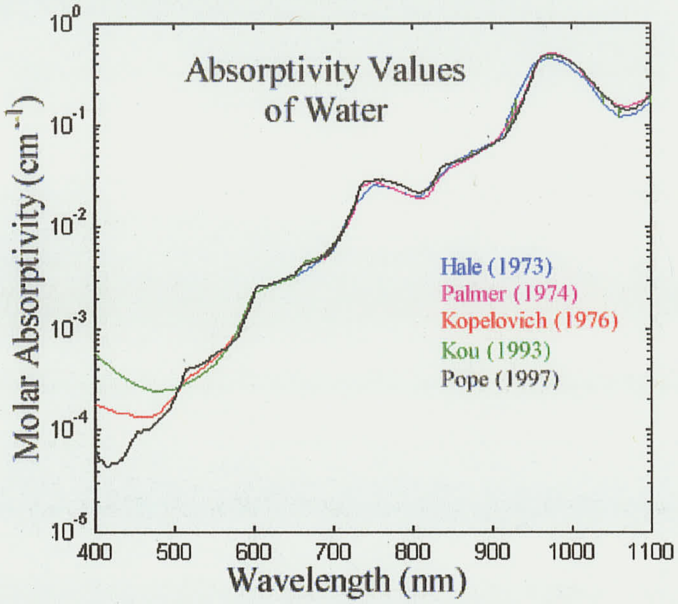

Figure 2.20. Absorptivity spectra of water acquired from different sources correspond well with each other between 500 and 1100 nm.

Palmer and Williams reported spectra with the closest data point spacing, their data were used for analysis in the region between 700 and 1100 nm.(184)

The peaks in this range are due to the following combinations of vibrational overtones: 980 nm ($2\nu_1+\nu_3$), 760 nm ($3\nu_1+\nu_3$), and 740 nm ($\nu_1+3\nu_3$).(32) The bands at 740 and 760 nm are sufficiently broad to coalesce into a single observable band centred near 750 nm. There is also a weak band at 850 nm that, surprisingly, is not mentioned in this list.(32) This band may be due to a $\nu_1+\nu_2+2\nu_3$ combination.

Although the intensity of these bands decrease by a factor of approximately 10 with every unit increase in the number of terms in the combination, it is the bands at 605 and 660 nm (corresponding to a reddish colour) that contribute to the blue colour of pure water. However, these bands do not contribute in any significant way to the absorbance spectra of cardiac tissue. The electronic transitions of water result in absorption bands confined to the ultraviolet region of the spectrum.

2.3.5. Blood Oxygen Saturation Studies

Early biomedical applications of NIRS in the early 1980's focused largely on determination of cerebral blood oxygen saturation(39,84,169) and cytochrome c oxidase redox state.(16,39,44) These studies established the foundation for *in vivo* near-infrared spectroscopy, and since then, NIRS has been exploited in a wide range of *in vivo* studies as a gauge of blood hemoglobin content and oxygen saturation.

The application of NIRS to cardiac studies has only emerged within the last decade.(52,186,187,252,271) These studies have validated NIRS as a means to monitor Hb and Mb oxygenation in exposed hearts. Although Hb and Mb spectra are virtually indistinguishable, myoglobin oxygenation has been effectively monitored when a Hb-free blood substitute was used as a perfusate (in isolated heart models).(52,139) These studies also monitored the redox reactions of mitochondrial cytochromes c and aa_3. Resolution of changes in Mb oxygenation in the presence of Hb has also been reported.(6) Many NIRS studies used discrete-wavelength spectroscopy,[64] with two or three laser sources at the wavelengths of interest. This approach allows faster acquisition but interpretation is less robust than in acquisition of full spectra. More recent studies have applied the methods to problems of direct physiological relevance. Among these were studies of the cardioprotective effects of ischemic preconditioning,(125) the classification of fibrous, fatty, and myocardial tissue in the heart based on the absorption bands of collagen,

---

[64] In this approach, absorbance is monitored at only a few wavelengths.

elastin, and cholesterol,(178) and the minimally invasive assessment of myocardial ischemia by NIRS with a fibre optic catheter.(14)

In addition to the investigations cited above, recent efforts have combined several NIRS point measurements to achieve low-resolution *in vivo* imaging. Most of these studies have focused on the brain, measured using a set of optodes distributed on the scalp. In traditional near-IR spectroscopy, a single optode transmits light from the source to the tissue under study while another optode placed some centimetres away receives the scattered light from the tissue, monitoring Hb oxygenation (for instance) in the tissue volume beneath the inter-optode space. To monitor different regions of the tissue, receptor fibres are placed at various points on the tissue, each of which acquires information for the volume between that probe and the emission fibre.(88,246) To further extend this approach, a mesh of emission and detection fibres may be placed against the tissue under study to improve the sensitivity and spatial resolution of the technique.(73,108,155,244) With discrete wavelength sources, these methods can also achieve excellent temporal resolution, making measurements at rates of up to 10 Hz. They also have all of the sensitivity of NIRS, allowing them to monitor both concentration and scattering properties of the tissue simultaneously and with high precision.

However, the spatial resolution of these multi-fibre techniques is limited, since a probe must be applied at each pixel for which information is sought. High spatial resolution using this model becomes a cumbersome and costly[65] proposition, and the

---

[65] A small increase in resolution can result in a large in cost, since the number of required fibre optic probes increases significantly with the resolution. For instance, an increase in resolution from a 5x5 grid to a 6x6 grid would require an increase of 44% in the number of probes and hence the cost.

grids used in reported studies do not extend beyond a 5x5 array. Franceschini et al. have finessed this limitation by placing eight detection fibres around the periphery of the region under study and back-projecting the data acquired at each fibre to an 18x8 grid encircled by the fibres. To do this, estimated values for the differential pathlength factor (DPF) and stochastic models for the path of light within the tissue were applied. However, since published DPF values (as well as the paths of light in tissue) are highly variable,(19,209) the accuracy of such estimation techniques is uncertain.

These studies also have the disadvantage of requiring probes to be placed in contact with the tissue under study. This can be severely limiting for a number of reasons. First, in some experiments (e.g. burn studies), placement of an imaging apparatus against the tissue may further aggravate areas of tissue at risk. Secondly, it can be difficult to interface with certain tissue geometries. Finally, tissue motion may prohibit such an approach. In the case of cardiac studies, the shape of the heart is constantly changing and this motion could seriously impair imaging efforts.

Thus, Chapter 4 will review and apply a new technique combining spectroscopy with imaging – one that uses a camera with a variable-wavelength filter rather than a collection of probes with conventional spectrometers. This technique can acquire images with much finer spatial resolution than is possible with the multi-fibre approach and it does not require contact with the tissue. Before this system is introduced and these spectroscopic images are analysed for the determination of tissue oxygenation, Chapter 3 describes a study to estimate the variability of optical pathlength with wavelength – a critical prerequisite to soundly-based quantitative analysis of near-IR images and spectra.

3. Effective Photon Pathlength

As mentioned in Chapter 2, quantitative analysis of *in vivo* optical spectra is not straightforward; since the absolute pathlength in a given experiment is generally unknown, absolute analyte/chromophore concentrations can not be determined. Moreover, the pathlength varies with wavelength. That is, photons of one wavelength detected in a spectroscopy experiment may travel a greater or lesser distance through the tissue on average than detected photons of a different wavelength. This wavelength-dependence of pathlength results from scattering and absorption properties of light in tissue, which are very difficult to model accurately due to the high degree of heterogeneity of tissue.

Many studies of tissue scattering properties have been carried out within various simple models, and some of these have further investigated the wavelength-dependence of pathlength as it is specifically relevant to spectroscopy of biological tissue.(19,53,65) While these have provided useful results and insights, a comprehensive understanding of pathlength and its wavelength-dependence remains elusive. In an effort to contribute further to this understanding, we have conducted an investigation into the wavelength dependence of optical pathlength, making use of a near-IR chromophore that is previously unexplored as a contrast agent in tissue. After a brief discussion of scattering theory, its application to cardiac tissue, and previous studies of pathlength in tissue, our approach and investigation will be presented and discussed.

3.1. Scattering and Absorption band Theory

This chapter discusses the nature of the optical pathlength. For the sake of clarity, a brief discussion of terminology is helpful. In the context of geometrical optics, the optical pathlength between points P and P' is defined as

$$OPL = \int_{P}^{P'} \frac{c}{v} dl = \int_{P}^{P'} c dt, \qquad (3.1)$$

where c is the speed of light in a vacuum, v is the speed of light in the medium, dl is an infinitesimal line segment, and dt is an infinitesimal time segment. Thus, the optical pathlength is often interpreted as a measure of the speed travelled by photons in the medium and the time spent in transit. In this chapter, this expression is still valid, but the interpretation is slightly different. Variability in the optical pathlength will not so much reflect differences in the index of refraction of tissue as it will differences in the scattering properties of the medium. In other words, increases in optical pathlength will be interpreted as reflecting increases in transit time (due to multiple scattering in the medium) rather than decreases in the speed of light (due to increased index of refraction).

When light (visible or infrared) impacts cardiac tissue, several things may happen (Figure 3.1). Some will be simply reflected off the surface; this is known as specular reflection. Some will enter the tissue and be absorbed. Most will enter the tissue and be scattered[66]. Multiple scattering events within the tissue may lead some of the photons back through the surface they entered. This scenario gives rise to the possibility of reflectance or interactance spectroscopy studies such as those described in this thesis.

---

[66] Although scattering is essentially absorption band and reradiation of light, it is usually treated as a separate phenomenon, since absorption band usually implies conversion of energy into heat. In scattering, this conversion does not occur. For thorough discussions of scattering of light by particles, the reader is referred elsewhere.(28,110,127)

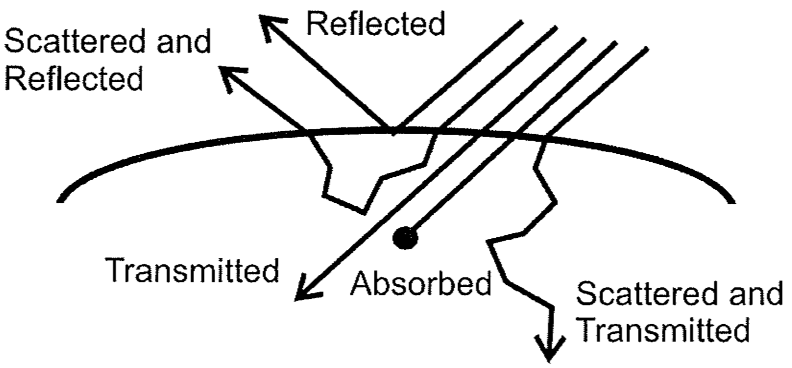

Figure 3.1. Incident light has several possible fates in a scattering medium.

Those that are not absorbed or scattered are simply transmitted through the tissue. However, since cardiac tissue is optically dense, virtually all photons are absorbed or scattered within the tissue.

The wavelength-dependence of optical pathlength in tissue is due to the wavelength-dependence of both absorption band and scattering. The effect of absorption band can be deduced from the absorptivity spectra of the respective chromophores (Figures 2.16, 2.19). The absorptivity of deoxyhemoglobin, for instance, is over 30 times as great at 555 nm as at 760 nm (50 $mM^{-1}cm^{-1}$ as compared to 1.5 $mM^{-1}cm^{-1}$). Thus, infrared light (760 nm) will travel over 30 times as far as green light (555 nm), on average, through a deoxy-Hb solution before being absorbed. To put it more generally, neglecting scattering, reduced absorptivity results in a longer effective pathlength.(80) Since tissue chromophores have few absorption bands in the near-infrared and those that do exist are weak relative to those in the visible (hemoglobin, myoglobin, cytochromes) and mid-infrared (water), near-IR spectroscopy can probe more deeply into tissue than visible or mid-IR spectroscopy.

In addition to absorption, optical pathlength is also highly dependent on light scattering in the tissue. Most photons detected in spectroscopy studies such as those presented here have been scattered multiple times in the tissue, and it is difficult to know either exactly how many times a detected photon was scattered or how far it had travelled between scattering events. Moreover, when light encounters a particle and is scattered, the intensity of light scattered in a particular direction is dependent on the wavelength of the light.

This was first demonstrated by Rayleigh in the case of scattering by a single particle much smaller than the wavelength, now known as Rayleigh scattering[67]. (203) In this case, Rayleigh demonstrated the intensity of scattered light to be inversely proportional to the fourth power of the wavelength. While this result is technically valid only for particles of diameter less than 5% of the wavelength[68], scattering by larger particles is also highly wavelength-dependent. The problem of scattering by a sphere of arbitrary size was solved by Mie almost one hundred years ago, and this result indicated that the intensity of scattered light was dependent on wavelength in a highly complicated and non-linear way, but (to a first approximation) directly proportional to the square of the wavelength.(127,164)(p. 47)

In any case, both the Mie and Rayleigh models assume existence of a single, spherical scatterer. Since the angular distribution of scattered light is also highly

---

[67] Lord Rayleigh was born John William Strutt (1842-1919). For an interesting discussion of uses and misuses of the phrase "Rayleigh scattering", see (272). Although this was only Rayleigh's 8th published paper (Young, 1982), it was immensely important as it was the first to explain adequately why the sky is blue.

[68] For light of 800 nm, particles must be smaller than 40 nm. By comparison, a hemoglobin molecule has a diameter of approximately 6 nm.(36) (p. 24) However, larger bodies, such as cardiac mitochondria and red blood cells, can also be effective scatterers.

dependent on the shape of the scattering bodies and the interactions among them, the presence of many scattering bodies of many different shapes and sizes in tissue makes scattering in tissue extremely difficult to model accurately. As was discussed in Chapter 2, the myocardium is very heterogeneous. Muscle cells, which comprise the bulk of the layer, are approximately 10 μm wide and 100 μm long, and capillaries can be as narrow as 4 μm in diameter. While these dimensions are much larger than the wavelengths used in the studies of this thesis (about 0.5 – 1.1 μm), the cells themselves are also inhomogeneous. Mitochondria have a roughly cylindrical shape and are less than 0.5 μm in thickness.(13)(p. 121) While these scatterers do not meet the criterion for Rayleigh scattering, individual molecules such as hemoglobin (which do meet the criterion) can also act as scatterers.

Optical properties such as absorption and scattering coefficients[69] have been compiled for a wide variety of biological tissues,(255)(p. 23) and while the absorption coefficients of the epicardium and myocardium are low (0.35 and 0.3 cm^{-1}, respectively, at 1060 nm) , their scattering coefficients are significantly higher (167 and 177 cm^{-1}). While the low absorption coefficients allow for deep penetration, the high scattering coefficients ensure that photons follow a tortuous path. The mean cosine of the scattering angle, known as the g-value, is very close to 1 (0.96 for myocardium, which corresponds to an average scattering angle of 16°), indicating that scattered light is not deflected very much. Thus, it would indeed require many scattering events to redirect the light toward

---

[69] These coefficient are measures of the frequency of these events. Specifically, the absorption band coefficient is the inverse of the mean distance between absorption band events. Similarly for the scattering coefficient.

the surface and/or the ones that do re-emerge are those that fall on the tails of the scattering distribution.

It should be recognized that pathlength is not simply proportional to scattering. In all of the studies described in this thesis, the emitter and detector are on the same side of the tissue. For this model, if the scattering coefficient is too low, then insufficient numbers of photons will be redirected toward the detector for pathlength to be a measurable quantity. For higher scattering coefficients, it is unclear how the pathlength relates to it. Patterson et al. have performed a theoretical study of incident light on a semi-infinite slab of homogeneous tissue, in which they developed a very complicated and highly non-linear mathematical relationship between pathlength and scattering coefficient.(188) According to that study, pathlength increases with increasing scattering coefficient, but in a very non-linear way. However, it remains unclear how applicable that formula is to studies in real tissue, since it also predicts an increase in pathlength with increasing absorption coefficients. This is unexpected, since increasing absorption coefficients should reduce the distance that light can travel in tissue and reduce the penetration depth of any spectroscopic study.

3.2. Previous Studies

One method which has often been applied to measure the distance travelled by photons is time-resolved spectroscopy. In a typical time-resolved spectroscopy study, an extremely short burst of light is sent into the tissue and the time between emission and detection of the light is measured. Since the refractive index of tissue, which determines

Table 3.1. Summary of previous relative pathlength results

Study	Relative Pathlength Results
Klassen, 2002 (129)	DPF decreases with wavelength between 750 and 900 nm. DPF (900 nm) = 0.8 * DPF (800 nm)
Pringle, 1999 (200)	No difference between DPF values at 744, 806, 834, and 860 nm.
Kohl, 1998 (132)	DPF decreases with wavelength between 750 and 950 nm. DPF (950 nm) = 0.7 * DPF(800 nm)
Duncan, 1996 (58)	DPF decreases with wavelength between 690 and 832 nm. DPF (832 nm) = 0.87 * DPF (690 nm) in newborns
Benaron, 1995 (18)	No difference between DPF values at 754 and 816 nm
Duncan, 1995 (59)	DPF decreases with wavelength between 690 and 832 nm. DPF (832 nm) = 0.89 * DPF (690 nm) in adults
Essenpreis, 1993 (65)	DPF decreases with wavelength between 740 and 840 nm. DPF (840 nm) = 0.9 * DPF (740 nm)

Table 3.2. Summary of previous absolute pathlength results

Study	Absolute Pathlength Results
Pringle, 1999	DPF (muscle) = 5.4 ± 1.0 (744 nm), 4.7 ± 1.0 (860 nm), source-detector separation of 3 cm
Duncan, 1996	DPF (newborn heads) = 5.4 ± 0.5 (690 nm), 4.7 ± 0.6 (832 nm), source-detector separation of 4.5 cm
Benaron, 1995	DPF (infant heads) = 3.7 ± 0.3 (754 nm, 816 nm), (source-detector separation of 1 mm)
Duncan, 1995	DPF (adult muscle) = 6.5 ± 1.1 (690 nm), 5.9 ± 1.0 (832 nm), source-detector separation of 4.5 cm
Essenpreis, 1993	DPF (adult muscle) = 5.7 ± 0.6 (800 nm), source-detector separation of 4 cm
Matcher, 1993 (160)	DPF (adult muscle) = 4.9 ± 0.5 (820 nm), 2.8 ± 0.3 (975 nm), source detector separation of 3.5 cm

DPF = mean pathlength / optode separation the speed of light in it, is approximately known, the distance travelled can be calculated as the speed of light (in tissue) multiplied by the time in transit. Due to the high value of the speed of light, measurements of the transit time in tissue has only been possible since the advent of ultrashort pulsewidth ($10^{-15} - 10^{-12}$ s) lasers.

Because lasers are monochromatic, most studies of this type have compared pathlengths at only two or three discrete wavelengths in the near-IR (between 690 and 860 nm).(19,53,65) The usual gauge in these studies is the differential pathlength factor (DPF), defined as the mean pathlength (for a given wavelength) divided by the straight-line distance between the emitting and detecting optical fibres.

Published DPF values in muscle tissue exhibit a slight decrease with increasing wavelength between 690 and 860 nm, indicating that the photon pathlength also decreases with increasing wavelength within this range (Table 3.1).(52,59,65,200) However, the differences between the DPF values at the different wavelengths are small, and the intersubject variability in DPF values has been shown to be high.(18,132) Moreover, DPF values are dependent on a range of factors, including subject age, source-detector separation and geometry, and photon wavelength. While actual DPF values reported in these studies range between 3 and 6 (indicating that the mean pathlength is several times the direct distance between probes), the wide variation in absolute DPF values makes it unlikely that these values can be used with any reliability to determine absolute concentrations *in vivo* with near-IR spectroscopy (Table 3.2).(20,54,58)

For the purpose of this thesis, the important point to note is how variability of pathlength influences the spectral fitting of spectra acquired *in vivo* with component

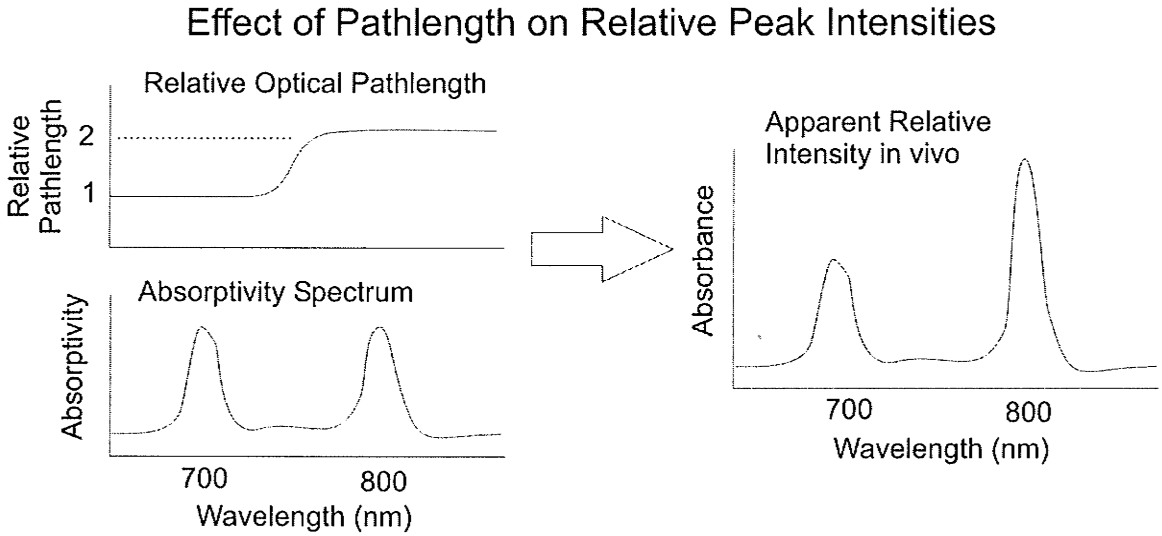

Figure 3.2. Effect of pathlength on relative peak intensities. Doubling of the optical pathlength doubles the apparent intensity *in vivo*.

absorptivity spectra measured *ex vivo*. For instance, if a chromophore has two absorption bands of equal absorptivity, for example at 700 and 800 nm, and if the pathlength in the absence of the chromophore is twice as long at 800 nm as at 700 nm, then 800 nm light will encounter twice as much of the chromophore as the 700 nm light (Figure 3.2). Thus, the 800 nm band will appear twice as intense in an acquired tissue spectrum as the 700 nm band even though they have equal absorptivities. Use of the pure absorptivity spectrum in spectral fitting of tissue spectra, then, would be inappropriate since one band would indicate a concentration twice as high as the other. Instead, the absorptivity spectrum should be scaled according to the relative pathlengths at each wavelength prior to spectral fitting.

The wavelength-dependence of pathlength distorts absorbance spectra so that acquired spectra are not exactly linear combinations of the absorptivity spectra of the constitutent chromophores. The practical effect of this distortion in the spectral fitting process can be minimized by using a limited wavelength range (in which pathlength would not likely vary significantly), but this distortion can also be capitalized upon to determine the wavelength-dependence of pathlength. The following sections of this chapter describe a new approach, using the rich array of absorption bands offered by neodymium (a lanthanide metal with several bands in the visible and near-IR), as well as those of hemoglobin and water.

3.3. Hemoglobin / Myoglobin Absorption

As discussed in Section 2.3.3, deoxy-Hb (and Mb) has prominent absorption bands at 555 nm and 760 nm. By comparing the relative apparent intensities (*in vivo*) of these bands with the corresponding relative intensities in the absorptivity spectra (*in vitro*), a measure of the relative photon pathlength can be obtained.

To illustrate, a spectrum of ischemic cardiac tissue (in which essentially all Hb and Mb is deoxygenated) is overlaid with the pure absorptivity spectrum of deoxy-Hb (which is nearly identical to that of Mb) (Figure 3.3). The absorptivity spectrum has been scaled uniformly so that the 760 nm band has the same apparent intensity as that of the *in vivo* spectrum. If pathlength were uniform between 500 and 800 nm, the bands at 555 nm in the two spectra would also have the same apparent intensity.[70] The fact that the *in vivo* band is less intense at 555 nm demonstrates the fact that the optical pathlength is shorter for visible light than for near-IR light.

Due to the weak penetration depth (strong absorption) of visible light in the range 400 – 450 nm through tissue, our spectra recorded only dark noise in this region, and the

---

[70] Actually, the *in vivo* band would appear more intense than the *in vitro* band because of additional contributions by cytochromes within the mitochondrial membrane. Small shoulders due to reduced forms of cytochromes c and aa_3 can be observed in the *in vivo* spectrum at 520 and 605 nm, respectively.

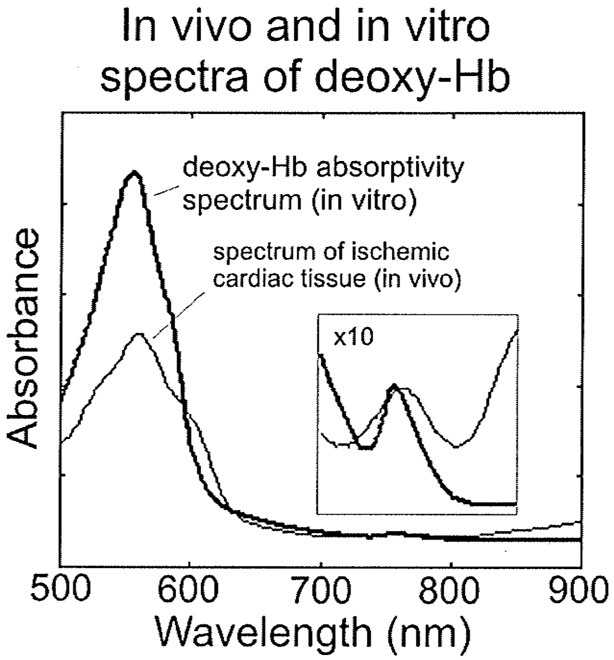

Figure 3.3. The apparent intensity of the 555 nm absorption band of deoxy-Hb relative to that of the 760 nm band is much lower in tissue than in solutions *in vitro.*

Soret bands could not be used in this analysis. Also, spectral contributions of cytochromes overlapped with those of Hb and Mb, making quantitative analysis of the relative pathlengths difficult.

3.4. Neodymium Absorption

3.4.1. Introduction

In order to assess relative pathlengths across the spectrum most accurately, a chromophore with as many distinct (and intense) absorption bands as possible within the wavelength range of interest is needed. Neodymium (Nd) is a lanthanide metal in the same row of the periodic table as gadolinium and dysprosium, both of which have been used clinically as contrast agents in magnetic resonance imaging studies.(3,182) Nd has several bands in the visible and near-IR regions, making it useful in the study of

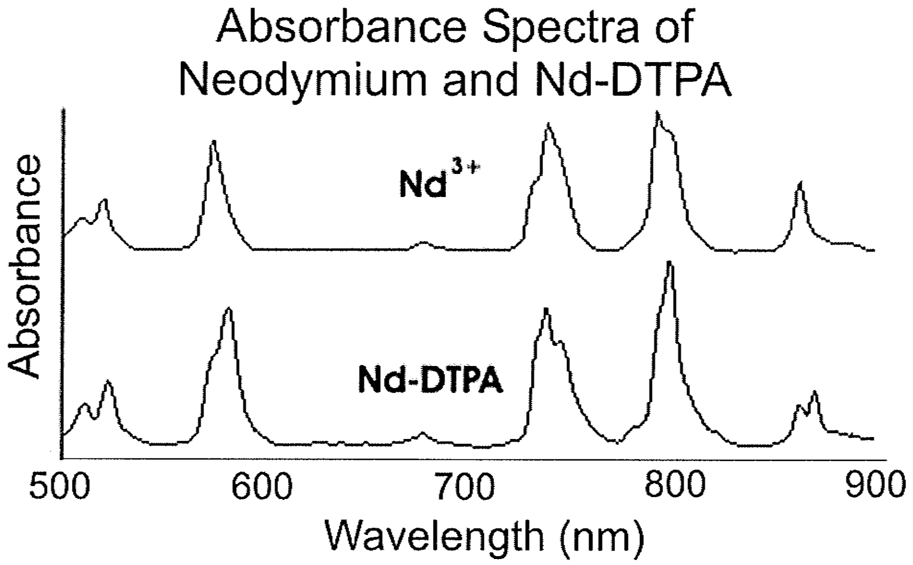

Figure 3.4. Absorbance spectra of neodymium (Nd). Binding Nd to DTPA does not substantially change its absorbance spectrum.

pathlength (Figure 3.4).(124,253) Although Nd is toxic in its ionic form (binding receptor sites for calcium and potassium and preventing those ions from entering the cells), when bound to a chelating agent such as diethylene-triamine-pentaacetic acid (DTPA), it becomes non-toxic with only minimal alteration to its absorbance spectrum.

Nd-DTPA exhibits distinct, narrow absorption bands at 512 and 524 nm (overlapping peaks with a full bandwidth at half maximum (FWHM) of 19 nm), 582 (FWHM=15 nm), 679 (11), 740 (19), 800 (12), and 864 and 871 nm (overlapping with FWHM of 12 nm). In the study reported here, point spectroscopy was carried out for isolated, beating hearts in which Nd-DTPA had been added to the perfusate. When Nd-DTPA is added to the perfusate of cardiac tissue, it is distributed throughout the vasculature and enters the interstitial space, but does not penetrate through the cell membranes. The relative intensities of the bands as they appear in spectra measured *in vivo* differ from the relative intensities as they appear in the *in vitro* spectra, and these changes in relative intensities may be interpreted to quantify the wavelength-dependence of photon pathlength in tissue in the visible and near-infrared regions. For instance, if the 582 nm band intensity (relative to that of the 740 nm band) is half *in vivo* what it is *in vitro*, then the pathlength at 582 nm is half that at 740 nm. The following experiments were designed to capitalize on the bands of Nd, as well as those of water, to determine the wavelength-dependence of optical pathlength in cardiac tissue.

3.4.2. Methods

Certain absorption bands of hemoglobin and myoglobin interfere with some Nd bands. To minimize this problem, spectral contributions of Hb were removed by perfusing the tissue with phosphate-free Krebs-Henseleit Buffer (KHB),[71] a Hb-free solution which has been shown to transport oxygen effectively.(140) Separate solutions of KHB with and without neodymium were prepared.

To provide the maximum Nd absorption band intensity and hence optimize the spectroscopic signal-to-noise, preliminary experiments were executed to determine the maximum Nd concentration that the heart could support. To that end, varying concentrations of a Nd stock solution[72] were added to low-sodium KHB solutions to bring the Nd concentration to between 5 and 30 mM.[73] The maximum acceptable Nd concentration was deemed to be 20 mM. When the Nd concentration exceeded this value,

---

[71] Phosphate-free KHB contains (in mM): NaCl (118), $NaHCO_3$ (25), KCl (4.7), $CaCl_2$ (1.75), $MgSO_4$ (1.2), EDTA-2Na (0.5), and glucose (11).

[72] Stock solutions of the Nd chelate (100 mM) were prepared by mixing equimolar amounts of $NdCl_3$ and DTPA (free acid). The acidic solution was titrated by NaOH to bring the pH to 7.4, which corresponded to mono-Na salt of DTPA (Nd-DTPA-Na•3NaCl).

[73] The sodium content of the KHB was reduced to account for sodium contributions from the Nd stock solution and maintain a free sodium ion concentration near 140 mM. Similarly, since Nd-DTPA binds some Ca^{++} and K^+, KCl and $CaCl_2$ were also added to maintain free [Ca^{++}] at 1 mM and free [K^+] at 4.7 mM, the levels measured in KHB.

adjustments to the KHB solution could not maintain free sodium, calcium, and potassium ion concentrations at normal levels. When Nd was present in the mixture (Nd-KHB) at 20 mM concentrations, the KHB solution was prepared with 28 mM NaCl instead of 118 mM. KCl and $CaCl_2$ were increased by 1 mM and 0.5 mM, respectively.

Sprague-Dawley rats (n=11) weighing 300-400 g were anesthetized with pentobarbital (120 mg/kg, intraperitoneally). When the animal was unresponsive to the toe pinch test, the chest cavity was opened and the heart was removed. The heart was then attached to a Langendorff perfusion setup and perfused through the aorta with phosphate-free KHB. The perfusate was bubbled with 95% O_2 / 5% CO_2 to maintain pO_2 at 500-600 mm Hg and pH at 7.35 – 7.45. Perfusion with this buffer was maintained for a minimum of ten minutes to allow the heart's functional parameters to reach equilibrium.

Spectra were acquired continuously (2 s acquisition time) throughout the experimental protocol (400-1100 nm, 0.5 nm spacing). Broadband visible/near-IR light from a fibre optic illuminator (Oriel Model 77501, Stratford, CT) was transmitted to the heart through one arm of a bifurcated fibre optic bundle. The common illumination/collection probe tip was placed in gentle contact with the heart, where scattered light was gathered and transmitted through the other arm of the fibre bundle to a visible/near-IR spectrometer (Control Developments, Inc.). The emitting and collecting fibre optic filaments were arranged in two concentric rings at the probe tip (emitting filaments formed the outer ring and collecting filaments formed the inner ring; the radial spacing between the rings was 2 mm). Sets of 10 spectra were averaged to increase signal-to-noise, providing one spectrum every 20 seconds.

Following five minutes of baseline perfusion with regular KHB, hearts were perfused with Nd-KHB for 20 minutes. Perfusion was then switched back to Nd-free KHB and spectra were acquired for 10 more minutes. To verify that this Nd concentration (20 mM) did not adversely affect cardiac function, functional data were recorded every minute throughout the protocol.

3.4.3. Spectral Analysis

In the raw spectra, only the bands at 740, 800, and 870 nm were clearly visible (Figure 3.5a). In order to highlight the other Nd absorption bands, the mean of tissue spectra acquired during baseline perfusion (prior to addition of Nd) was calculated and subtracted from each spectrum acquired during the trial (Figure 3.5b). Assuming that addition of Nd has little effect on Mb oxygenation, cytochrome redox state, or water content, the contributions of these chromophores to the absorption profile would be virtually eliminated in the difference spectra. This assumption has been validated for low (5 mM) concentrations of neodymium,(177) and observation of the spectra in this study indicates that in most cases, this assumption was justified. However, four of the trials did exhibit intensity changes in cytochrome and myoglobin absorption when Nd-KHB was substituted for KHB perfusate. Since these spectral features obscured the Nd bands, these trials were excluded from our analysis. The wavelength-dependence of photon pathlength was studied in the remaining seven trials.

The difference spectra after addition of Nd were dominated by the Nd absorption bands (Figure 3.5b). To compensate for residual non-Nd contributions to the spectra, a baseline was calculated for each difference spectrum, using a linear interpolation of the

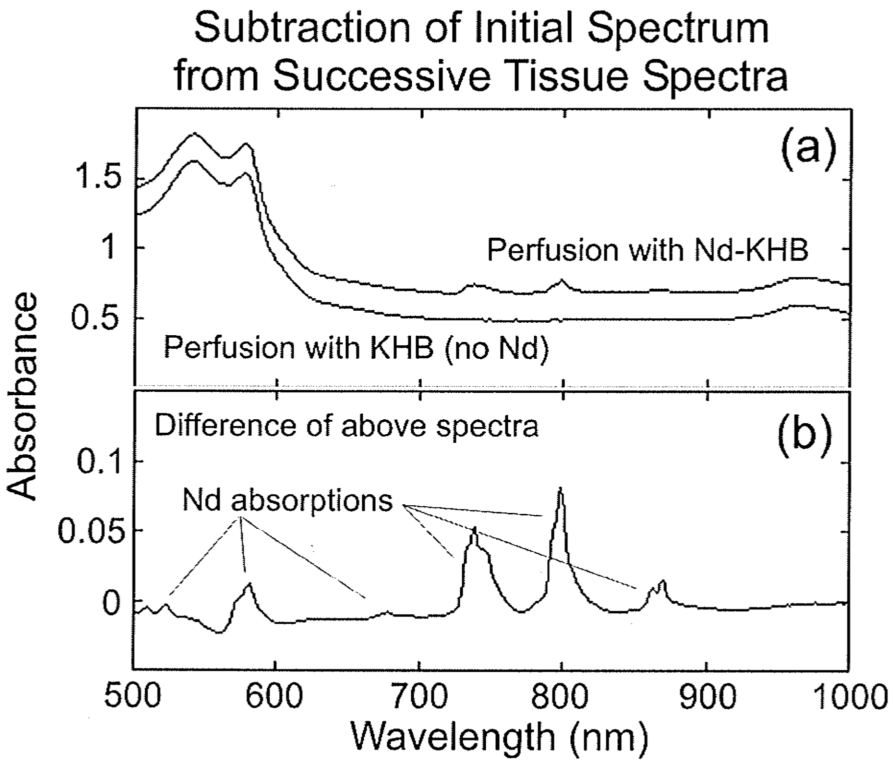

Figure 3.5. (a) Sample tissue spectra acquired during perfusion with Krebs-Henseleit buffer with and without Nd. (b) Differences in spectra are almost entirely due to Nd contributions.

absorbance values on either side of each Nd absorbance band, namely at 491, 536, 560, 602, 660, 705, 840, and 920 nm (Figure 3.6). These baselines were subtracted from the corresponding spectra, leaving only the Nd bands.

The ratio of the *in vivo* band intensity to the molar absorptivity (represented here by the *in vitro* band intensity) is the product of the concentration (which is constant for different wavelengths) with the pathlength.

$$(A_{\text{in vivo}} / \varepsilon_{\text{in vitro}})_\lambda = CL_\lambda \qquad (3.2)$$

This ratio was determined for each Nd band. The intensity ratios for bands at 520, 580, 679, 740, and 870 nm were normalized against the corresponding intensity ratio for the 800 nm peak, hence providing relative pathlength values for the different wavelengths (Table 3.3).

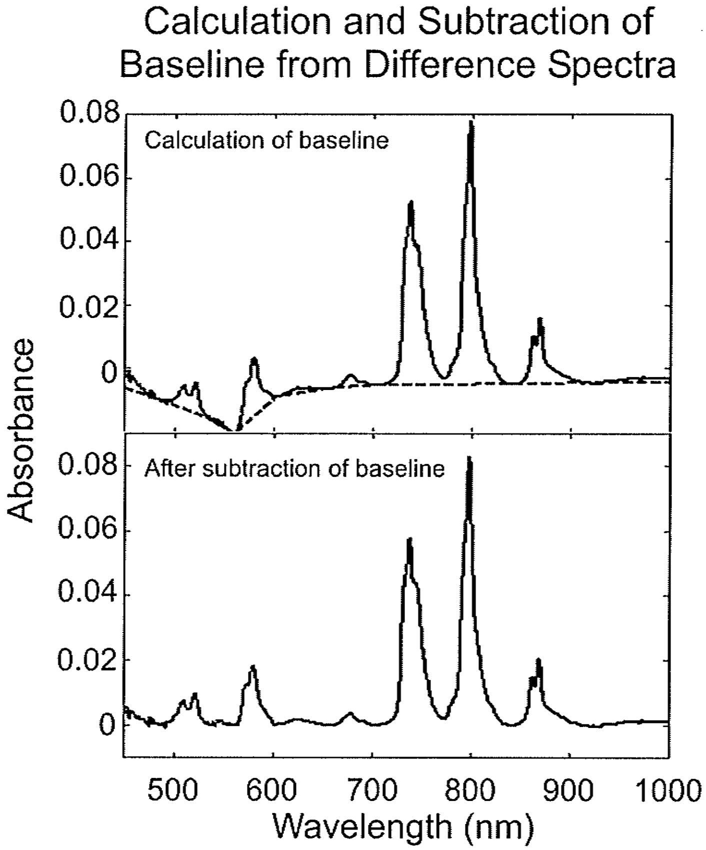

Figure 3.6. Evaluation and subtraction of baseline from tissue difference spectra. (top) solid line: sample difference spectrum. dotted line: baseline interpolated from data points on difference spectrum. (bottom) subtraction of baseline reveals absorption bands whose relative intensities can be compared to those in vitro (see Figure 3.4).

3.4.4. Results and Discussion

The effects of Nd-KHB perfusion on cardiac function are summarized in Table 3.4. While there was a small increase in perfusion pressure and coronary resistance with Nd perfusion, there was no significant effect on heart rate or systolic or diastolic pressure. These data confirm that the high concentration of Nd (in the perfusate) used here had only minor effects on cardiac function.

Table 3.3 Relative Pathlength Values

Wavelength (nm)	$(A_{\text{in vivo}} / \varepsilon_{\text{in vitro}})_\lambda$	Relative pathlength (L_λ)
520	0.12 ± 0.04	0.41 ± 0.13
580	0.12 ± 0.07	0.49 ± 0.21
679	0.24 ± 0.03	0.90 ± 0.09
740	0.27 ± 0.03	0.94 ± 0.01
800	0.28 ± 0.03	1 ± 0
870	0.22 ± 0.03	0.84 ± 0.01

Table 3.4 Cardiac Functional Parameters

Heart	Baseline (n=11)	15 min. Nd-KHB Perfusion (n=11)
Heart Rate (bpm)	225 ± 17	224 ± 18 (NS)
Systolic Pressure (mm Hg)	103 ± 10	101 ± 17 (NS)
Diastolic Pressure (mm Hg)	7 ± 2	7 ± 3 (NS)
Pressure-Rate Product	21600 ± 3000	21200 ± 4500 (NS)
Perfusion Pressure	66 ± 2	74 ± 12 ($p < 0.05$)
Perf Press / Coronary Flow	4.6 ± 0.4	5.2 ± 1.0 ($p < 0.05$)

The difference spectrum plotted in Figure 3.5 clearly demonstrates that the visible-wavelength Nd absorption bands are much less intense relative to the near-IR bands *in vivo* than they are in the *in vitro* spectrum (Figure 3.4). This is consistent with the Hb band results, indicating that near-IR light travels a greater distance through the tissue than visible light and hence near-IR bands appear more intense than visible bands. Relative pathlengths were plotted against wavelength for each trial (Figure 3.7a)

According to these plots, pathlength reaches a maximum near 800 nm, falling rapidly as wavelength increases beyond this value and more gradually with decreasing wavelength. The results are much more precise for the strong near-IR bands than for the weaker visible bands. This is due both to the high intensity of these near-IR absorption bands and to the fact that no other absorption bands interfere with them. While water has spectral features at 740 and 850 nm, they are very weak and subtraction of the mean spectrum effectively eliminates them.

While the 679 nm pathlength is not significantly different from that at 740 nm, it is lower than that at 800 nm ($p < 0.05$)[74] and greater than that for 870 nm ($p < 0.05$). Moreover, even with the large margins of error, the normalized intensities for the 520 and 580 nm bands are still significantly less than those for the 870 nm band ($p < 0.001$ and $p < 0.01$, respectively).

Mean (and standard deviation) relative pathlength values were computed and plotted. (Figure 3.7b) These data indicate that the pathlengths at 679, 740, and 870 nm are 90 ± 9%, 94 ± 1%, and 84 ± 1% of the pathlength at 800 nm, respectively. In contrast, the pathlengths at 520 and 580 nm were 41 ± 13% and 49 ± 21% of the pathlength at 800 nm. These results are not consistent with published reports, which suggest that pathlength decreases with increasing wavelength in the range between 690 and 860 nm, but they are consistent with the prevalent notion, originally forwarded by Jöbsis in his seminal 1977 paper, that the near-IR offers a "therapeutic window" due to the deep penetration of near-IR as compared to visible light.

---

[74] The p-value is a measure of statistical significance (see footnote 96 in Section 7.2.1.1), determined by Sandler's A-test (which has been demonstrated to be equivalent to the paired Student's t-test). The A-test is named after J. Sandler, who introduced it in 1955 as a simplification to the t-test.(222) The t-test was created by W.S. Gosset, who published it under the name "Student" because his employer (a brewery) did not allow publication by employees.(76)

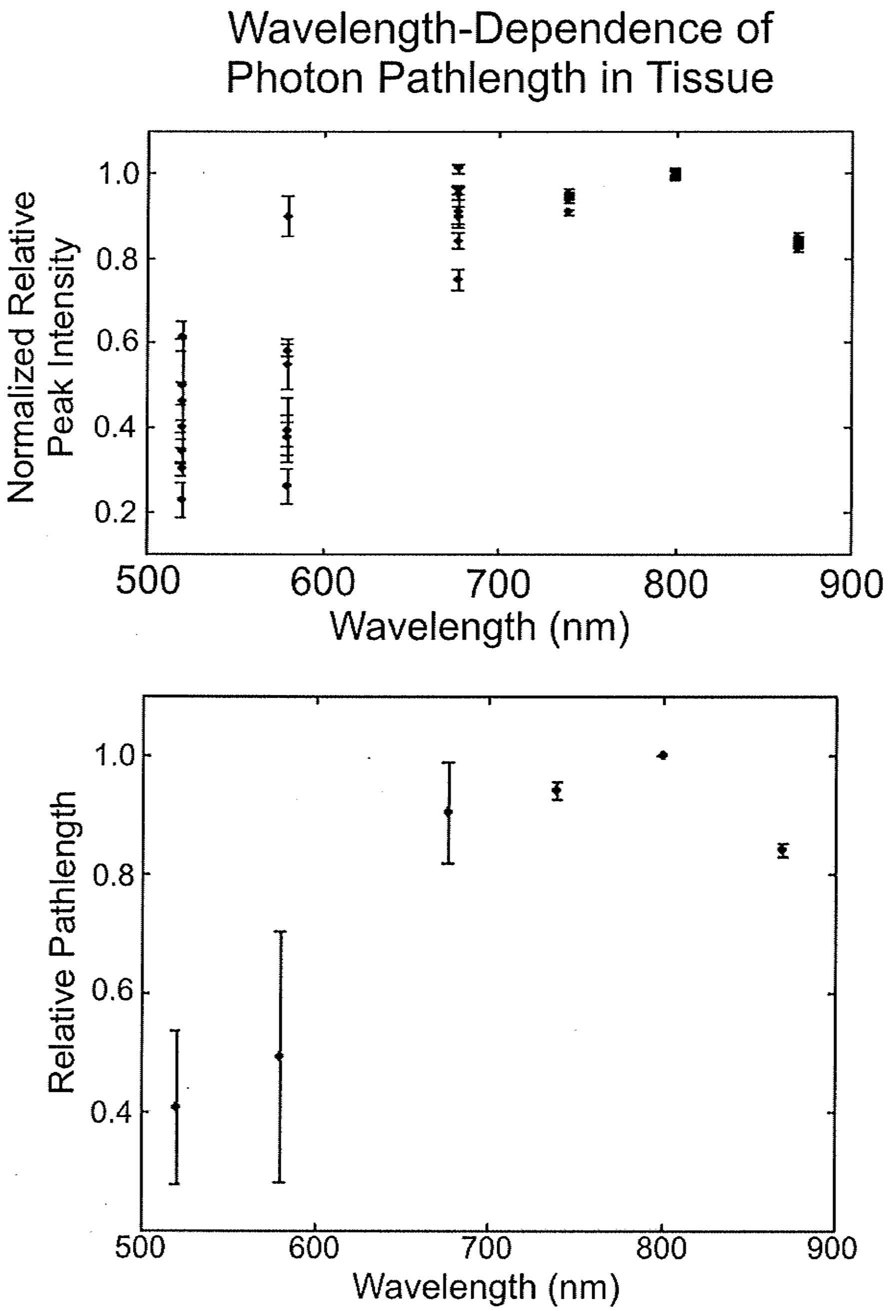

Figure 3.7. Pathlengths at 520, 580, 679, 740, and 800 nm relative to that at 800 nm, as determined by normalized relative peak intensities in isolated rat hearts (n=7). (top) individual results (bottom) means and standard deviations across the trials.

These results, and the observed difference spectra, also explain why only the three near-IR absorption bands appear prominently in *in vivo* spectra. The 679 nm absorption band is too weak to be visible without preprocessing, and the 520 and 580 nm bands suffer from a combination of relatively short pathlength and interference by myoglobin and cytochrome absorption.

3.5. Water Absorption

While neodymium absorption bands provide a basis to gauge the changes in optical pathlength between 500 and 900 nm, the analysis may be extended to longer wavelengths by making use of endogenous water absorption bands. In the spectral range between 500 and 1100 nm, the most intense water band by far is at 975 nm; a much weaker band is present at 840 nm (Figure 3.8).[75] Other than Nd, the only significant chromophores absorbing in the region between 800 and 1000 nm are myoglobin and water. Since the perfusate was well-oxygenated, deoxy-Mb contributions were negligible. While the oxy-Mb band centred at 920 nm overlaps with the water bands, this absorption band is very broad relative to that of water, and therefore its contribution can be effectively removed by taking the second derivative of the tissue spectra.

The second derivative of a cardiac tissue spectrum (acquired during normal perfusion with KHB) and of the water absorptivity spectrum are displayed in Figure 3.9. Both spectral features attributable to water (near 835 and 970 nm) are clearly visible,

---

[75] Water also has several absorption bands between 1100 and 2500 nm that are much more intense than those mentioned here. However, we did not record absorbance in this wavelength range.

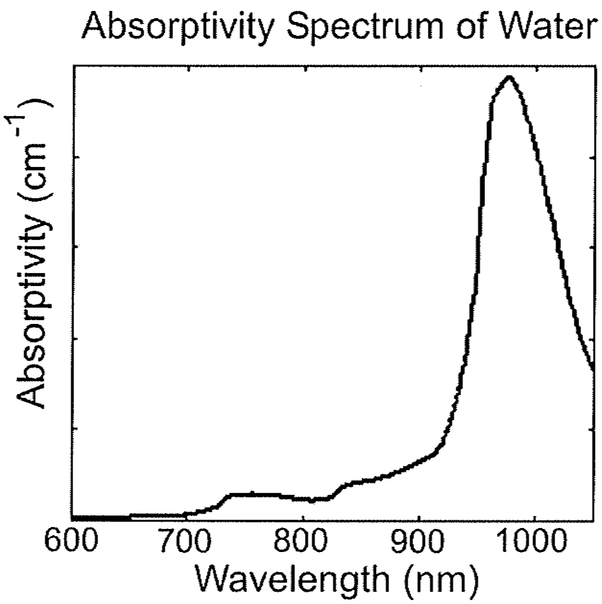

Figure 3.8. Absorptivity spectrum of water.

although the spectral features observed in tissue spectra are shifted by a few nanometres relative to the corresponding bands in the absorptivity spectrum. This may be due to chemical interactions of water with various biological micro-environments, a factor that also broadens the 970 nm band. The salient[76] feature of Figure 3.9 is the relative intensities of the two water bands (as was the case with the neodymium absorption bands). When the second derivative of the cardiac tissue spectrum is scaled so that the intensity of the spectral feature at 835 nm matches that observed for pure water, the intensity of the 970 nm feature for tissue water is weaker than the corresponding band for pure water. This suggests that the optical pathlength is shorter at 970 nm than at 835 nm.

In order to quantify this relationship, the ratio I_{975}/I_{840} was evaluated for (second derivative) spectra representative of each heart, as well as the water absorptivity spectrum. The relative pathlength value was then calculated by dividing the *in vivo* ratio

---

[76] From the Latin *salio* (meaning *leap*), it means prominent or conspicuous.

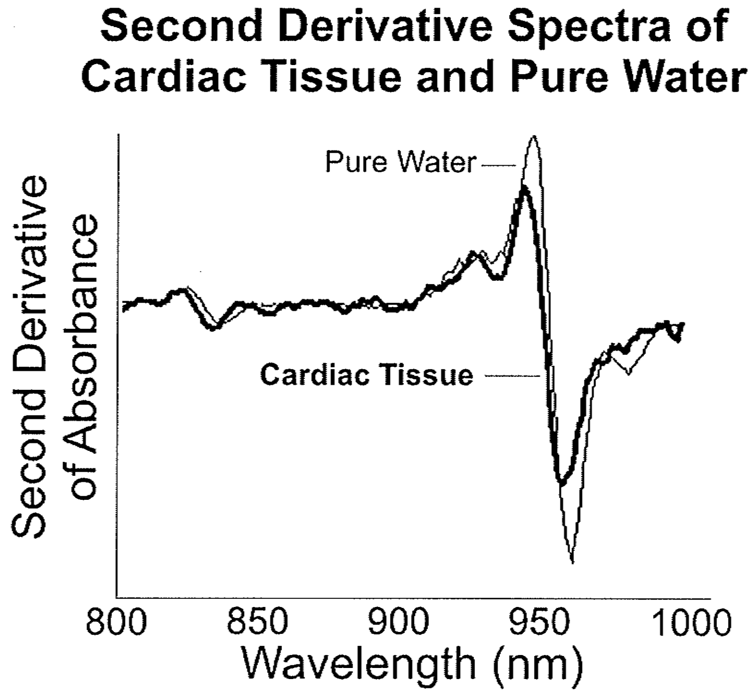

Figure 3.9. The intensity of the second derivative of the 970 nm water absorption band relative to that of the 835 nm absorption band is much lower in tissue than in solutions *in vitro.*

(heart) by the *in vitro* ratio (water absorptivity) as in Equation 3.2. Mean and standard deviation relative pathlength values for each trial are displayed in Figure 3.10. The values derived in this fashion suggest that the pathlength at 975 nm is 83 ± 9% of the optical pathlength at 835 nm. The variance may be due to a combination of the low signal-to-noise ratio of the 835 nm band and variations in the contributions of oxy-Mb or deoxy-Mb, placement of the fibre optic probe against the cardiac tissue (affecting the path travelled by the photons), or cardiac structural parameters.

In order to integrate these results with those of the Nd analysis, the pathlength at 835 nm was estimated[77] to be 94% of that at 800 nm. This implies that the pathlength at 975 nm is approximately 78% of the pathlength at 800 nm. Combining these new values

---

[77] A third-degree polynomial was fit to the Nd data plotted in Figure 3.7b.

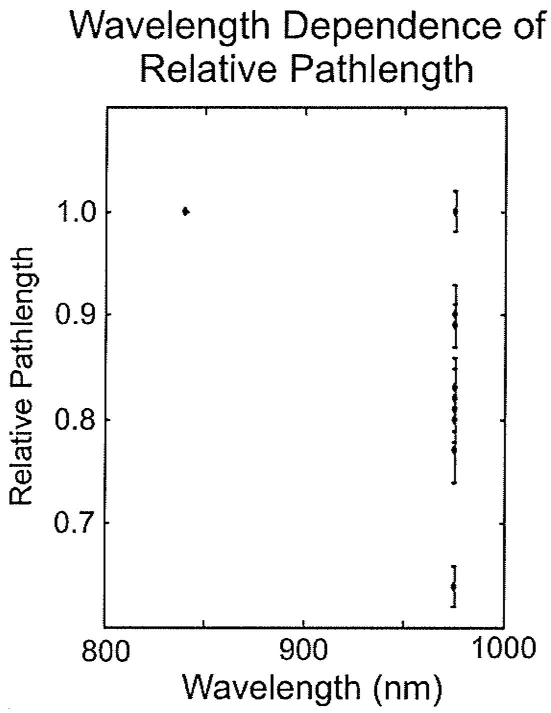

Figure 3.10. Pathlength at 970 nm relative to that at 835 nm, as determined by the normalized water absorption band intensities (n=11).

with those from the previous section yields the wavelength-dependence of the photon pathlength shown in Figure 3.11. Scaling the absorptivity spectra by this optical pathlength function results in a visible distortion (Figure 3.12).

The neodymium-derived data indicate no significant difference between pathlengths at 520 and 580 nm, and this conclusion is consistent with the fact that relative oxy-Mb absorption band intensities at 540 and 580 nm in tissue spectra are comparable to those in the oxy-Mb absorptivity spectrum. This indicates that the pathlength varies little with wavelength between 500 and 600 nm. However, given the Nd data between 500 and 800 nm, this indicates a steep rise in pathlength between 600 and 700 nm.

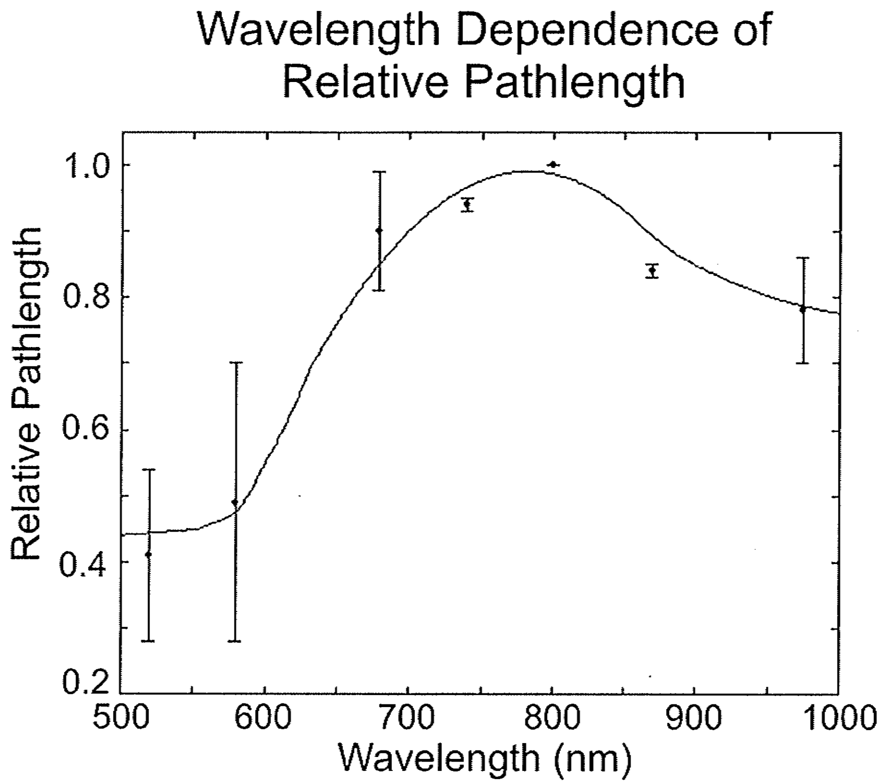

Figure 3.11. Optical pathlength as a function of wavelength, combining results from neodymium and water.

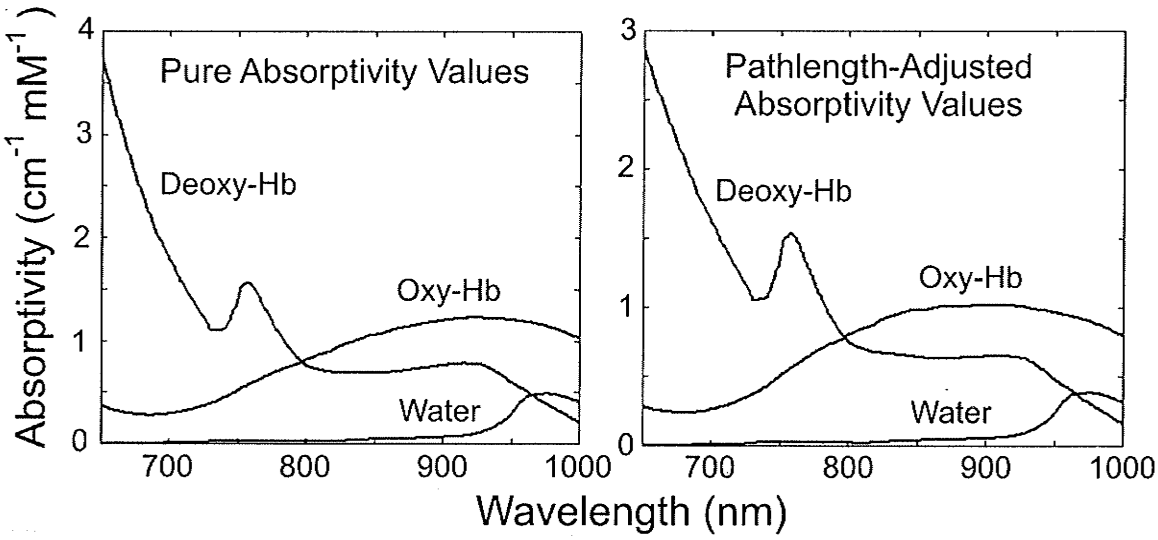

Figure 3.12. Effect of pathlength on component absorptivity spectra. Reduced pathlength near 600 and 1000 nm (relative to 800 nm) results in subtle distortions in the spectra.

3.6. Conclusion

The combined information available from an exogenous agent (Nd) and two endogenous chromophores (Mb and water) has been interpreted to provide a measure of relative photon pathlength in tissue as a function of wavelength (Figure 3.11). While these results are interesting in their own right, they also have practical application in analysis of *in vivo* spectra. Knowledge of the relative pathlengths can allow for more exact spectroscopic determination of chromophore concentrations. However, it should be recognized that the results presented here apply strictly for this experimental setup only – an optical probe with emission and collection fibres in concentric rings spaced 2 mm apart. Alteration of the probe geometry (or of the tissue type) may result in different relative pathlength values. The assumption underlying the analyses in the following chapters is that the pathlength-corrected absorptivity spectra of Figure 3.12 provide a better basis to reconstruct *in vivo* reflectance spectra (from spectroscopic images) than do the uncorrected absorptivity spectra.

4. Arrested Hearts

This chapter and the following two discuss three sets of experiments to implement and test near-IR spectroscopic imaging (NIRSI) as a diagnostic tool for myocardial ischemia. All of these studies applied regional ischemia to pig hearts, followed by a period of reperfusion with the three studies moving progressively closer to mimicking the open chest surgical situation. The porcine heart model was chosen because of its similarity to human hearts in size,(263) vascular distribution,(262) innate coronary circulation,(47,262) and oxygen-carrying capacity;(97,263) these similarities indicate that ischemia-induced changes in blood and tissue oxygenation in pig hearts would be similar to those in human hearts.(25) While no human studies are included in this thesis, it is hoped that further studies building on this foundation will develop near-infrared spectroscopic imaging as a clinical tool for monitoring oxygenation during cardiac surgery. All animals were treated in accordance with guidelines provided by the Canadian Council on Animal Care.(37)

4.1. Introduction

The primary aim of this study was to develop the means to visualize regional variations in the proportions of oxygenated and deoxygenated hemoglobin in the bloodstream with NIRSI. The experimental design was simplified (in comparison to surgical conditions) in order to focus only on the question of whether the method can provide images carrying the desired information and avoid the difficulties associated with motion (heart beart, breathing) in the real surgical setting. First, hearts were isolated from the chest cavity. By isolating the hearts and perfusing them artifically, coronary flow and blood oxygenation could be monitored and controlled more precisely than in a study of *in vivo* hearts. It was initially unclear how sensitive the imaging system would be in assessing the degree of ischemia or the size of the ischemic region, so in order to produce ischemia over a large region of tissue (but small enough so that the whole heart would not be jeopardized), a major coronary artery (the left anterior descending) was occluded. Moreover, complete arterial occlusion was maintained for two hours to ensure that significant damage was done to the tissue. This allowed imaging of compromised and healthy tissue simultaneously. Hearts were arrested during the imaging procedure. Since hearts undergo significant contortion in the process of beating, motion artifacts due to contortion could add significant noise to the signal, potentially obscuring the features of interest.

4.2. Materials and Methods

4.2.1. Surgery and Perfusion

4.2.1.1. Surgery

Domestic pigs weighing 29-34 kg (n=4, heart weight=150-200 g) were conditioned for two weeks in an animal care facility at the Institute for Biodiagnostics (IBD) to minimize transport stress. The following surgery and perfusion procedures were then carried out by IBD staff in the Animal Resources group, as described previously.(140) Pre-medication was performed with an intramuscular injection of ketamine-HCl (20 mg/kg), xylazine (2.2 mg/kg) and atropine (0.03 mg/kg) to relax the animal. Anesthesia was started with isoflurane (5% in oxygen) via an inhalation mask. Pigs were then intubated and mechanically ventilated with oxygen, medical air and 1.5-2% isoflurane. Once the pigs were completely unconscious, the right carotid artery was isolated and cannulated, and the cannula was advanced to the aortic root for arterial blood pressure monitoring, blood sampling during the surgery, and subsequent infusion of the cardioplegic[78] solution described below.

Following a median sternotomy, the superior vena cava and the brachiocephalic and subclavian arteries were isolated. The pericardium was opened, the descending aorta was isolated, and heparin (1000 U / kg body weight) was injected into the superior vena cava to prevent clotting of blood. The position of the catheter at the aortic root was secured, and the brachiocephalic artery, the subclavian artery, the superior vena cava and the descending aorta were occluded; the inferior vena cava was also clamped distally and cut proximally to the heart. Cold (12°C), cardioplegic, high-potassium Krebs-Henseleit buffer[79] (KHB) (10 mL / kg body wt), containing 10 U/mL of heparin, was then injected through the brachiocephalic artery catheter in order to arrest the heart. Once the heart was arrested, the brachiocephalic and subclavian arteries were cut, as were the descending aorta (past the subclavian branch), the pulmonary arteries and veins, and the superior vena cava. The heart was quickly removed along with the lungs, cleaned from the outside with cold saline and placed in a cold saline bath. Over one litre of blood (mixed with high-potassium KHB) was collected for perfusion during the experiment.

---

[78] From the Greek *kardia* (meaning *heart*) and *plēgē* (meaning *stroke*), it refers to an arrest of cardiac activity.

[79] Normal KHB contains 25 mM $NaHCO_3$, 118 mM NaCl, 4.7 mM KCl, 1.2 mM KH_2PO_4, 1.75 mM $CaCl_2$, 1.2 mM $MgSO_4$, 0.5 mM EDTA-2Na, 11.0 mM glucose, and 6 g/L albumin. For the cardioplegic solution, 20 mM KCl was used.

A drain was placed in the left ventricle and a cannula was inserted into the brachiocephalic artery to provide connection with the perfusion (aortic) pressure line. The left atrium was opened and a purse string was sutured on the mitral valve. Following an incision in the left atrium, a latex balloon was inserted into the left ventricle through the incision, positioned and secured by closing the mitral valve leaflets, and connected to a pressure transducer (Gould P23Db). The balloon was filled with water and used to monitor left ventricular systolic (LVSP) and end-diastolic pressure (LVEDP), and heart rate (HR). A catheter was placed in the coronary sinus to collect venous effluent samples and a perfusion cannula was secured in the subclavian artery. The subclavian cannula was used to collect arterial samples and measure perfusion pressure, and an air bubble trap was connected to this cannula as well.

4.2.1.2. Perfusion

Once isolated as described in the previous section, the heart was attached to a perfusion pump and perfused by the Langendorff method in the recirculation mode.[80] Regular cardiac contractions were restarted with a defibrillator to ensure that all cardiac functional parameters were at normal levels. Prior to perfusion, the extracted mixture of blood and cardioplegic solution was diluted with low-K^+ (1.2 mM) KHB (36°C, no KCl was added) to restore the potassium concentration to normal levels and bring the total circulation volume to approximately two litres. If the K^+ concentration in the perfusate

---

[80] The Langendorff method is a reverse perfusion system where the perfusate (blood) enters, rather than leaves, the heart via the aorta, feeding the coronary arteries.(112) It is named after Oscar Langendorff, a 19th-century German physiologist. The recirculation mode indicates that the perfusate was recirculated through the system.

was too low, more KCl was added to the perfusate to maintain a mean K^+ concentration of 4.4 ± 0.6 mM.

At the beginning of perfusion, the perfusate contained 8.7 ± 0.6 mM glucose (this high level of glucose compensates for the low levels of fatty acids), 1.4 mM lactate, 38.8 g/L hemoglobin (Hb, 40% of normal content in pig blood), heparin (10 000 U/L) (to prevent blood clotting) and 1 μM propranolol. Propranolol is a β-adrenergic blocking agent. These agents bind to cardiac receptors for epinephrine and norepinephrine, which stimulate cardiac contraction. By binding these receptors, propranolol reduces the contraction rate and hence the myocardial oxygen demand.

The perfusate was aerated in a membrane oxygenator (Cobe, Arvada, CO, USA) with a 95% O_2/5% CO_2 gas mixture. Because hemoglobin content was only 40% of normal, it was necessary to maintain high levels of diffused oxygen in the blood plasma. Cardiac performance was determined as a pressure-rate product (PRP = HR x (LVSP - LVEDP)). The balloon volume was adjusted to bring LVEDP to 0-5 mm Hg and LVSP to 75 mm Hg at a HR of 113 bpm. Although these pressure values are lower than normal physiological values, they were chosen in order to reduce the volume of flow while maintaining cardiac function. Perfusion pressure (in mm Hg) was measured near the aortic valve, and the ratio of perfusion pressure to coronary flow provides an index of coronary resistance.

Arterial and venous samples were acquired every 30 min and tested for glucose, lactate, pO_2, pCO_2, pH, Na^+, K^+, Ca^{+2}, and Cl^- using NOVA biomedical analysers (Stat 9 Profile). Hb and its oxygen saturation were measured immediately after sampling using an OSM3 hemoxymeter (Radiometer, Copenhagen) analyser. Arterial pO_2 was maintained at 460-560 mm Hg and arterial pH was in the range of 7.35-7.45. The oxygen consumption rate ($V(O_2)$, µmol/min/g) was calculated as a product of arterio-venous [O_2] difference and total coronary flow (*CF*) divided by heart mass (*m*).

$$V(O_2) = (pO_{2,art} - pO_{2,ven}) * CF / m \qquad (4.1)$$

Because of the high oxygen levels in the plasma, hemoglobin was almost fully saturated in venous as well as arterial blood. Thus, changes in Hb oxygen saturation were not included in the above expression. Following an equilibration period in the perfusion system (30-40 min), hearts were arrested by addition of KCl to the perfusate (final [K^+] = 16.4 mM, Table 4.1).

4.2.2. Spectroscopic Imaging

4.2.2.1. Equipment

Once the heart was suspended, perfused, and arrested, the imaging equipment was positioned around it, as shown in Figure 4.1. The camera consisted of an infrared-sensitive 512 x 512 back-illuminated charge-coupled device (CCD) array and 14/16-bit ST-138 analog to digital converter run in 14-bit mode (Princeton Instruments, Trenton, NJ). The camera was fitted with a Nikon Micro AF60 lens with an aperture setting of f/4 and 2x2 binning was performed to produce images with 256 x 256 pixel resolution. A liquid crystal tuneable filter (LCTF, Cambridge Research & Instrumentation, Woburn, MA) was mounted to the camera lens, providing an adjustable bandpass between 650 and 1050 nm and a bandwidth of approximately 7 nm. The bandpass profile of the LCTF, as

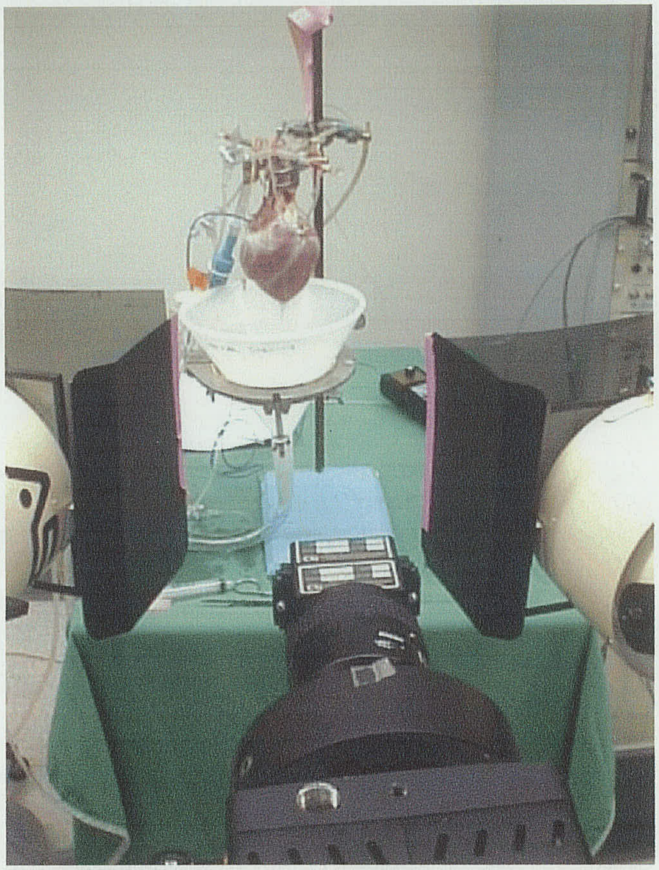

Figure 4.1. Photograph of experimental setup.

provided by CRI, is shown in Figure 4.2.[81] Labview software (National Instruments, Austin, TX) written in-house controlled both LCTF wavelength selection and image acquisition. The camera-LCTF unit was placed facing the anterior side of the heart, so that both ventricles were visible and the heart nearly filled the field of view. Each binned pixel corresponded to an area approximately 0.4 x 0.4 mm on the heart surface.

Tungsten halogen floodlights were placed on either side of the camera, illuminating the entire field of view with approximately 150 watts of light. The floodlights were controlled by rheostats (Variac, Madras, India), that maintained a

---

[81] This bandpass profile was scanned in from a personal communication from Ross Nakatsuji (CRI) to Mark Hewko (NRC) (11.04.1999). Used with permission.

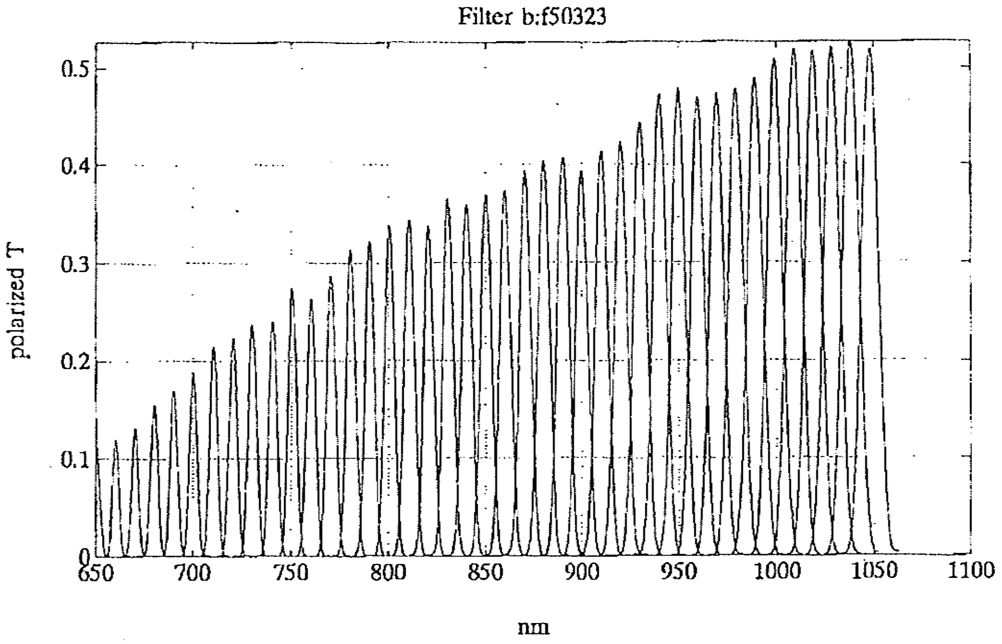

Figure 4.2. Superposition of LCTF bandpass profiles between 650 and 1050 nm (10 nm spacing).

constant voltage output to the lights, which in turn ensured a constant illumination power. The lamps were also placed in an effort to illuminate the anterior side of the heart as uniformly as possible, and the intensity of the light was adjusted for each trial in order to maximize signal-to-noise. Even for low intensities, some pixels were saturated due to specular reflection; therefore, an illumination was selected with the aim of filling the A/D converter for most pixels while minimizing the number of saturated pixels. Once the illumination power was selected, it was maintained at that level for the duration of the trial. The heart, perfusion apparatus, camera system, and lamps were also left in place throughout the course of the trial.

Each raw reflectance image sequence consisted of images taken at 41 discrete wavelengths between 650 and 1050 nm (10 nm intervals). In order to increase signal-to-noise, five images of approximately 100 ms exposure time each were averaged together at each wavelength. Thus, each reflectance image sequence consisted of a 256 x 256 x 41 matrix. Total acquisition time for the image sequence was about 5 minutes.

In a typical reflectance spectroscopy experiment, the intensity of the light reflected from the sample is divided by that reflected off a reflectance standard and the pseudo-absorbance determined in a fashion analogous to the absorbance measurement (see Section 2.3.1). A similar approach was used for the present experiments. At the end of each trial, a standard reference card (Kodak Gray Card, Eastman Kodak, Rochester, NY) with uniform 18% reflectance at visible and near-IR wavelengths was placed in the position of the heart and a reference reflectance image sequence of it was acquired.

4.2.2.2. The Spectroscopic Image

Raw reflectance image sequences of the heart were divided pointwise by the corresponding reference image sequence and converted to a logarithmic scale according to the formula

$$A_\lambda = \log (I_R / I_S)_\lambda, \qquad (4.2)$$

where "I_R" represents the intensity read for a camera pixel with the reference card in place, "I_S" is the intensity of the corresponding pixel at the same wavelength "λ" with the sample in place, and A_λ is analogous to the absorbance. The resulting spectroscopic image is a 3-dimensional matrix, combining both spatial and spectral information. Each 2-D slice provides a 256 x 256 image of absorbance values at a particular wavelength, while the absorbance values extracted for a single pixel through all 41 slices is the absorbance spectrum for that pixel (Figure 4.3).

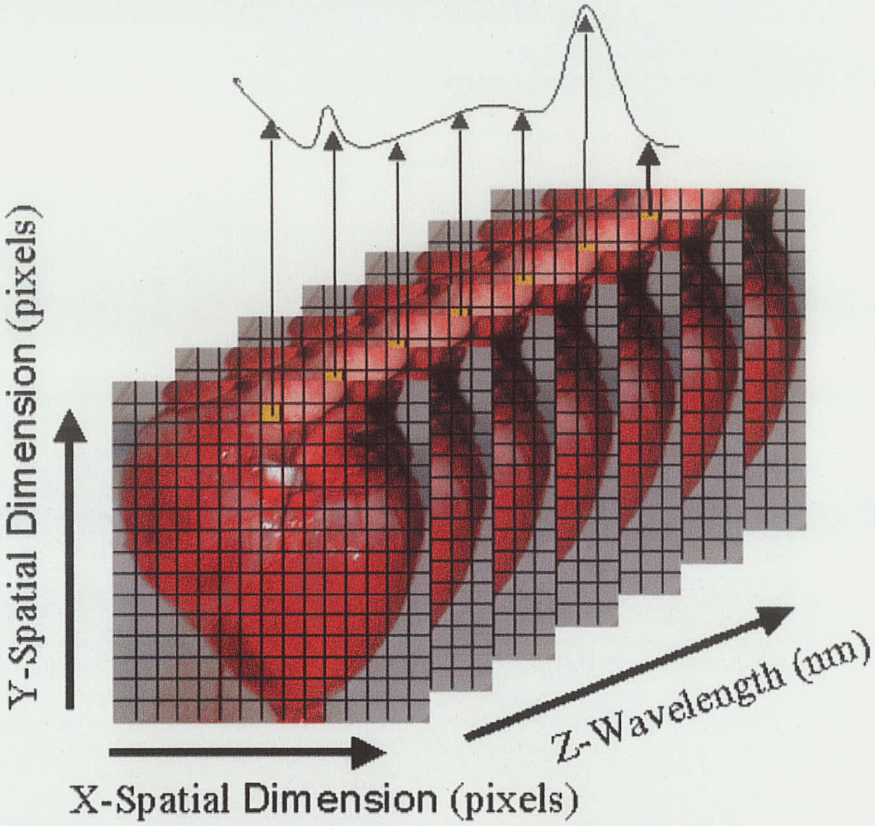

Figure 4.3. A spectroscopic image. Each slice shows the absorbance at a particular wavelength. Following a pixel through the slices provides an absorbance spectrum for that pixel.

4.2.3. Experimental protocol

The experimental protocol is depicted graphically in Figure 4.4. After 10 min of perfusion, the first spectroscopic image of the anterior side of the arrested heart was acquired. The left anterior descending (LAD) artery was then occluded, inducing ischemia in the anterior left ventricle for 120 min while perfusion to the rest of the heart was maintained. Spectroscopic images were collected at 10 min, 1 hr, and 2 hrs following the occlusion. The occlusion was then released to reperfuse the LAD bed and the first reperfusion image was acquired after 10 min. The perfusion pump was then shut off, stopping blood flow to the heart completely for 10 min to produce global ischemia, and

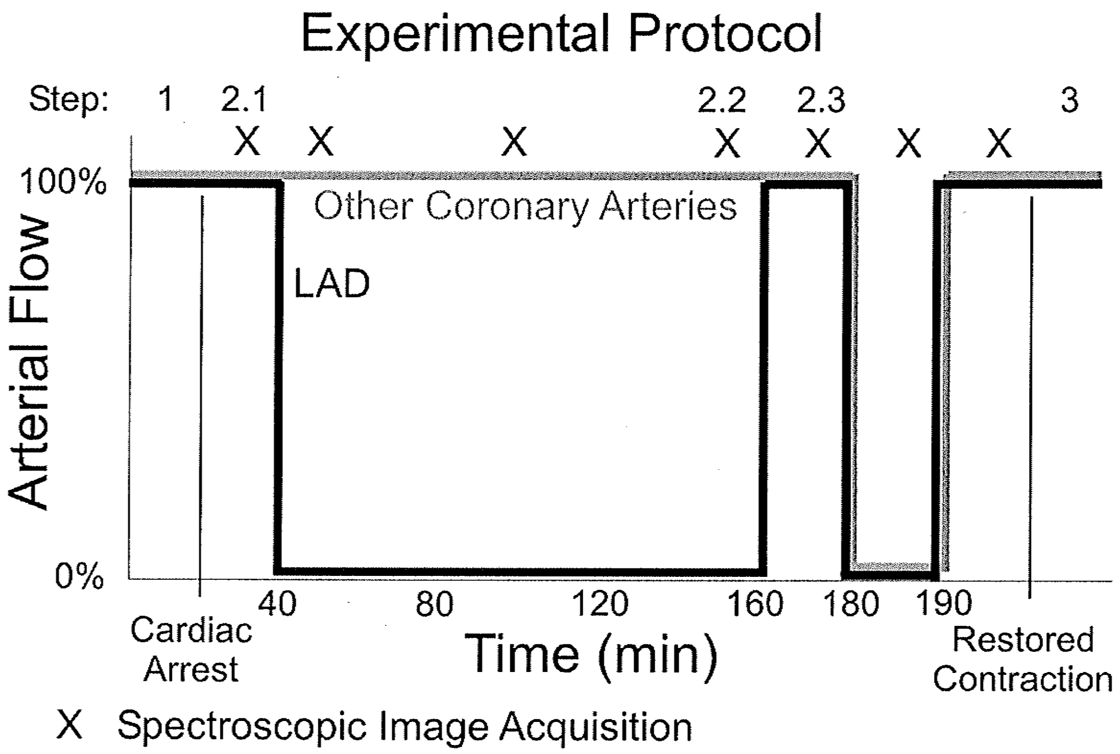

Figure 4.4. Experimental protocol. Flow through the LAD artery (black) and other coronary arteries (grey) are shown. Step numbers correspond to those in Tables 4.1 and 4.2.

normal flow was then restored again for 10 min. Spectroscopic images were collected after 5 min of global ischemia and again after 5 min of restored flow.

4.2.4. Image Analysis

Oxygenation was assessed for each pixel in the spectroscopic image, using a procedure outlined here, running under Matlab (ver. 5.3, The Mathworks, Natick, MA). As described in Section 2.3.2, absorbance spectra can be expressed as linear combinations of the molar absorptivities of the constituent chromophores (deoxy-Hb, oxy-Hb, and water).(161,197) Since the photon pathlength is variable with wavelength and since the wavelength-dependence of pathlength has the effect of altering the relative intensity of absorption bands as they appear in spectra acquired *in vivo* (see Chapter 3), this dependence must be taken into account in the spectral analysis. While the relative pathlength values determined in that study were specific to that equipment geometry, they are assumed to be reasonable approximations of the relative pathlengths in this study as well, or at least more appropriate than the uncorrected absorptivity spectra. The impact of incorporating the wavelength-dependence of pathlength in the analysis is discussed in Section 4.4.2.

To account for offsets in the spectral baseline (B in Equation 2.19), another "spectrum" with "absorptivity" values of 1 at each wavelength, denoted below as [1], was also included in the spectral fits. Thus, for each pixel, the absorbance A for the wavelength λ is written as

$A(\lambda) = C_{water}\, L(\lambda)\, \varepsilon_{water}(\lambda) + C_{dHb}\, L(\lambda)\, \varepsilon_{dHb}(\lambda) + C_{oHb}\, L(\lambda)\, \varepsilon_{oHb}(\lambda) + B_{offset}\ [1].$[82] (4.3)

This expression can be written in matrix notation for each pixel as

$$\begin{bmatrix} A_{650} & \cdots & A_{1050} \end{bmatrix} = \begin{bmatrix} C_{dHb} & C_{oHb} & C_{water} & B_{offset} \end{bmatrix} \begin{bmatrix} \varepsilon_{dHb,650}L_{650} & \cdots & \varepsilon_{dHb,1050}L_{1050} \\ \varepsilon_{oHb,650}L_{650} & \cdots & \varepsilon_{oHb,1050}L_{1050} \\ \varepsilon_{water,650}L_{650} & \cdots & \varepsilon_{water,1050}L_{1050} \\ 1 & \cdots & 1 \end{bmatrix} \qquad (4.4)$$

or $\mathbf{A}_{1x41} = \mathbf{C}_{1x4}\, (\boldsymbol{\varepsilon}\mathbf{L})_{4x41}$.[83]

Equation 4.4 can be applied to all pixels in one matrix equation,

$$\mathbf{A}_{65536x41} = \mathbf{C}_{65536x4}\, (\boldsymbol{\varepsilon}\mathbf{L})_{4x41}. \qquad (4.5)$$

The above equation could be solved for the concentration matrix **C** simply by multiplying on the right by the inverse of the matrix (εL), but since (εL) is not square, it

---

[82] For the sake of space and clarity, Mb is not included in the subscripts in the equations. Deoxy-Hb and oxy-Hb are listed as dHb and oHb, respectively.

[83] The subscripts indicate the sizes of the matrices. Since **ε** and **L** are multiplied pointwise rather than by the rules of normal matrix multiplication, **εL** is treated in the following discussion as one matrix, rather than as a product of matrices. As a reminder, parentheses are placed around the characters.

does not have an inverse. However, multiplication of $(\varepsilon\mathbf{L})$ by its transpose, $(\varepsilon\mathbf{L})^T$, produces a square matrix with an inverse. Thus, Equation 4.5 becomes

$$\mathbf{A}\,(\varepsilon\mathbf{L})^{\mathbf{T}}\,[(\varepsilon\mathbf{L})(\varepsilon\mathbf{L})^{\mathbf{T}}]^{-1} = \mathbf{C}\,[(\varepsilon\mathbf{L})(\varepsilon\mathbf{L})^{\mathbf{T}}]\,[(\varepsilon\mathbf{L})(\varepsilon\mathbf{L})^{\mathbf{T}}]^{-1}. \qquad (4.6)$$

Multiplication of the square matrix by its inverse results in the identity matrix, meaning that the right-hand side is equivalent to the concentration matrix **C**.

$$\mathbf{C} = \mathbf{A}\,(\varepsilon\mathbf{L})^{\mathbf{T}}\,[(\varepsilon\mathbf{L})(\varepsilon\mathbf{L})^{\mathbf{T}}]^{-1} \qquad (4.7)$$

It should be noted here that since the absolute pathlength is unknown, the absolute concentrations are also indeterminable. Thus, the values calculated here are the weighting coefficients of the absorptivity spectra in Equation 4.3, so they will be referred to as coefficients rather than concentrations. Nevertheless, these values should accurately provide both relative dHb and HbO_2 concentrations over the image and dHb and HbO_2 concentrations relative to each other (a measure of oxygen saturation).

Myoglobin was not included separately in the linear combination because the differences between it and hemoglobin are insignificant. The absorption bands of Mb are shifted by a maximum of 3 or 4 nm from those of Hb (and in some cases less). This difference is small relative to the widths of the near-IR absorption bands (a minimum of 20 nm), the LCTF bandwidth (7 nm), and the image sample spacing (10 nm). Therefore, the contributions of Hb and Mb are treated together and referred to as deoxy-(Hb+Mb) and oxy-(Hb+Mb). An estimate of the relative contributions of Mb and Hb to the overall absorbance signal is discussed in Section 4.4.4, and a more detailed study will be presented in Section 5.4.5.

The spectra extracted from the spectroscopic images were fit with pathlength-adjusted absorptivity spectra between 700 and 1000 nm, in order to determine the relative concentrations of the individual chromophores. These were then incorporated into images depicting the relative deoxy-(Hb+Mb) and oxy-(Hb+Mb) concentrations at each point in the entire heart and used to provide oxygen saturation images. The "area at risk" as discussed below is defined as the area exhibiting reduced oxygenation values during ischemia, relative to those exhibited during normal perfusion.

4.3. Results

4.3.1. Blood Sample Data

Blood-perfused hearts exhibited stable contractile function during the equilibration period (Table 4.1). Upon cardiac arrest, the oxygen consumption rate $V(O_2)$ fell to roughly a third of its previous value (0.49 ± 0.13 μmol/min/g, not shown). LAD occlusion further decreased $V(O_2)$, which reached 0.31 ± 0.04 μmol/min/g by the end of the occlusion period. Simultaneously, blood lactate increased and glucose decreased by 1.25 and 1.5 mM respectively, by the end of ischemia (Table 4.2). Hb, pH, Na^+, Ca^{++}, and Cl^- levels remained stable throughout. Occluder release and perfusion with normal KHB partially restored mechanical function (PRP, 62% of the initial value) and oxygen consumption rate (79%).

The reduction in oxygen consumption upon LAD occlusion is reflected by changes in arterial and venous oxygen partial pressures. While arterial pO_2 remained steady at 520 ± 33 mm Hg throughout the experimental protocol, venous pO_2 increased from 269 ± 14 mm Hg during normal perfusion (post-occlusion) to 363 ± 40 mm Hg at the end of the ischemic period ($p < 0.05$). Upon reperfusion, venous pO_2 decreased to 305 ± 33 mm Hg. Carbon dioxide levels in both arterial and venous samples remained steady

Table 4.1. Cardiac Functional Data

Step	HR (bpm)	LVSP (mm Hg)	LVEDP (mm Hg)	PRP (mm Hg / min)	$V(O_2)$ (μmol / min / g)
1. Pre-arrest	113 ± 5	75 ± 0	3.3 ± 1.7	8065 ± 632	1.31 ± 0.24
3. Restored Contraction	91 ± 7	57 ± 8 (76%)	2.2 ± 3.1	5033 ± 728 (62%)	1.03 ± 0.20
P	0.01	0.05	NS	0.05	NS

Means ± standard deviations for 4 hearts_are shown. Pre-arrest parameters were measured during blood-KHB perfusion whereas those for reflow were measured when hearts were perfused with KHB. P values for comparisons with pre-arrest were calculated using the directional Sandler's A-test. NS=not significant

Table 4.2. Blood Component Data

Step	**Glucose (mmol/L)**	**Lactate (mmol/L)**	**K^+ (mmol/L)**	**Hb (g/L)**
1. Beating Heart	8.7 ± 0.4	1.4 ± 0.3	4.4 ± 0.6	39 ± 13
2. KCl Arrest				
2.1 Pre-ischemia	8.5 ± 0.3	1.5 ± 0.1	16.4 ± 1.9	37 ± 10
2.2 End-ischemia	7.2 ± 0.5	2.7 ± 0.4	17.0 ± 0.6	39 ± 8
p (vs. 2.1)	0.01	0.01	NS	NS
2.3 Reflow	7.1 ± 0.3	3.1 ± 0.4	17.0 ± 0.6	40 ± 9
p (vs. 2.1)	0.001	0.005	NS	NS
3. Beating Heart	8.4 ± 0.4	2.7 ± 0.2	5.5 ± 0.9	41 ± 9
p (vs. 1)	NS	0.01	NS	NS

Means ± standard deviations for 4 hearts_are shown. Data correspond to end of each protocol step. P values for comparisons with baseline parameters (steps 1 and 2.1) were calculated using the directional Sandler's A-test. NS=not significant at 37 ± 4 mm Hg. TTC-stained myocardium in both the area at risk and the unaffected area indicated that the ischemic episode produced no irreversible damage (necrosis). The lack of necrosis is a result of the sharply reduced oxygen demand due to cardiac arrest.

Binding of molecules other than oxygen to hemoglobin can have potentially serious consequences on the appearance and interpretation of acquired spectra, if the hemoglobin compounds are present in significant quantities. For this reason, we also monitored levels of carboxy-hemoglobin (HbCO) and methemoglobin (metHb) in bloodsamples. Since carbon monoxide is not produced in isolated hearts in significant quantities, we did not expect that HbCO would impact our results. However, deoxy-Hb can be oxidized to metHb – especially during ischemia – so it was necessary to monitor its levels. HbCO levels determined by the hemoximeter were 1.7 ± 0.8 % and 1.3 ± 0.4 % during normal perfusion (after arrest) and after 2 hrs regional ischemia, respectively. Similarly, metHb levels were 1.0 ± 0.3 % and 1.1 ± 0.1 % during normal perfusion and regional ischemia, respectively. At no point did either hemoglobin derivative exceed 3% of total hemoglobin content, confirming that these hemoglobin derivatives were present in low enough quantities that they did not need to be included in our spectral analysis.

4.3.2. Acquired Spectra

Sample absorbance spectra are displayed in Figure 4.5. Perhaps the most striking feature was the uncharacteristically high noise level, as observed in spectra acquired both during normal perfusion and after 2 hrs ischemia (Figure 4.5a,b). Spectra acquired in other studies with NIRSI were substantially smoother,(11,148) and the source of this

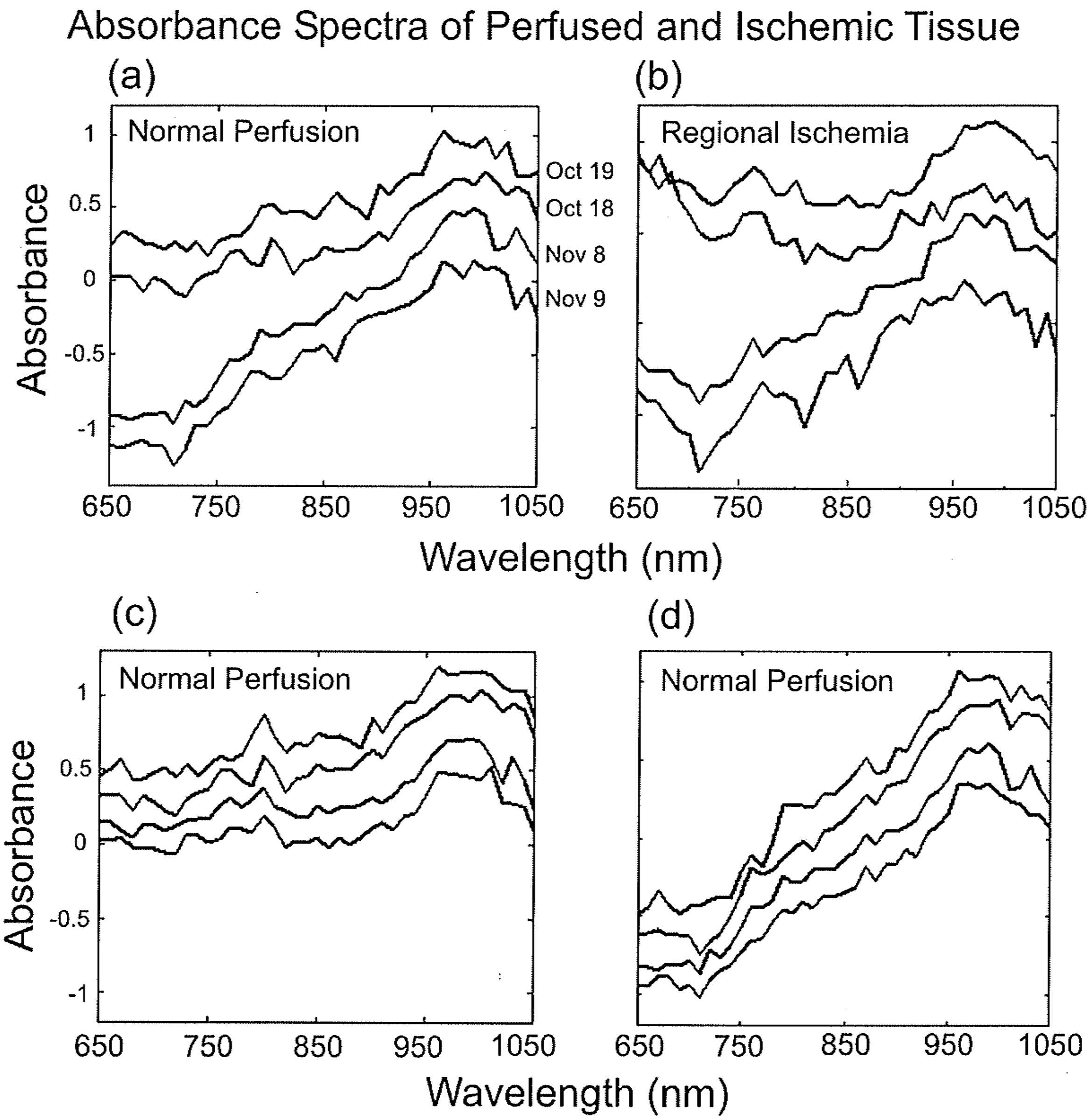

Figure 4.5. Sample absorbance spectra from tissue within the left ventricle proximal to the centre of the area at risk from each trial during (a) normal perfusion and (b) LAD artery occlusion. Panels (c) and (d) show the same spectra, evaluated using different background image sets. The data set exemplified by (d) was adopted for all further analysis.

noise was not entirely clear. It likely arises from the camera-filter system rather than properties of the heart or reference card, since raw reflectance spectra of the heart and the reference card appeared equally noisy. The fact that each individual image within the sequence is smooth and devoid of excessive noise suggests that the effect is not likely to be a result of differences in sensitivity among individual detectors within the CCD array. One likely possibility is random variability in the camera shutter speed. Non-uniformshutter speed would lead to variations in detected intensity among images, irrespective of absorbance or reflectance of the imaged object and treating all pixels within each image equally.

Despite the noise, absorption bands are still apparent and meaningful oxygenation information may still be gleaned from the spectra. For instance, in the spectra shown in Figure 4.5b, the peak at 760 nm and the increased absorbance near 650 nm characteristic of deoxy-Hb, as well as the 970 nm water absorption band, are readily apparent. Under these conditions, spectral fitting shows a clear advantage over discrete wavelength "spectroscopy", since the overall shape of the spectra, rather than absorbance values at individual wavelengths, are used to determine the chromophore coefficients.

In Figure 4.5 (a, b), spectra from two of the trials have visibly different profiles compared to spectra from the other two trials, primarily between 650 and 900 nm. While these differences were initially suspected to be due to differences in hemoglobin content or oxygenation, it appears that they are actually due to differences among the reference image sequences. To demonstrate this, raw reflectance cardiac image sequences were all ratioed against a single reference image sequence (from the Oct. 18 trial), and then against a different reference image sequence (from the Nov. 8 trial). Representative absorbance spectra from these spectroscopic images are depicted in Figure 4.5 (c and d), respectively. Clearly, when all cardiac image sequences are analysed with the same reference, spectra from all trials exhibit the same profile. Since the spectra corresponding to the Oct. trials in Figure 4.5a showed greater similarity in profile to spectra acquired in point spectroscopy studies, the Oct. 18 reference image sequence was used for spectroscopic images in all trials.

4.3.3. Imaging Data

In order to test the hypothesis that NIRSI can detect changes in cardiac deoxy-(Hb+Mb) and oxy-(Hb+Mb) concentrations resulting from ischemia, Figures 4.6 and 4.7 depict maps of the deoxy-(Hb+Mb) and oxy-(Hb+Mb) coefficient values for the four trials. Pixels coloured red correspond to good oxygenation (high oxy-Hb or low deoxy-Hb) and pixels coloured blue correspond to poor oxygenation.

4.3.3.1. Deoxy-(Hb + Mb)

Deoxy-(Hb+Mb) coefficient values were near zero during normal perfusion, as expected. Normal arterial and venous O_2 concentrations (600 and 300 mm Hg, respectively, when aerated with pure oxygen) are sufficient to result in hemoglobin being almost completely saturated in both arterial and venous blood, given the Hb p_{50} of approximately 26 mm Hg. While the intracellular O_2 concentration is only 2-7 mm Hg under normal perfusion conditions,(83,268) the low half-dissociation point of myoglobin

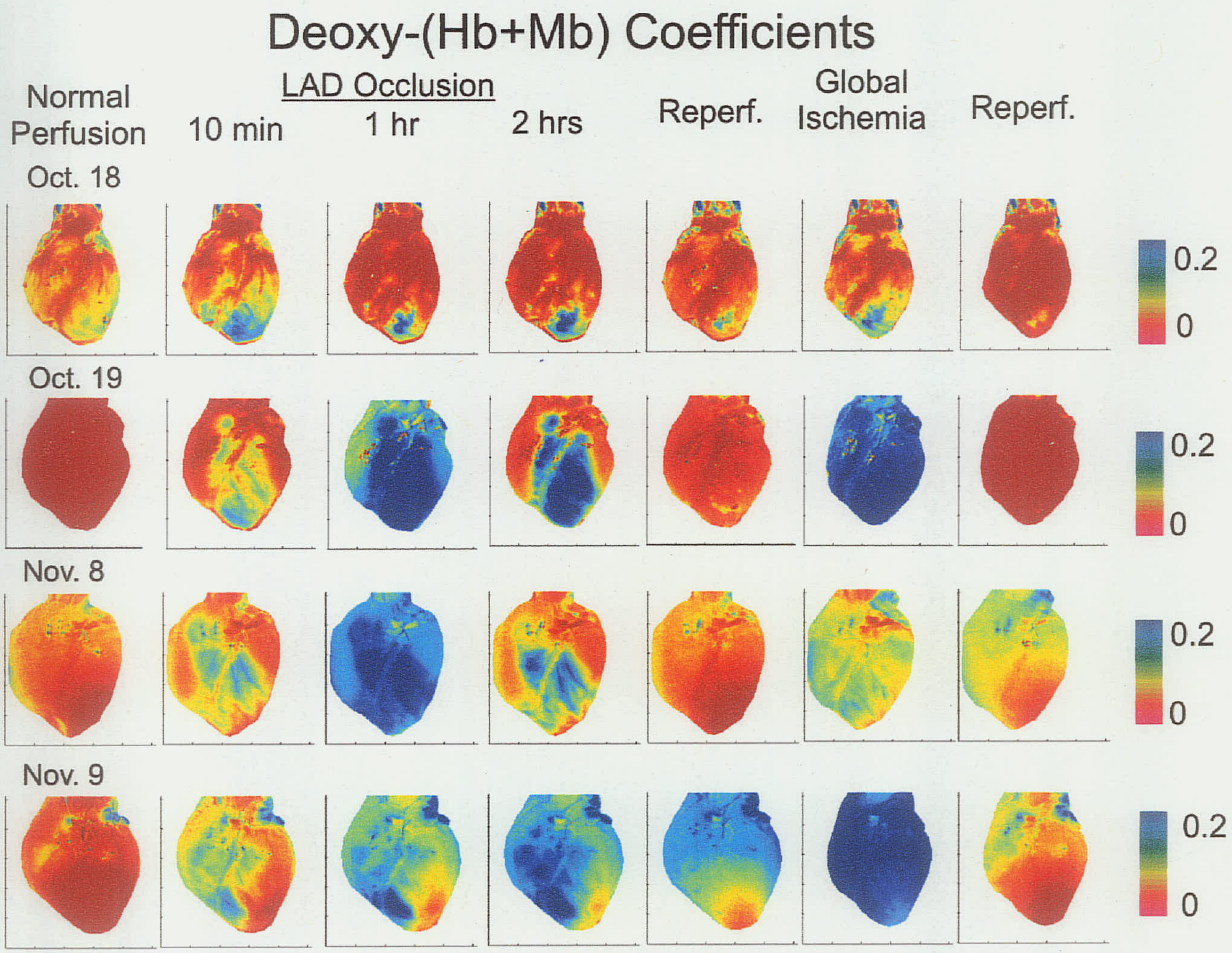

Figure 4.6. Deoxy-(Hb+Mb) concentration maps. High deoxy-(Hb+Mb) levels are shown in blue and low levels are shown in red.

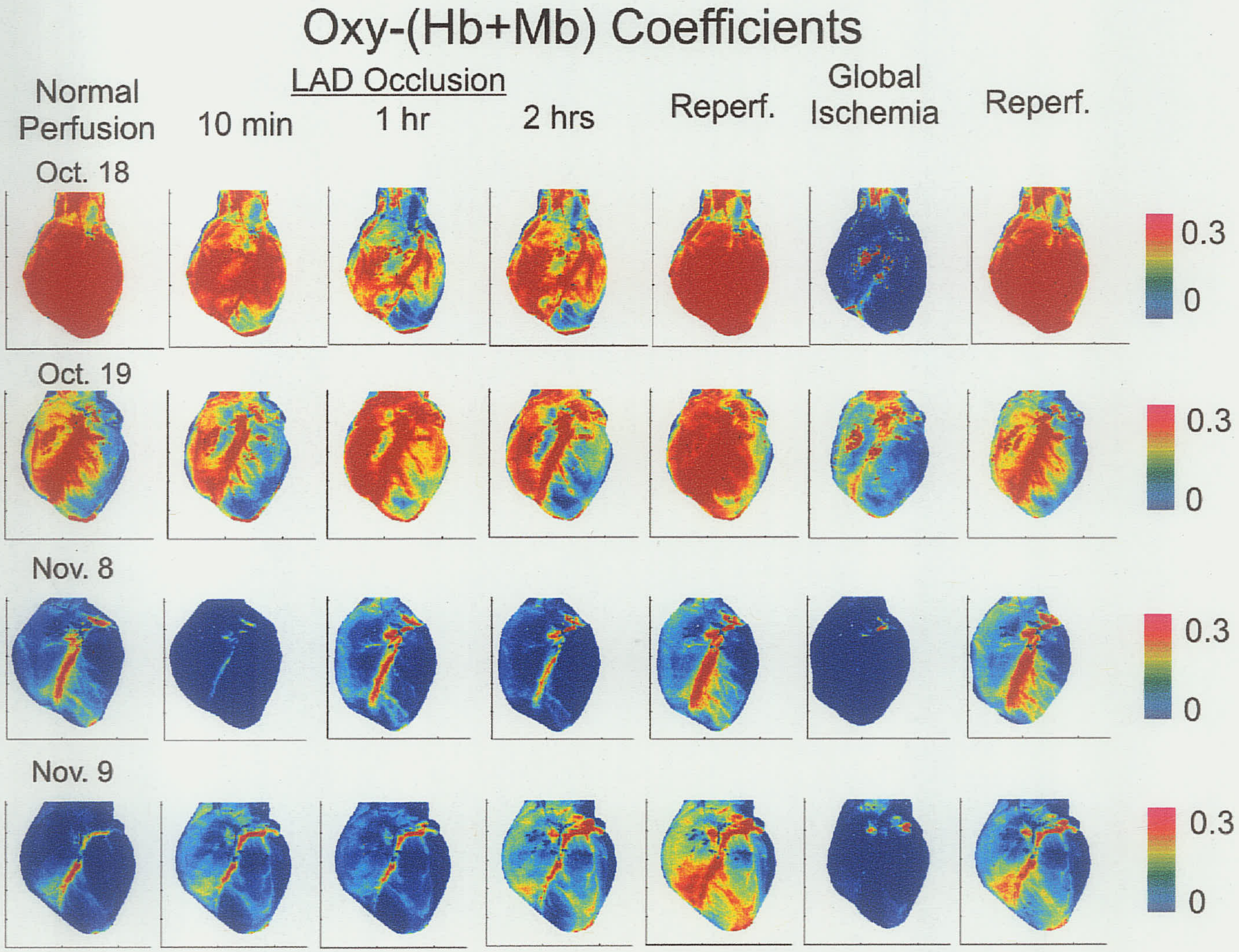

Figure 4.7. Oxy (Hb+Mb) concentration maps. High oxy-(Hb+Mb) levels are shown in red and low levels are shown in blue.

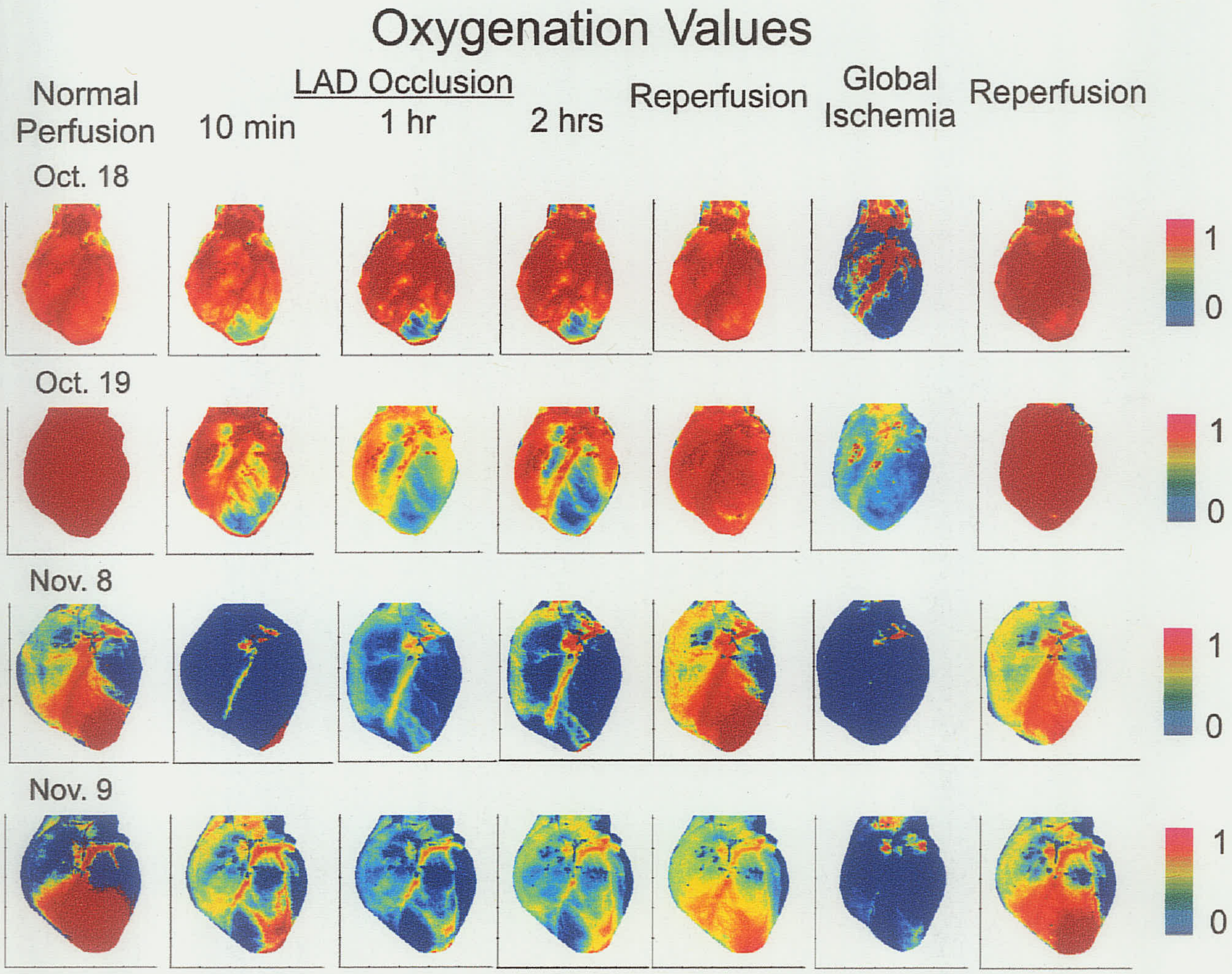

Figure 4.8. Oxygenation maps. High oxygenation levels are shown in red and low levels are shown in blue.

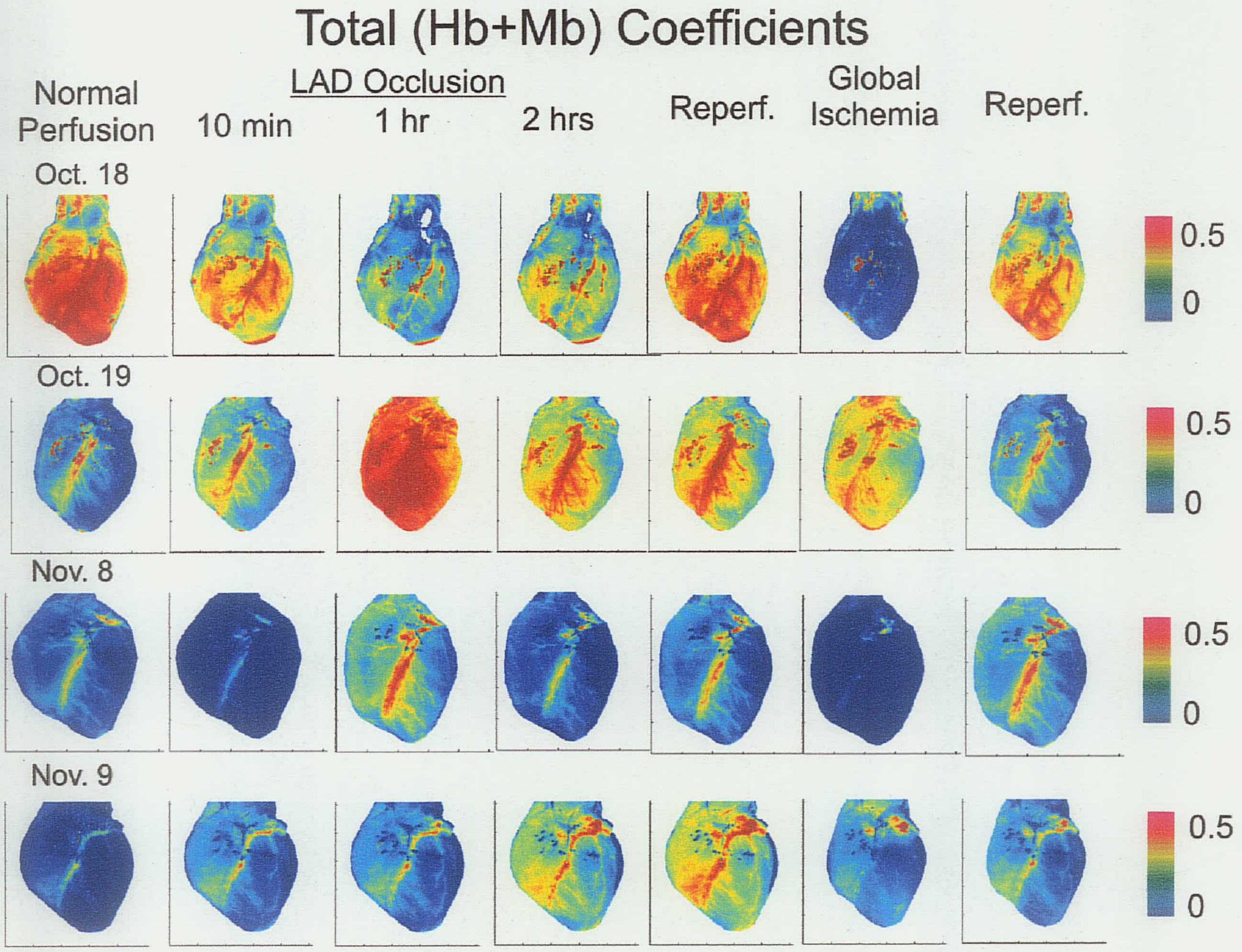

Figure 4.9. Total (Hb+Mb) concentration maps. High total (Hb+Mb) levels are shown in red and low levels are shown in blue.

of 2.5 mm Hg(268) or 5.3 mm Hg(83) ensures that intracellular myoglobin is also largely saturated. Thus, deoxy-(Hb+Mb) levels should be very low throughout the heart during normal perfusion, and this is reflected in the images.

Upon LAD occlusion, deoxy-(Hb+Mb) levels in the areas at risk rose almost immediately. As ischemia was prolonged, deoxy-(Hb+Mb) levels increased even further, as the blood and tissue in those areas became more severely deoxygenated. In mostcases, the boundaries of the areas at risk were also clear, and deoxy-(Hb+Mb) levels outside the areas remained comparable to those during normal perfusion. Moreover, the most severe deoxygenation was usually observed near the apex, which is most distal to the source of oxygen. A related factor that may play a role in these images is that during LAD occlusion, the decrease in blood volume (due to concomitant shrinkage of the extracellular space) could attenuate the observed increase in deoxy-(Hb+Mb) levels.

Upon reperfusion, deoxy-(Hb+Mb) generally returned to levels comparable to those of normal perfusion. Global ischemia precipitated a widespread and severe increase in deoxy-(Hb+Mb) in only two of the four trials (Oct. 19, Nov. 9). In one of the remaining two (Nov. 8), although the increase was widespread (affecting tissue that remained unaffected during regional ischemia), the increase was not nearly as severe as that observed during regional ischemia. In the fourth trial (Oct. 18), the increase was severe in the previous area at risk, but deoxy-(Hb+Mb) values for other regions of tissue did not change. In all cases, reperfusion following global ischemia resulted in the return of deoxy-(Hb+Mb) values to normal levels.

4.3.3.2. Oxy-(Hb + Mb)

The oxy-(Hb+Mb) maps displayed in Figure 4.7 demonstrate a similar trend to that seen in the deoxy-(Hb+Mb) maps – the area at risk exhibits reduced oxygenation in response to regional ischemia. The areas at risk as highlighted in the oxy-(Hb+Mb) maps also corresponded roughly to the areas at risk as revealed in the deoxy-(Hb+Mb) maps. In response to reperfusion, oxy-(Hb+Mb) levels rose to levels matching or exceeding those for normal perfusion. Most strikingly, global ischemia provoked a severe decrease in oxy-(Hb+Mb) values throughout the field of view. Oxy-(Hb+Mb) levels rose again in response to reperfusion. As was the case of deoxy-(Hb+Mb), blood volume changes may also play a role, but for oxy-(Hb+Mb), reduced blood volume during ischemia would exacerbate any decrease, making it more pronounced.

The oxy-(Hb+Mb) maps corresponding to global ischemia and reperfusion clearly demonstrate the applicability and validity of this technique in principle. There is a stark difference in coefficient values determined for these two extreme conditions. In all cases, oxy-(Hb+Mb) approached zero during global ischemia throughout the hearts, not just in the area at risk during LAD occlusion. Combined with the substantial increase in deoxy-(Hb+Mb) values observed in parallel, the validity of the approach to imaging regional cardiac oxygenation is clearly evident.

4.3.3.3. Oxygenation

To circumvent the influence of blood volume on these parameters, a parameter reflecting the oxygen saturation was defined as the ratio of oxy-(Hb+Mb) to total (Hb+Mb) (i.e. the sum of oxy-(Hb+Mb) and deoxy-(Hb+Mb)). While this parameter is not identical to real tissue oxygenation and the absolute scales may not correspond exactly (for reasons described below), this parameter is undoubtedly related to real oxygenation. Thus, for the sake of readability, it will be referred to as blood/tissue oxygenation. An oxygenation value of 1 corresponds to complete oxygen saturation of Hb and Mb and an oxygenation value of 0 indicates complete desaturation. The maps displayed in Figure 4.8 illustrate the deoxygenation in the areas at risk during regional ischemia, as compared to normal perfusion, and the restoration ofoxygenation upon reperfusion. As observed in the oxy-(Hb+Mb) maps, global ischemia results in severe deoxygenation throughout the tissue.

4.3.3.4. Total Hemoglobin and Myoglobin

The sum of oxy-(Hb+Mb) and deoxy-(Hb+Mb) coefficients should provide a measure of total hemoglobin and myoglobin in the tissue. To that end, total hemoglobin/myoglobin levels were evaluated as the sum of deoxy-(Hb+Mb) and oxy-(Hb+Mb) coefficients and mapped in an analogous fashion (Figure 4.9). With blood Hb levels constant and total myoglobin levels fixed, reduced total-(Hb+Mb) coefficient values would reflect decreased blood volume in areas at risk during ischemia. While only one of the four trials exhibited decreased total (Hb+Mb) values during regional ischemia, 3 of the 4 trials exhibited sharp decreases upon global ischemia. Nevertheless, there was significant variability in total (Hb+Mb) values, both among time points within the same trial and for the same time point of different trials. The fact that these values did not reflect total heme protein levels suggests the individual coefficient values should also be interpreted with caution, since they may not accurately reflect constituent concentrations.

4.4. Discussion

The experiment described in this chapter represented the first application of spectroscopic imaging to characterize cardiac ischemia. As such, a variety of issues – both foreseen and unforeseen – needed to be addressed. These involved choice of equipment, methods of data acquisition, and methods of spectral and data analysis. One surprising development was the uncharacteristically high noise level in the extracted spectra. This noise was later traced to variability in the camera shutter speed, although other factors may also have contributed. Although the noise could not be removed from the spectra, the spectral fitting algorithm was successful in gleaning oxygenation information from the overall spectral profiles. Moreover, although the noise level placed a limit on the precision of the derived coefficient values, the maps derived from them validated the principle that near-IR spectroscopic imaging can assess heme oxygenation in cardiac tissue. Several other factors also impact the validity and potential of this technique, as discussed here.

4.4.1. Extent of Ischemia

As discussed in Section 2.1.2.1, total ischemia is expected to result in severe deoxygenation of Hb and Mb almost immediately. After 10 minutes of total ischemia, certainly, essentially all heme proteins should be deoxygenated in the ischemic region. The coefficient maps graphically demonstrate this qualitatively. To place the results on a quantitative footing, regions of interest (ROIs) containing approximately 1000 pixels each were defined well within the area at risk and well outside the area at risk (control region) as depicted by the oxygenation maps at 2 hrs LAD occlusion. Mean (dHb+dMb) and (HbO_2+MbO_2) levels were calculated within those ROIs and are plotted in Figure 4.10. Error bars represent the standard deviations among the four trials.

After 10 min ischemia, oxy-(Hb+Mb) levels in the area at risk dropped significantly ($p < 0.05$), and remained constant throughout the ischemic period. Deoxy-(Hb+Mb) values also rose within the first 10 min ($p < 0.01$), but in contrast to oxy-(Hb+Mb), deoxy-(Hb+Mb) values after 1 hr ischemia were even higher than those at the 10 min time point ($p < 0.05$). However, the oxygenation values showed no significant difference within the area at risk between the 10 min and 1 hr time points (Figure 4.11). Upon reperfusion, both deoxy-(Hb+Mb) and oxy-(Hb+Mb) levels within the areas at risk all returned to those observed during normal perfusion. There was no change in the control region in any of these parameters throughout the regional ischemia protocol.

It was noted above that global ischemia triggered substantial changes in both deoxy-(Hb+Mb) and oxy-(Hb+Mb) levels throughout the entire heart, and these were observed within and outside the area at risk ($p < 0.05$). The changes in the oxygenation values were even more substantial ($p < 0.001$). Oxygenation was completely restored to normal perfusion levels during the final period of reperfusion.

It was found that tissue regions distal to the major arteries showed the most severe deoxygenation (they would be first affected by a reduction in flow), as demonstrated in Figure 4.12. The oxygenation maps for normal perfusion and prolonged ischemia are displayed using different colour scales, to maximize the contrast separately in each image. Arterial blood is more fully oxygenated than is capillary or venous blood, and the

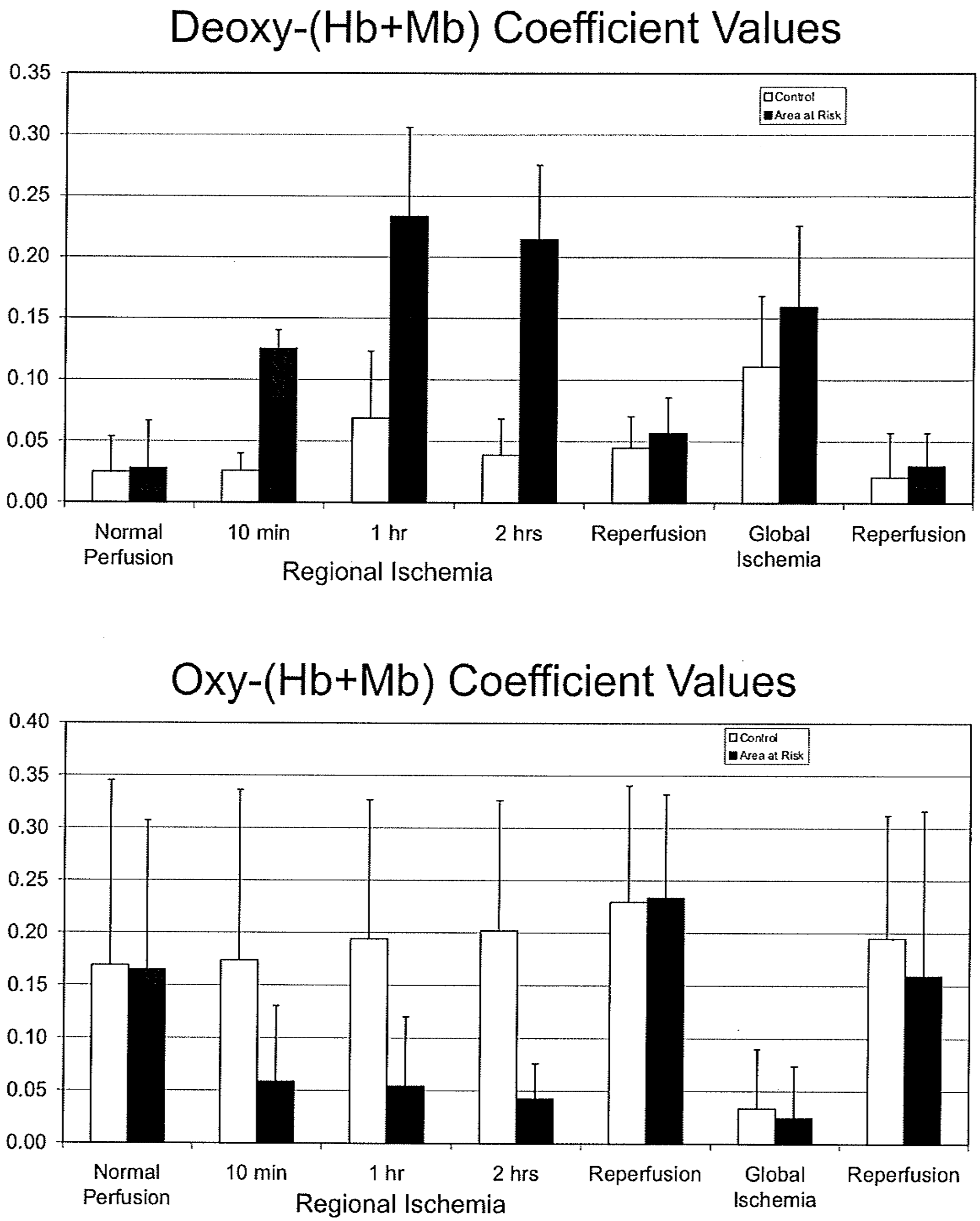

Figure 4.10. (a) Deoxy-(Hb+Mb) levels and (b) oxy-(Hb+Mb) levels within and outside the area at risk (black and white, respectively) at each time point.

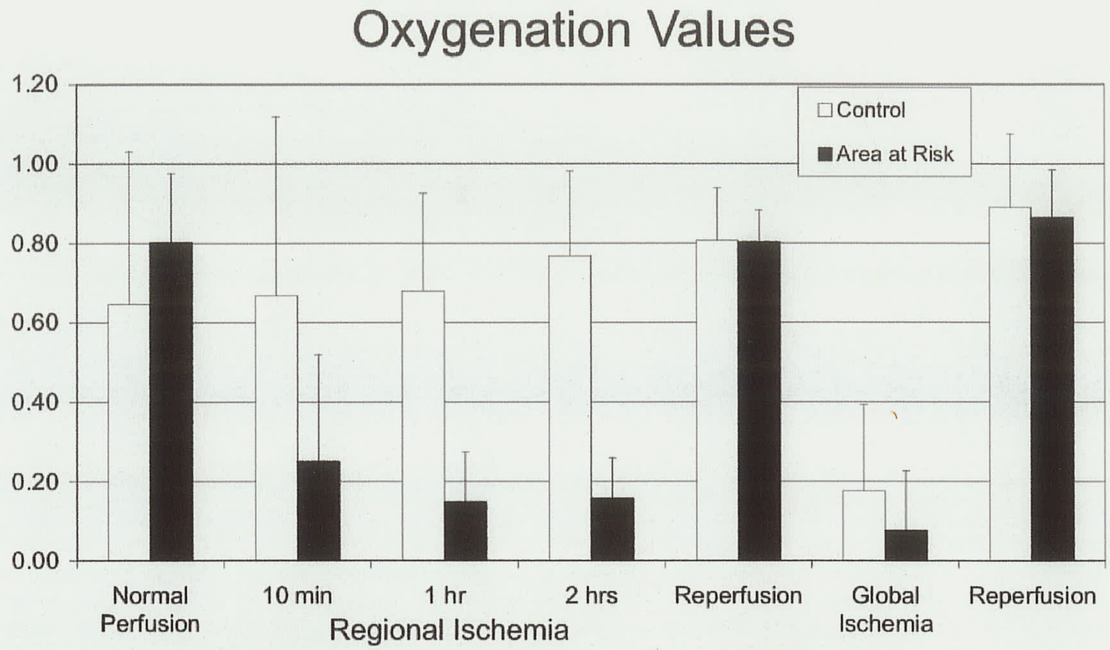

Figure 4.11. Tissue oxygenation within and outside the area at risk (black and white, respectively) at each time point.

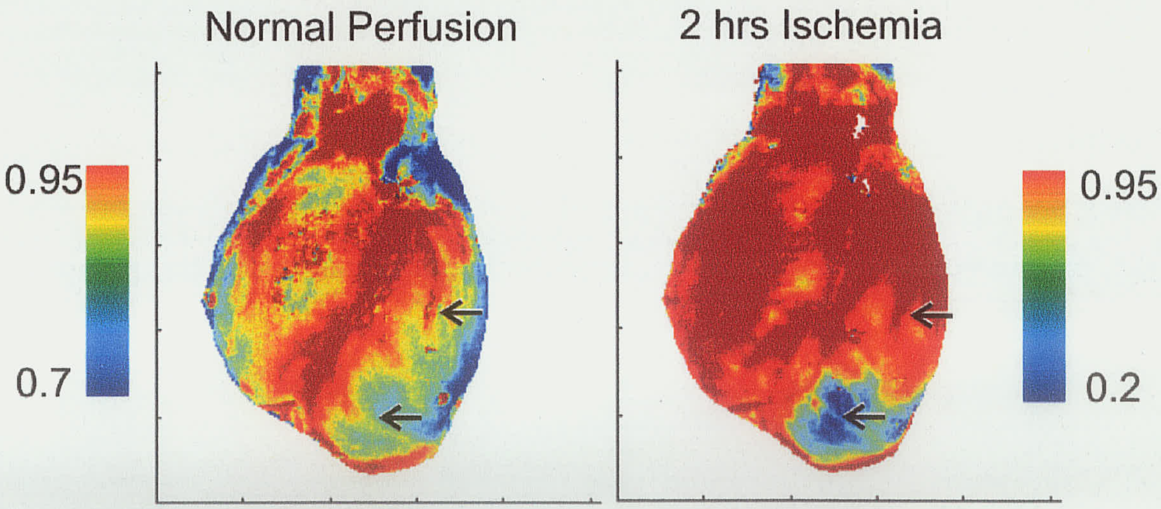

Figure 4.12. Oxygenation maps. Diagonal branches off the LAD artery exhibit greater oxygenation than surrounding tissue during normal perfusion and regional ischemia.

positions of the arterial branches off the LAD in the left ventricle are readily apparent in the normal perfusion map (arrows). After two hours of ischemia, these branches (arrows) still exhibit slightly higher oxygenation than the tissue immediately surrounding the arteries. This is most clearly evident within the area at risk, where a small artery can be identified, and could be due in part to residual oxygen remaining in the coronary vessels or slow diffusion of oxygen from the surrounding air. While it would diffuse into both the vessels and the surrounding tissue, oxygen diffusing into the tissue would be consumed immediately, whereas oxygen diffusing into the arteries would not.

4.4.2. Optical Pathlength

The issue of optical pathlength is perhaps the most significant single complicating factor in analysis of *in vivo* spectra.(7,59,188) An attempt was made in this study to account for the wavelength-dependence of pathlength, using the relationship derived in the previous chapter, but it remains unclear how transferable that relationship is to the present measurement protocol. In order to measure this effect, the spectra acquired in the present study were fit in three ways.

In the first approach, spectra were fit between 700 and 1000 nm with absorptivity spectra of deoxy-Hb, oxy-Hb, and water scaled by the relative pathlength function presented in Figure 3.11. In the second approach, only the deoxy-Hb and oxy-Hb absorptivity spectra were scaled by the relative pathlength function, and the spectra were then fit with these pathlength-adjusted absorptivity spectra between 650 and 890 nm. This region was chosen because it minimizes the wavelength range while including the distinctive absorption bands of hemoglobin (and myoglobin). For the third analysis, the same wavelength range was used, but the wavelength-dependence of pathlength was not accounted for. Instead, the acquired spectra were fit with pure absorptivity spectra. A baseline offset was included in all cases.

Samples of the original, acquired spectra and the spectra reconstructed from coefficients derived by the three approaches listed above are shown in Figure 4.13. The thin curves are the original spectra and the thick curves are the reconstructed spectra. Given the high level of noise in the measured spectra, it remains unclear whether the data from any one method are more accurate than data from the other methods; each approach appears to fit the original spectra adequately.

The maps of oxy-(Hb+Mb) and deoxy-(Hb+Mb) distribution, as determined by these approaches, are shown in Figure 4.14. First, it is worthwhile to point out that the maps for both deoxy-(Hb+Mb) and oxy-(Hb+Mb) are nearly identical for the two fits applying pathlength-adjusted spectra; the choice of wavelength region over which to fit appears to be inconsequential. However, when the pure spectra, rather than the pathlength-adjusted spectra are used in the fit, calculated oxy-(Hb+Mb) coefficients are lower and deoxy- (Hb+Mb) coefficients are higher. Thus, the use of pathlength-adjusted spectra in the fit does have a subtle effect on the calculated coefficients. However, it still remains unclear which of the derived values (and maps) are more accurate.

In addition to pathlength, other issues are worth considering to further refine the spectral analysis. For example, some absorption bands may shift and/or broaden in *in vivo* spectra as compared to the absorptivity spectra. In Figure 4.13, the 970 nm

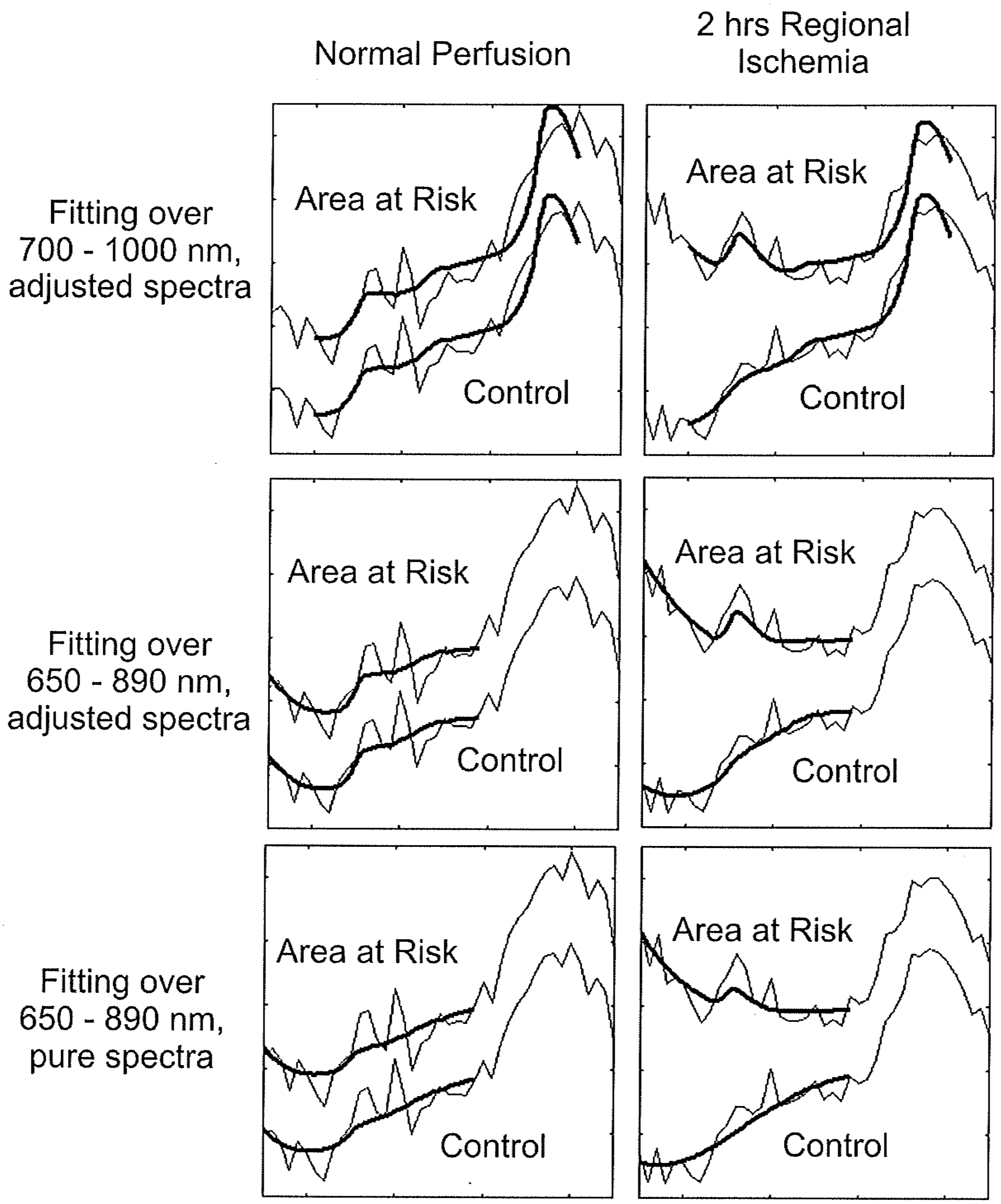

Figure 4.13. Effect of choice of fitting parameters on closeness of fits in representative spectra.

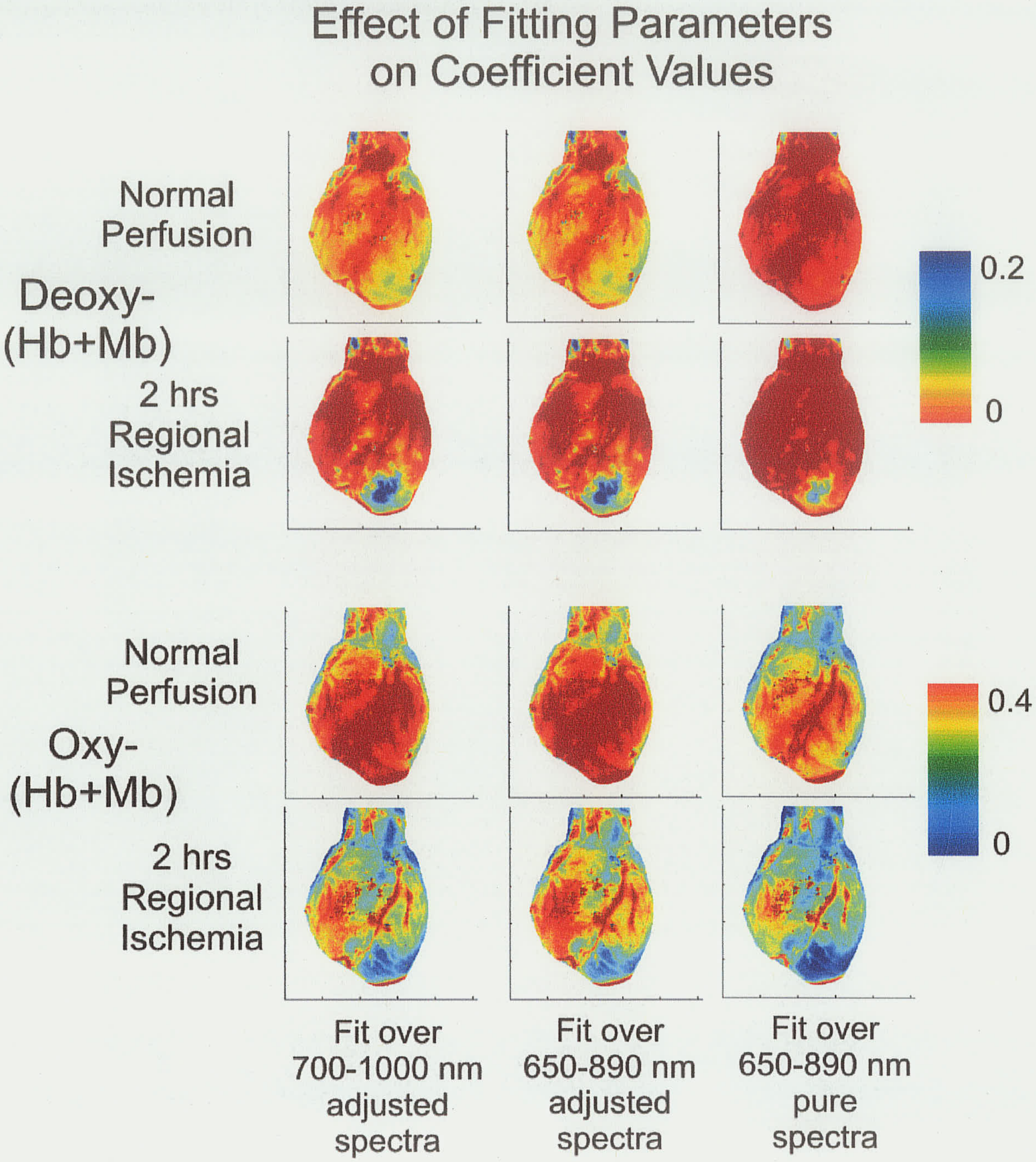

Figure 4.14. Effect of choice of fitting parameters on deoxy-(Hb+Mb) and oxy-(Hb+Mb) coefficient maps.

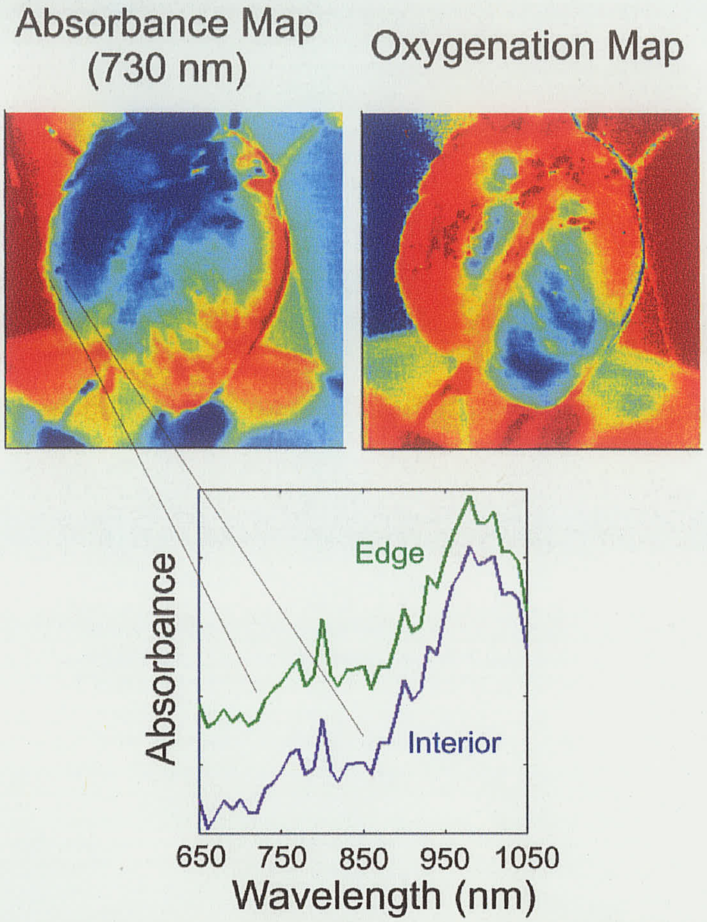

Figure 4.15. Effect of curvature in heart on tissue spectra and absorbance maps.

absorption band (due to water) in the acquired spectra consistently appears broader than the band in the pure absorptivity spectrum of water, and this broadening is suspected to be due largely to chemical interaction of water with various micro-environments within the heart tissue.

4.4.3. Effect of Curvature

Curvature of the heart was expected to result in an artifact along the periphery of the heart, where the heart surface was not normal to the line of sight. Such an effect was indeed observed. Absorbance images at every wavelength exhibited values higher near the periphery of the imaged heart than in the centre of the image. This is demonstrated in Figure 4.15 for the case of 730 nm. The increased absorbance values are due to decreased light intensity from those regions reaching the detector. Since the surface of the heart in those regions is not normal to the line of sight, light illuminating that tissue is not strongly directed to the camera, and little intensity is detected. Since the reflectance standard used in these studies was not curved, the low intensity detected along the edge in the cardiac images were not corrected in creation of the spectroscopic images.

Nevertheless, comparison of spectra corresponding to the edge and centre of the field of view demonstrate that, under the same perfusion conditions, spectra corresponding to the edge are not distorted relative to those corresponding to the centre but simply shifted uniformly upward. As a result, the baseline correction factor B (Equation 4.3) incorporated into the spectral fitting algorithm corrected for spectral variations due to curvature, and deoxy-(Hb+Mb) and oxy-(Hb+Mb) fitting coefficients were not substantially affected by such variations. Thus, there is virtually no artifact in the coefficient or oxygenation maps resulting from curvature.

4.4.4. Hemoglobin and Myoglobin

As mentioned in Section 4.2.4, hemoglobin and myoglobin have nearly identical absorptivity spectra, and direct determination of their relative concentrations from the acquired spectra is difficult. However, a rough estimate may be achieved by other means. The relative spectral contributions of Hb and Mb depend on the Hb concentration in the blood, the local blood volume in the area of interest, and the Mb concentration in the cardiac tissue. In the present case, mean blood Hb levels were maintained at 40 g/L throughout the experimental protocol (Table 4.2), which translates into 0.63 mmol Hb / L (2.52 mmol heme / L). Blood is not uniformly distributed throughout the heart, but rather concentrated near the major arteries, and in regions of tissue distal to major arteries, most of the blood is in the capillary space. Since capillaries have been estimated to comprise approximately 8% of tissue volume,(5) tissue heme content from Hb will be approximately 0.2 mmol/L in regions of tissue away from major vessels (2.52 x 0.08), which is just over half of the average Mb content (0.36 mmol/kg in pig hearts).(5) Thus, in cardiac tissue spectra, Mb can be expected to account for approximately two thirds of the total signal from oxy- and deoxy-(Hb+Mb). However, for pixels overlying major arteries such as the LAD and its primary branches, the contribution of Hb is expected to dominate over the contribution of Mb.

4.5. Conclusions

In conclusion, this study demonstrates that near-IR spectroscopic imaging can in principle monitor regional changes in heme protein oxygenation in myocardial tissue, even in the presence of significant noise. Despite this noise, spectral fitting extracted useful oxygenation data for the cardiac tissue, and analysis of the images validates the hypothesis that spectroscopic imaging can distinguish between normally perfused and ischemic regions of tissue.

Under the same physiological conditions, there was still significant variability in both deoxy-(Hb+Mb) and oxy-(Hb+Mb) values among the different trials, but it remains unclear whether this is due to real variability in cardiac anatomy or physiology or error in the measurement procedure. The number of samples used in this study (four) does not provide reliable statistical data; a small number was chosen for financial reasons, as well as those of animal conservation, since this was a proof-of-concept study. The success encountered here lays the foundation for more elaborate investigations presented in the following two chapters.

5. Isolated, Beating Hearts

5.1. Introduction

The study described in the previous chapter demonstrated that despite uncharacteristically noisy spectra (due to mechanical difficulties with the camera), spectroscopic imaging can highlight regions of cardiac tissue suffering from severe regional ischemia under idealized conditions. The present study extends the technique in a number of directions so as to approximate surgical conditions more closely. Perhaps the most glaring shortcoming of the previous study was poor signal-to-noise. Since the high noise level appeared to arise from variability in the camera's shutter speed, that camera/filter system was replaced for the present study. As shown below, this significantly improved the spectra.

This protocol was designed with three primary objectives. The first was to assess the feasibility of imaging beating hearts without excessive blurring or motion artifacts, since this is a prerequisite for broad clinical applicability. Thus, hearts in all trials were beating continuously during the imaging procedure. The impact of motion artifacts was minimized by triggering image acquisition to the electrocardiogram, ensuring that all images were acquired at the same point of the cardiac cycle.

Secondly, the sensitivity of oxygenation maps to the degree of ischemia was gauged by imaging during partial coronary occlusion. Arterial flow was reduced to 50% and 20% of normal values before completely occluding the artery and oxygenation maps were derived for each stage. The value of 50% was taken as a benchmark because even this reduction of flow is not deemed significant enough by cardiac surgeons to warrant surgical intervention. The third objective was to assess the impact of intermediate reperfusion on the oxygenation maps during graded, regional ischemia. In addition to these primary objectives, some secondary questions were addressed:

- Does spectroscopic imaging have the necessary time resolution to monitor kinetics of deoxygenation resulting from ischemia and reperfusion?
- Can spectroscopic imaging reveal differences in tissue oxygenation between systole and diastole?
- Are measured oxygenation values (determined from the spectroscopic images) related to blood oxygen saturation?

5.2. Materials and Methods

5.2.1. Surgery and Perfusion

Regional ischemia protocols were carried out using isolated pig hearts (n=8, 150 – 200 g). The surgery and heart removal procedures were identical to those described in Chapter 4, except that after insertion of the cannula into the brachiocephalic artery for connection with the perfusion pressure line, a second cannula was inserted into the left anterior descending (LAD) artery, distal to the first diagonal branch off the LAD (Figure 5.1). The purpose of this cannula was to control downstream flow independently of flow to the rest of the heart. The insertion point was distal to the first diagonal branch in order to keep the area at risk to a manageable size. This had a two-fold purpose: first, it ensured that normally perfused tissue would also be well within the field of view of the camera; second, it reduced the risk of cardiac functional problems such as arrhythmias during periods of severe ischemia. These cannulas were connected to the main perfusion line via

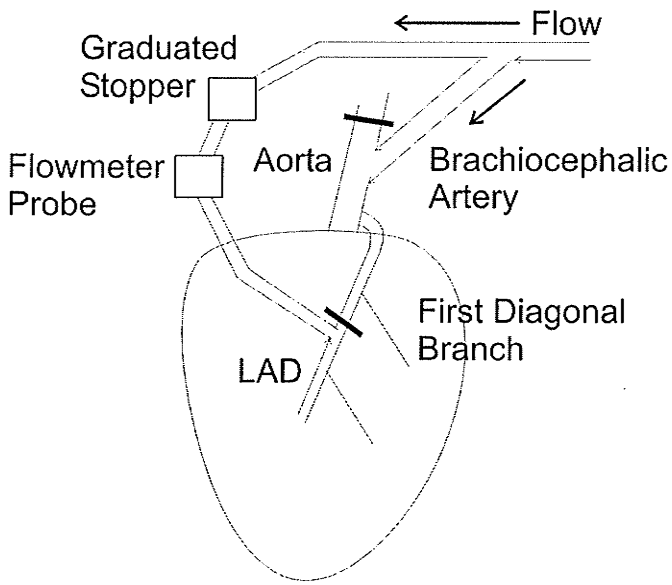

Figure 5.1. Schematic diagram of heart and equipment for control of LAD flow.

a T-junction. A graduated stopper was placed between the junction and the LAD cannula to reduce LAD flow gradually. A flowmeter probe (Transonic Systems, Ithaca, NY) was placed between the graduated stopper and the cannula to monitor LAD flow.

Perfusion hardware and methods were also identical to the previous study, except that the heart was not arrested. At the beginning of perfusion, the perfusate contained 8.8 ± 1.1 mM glucose, 2.0 ± 0.2 mM lactate, 48.0 ± 8.3 g/L hemoglobin (Hb, ~45% of normal content in pig blood), heparin (10 000 U/L) and 1 μM propranolol (β-blocker). Left ventricular (LV) systolic pressure (LVSP, 90 ± 14 mm Hg), end-diastolic pressure (LVEDP, 3.6 ± 1.9 mm Hg), and heart rate (HR, 102 ± 15 bpm) were monitored. The pressure-rate product, an index of cardiac performance, was maintained at 8980 ± 1810 mm Hg / min. Metabolite levels were also monitored as in the previous study.

5.2.2. Image Acquisition and Gating

In an effort to improve signal-to-noise, the imaging system used in the previous study was replaced with a new system (although with nearly identical nominal specifications). The camera included an infrared-sensitive 512 x 512 back-illuminated charge-coupled device (CCD) element and 14/16-bit ST-138 analog to digital converter run in 16-bit mode (Photometics, Tucson, AZ), and the lens was a Nikon Micro AF60 with an aperture setting of f/4. Binning (2x2) was performed to produce images with 256 x 256 pixel resolution as before. The LCTF (Cambridge Research & Instrumentation, Woburn, MA) had a bandwidth of approximately 10 nm. While this is slightly larger than the 7 nm bandwidth used in the previous study, the difference is low compared to the width of the absorption bands of interest (30-250 nm). The lamp and equipment configuration and image acquisition software were unchanged from the arrested heart study, except for an adaptation in the software to allow external triggering of acquisition.

To ensure that images of beating hearts were consistently taken at the same point of the cardiac cycle, acquisition was triggered by the QRS peak of the electrocardiogram (ECG)[84]. Electrodes were placed on lateral faces of the heart outside the camera's field of view, and connected to a recorder (Grass Telefactor, West Warwick, RI) which transmitted the ECG voltage wave to a gating box (developed in-house) that in turn supplied a square voltage pulse to the computer when the ECG voltage surpassed an assigned threshold value. This square pulse served as an external trigger for the image

---

[84] From the Greek *ēlektron* (meaning *amber*, on which static electricity can be generated by friction), *kardia* (meaning *heart*), and *gramma* (meaning *drawing*), it is a graphic record of electrical currents within the heart. It is often referred to as an EKG, since it was developed in 1903 by Willem Einthoven, a Dutch physiologist, and this is the abbreviation for the Dutch word. For this discovery, Einthoven won the Nobel Prize in Medicine in 1924.

acquisition software. Gating software (also developed in-house) allowed for adjustment of both the threshold voltage and the delay between detection of the QRS peak and emission of the square pulse.

To minimize blurring during imaging, the exposure time was adjusted to the minimum level compatible with good signal-to-noise. It was found that an 80 ms exposure time (with appropriate lamp intensity levels) provided the best compromise to satisfy both requirements. To reduce the total acquisition time for complete spectroscopic images (for practical and potential clinical purposes), the number of images co-added at each wavelength was reduced from five to three. There was no substantial loss in signal-to-noise with this change, and total acquisition time was reduced from five minutes to four. Images were acquired as before at 10 nm intervals between 650 and 1050 nm (41 images per data set).

Finally, in order to monitor the kinetics of deoxygenation, additional, "fast" image sets were collected. In this approach, a single image was acquired at each wavelength and images were acquired at 30 nm intervals between 650 and 890 nm. This reduced the number of acquisition wavelengths from 41 to 9, and the total acquisition time to about one minute. The wavelength range was chosen to encompass the major spectral features of oxy-Hb and deoxy-Hb. These 1-min image sets were acquired immediately after onset of ischemia and reperfusion in the second group of trials.

5.2.3. Experimental Protocol

The trials in this study were divided into two groups of four hearts each; the aim of the first group was to assess the sensitivity of NIRSI to different degrees of ischemia, and the aim of the second group was to assess the impact of intermediate reperfusion. The first group followed protocol #1, outlined schematically in Figure 5.2. Following an equilibration period (30-40 min, 42 ± 5 mL/min), flow through the LAD artery was reduced to half its initial value (21 ± 4 mL/min) and maintained at that level for 15 min. The LAD arterial flow was then further reduced to approximately 20% of normal flow (15 min at 8.2 ± 0.8 mL/min), followed by 15 min of complete LAD occlusion. Two image sets were acquired during each period. The occlusion was then released to reperfuse the LAD bed for 10 min. Blood flow to the entire heart was then completely stopped for 10 min to produce global ischemia, followed by 10 min of restored flow. Two image sets were acquired at each stage of the protocol.

The second group of hearts followed the same protocol except that the LAD perfusion bed was reperfused with normal flow for 10 min in between each period of ischemia. This reperfusion was to ensure that any differences in oxygenation maps reflected the severity of ischemia rather than its duration. Since preliminary analysis of the first group of hearts confirmed good signal-to-noise and reasonable consistency in results, the second protocol included the experiments to address the secondary objectives listed in the introduction to this chapter. In order to monitor kinetics, 1-min (fast) image sets were acquired repeatedly during at least the first six minutes following the onset of each period of ischemia. To permit this, only a single 5-min image set (instead of two) was acquired during each stage of the protocol. Differences in oxygenation between systole and diastole were studied in the 1-min image sets for three of the four trials of Group II. To this end, the delay between the trigger pulse and image acquisition was

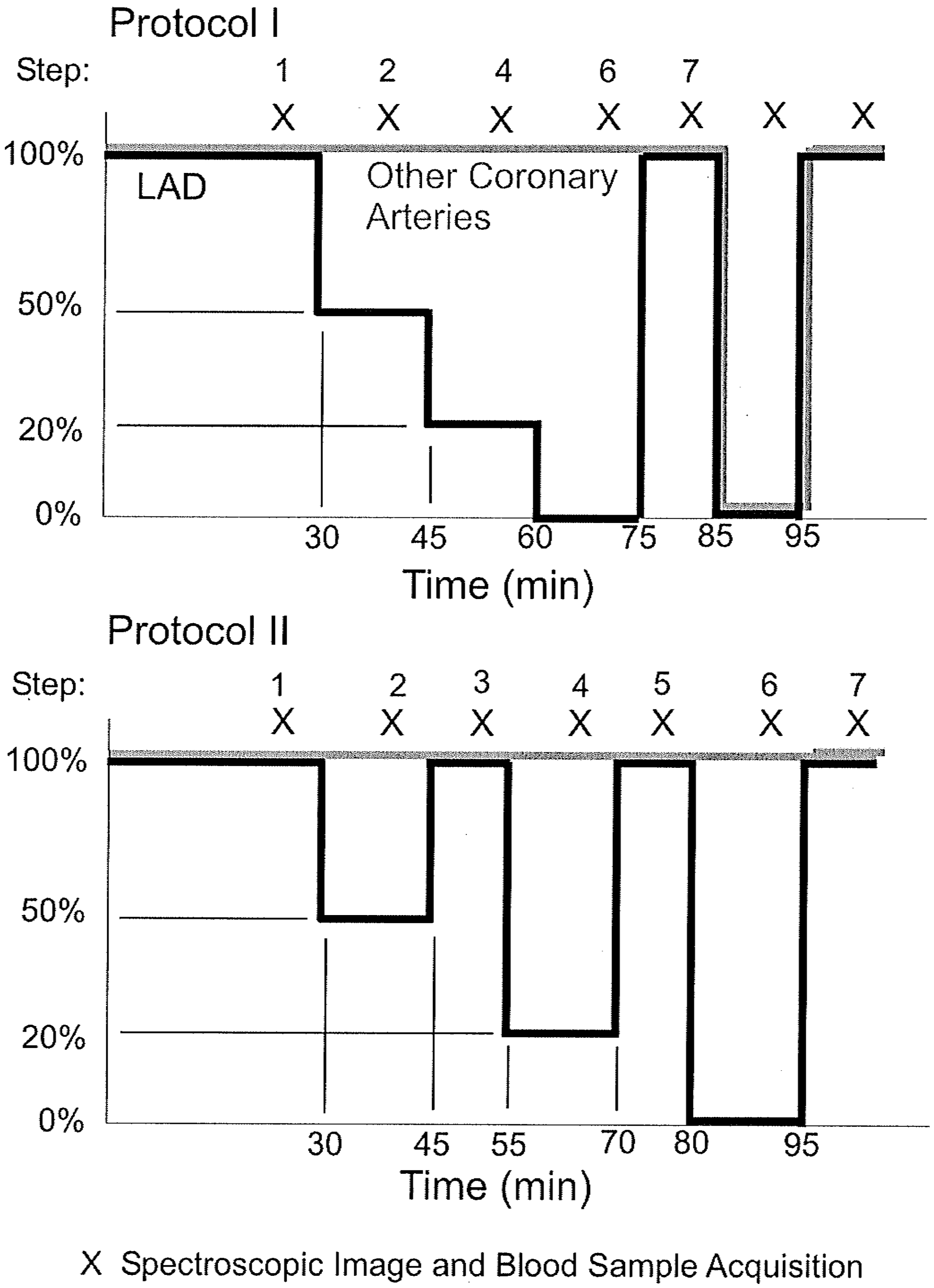

Figure 5.2. Experimental protocols for the two groups of trials. Step numbers correspond to those in Tables 5.1 and 5.2.

adjusted so that acquisition of the 1-min image sets alternated between systole and diastole.

Global ischemia was not induced in Protocol #2. Instead, once the regional ischemia protocol was complete, the hearts were subjected to four 15-min periods of increasingly severe hypoxia at constant flow (48.5 ± 9.3 mL/min), during which arterial (and venous) oxygen saturation of hemoglobin was reduced stepwise from 100% (97 ± 1%) to 34 ± 7% (19 ± 6%), followed by restoration of oxygen saturation to 100%. Hypoxia was induced by replacing oxygen with nitrogen in the gas mixture (95% O_2 / 5% CO_2 + 95% N_2 / 5% CO_2). Five-minute spectroscopic images were acquired at time points at least 10 min after each reduction of oxygen content. Blood samples were acquired either immediately before or immediately after acquisition of each 5-min spectroscopic image.

At the end of each trial, the heart was arrested, the LAD was reoccluded, and perfusion was stopped. The hearts were then stained with a 0.25% Evans Blue solution (which has a broad absorption band centred near 650 nm) in 60 ml of isotonic saline, injected through the aorta for 30-40 s in order to highlight the area at risk, and a final spectroscopic image was then acquired. While in the previous study, the only means of identifying the area at risk was via oxygenation maps, Evans Blue was used in the present study to test the reliability of these maps in this regard. As described in Section 2.1.3, LAD occlusion prevents Evans Blue from staining the area at risk. Following Evans Blue staining, each heart was then sliced and stained with TTC to identify any necrotic tissue.

5.3. Results

5.3.1. Physiological Data

As in the previous study, all hearts showed stable contractile function during the equilibration period (Table 5.1). The size of the areas at risk, as determined by Evans Blue staining, was comparable in the two groups. The areas at risk in Group I and Group II trials were 34 ± 3% and 33 ± 3% of the left ventricular mass, respectively. Only one of the eight hearts exhibited any necrosis. In that heart, 8% of the area at risk was necrotic. In hearts of the first protocol, upon the initial 50% reduction in LAD flow, left ventricular systolic pressure (LVSP) and the pressure-rate product (PRP) both decreased to 81% of normal levels, although there was no significant change in the rate of oxygen consumption. Following a further flow reduction to 20% of equilibrium values, the LVSP and PRP both fell to nearly half of equilibrium levels and the oxygen consumption rate fell to 76% of equilibrium levels. When regional flow was stopped completely, LVSP and PRP dropped further to 27% and 26% of equilibrium levels, respectively, while oxygen consumption remained near the level of 20% flow. Upon reperfusion, LVSP and PRP levels recovered partially, rising to 60% of equilibrium levels and the oxygen consumption decreased further slightly. The heart rate was constant throughout the protocol.

For hearts of the second protocol, a reduction of LAD flow by half dropped LVSP and PRP to 73% and 68% of normal levels, respectively (reperfusion values were not significantly different from baseline). Reduction in flow to 20% reduced LVSP and PRP to 42% and 34%, respectively. At this stage, however, reperfusion only partially restored LVSP and PRP, to 68% and 62%, respectively. Cessation of flow reduced these

Table 5.1. Cardiac Functional Parameters and Oxygen Consumption Data

Step	***HR (bpm)***		***LVSP (mm Hg)***		***PRP (mm Hg / min)***		***V(O$_2$) (μmol/min/g)***	
Protocol:	I	II	I	II	I	II	I	II
1. Baseline	93 ± 4	103 ± 20	82 ± 14	81 ± 16	7203 ± 1240	7998 ± 1777	1.29 ± 0.21	0.83 ± 0.14
2. 50% flow	92 ± 3	102 ± 21	66 ± 11	59 ± 17	5823 ± 956	5428 ± 1706	1.23 ± 0.23	0.75 ± 0.07
p value	*NS*	*NS*	*0.005*	*0.005*	*0.005*	*0.001*	*NS*	*NS*
3. Reperfusion	N/A	99 ± 23	N/A	70 ± 21	N/A	6930 ± 2497	N/A	0.78 ± 0.05
p value	N/A	*NS*	N/A	*NS*	N/A	*NS*	N/A	*NS*
4. 20% flow	94 ± 4	101 ± 22	42 ± 8	34 ± 11	3840 ± 590	2713 ± 699	0.98 ± 0.21	0.75 ± 0.06
p value	*0.05*	*NS*	*0.005*	*0.001*	*0.005*	*0.005*	*0.05*	*NS*
5. Reperfusion	N/A	103 ± 22	N/A	55 ± 9	N/A	4958 ± 952	N/A	0.87 ± 0.18
p value	N/A	*NS*	N/A	*0.005*	N/A	*0.01*	N/A	*NS*
6. No flow	93 ± 4	106 ± 20	22 ± 9	21 ± 4	1875 ± 569	1465 ± 795	1.01 ± 0.11	0.70 ± 0.12
p value	*NS*	*NS*	*0.001*	*0.005*	*0.001*	*0.005*	*NS*	*0.05*
7. Reperfusion	91 ± 4	99 ± 12	49 ± 9	45 ± 7	4148 ± 615	3688 ± 901	0.94 ± 0.25	0.82 ± 0.20
p value	*NS*	*NS*	*0.01*	*0.005*	*0.005*	*0.01*	*0.05*	*NS*

Means ± standard deviations (n=4) for hearts in Groups I and II are shown. Data correspond to end of each protocol step. P values for comparison with baseline parameters were calculated using the directional Sandler's A-test.

(NS = not significant; N/A = not applicable)

Table 5.2. Blood Component Data

Step	*K^+ (mmol/L)*		*Glucose (mmol/L)*		*Lactate (mmol/L)*		*Hb (g/L)*	
	I	II	I	II	I	II	I	II
1. Baseline	4.9 ± 0.4	4.6 ± 0.2	9.2 ± 1.0	8.4 ± 1.2	2.0 ± 0.2	2.0 ± 0.1	46 ± 6	51 ± 10
2. 50% flow	4.8 ± 0.5	4.6 ± 0.3	8.9 ± 1.0	8.1 ± 1.1	1.8 ± 0.3	2.0 ± 0.2	46 ± 7	52 ± 9
p vs.1	*NS*	*NS*	*0.01*	*0.05*	*NS*	*NS*	*NS*	*NS*
3. Reperfusion	N/A	4.7 ± 0.3	N/A	8.1 ± 0.9	N/A	2.0 ± 0.4	N/A	53 ± 10
p vs.1.	N/A	*NS*	N/A	*NS*	N/A	*NS*	N/A	*NS*
4. 20% flow	4.9 ± 0.5	4.8 ± 0.2	8.7 ± 0.9	7.7 ± 0.8	1.9 ± 0.5	2.3 ± 0.3	47 ± 7	53 ± 10
p vs.1.	*NS*	*0.01*	*0.01*	*0.05*	*NS*	*NS*	*NS*	*NS*
5. Reperfusion	N/A	4.7 ± 0.2	N/A	7.6 ± 0.8	N/A	2.5 ± 0.4	N/A	53 ± 9
p vs.1.	N/A	*NS*	N/A	*0.05*	N/A	*0.05*	N/A	*NS*
6. No flow	5.0 ± 0.5	4.8 ± 0.2	8.7 ± 0.8	7.3 ± 0.8	2.0 ± 0.5	2.7 ± 0.5	47 ± 7	53 ± 8
p vs.1.	*0.05*	*0.05*	*0.005*	*0.01*	*NS*	*0.05*	*NS*	*NS*
7. Reperfusion	5.1 ± 0.4	4.8 ± 0.3	8.5 ± 0.8	7.1 ± 0.8	2.5 ± 0.9	3.2 ± 0.6	48 ± 7	54 ± 10
p vs.1.	*0.02*	*NS*	*0.05*	*0.01*	*NS*	*0.05*	*0.005*	*NS*

Means ± standard deviations (n=4) for hearts in Groups I and II are shown. Data correspond to end of each protocol step. P values for comparisons with baseline parameters were calculated using the directional Sandler's A-test.
(NS = not significant; N/A = not applicable).

parameters further to 21% and 18% of the equilibrium values, and oxygen consumption also fell to 80% of baseline levels. Reperfusion again partially restored LVSP and PRP to 56% and 46% of normal values, respectively. Heart rate again remained unchanged throughout the protocol.

These results demonstrate that reperfusion between periods of successively more severe regional ischemia does not alter cardiac performance, relative to the same graded regional ischemia protocol without intermediate reperfusion. Differences in LVSP, PRP, or HR values between the two protocols were not significant, either during any corresponding period of regional ischemia or during the final period of reperfusion. Of particular relevance are the findings that blood Hb levels remained constant in all hearts (Table 5.2) and changes in oxygen consumption were also comparable between the two groups of hearts. That is, while oxygen consumption rates for the two groups were significantly different at corresponding steps of the protocol (including baseline), normalization of these rates to baseline values eliminated this difference. This observation suggests that changes in heme protein oxygenation as determined by spectroscopic imaging should also be comparable.

Ischemia had little impact on blood component concentrations. K^+, Hb, pH, Na^+, Ca^{++}, and Cl^- levels remained constant throughout the protocol. While ischemia might be expected to cause a rise in blood lactate levels (due to increased anaerobic glycolysis, see Section 2.1.2.1), no such rise was observed during either 50% or 20% LAD flow (Table 5.2), although complete regional ischemia did trigger a small increase in lactate, from 2.0 ± 0.1 to 2.4 ± 0.6 ($p < 0.05$, n=8). Reperfusion further increased blood lactate levels to

2.9 ± 0.8 ($p < 0.01$). Glucose also continued to decrease gradually throughout the protocol ($p < 0.05$). These changes could be due in part to removal of glycolysis-inhibiting agents such as hydrogen ions,(167,175) but it more likely reflects the fact that the perfusate is in a closed system. Thus, changes in lactate and glucose levels are simply distributed throughout the perfusate without replenishment or release.

5.3.2. External Triggering of Image Acquisition

In order to minimize motion artifacts in images of the beating heart, image acquisition was triggered by the QRS peak of the ECG, as described above. Since external triggering of image acquisition was unsuccessful in the first trial of the present study (Nov. 9), slices of each spectroscopic image represented different points in the cardiac cycle. The effect of triggering can be observed then by comparison of successive images acquired in this trial with those in a later trial where triggering was successful (Figure 5.3). Three successive images from the first trial are displayed in the top row; three successive images taken from a successful trial are displayed in the bottom row.

Inspection of the images in the first row reveals several obvious differences that suggest that acquisition of the first image took place during diastole (when the heart muscle is relaxed and largest), the second image during systole (when it is maximally contracted), and the third image at some intermediate point. The images along the second row are much more similar, reflecting the fact that they were consistently acquired at the same point in the cardiac cycle.

Acquisition of images at different points in the cardiac cycle adds two types of noise to the spectroscopic images: spatial noise, noticeable as blurring of cardiac features,

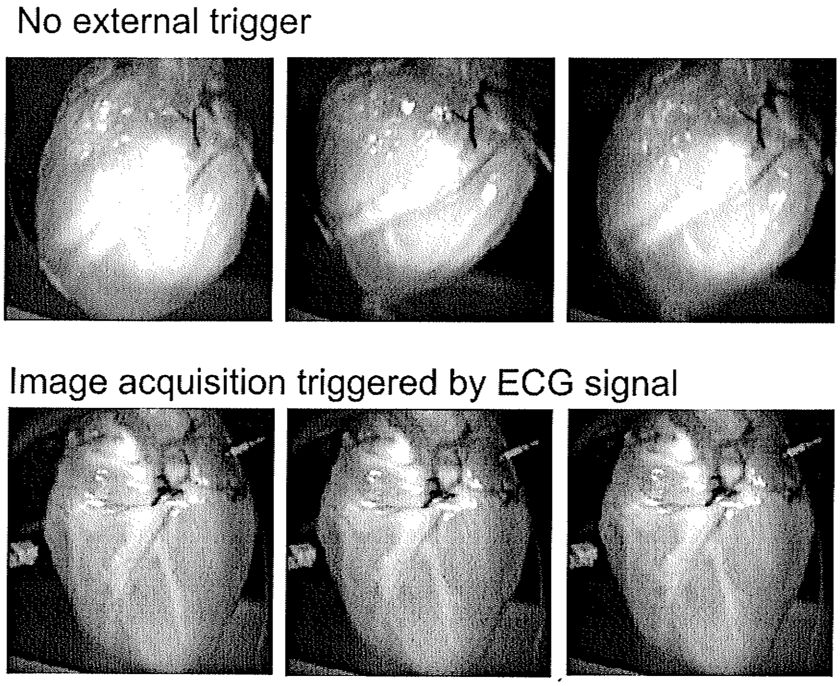

No external trigger

Image acquisition triggered by ECG signal

Figure 5.3. Effect of external triggering of image acquisition on reproducibility of cardiac images. All images were acquired at 650 nm and are displayed with the same illumination scale

and spectral noise. The spatial noise arises from the fact that the three images acquired at each wavelength are averaged (ostensibly to increase the signal-to-noise ratio). The resulting blurring is most apparent at the periphery of the heart in the mean images (Figure 5.4). The mean of the non-triggered images is more blurred along the edges in comparison with the mean of the triggered images. Use of a Sobel edge-detection filter highlights this effect further (second column of Figure 5.4).

The influence of unsuccessful triggering (or no triggering) also adds noise to the spectra extracted from the spectroscopic images, reflecting the fact that a particular camera pixel samples different regions of the heart in successive images; the absorbance value recorded at that pixel will therefore also be different for the different images. As a result, spectra from the non-triggered image set (Figure 5.4, right hand side) are much noisier than those from the triggered image set.

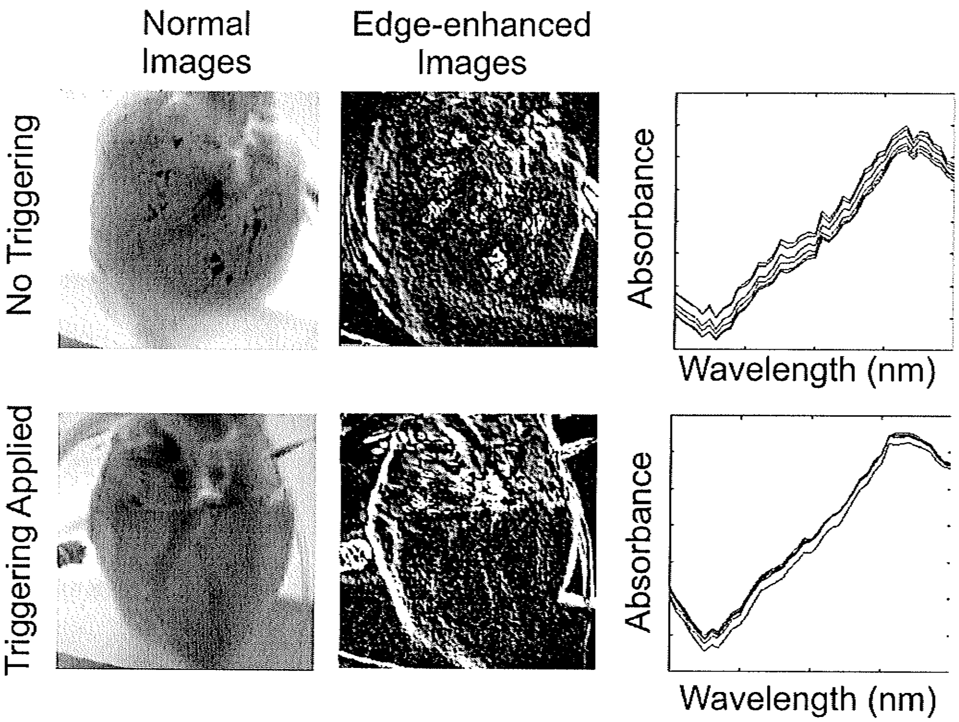

Figure 5.4. Effect of external triggering on reproducibility of averaged images and noise in extracted spectra. The images on the far left are mean absorbance images (at 650 nm) for the two sets of images displayed in Figure 5.3.

5.3.3. Spectroscopic Imaging Data

5.3.3.1. <u>Spectral Resolution</u>

Spectroscopic images were created as described in Section 4.2.2.2. The extracted spectra were extremely smooth and free of noise, as compared to those of the previous study (Figure 5.5, compare with Figure 4.5). One spectrum is visibly noisier than the others, especially in the plot of ischemic spectra; this spectrum was from the first trial (Nov. 9), where image triggering did not work.

5.3.3.2. <u>Spectral Fitting</u>

In the previous study, the high degree of noise hindered comparison of the spectral fits using raw absorptivity spectra with those using component spectra scaled by

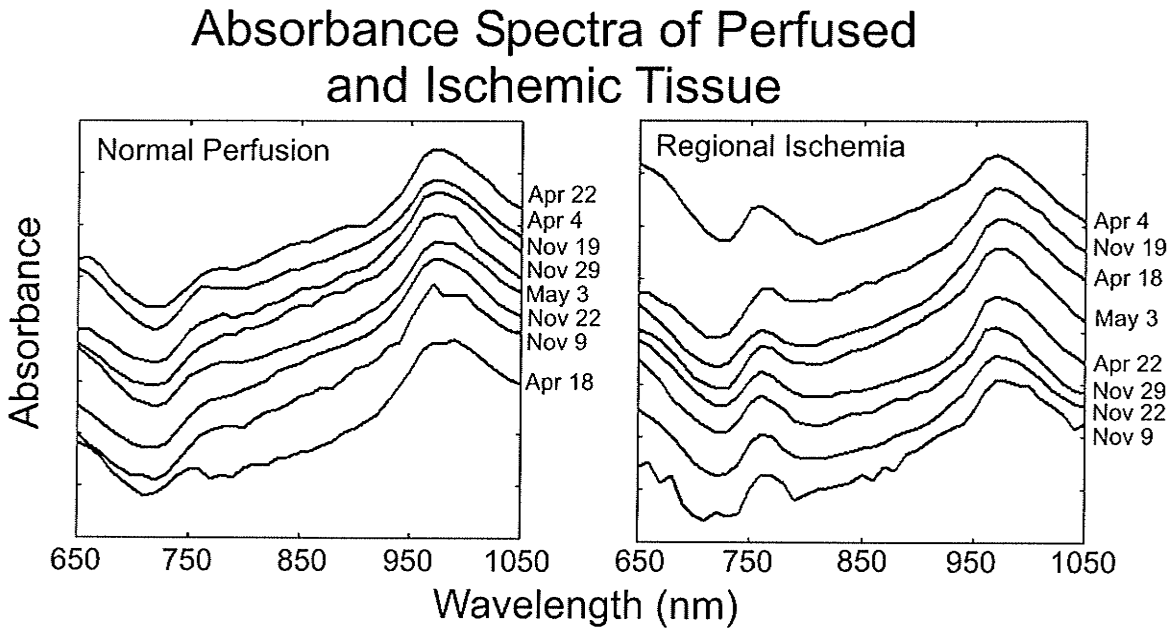

Figure 5.5. Representative tissue spectra acquired during normal perfusion and ischemia.

the optical pathlength function presented in Chapter 3. The relative smoothness of the present spectra allows for such a comparison here. Four sets of oxy-(Hb+Mb) and deoxy-(Hb+Mb) coefficient values (i.e. relative concentrations) were calculated as described in Section 4.2.4, varying: i) the wavelength range over which the spectra were fit (A,C: 700-1000 nm vs. B,D: 650-890 nm); and ii) the absorptivity spectra used in the fit (A,B: spectra scaled by the optical pathlength vs. C,D: pure, unscaled spectra) (Figure 5.6). Reconstructed spectra were then compared with the measured spectra, including spectra of both well-oxygenated and poorly oxygenated tissue.

Comparison of the reconstructed spectra with the original spectra provides a visual gauge of the error in the coefficient values and/or the assumptions underlying this fitting procedure. For instance, use of the pathlength-adjusted spectra results in an overestimation in deoxy-(Hb+Mb) content during normal perfusion, as indicated by the stronger intensity of the 760 nm absorption band (Figure 5.6A). Moreover, these

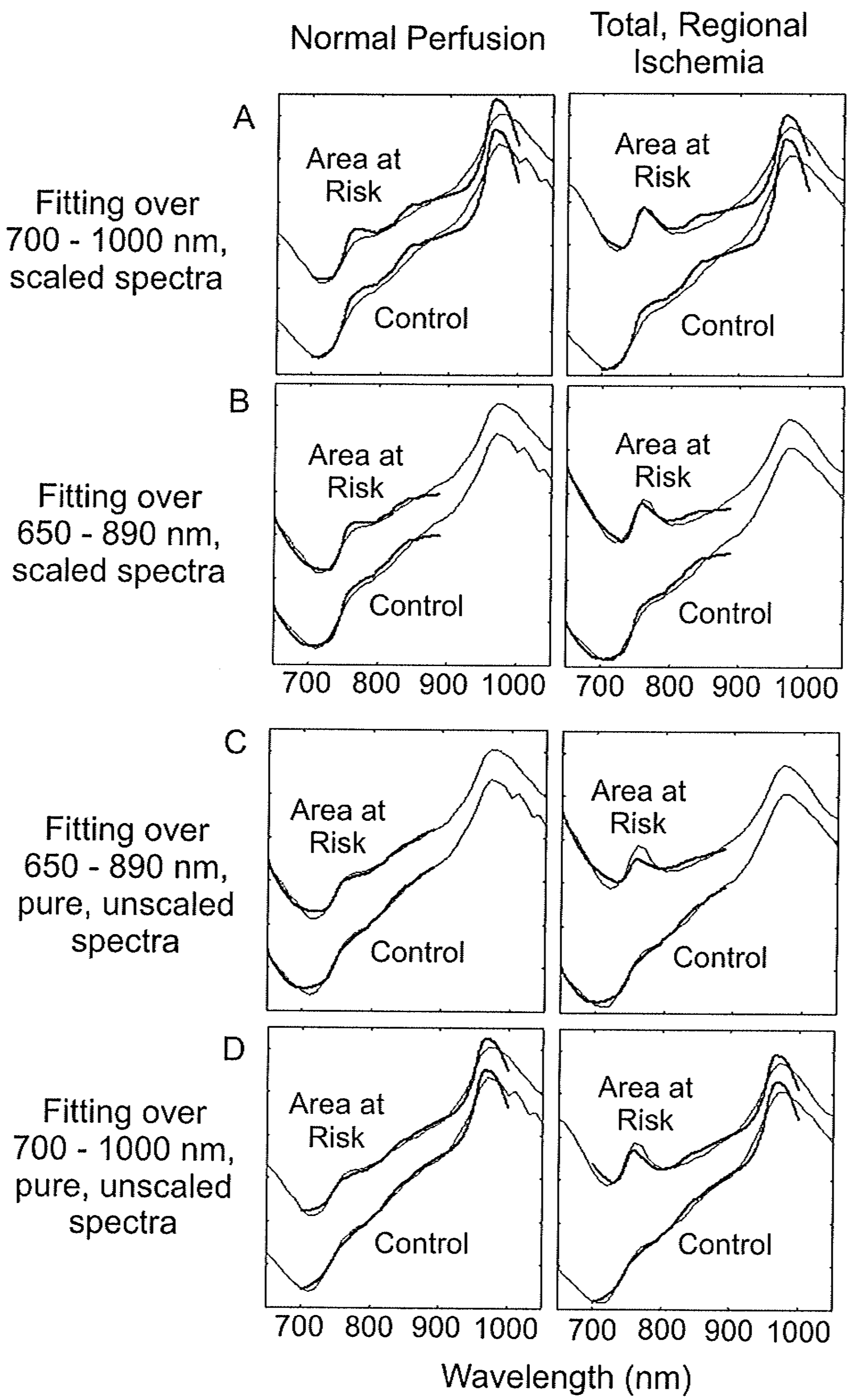

Figure 5.6. Effect of choice of fitting parameters on closeness of fits in representative spectra. Light lines are measured spectra, dark lines are spectral reconstructions.

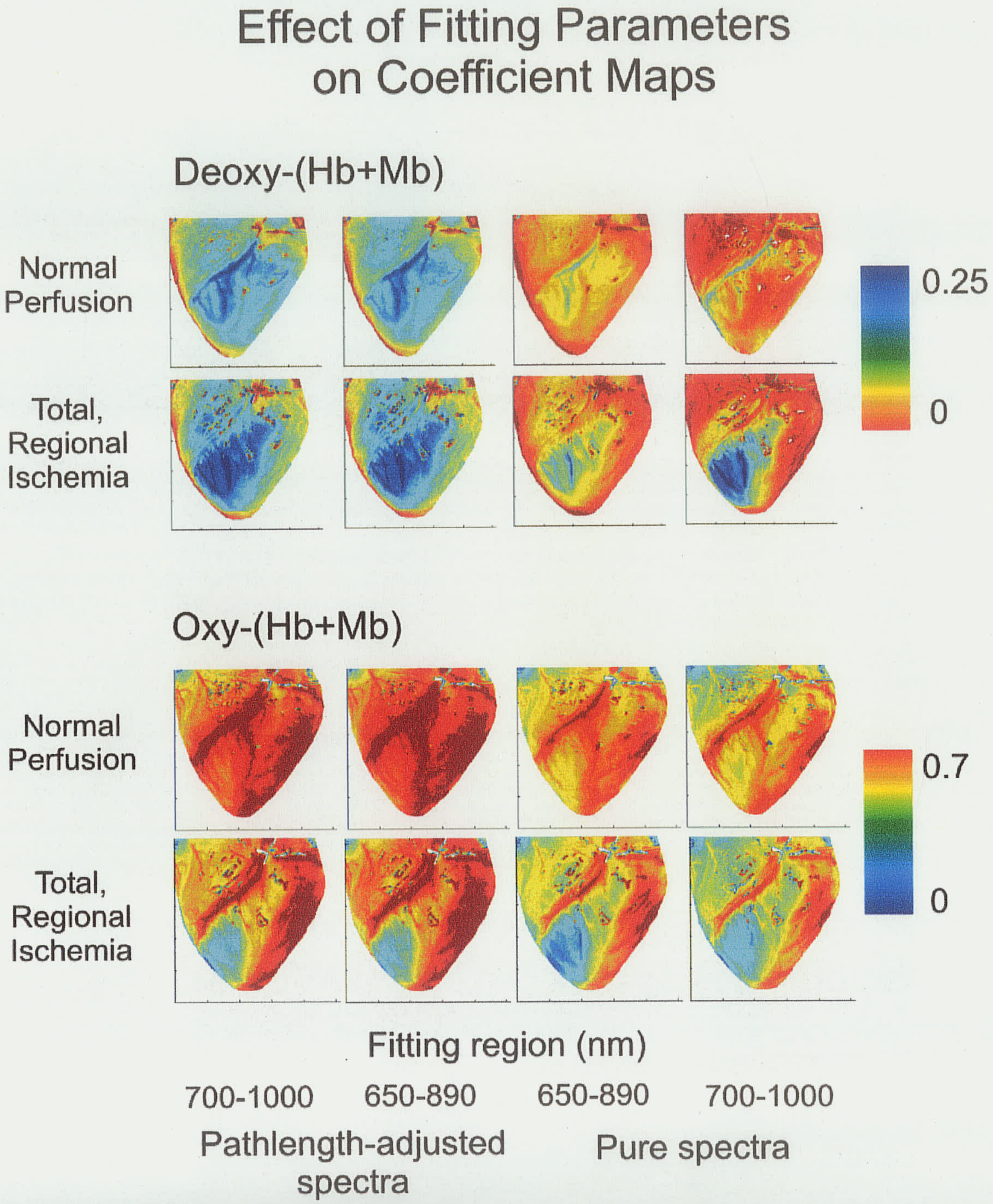

Figure 5.7. Effect of fitting parameters on coefficient maps for a representative trial.

reconstructed spectra fail to model the slope of the experimental spectra between 800 and 950 nm. Use of the unscaled absorptivity spectra actually results in more accurate modelling of the original spectra acquired during normal perfusion, although fitting between 650 and 890 nm results in an underestimation of the deoxy-(Hb+Mb) content in ischemic tissue. Nevertheless, fitting with pure spectra over 700-1000 nm results in good estimation of the deoxy-(Hb+Mb) content and models the slope of the spectra between 800 and 950 nm more accurately than fitting with pathlength-adjusted spectra.

In all cases, the 970 nm absorption band (due to water) is broader in the experimental spectra than in pure and pathlength-adjusted absorptivity spectra (and hence wider than in the reconstructed spectra). This band broadening may be due either to chemical interaction of water with the chemical environment or elements of the wavelength-dependence of pathlength that were not accounted for in the study discussed in Chapter 3, or both. The choice of component absorptivity spectra (scaled vs. unscaled) influences the appearance of maps of relative concentration values (Figure 5.7). Under conditions of normal perfusion, use of the pathlength-adjusted absorptivity spectra yielded substantially higher deoxy-(Hb+Mb) concentrations and slightly higher oxy-(Hb+Mb) concentrations than use of the pure absorptivity spectra. Since the fit over 700-1000 nm with the pure absorptivity spectra most closely approximated the measured spectra, all extracted spectra were subsequently fit using this wavelength range and choice of component spectra.

5.3.3.3. Imaging Data

Oxygenation maps derived from the relative oxy- and deoxy-(Hb+Mb) concentrations are presented in Figures 5.8 and 5.9. These maps yield the following observations:

- Different grades of ischemia yielded visibly distinct maps (albeit marginally in some cases) and these distinctions exist regardless of whether the heart was reperfused between periods of regional ischemia. This result responds to one of the objectives of this study, namely that NIRS imaging can distinguish between different degrees of partial ischemia. Upon reperfusion, the oxygenation returned to or exceeded normal perfusion values.
- During global ischemia, areas of cardiac tissue on the far left and far right of the field of view (perfused by the right coronary and left circumflex arteries, respectively) also became deoxygenated.
- Most images acquired during normal perfusion exhibit signs of partial ischemia in the area at risk that was subsequently rendered ischemic by LAD occlusion. This is likely due to the partial restriction of LAD flow that inevitably resulted from placement of the cannula in the LAD.
- The Apr. 18 trial showed anomalously low oxygenation in the LAD perfusion bed throughout the protocol. This may be due to some pre-existing heart damage or poor placement of the cannula and flow probe, resulting in more restricted LAD flow than usual from the outset.

5.4. Discussion

This study demonstrates that near-IR spectroscopic imaging can detect reductions in blood and tissue oxygenation resulting from reductions in coronary flow by as little as 50%. In fact, NIRSI was able to detect oxygenation changes resulting from relatively mild reductions in LAD flow induced by insertion of the cannula. The fact that oxygenation maps for 50% LAD flow, 20% LAD flow, and no LAD flow showed substantial differences lends credence to the idea that NIRSI can, in principle, determine not only the extent of the ischemic region but also the severity of the ischemia.

5.4.1. Sources of Error

Despite the closeness with which the reconstructed spectra matched the acquired spectra, subtle differences were still evident (especially in ischemic spectra), which translate to uncertainties in the derived concentrations. Uncertainty of the wavelength-dependence of the effective optical pathlength in tissue remains one of the most significant factors limiting the reliability of the derived oxygenation values. While adjustment of the absorptivity spectra according to the pathlength relationship derived in Chapter 3 did not improve the fit, this may simply reflect the inapplicability of that pathlength function to the present experimental design. Derivation of a pathlength relationship for the same experimental geometry may result in closer fits. Artifacts due to specular reflection may also contribute to uncertainties in the concentrations. Blurring due to heart motion within the 80 ms exposure time and motion artifacts that remain even with triggering are minor factors and can likely be neglected.

5.4.2. Quantitative Analysis

The oxygenation maps in Figures 5.8 and 5.9 illustrate that deoxygenation in the area at risk during total, regional ischemia and during global ischemia is much more severe than that observed during partial, regional ischemia. This difference may be related to the relative spectroscopic contributions of myoglobin and hemoglobin. During partial ischemia, although a greater proportion of Hb-bound oxygen is consumed, tissue oxygen concentrations may remain high enough that myoglobin is not significantly deoxygenated. During complete ischemia, however, tissue may consume more oxygen from the myoglobin reserves.

5.4.2.1. <u>Mean Oxygenation within Area at Risk</u>

To distinguish quantitatively between different degrees of ischemia, mean oxygenation values were calculated for two regions of interest (ROIs) – one well within the area at risk and one well inside a continuously perfused region (control). The oxygenation values are plotted in Figure 5.10 for each time point and each group. These plots demonstrate increasingly severe deoxygenation in the area at risk with increasingly severe regional ischemia, whether the heart is reperfused between ischemic episodes or not. Oxygenation within the control region remained constant throughout regional ischemia and reperfusion. During global ischemia, oxygenation throughout the heart fell to levels experienced by the area at risk during total, regional ischemia. Reperfusion consistently restored oxygenation to levels observed during normal perfusion.

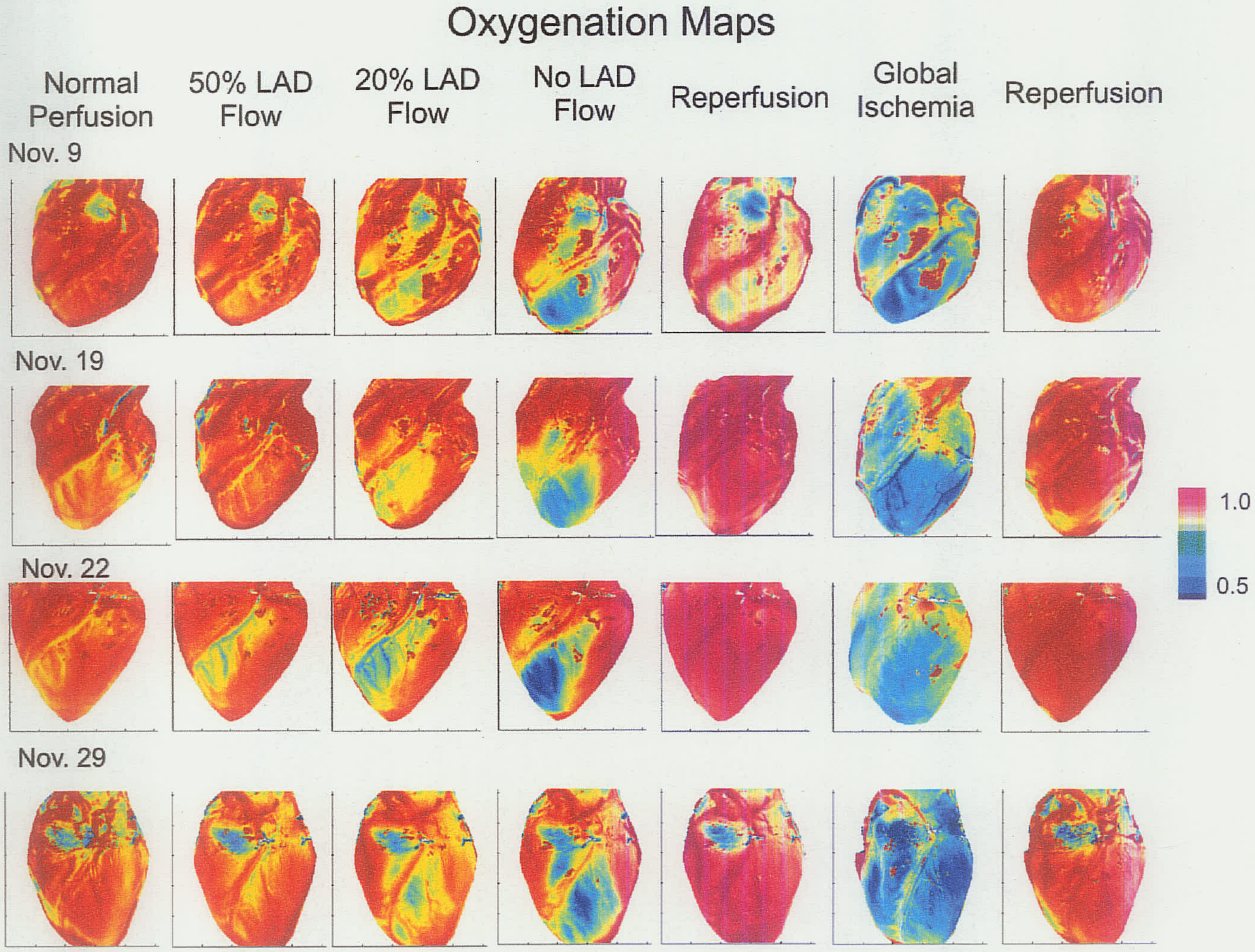

Figure 5.8. Oxygenation maps for each Group I trial. High oxygenation is shown in red and low oxygenation is shown in blue.

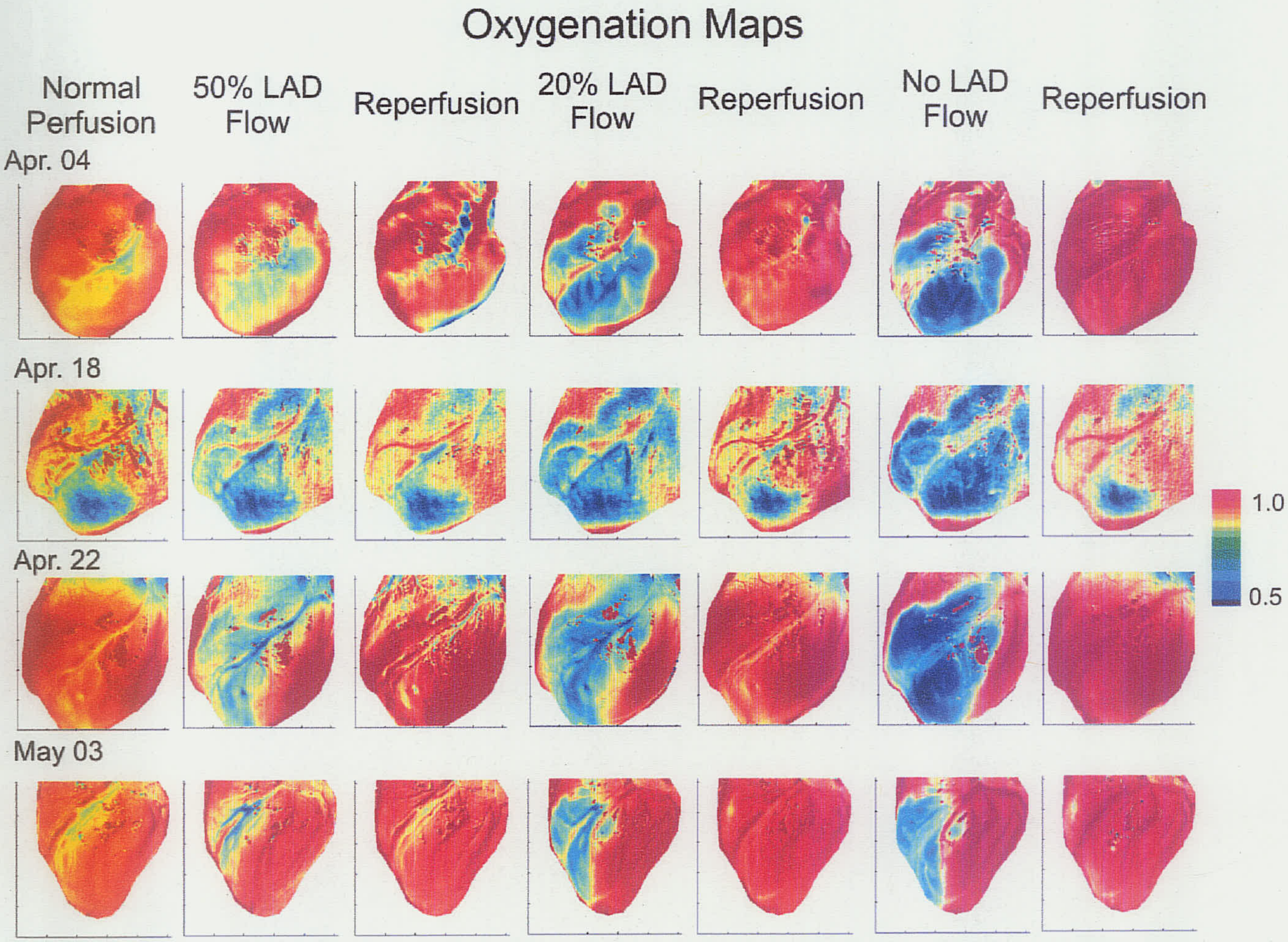

Figure 5.9. Oxygenation maps for each Group II trial. High oxygenation is shown in red and low oxygenation is shown in blue.

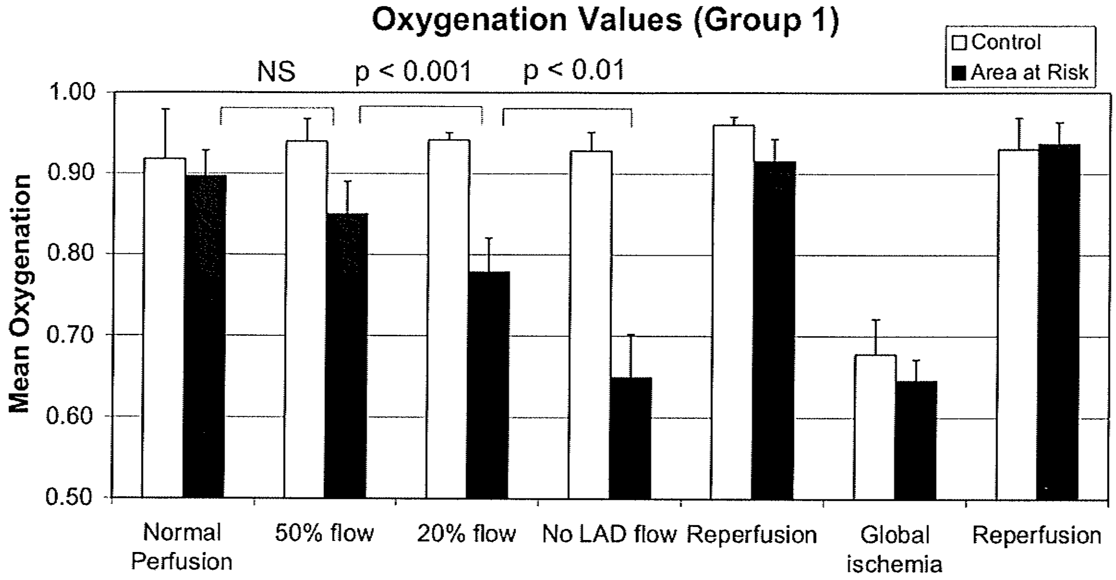

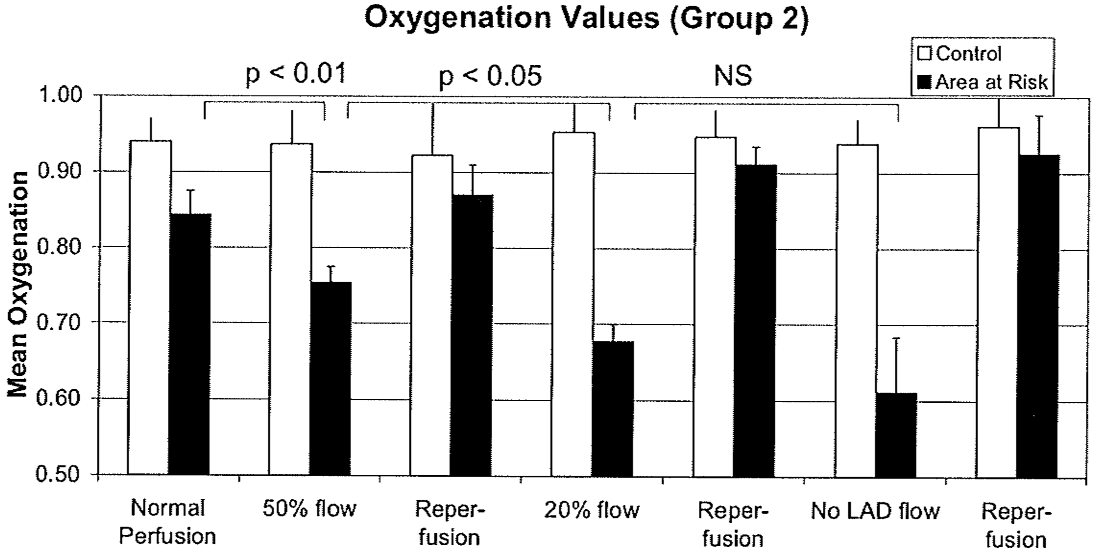

Figure 5.10. Oxygenation within and outside the area at risk (black and white, respectively) at each time point. Error bars represent the standard deviations among the four hearts of each group

5.4.2.2. Spatial Extent of Ischemia

Another way to gauge the severity of deoxygenation at each stage in the protocol is to monitor the size of the ischemic region throughout the protocol. To that end, a region of interest (ROI) encompassing the entire heart was defined for each trial. For each spectroscopic image acquired after normal perfusion, the fractional area within that ROI for which oxygenation was lower than that observed during normal perfusion was determined for each time point (Figure 5.11).

As these plots illustrate, increasing the severity of ischemia seems to have little effect on the size of the ischemic area (represented by the total height of all bars). Put another way, the LAD perfusion bed is rather evenly affected by even mild, partial ischemia. While LAD flow reduction from 50% to 20% of normal increased the affected area from 54% to 66% in Group I, this increase is not substantial. Moreover, the total area affected in Group II trials remained constant at 70% for 50% and 20% flow. In contrast, the severity of ischemia was significantly affected. The proportion of tissue exhibiting moderate deoxygenation rose from 7% (at 50% flow) to 17% (at 20% flow) in Group I trials ($p<0.05$) and from 15% to 28% in the corresponding Group II trials. While only 2% of tissue experienced severe deoxygenation in Group I trials (during both 50% and 20% LAD flow), the fraction of severely deoxygenated tissue increased from 3% (50% flow) to 11% (20% flow) in Group II trials ($p<0.05$).

Complete LAD occlusion also produced no significant change in the size of the ischemic area in either group. However, the proportion of tissue in Group I trials showing moderate deoxygenation increased again from 17% (at 20% flow) to 23% and the area

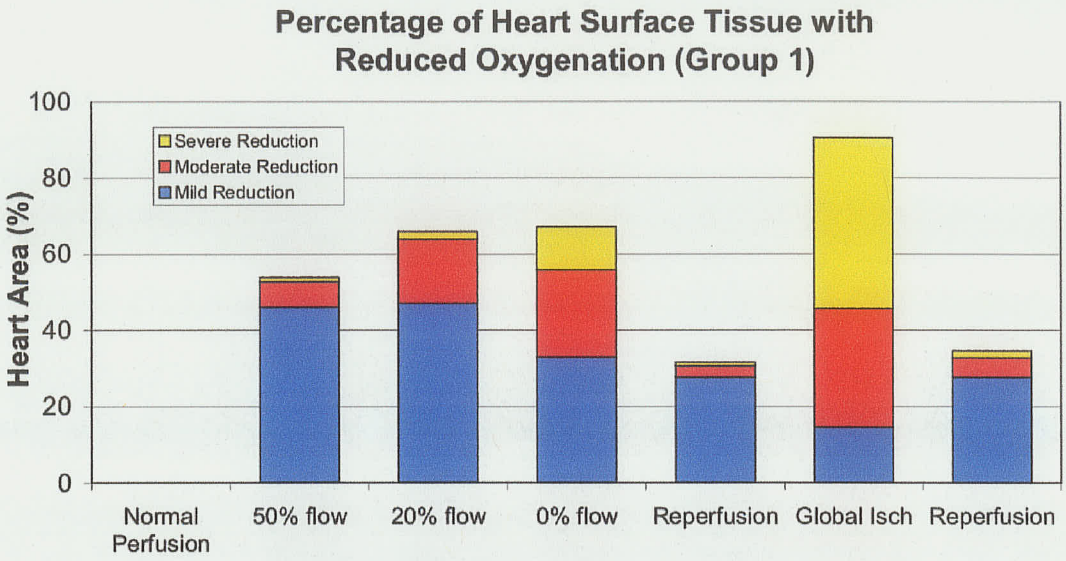
Percentage of Heart Surface Tissue with Reduced Oxygenation (Group 1)

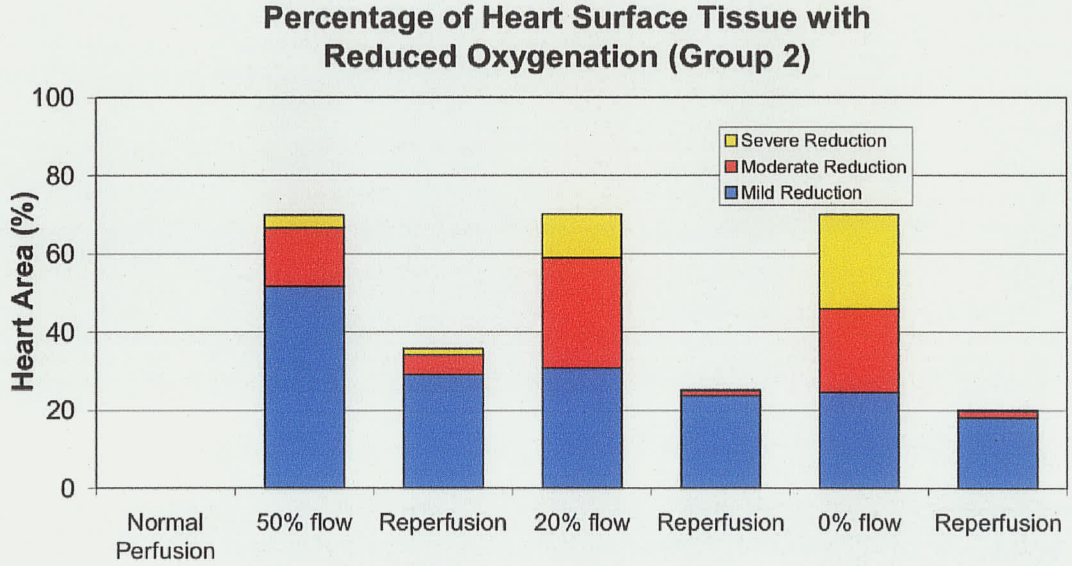
Percentage of Heart Surface Tissue with Reduced Oxygenation (Group 2)

Figure 5.11. Percentage of heart tissue within the field of view exhibiting oxygenation mildly, moderately, or severely reduced from normal levels. The blue bars depict the proportion of tissue exhibiting mildly reduced oxygenation. The proportion whose oxygenation is below normal perfusion by at least 10% but less than 20% (moderate reduction) is shown by the orange bars. The proportion of tissue exhibiting severely reduced oxygenation (more than 20% difference) is shown by the yellow bars.

showing severe deoxygenation rose from 2% to 11% (p<0.01). In Group II trials, the proportions of tissue showing moderate deoxygenation actually decreased slightly from 28% to 21%, but this was more than compensated for by a sharp increase in the proportion of severely deoxygenated tissue, from 11% (20% flow) to 24% (p<0.05). These results indicate that the main feature distinguishing partial from complete regional ischemia is not the regional extent of tissue affected, but rather the extent to which that area becomes deoxygenated.

Upon reperfusion (following complete ischemia), the proportions of tissue experiencing moderate or severe deoxygenation dropped to near-zero levels in both groups (4% and 1% in Group I, respectively; 1% and 0% in Group II). However, mild ischemia persisted in 32% and 25% of the ROI for Group I and Group II, respectively

Not surprisingly, a much greater fraction of tissue exhibited deoxygenation during global ischemia than was observed during regional ischemia; the size of the ischemic region increased from 67% to 91% (p<0.01). The 9% of the ROI that did not exhibit reduced oxygenation included areas corresponding to detector saturation, cannulas, and some tissue along the edge of the heart. The ischemic tissue also became more severely deoxygenated than was the case for total, regional ischemia. The proportion of tissue exhibiting moderate deoxygenation increased from 23% to 31%, and the size of the severely deoxygenated region increased from 11% to 45% (p<0.01). The oxygenation map during reperfusion after global ischemia was virtually identical to that acquired during the previous reperfusion period.

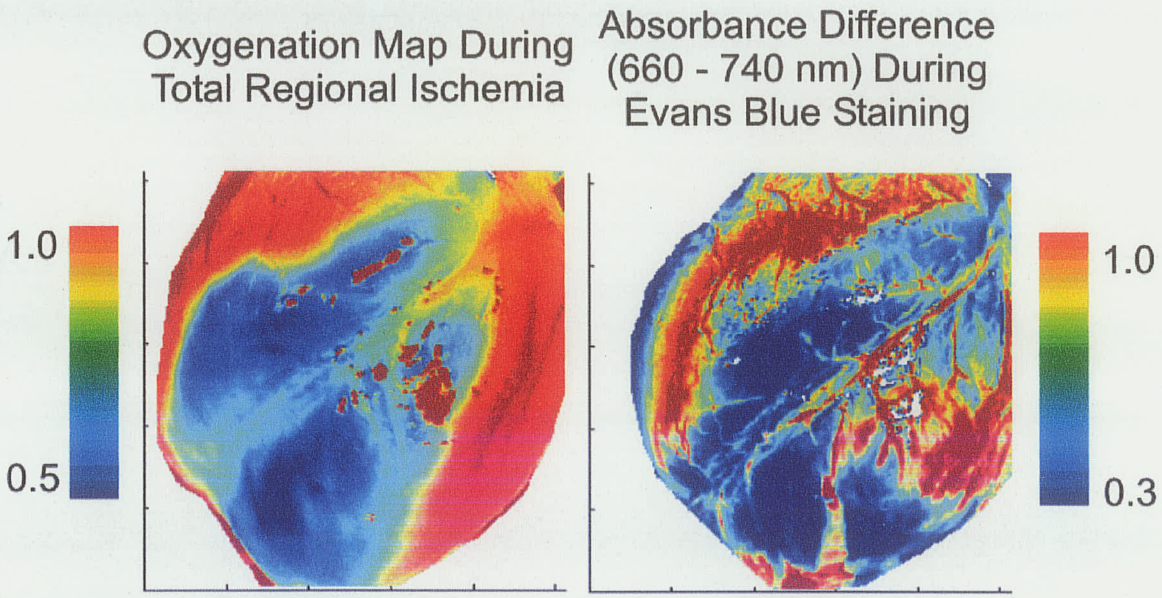

Figure 5.12. Comparison of the tissue area exhibiting reduced oxygenation (left) with that experiencing no flow (right), as determined by Evans Blue staining (for the Apr. 22 trial). The blue regions which demarcate the area at risk as determined from *in situ* oxygenation and post-protocol staining are nearly identical.

5.4.2.3. Evans Blue Staining

The size of the ischemic region as determined by spectroscopic imaging was compared to the size determined by Evans Blue staining at the end of each trial. Since Evans Blue has a strong absorption band near 650 nm, the difference between absorbance images at 660 nm and 740 nm provides a picture of the Evans Blue distribution (and hence an image of the area at risk). The oxygenation map for complete, regional ischemia is nearly identical to the absorbance difference map (Figure 5.12)

To quantify the above comparison, the proportion of Evans Blue-stained tissue with an absorbance difference of more than 0.8 units was adopted as a gauge of the area at risk. Adopting this definition, Evans Blue staining revealed that the area at risk during LAD occlusion constituted 63 ± 18% of the tissue within the field of view. This result corresponds well to the oxygenation results, in which 65 to 70% of the tissue within the field of view was included in the area at risk. This correlation validates our conclusion that all areas affected by a reduction in flow, even by only 50%, exhibit a reduction in blood/tissue oxygenation observable with spectroscopic imaging.

5.4.3. Fast Spectroscopic Imaging

5.4.3.1. Wavelength Selection

Fast spectroscopic images comprising fewer wavelengths (9 vs 41 wavelengths) and with less signal averaging (1 vs. 3 acquisitions at each wavelength) provided spectra with resolution and signal-to-noise sufficient to monitor changes in blood/tissue oxygenation in response to changes in flow. Figure 5.13 compares spectra (for the same pixel) extracted from 5-min (thick) and 1-min (thin) spectroscopic images acquired sequentially for the same ischemic region of tissue. The absorbance values for the 1-min spectrum are nearly identical to those of the 5-min spectrum at virtually every common wavelength.

The selected wavelengths were chosen because the software required the wavelength spacing to be fixed (e.g. 30 nm). With a 30 nm spacing, it is impossible to capture fully the absorbance minima at 720 and 810 nm and the maximum at 760 nm. However, acquisition of images between 670 and 910 nm (30 nm spacing) would perhaps have better captured the variation in key absorption band intensities without increasing the acquisition time.

Despite the perceived compromises, calculated oxy and deoxy concentrations for the 1-min spectroscopic images very closely matched those for the 5-min images. For the sample spectrum depicted in Figure 5.13, the oxy and deoxy concentrations derived for

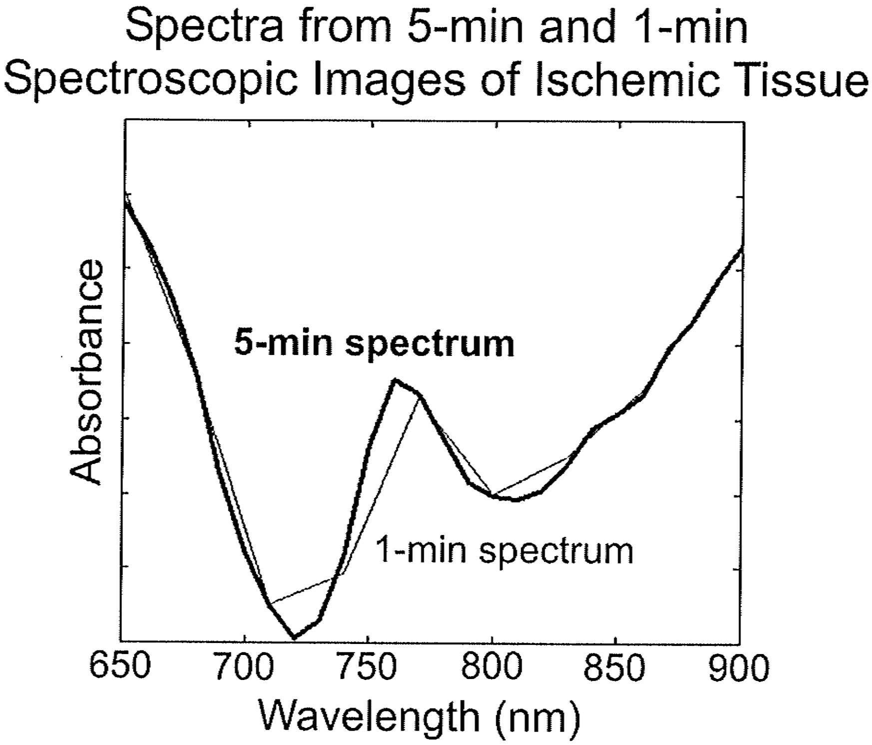

Figure 5.13. Absorbance spectra extracted from 1-min (thin line) and 5-min (thick line) spectroscopic images of ischemic tissue.

the 1-min image set deviated from corresponding values for the 5-min image set by only 0.04% and 4.8%, respectively. The median deviations were only 1.8% and 5.7% for the entire heart during complete, regional ischemia. During normal perfusion, median deviations were 3.1% and 7.8%, respectively. Oxy and deoxy coefficients were both generally underestimated in the 1-min image sets, yielding oxygenation values that did not deviate from those of the 5-min image sets as substantially. Median deviations in oxygenation over the entire heart were 0.9% during regional ischemia and 1.3% during normal perfusion. Thus, the loss in accuracy of oxygenation information with fast imaging is negligible.

5.4.3.2. Oxygenation Kinetics

We now exploit the 1-min image sets to follow the kinetics of deoxygenation and reoxygenation upon LAD flow reduction and reperfusion. Figures 5.14(a,b) track changes in oxygenation throughout the protocol. For the Apr. 04 trial, images were acquired every 20 nm between 660 and 1000 nm, for a total acquisition time of about 2 min for each image set. For the three subsequent trials, images were acquired at 30 nm intervals between 650 and 890 nm for a 1 min acquisition time.

As expected, these figures reveal stable oxygenation during the course of normal perfusion. Upon 50% flow reduction, oxygenation values dropped immediately and remained at the new value for the duration of that period. Upon reperfusion, equilibrium was again reached in less than a minute in all but one of the trials (May 3). Upon reduction of flow to 20% of baseline, equilibrium was again reached very quickly, although a very gradual decrease in oxygenation over time was observed.

In contrast to reperfusion following 50% flow, equilibrium was not attained immediately upon reperfusion after the 20% flow period. This is most clearly evident for the Apr. 4 and May 3 trials; in the latter case, oxygenation at the 1 min time point was much lower than that at the 2 min time point, and oxygenation continued to recover gradually over the following minutes. In the Apr. 4 trial, the difference between the first two minutes is less dramatic, but there is a steady increase in oxygenation values during the reperfusion period (following 20% flow). Finally, the other two trials showed the sudden increase in oxygenation from the 1 min to 2 min time points but no further increase over time.

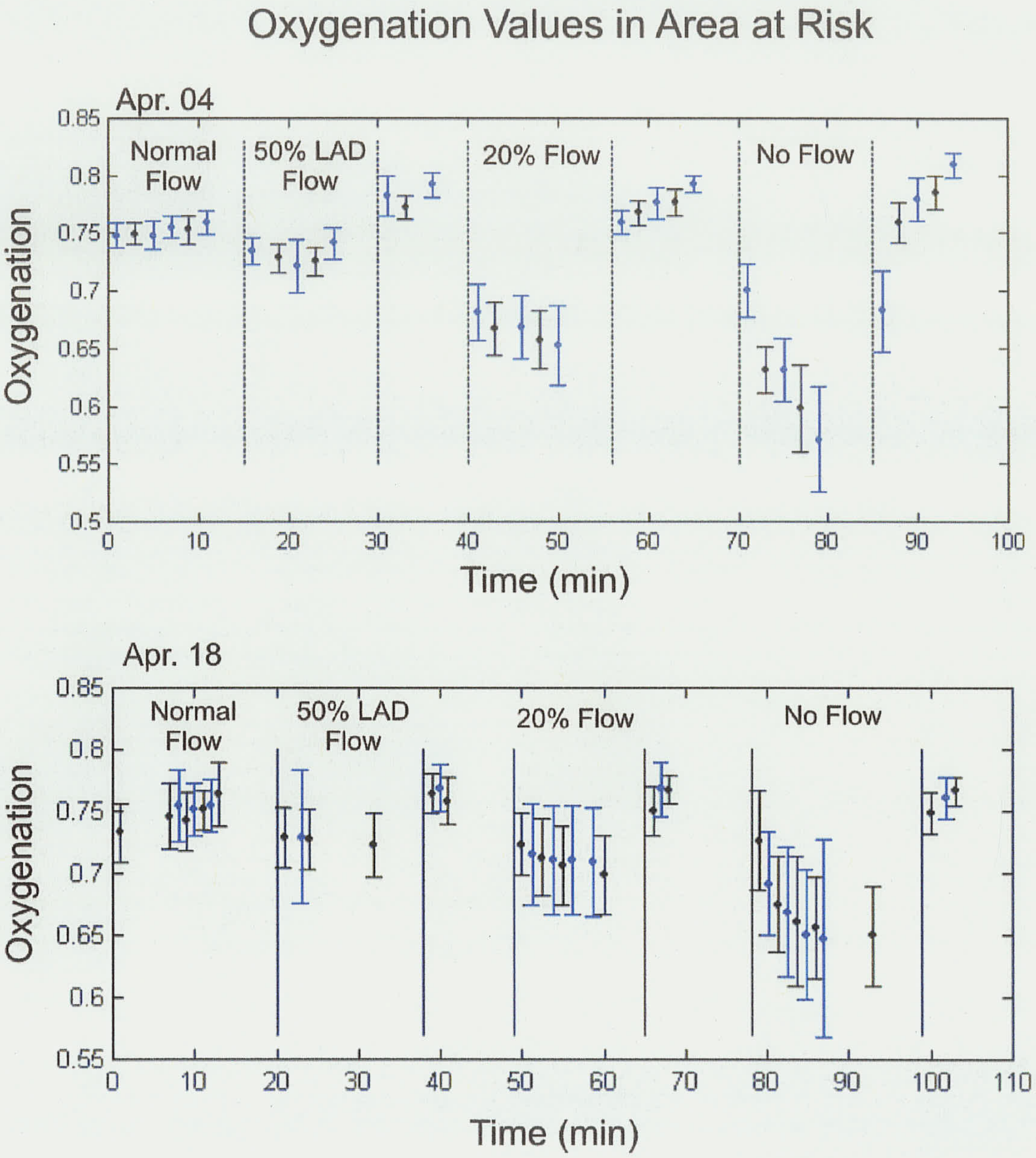

Figure 5.14a. Kinetics of deoxygenation and reoxygenation within areas at risk. The mean oxygenation over an ROI within the area at risk is shown (the error bars depict the standard deviations within the ROI). Oxygenation values for images acquired during systole are shown in blue, and those for images acquired during diastole are shown in black. The four plots in Figures 5.14a and b are plotted with different scales along the y axis.

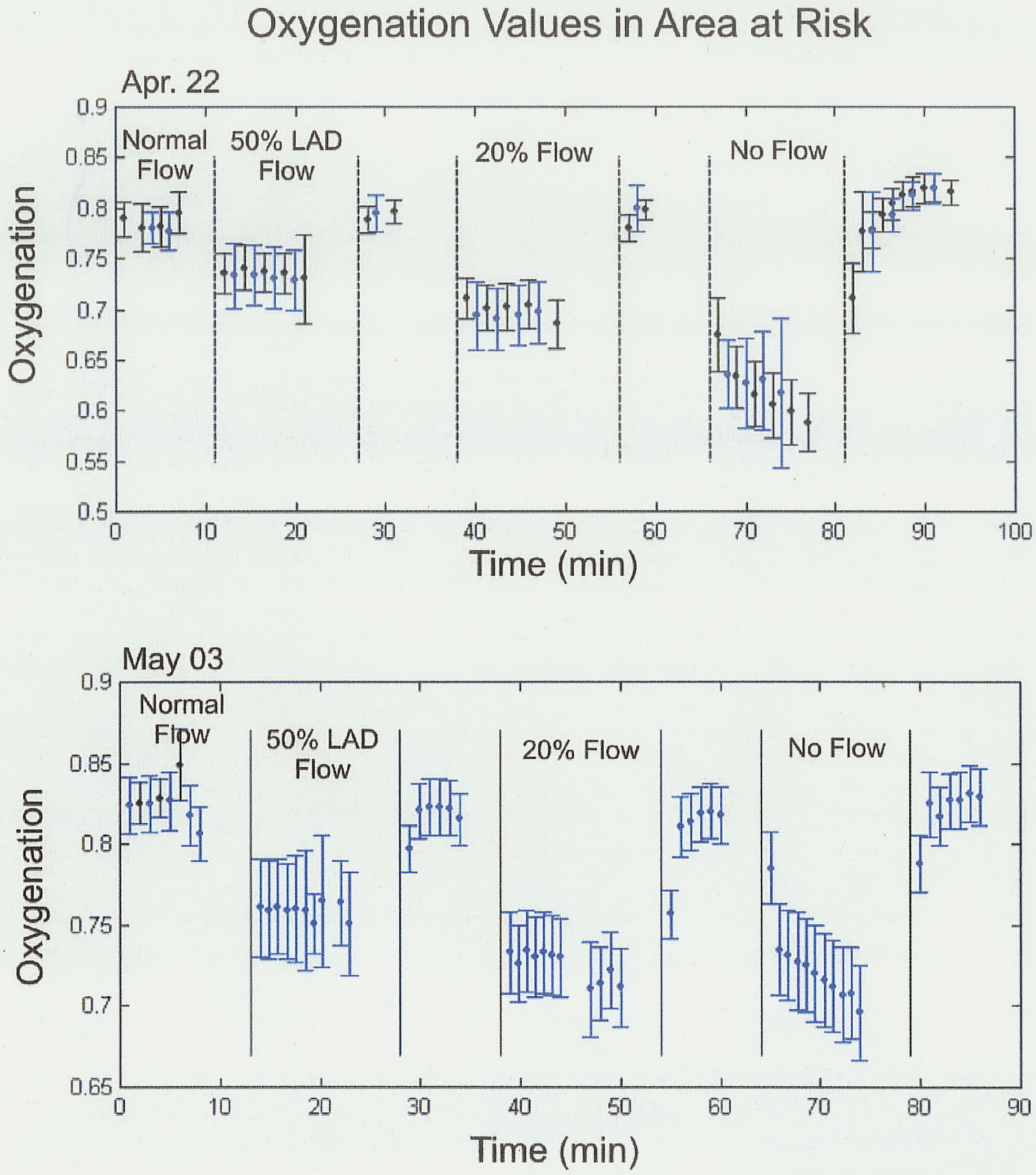

Figure 5.14b. Kinetics of deoxygenation and reoxygenation in areas at risk. For the May 3 trial, software difficulties prevented acquisition of images corresponding to diastole; all images in this trial were acquired during systole. The four plots in Figures 5.14a and b are plotted with different scales along the y axis.

Complete stoppage in LAD flow produced a unique set of time-series, reflecting increasingly severe deoxygenation during the entire 15 min-period of occlusion. This runs counter to previous studies that indicate complete deoxygenation of heme proteins within the first minute following severe ischemia.(187,223) Upon final reperfusion, more than 10 min was required for the oxygenation to reach equilibrium, as is most clearly evident in the Apr. 22 trial.

A secondary aim was to determine whether any difference in oxygenation kinetics could be observed at systole vs. diastole. Previous studies have suggested that while cardiac Mb oxygenation remains constant throughout the cardiac cycle,(156) blood Hb oxygenation varies periodically, reaching a maximum at end-diastole.(254,277) The plots of Figures 5.14 (a,b) appear inconclusive in supporting or refuting this claim. In some cases (e.g. Apr. 22, 20% flow), oxygenation values during systole are lower than those during diastole, but in other cases (e.g. Apr. 22, no flow) they are higher. For all comparisons, the error bars are large relative to the systole-diastole differences.

Finally, we examined changes in oxygenation that occur outside the area at risk during the above protocol; i.e. compensatory global changes in response to local ischemia. To that end, a region of interest was defined over a continuously perfused region, and the mean and standard deviation oxygenation values were calculated and plotted for each time point (Figure 5.15). In contrast to the area at risk, oxygenation values in this remote region actually increased with each successive decrease in LAD flow. This increase might be due to an increase in blood flow (through the normal area) resulting from diversion of flow from the area at risk.

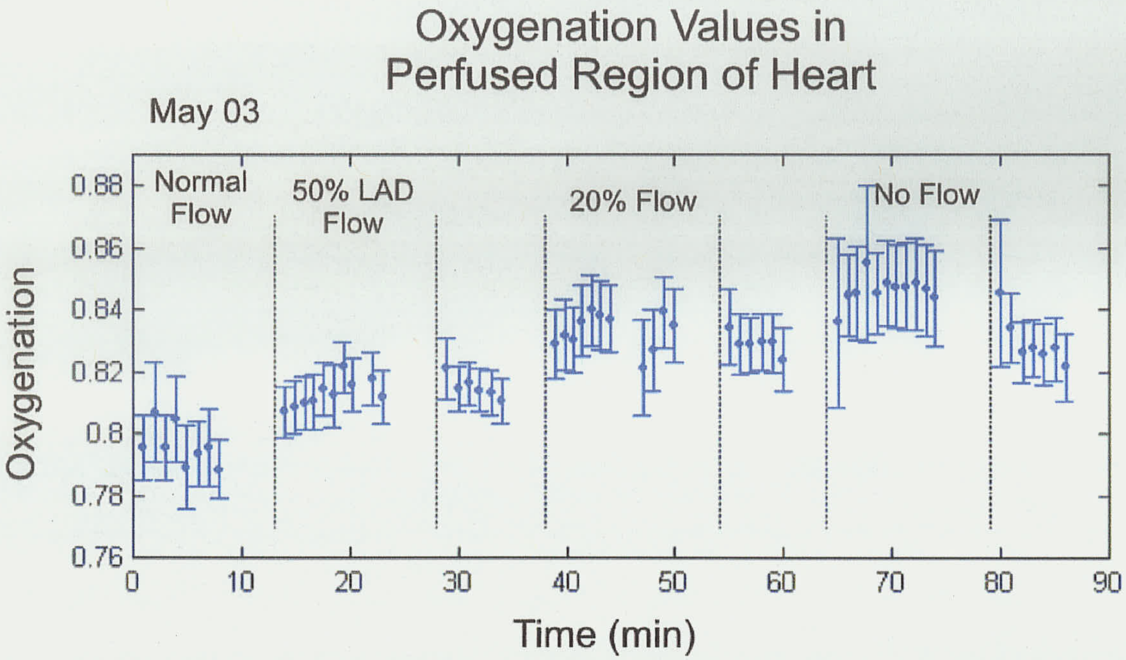

Figure 5.15. Kinetics of oxygenation changes within continuously perfused regions of tissue during the regional ischemia protocol (May 3 trial).

Changes in oxygenation within the perfused region occurred only gradually, increasing steadily for the first 5 min during each partial ischemia time period. Upon complete LAD occlusion, equilibrium was reached at the maximum observed oxygenation after 4 min. Upon reperfusion, oxygenation dropped steadily, and image acquisition was stopped before oxygenation values reached equilibrium.

5.4.4. Calibration of Spectrally-Derived Oxygenation

Following completion of the protocols described above, the heart was exposed to 15-min periods of increasingly severe global hypoxia, as described in Section 5.2.3, to provide the basis to relate spectrally-derived oxygenation to blood oxygen saturation values. During each period, 1-min spectroscopic images were acquired sequentially over the first 10 min, followed by acquisition of a single 5-min spectroscopic image (only the

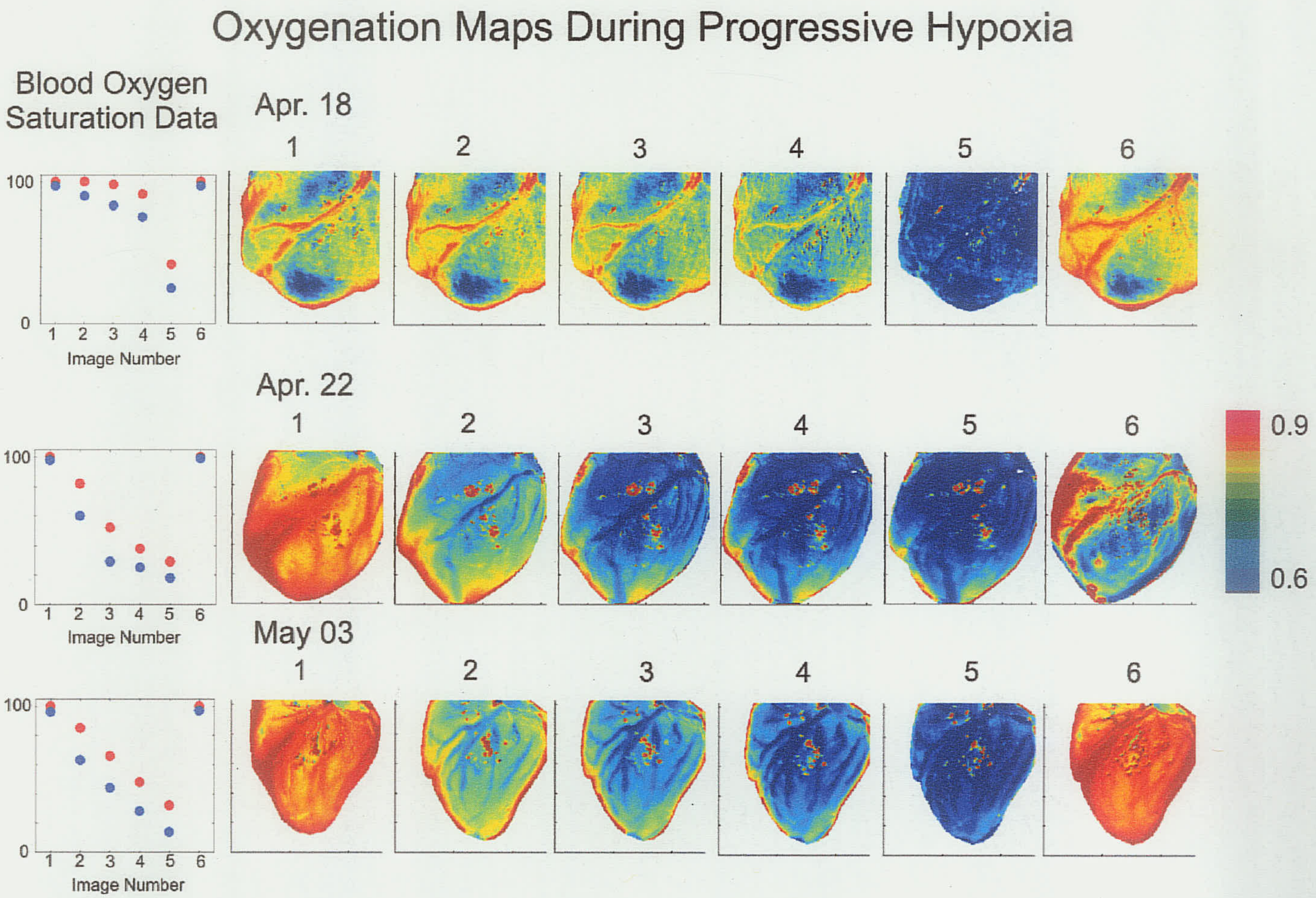

Figure 5.16. Cardiac oxygenation maps during periods of increasingly severe global hypoxia. On the far left are plots depicting arterial (red) and venous (blue) oxygen saturation values at each corresponding time point.

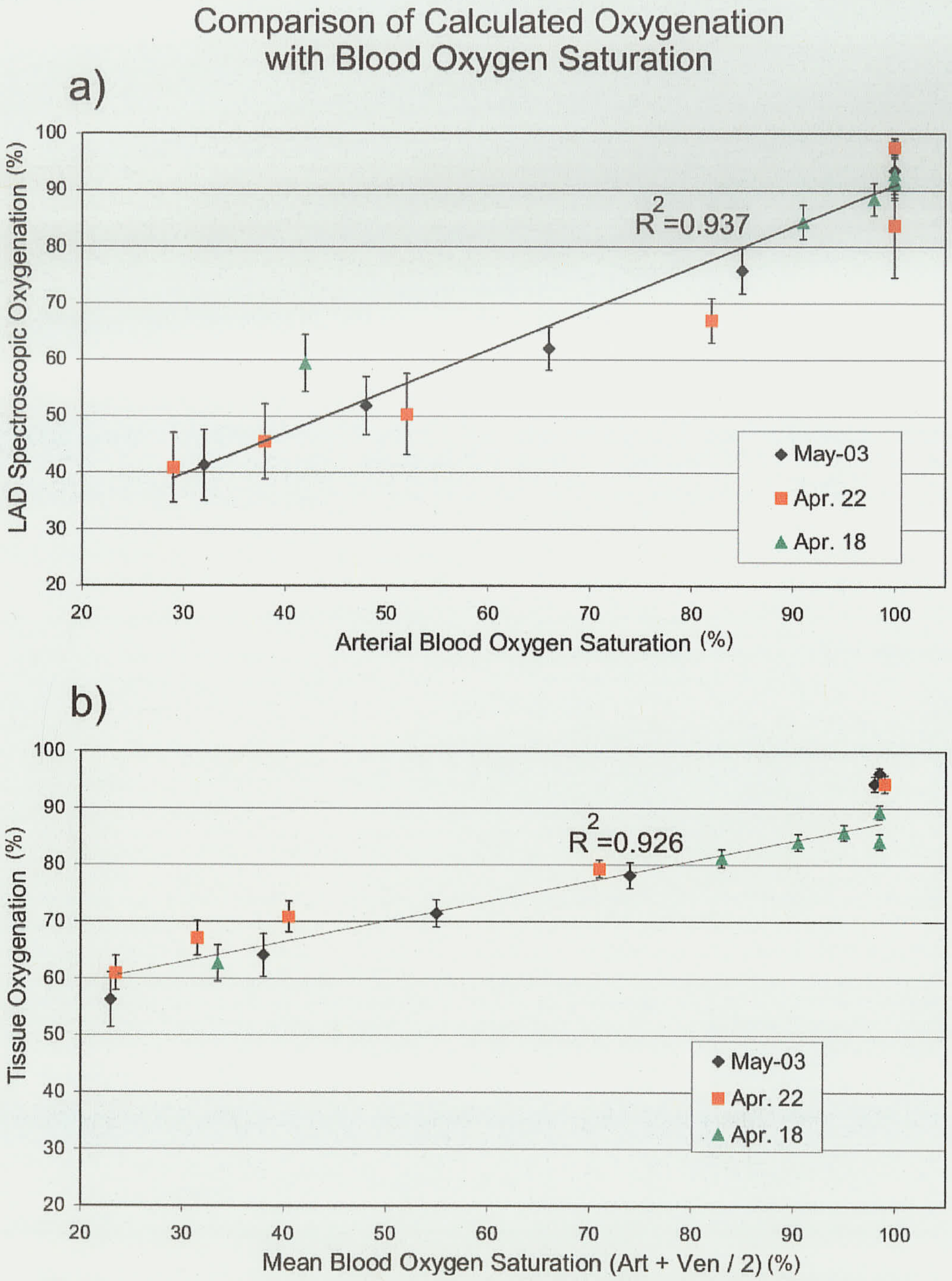

Figure 5.17. Comparison of spectrally-derived oxygenation (for the LAD artery and tissue distal to major arteries) with arterial and mean blood oxygen saturation values. An outlier was discarded in this analysis of the results.

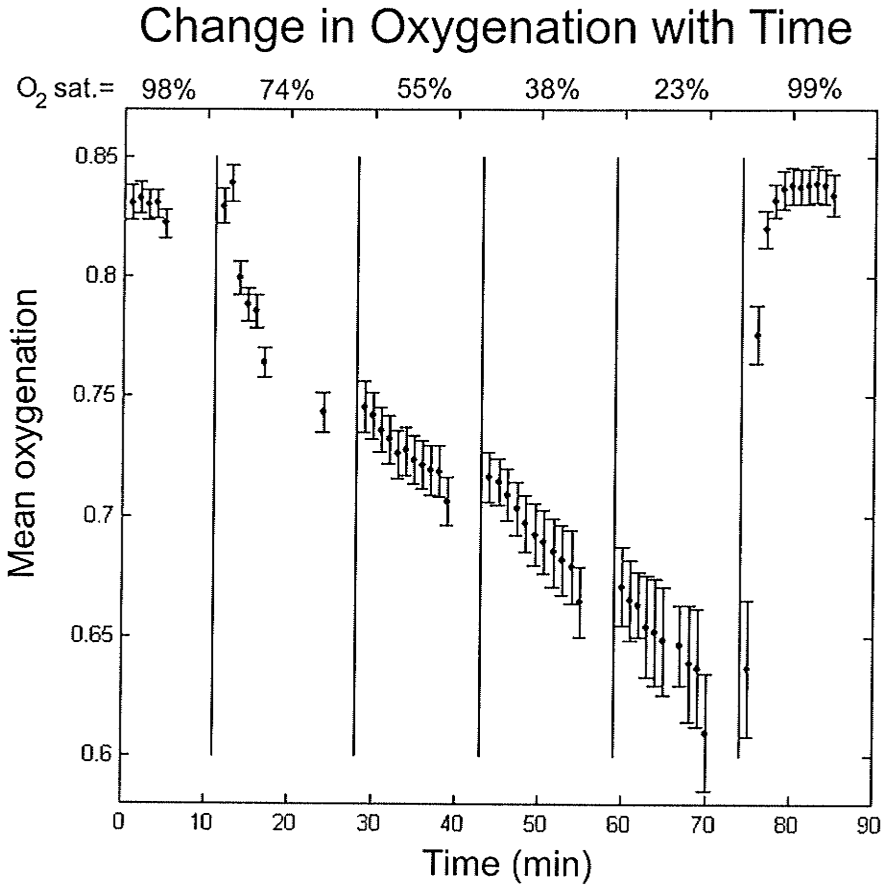

Figure 5.18. Kinetics of deoxygenation during successive, increasingly severe periods of global hypoxia (May 03 trial).

For comparison, the second analysis compared spectrally-derived oxygenation values for tissue regions remote from major arteries to mean (arterial and venous) blood oxygen saturation values. These data also exhibited an excellent linear trend (Figure 5.17b), although the slope deviated much more from unity[85]. The increased deviation in the slope likely originated in part from contributions of Mb. At each stage of partial hypoxia, tissue oxygenation values were consistently higher than LAD oxygenation

---

[85] The tissue oxygenation data set included an outlier (100% oxygen saturation, 71% oxygenation, corresponding to reperfusion in the Apr. 22 trial) that when included in the analysis, provided an R^2 value of 0.794. Removal of this single data point increased the R^2 value to 0.926; thus, it was excluded from Figure 5.17b.

values, possibly reflecting a time lag between reductions in Hb oxygen saturation and Mb oxygen saturation. At the same time, mean oxygen saturation values were consistently lower than arterial oxygen saturation values.

The other factor that impacts the validity of this study is that each stage of the protocol did not last long enough for (spectrally-derived) oxygenation values to reach equilibrium (Figure 5.18). Several observations are of interest. First, it is reasonable to assume that changes in Hb oxygen saturation precede those in Mb oxygen saturation (in response to hypoxia). Thus, it may be possible that in the first 10 min following each reduction in oxygen pressure, Hb saturation had reached equilibrium but Mb saturation continued to decrease. In this event, Figure 5.18 may provide a visual indicator of Mb deoxygenation. Secondly, the fact that oxygenation values had not reached equilibrium may account for the deviations of the slope and intercept (in Figure 5.17b) from unity. With extended periods of hypoxia, more accurate calibration of oxygenation values to blood oxygen saturation may be possible.

5.4.5. Myoglobin and Hemoglobin

Myoglobin[86] has long been recognized as a distinct chromophore in muscle tissue.(122) Speculation that the red colour of muscle might be due to a chromophore in tissue rather than circulating blood dates to 1803,(23) decades before the term "hemoglobin" had even been coined.(103). Moreover, the slight shift in (visible-wavelength) Mb absorption bands to longer wavelengths relative to those of Hb was

---

[86] The term "myoglobin" was first coined by Günther in 1921, in reference to muscle-bound heme protein, but it did not become universally accepted until the 1930s or 1940s. Other terms, including "myohemoglobin" and "muscle hemoglobin" were also used frequently until this time.(165)

noted late in the 19th century.(138,171) Although the question of whether Mb was a form of Hb or something substantially different remained controversial for some time, work by Ray and Paff (202) and Theorell,(251) among others, helped elucidate the properties of Mb.

Like Hb, Mb is a heme-protein compound, but while Hb is a tetramer[87] of heme-globin compounds, Mb is a monomer. Thus, unlike Hb which has chemically distinct α and β globin chains, there is only one variety of Mb globin chain. Since Mb only has one heme, oxygen binding is not cooperative and the Mb oxygen saturation curve is hyperbolic rather than sigmoidal. The oxygen pressure at which Mb is half-saturated (2.3 (268) or 5.3 mm Hg (83)) is much lower than that of Hb (26 mm Hg (274)) to compensate for the much lower oxygen pressures within cells than in the bloodstream.

The relative spectroscopic contributions of Mb and Hb to the overall heme absorbance in cardiac tissue is an important consideration in the studies presented in this thesis. The contributions of oxy- and deoxy-forms of Hb and Mb depend on the total Hb concentration in the blood, the blood volume in the area of interest, and the tissue Mb concentration. An estimate of the relative contributions was provided in Section 4.4.4, which concluded that Mb comprised 64% of the total heme absorption band.

In order to assess the relative contribution of Mb experimentally, we conducted a parallel study to this one in which hearts were perfused with an oxygen-carrying, hemoglobin-free blood substitute (Krebs-Henseleit buffer, KHB). As before, porcine hearts (n=8) were isolated and suspended in a perfusion apparatus, and a cannula and

---

[87] From the Greek *tetra* (meaning *four*) and *meros* (meaning *part*), it refers to a compound with four similar parts (e.g. four globin-heme compounds). Similarly, monomer refers to a compound with a single part.

flow probe were attached to the LAD. In some cases, their placement atop the LAD had the effect of reducing flow to the perfusion bed, as observed here. After a period of normal perfusion, the LAD was completely occluded for two hours, followed by reperfusion. Near-infrared spectroscopic images were acquired for the anterior side of the heart during each period of the protocol.

In this parallel study, only Mb and water (and not Hb) contributed to the absorption band profile. Since the Mb concentration in tissue should be approximately the same for both the present and previous studies, the contribution of Mb (as determined in the present study) may in principle be subtracted from the total (Hb+Mb) contribution determined from spectroscopic images acquired during blood perfusion, providing an estimate of the Hb contribution. Sample tissue spectra from spectroscopic images acquired during normal perfusion and regional ischemia are displayed in Figure 5.19. Spectral features characteristic of deoxygenated heme proteins (noticeable in the steepness of the slope between 650 and 720 nm) and oxygenated heme proteins (noticeable in the absorbance rise around 850 to 900 nm) are observed in the spectra of both blood-perfused and KHB-perfused hearts. These contributions are clearly more intense for the blood-perfused tissue (due to increased heme content).

The elevated heme content in blood-perfused (as compared to KHB-perfused) hearts is evident in maps of oxy- and deoxy-heme levels during normal perfusion (Figure 5.20). Both oxygenated and deoxygenated heme protein levels are substantially higher across the entire heart. Large arteries are also much more clearly defined in the blood-perfused hearts, due to the high arterial hemoglobin concentration. In contrast, the major arteries in KHB-perfused hearts exhibit below-average heme protein levels.

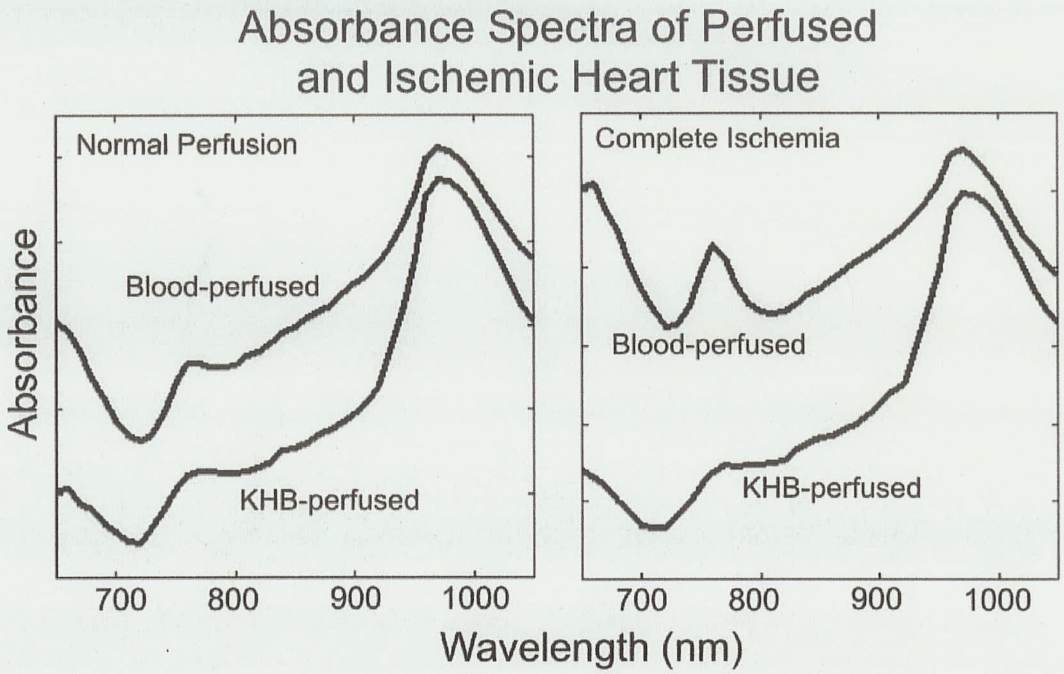

Figure 5.19. Sample spectra acquired during normal perfusion and during complete, regional ischemia from tissue perfused with blood and with Hb-free Krebs-Henseleit buffer (KHB).

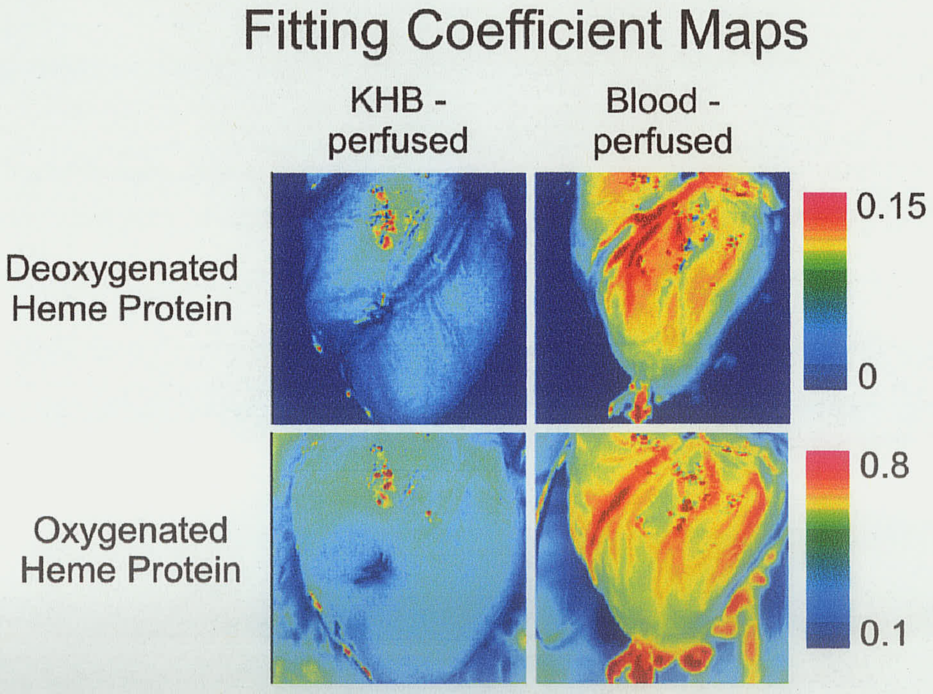

Figure 5.20. Deoxy- and oxy-(heme protein) distribution during normal perfusion with Krebs-Henseleit buffer (left) and with blood (right).

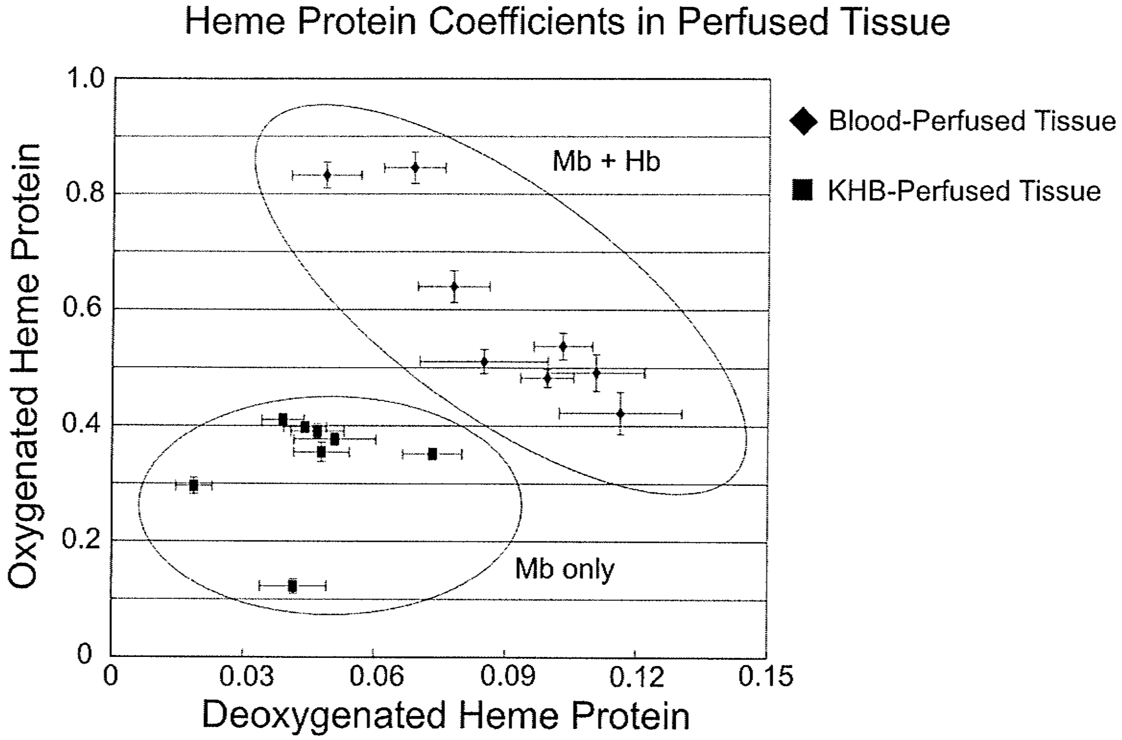

Figure 5.21. Spectrally-derived oxygenated and deoxygenated heme protein levels for cardiac tissue perfused with KHB (squares) or blood (diamonds). The heme content (sum of oxy and deoxy coefficients) is clearly higher in blood-perfused than KHB-perfused tissue, reflecting additional contributions of Hb.

The higher heme content in blood-perfused hearts is portrayed most clearly by Figure 5.21. Mean tissue heme protein levels during normal perfusion are plotted for each trial in the two studies. These plots demonstrate clearly that total (Mb+Hb) levels in the blood-perfused hearts were consistently higher than total Mb levels in the KHB-perfused hearts; total Mb and total (Hb+Mb) values are 0.38 ± 0.10 and 0.68 ± 0.14, respectively. The Mb contribution may therefore be estimated as 56 ± 3% (of the total heme absorbance, 0.38 / 0.68 = 0.56).

To corroborate this estimate, a train of calculations analogous to that described in Section 4.4.4 was performed. Since blood Hb concentrations ranged between 42 – 61 g/L, the overall tissue Hb heme concentration was approximately 0.25 mmol/kg wet weight. Given the Mb concentration in pig hearts of 0.36 mmol/kg,(5) the Mb contribution should be 59% of the total heme signal (0.36 / (0.36 + 0.25)). This coincides excellently with our spectroscopic estimate.

Intriguingly, there was little apparent difference between the spectra of the KHB-perfused heart acquired during normal perfusion and during complete, regional ischemia. This similarity was observed consistently and is difficult to explain. Since oxygen is being completely restricted from the tissue region of interest, the myoglobin can not remain oxygenated. Yet, the fitting coefficients representing [dMb] and [MbO_2] during ischemia remained near the values observed during normal perfusion (for the spectra illustrated in Figure 5.19, oxy-Mb and deoxy-Mb coefficients were 0.25 and 0.07, respectively).

5.5. Conclusions

In conclusion, the questions listed in the introduction can be addressed.

- The change in imaging equipment was very effective in reducing the spectral noise and triggering image acquisition with the ECG successfully allowed imaging of beating hearts without significant motion artifacts or low signal-to-noise.
- Spectrally-determined oxygenation values clearly resolved different degrees of partial ischemia within each group, although substantial inter-subject variability hindered accurate quantification of the effects observed.

- Intermediate reperfusion had little effect on either cardiac function or spectrally-derived oxygenation parameters.
- By reducing the number of images acquired within each spectroscopic image, the total acquisition time was reduced sufficiently to monitor oxygenation kinetics in response to ischemia and reperfusion. Changes in oxygenation, especially in response to complete ischemia, occurred on a curiously long time scale, perhaps reflecting low Mb deoxygenation.
- No clear differences in oxygenation were observed in comparing images acquired during systole and diastole. Any difference that might exist appeared to be small relative to regional variations.
- Calibration of oxygenation values to blood oxygen saturation was possible for both arterial and tissue oxygenation values, although hypoxic periods were not sustained sufficiently long for heme proteins to reach equilibrium.
- Finally, the relative contributions of myoglobin and hemoglobin to the overall absorbance profile of blood-perfused cardiac tissue were determined to be approximately 60% and 40%, respectively.

6. In vivo Hearts

6.1. Introduction

The studies described in Chapters 4 and 5 established the feasibility of using spectroscopic imaging to identify regions of tissue suffering from total ischemia in arrested and beating, isolated hearts. Chapter 5 also demonstrated that spectroscopic imaging can differentiate between different degrees of partial ischemia and that excellent signal-to-noise can be achieved in spectroscopic images of beating hearts. To demonstrate the feasibility of intraoperative heart monitoring, this study applies spectroscopic imaging to a model that very closely mimics surgical conditions (opening the chest cavity and exposing the heart, but leaving the natural perfusion system intact).

With this experimental model came some challenges. Perhaps the most significant were motion artifacts resulting from both cardiac contractions and breathing-induced heart motion. In addition, blood circulation (and oxygenation) was governed by the normal physiological mechanisms rather than by external controls. Thus, blood oxygen pressures were not as high as in the previous studies. Finally, blood pooling in the chest cavity and possible interference by the surrounding rib cage necessitated careful positioning of the imaging and illumnitation systems.

The primary objective of this study was to highlight ischemic regions of heart tissue in a working heart model with the same efficacy as seen previously for isolated hearts. A secondary objective was to exploit the absorption bands of an exogenous, intravascular contrast agent, indocyanine green (ICG), in order to monitor coronary flow spectroscopically. To that end, image sequences[88] acquired at the absorption band maximum of ICG (800 nm) were interpreted to follow the changes in ICG distribution.

6.2. Materials and Methods

6.2.1. Surgery and Perfusion

Domestic pigs (n=17, 25-30 kg at use) were acquired and treated as described in Section 4.2.1.1. Pre-medication was performed with ketamine hydrochloride (22 mg/kg), midazolam (0.33 mg/kg), and atropine (0.05 mg/kg). Anesthesia was established with isofluorane (3-4% with oxygen via an inhalation mask). The pig was intubated and ventilated with oxygen and isofluorane was then reduced to 2%. The rate and volume of positive pressure ventilation were adjusted to keep the blood gas concentrations in the normal physiological range. Once the pig was fully anesthetized, a sternotomy[89] was performed to expose the heart to the imaging equipment. At the same time the right femoral artery and vein were isolated and cannulated. Systolic (SP) and diastolic (DP) blood pressure and heart rate (HR) were monitored via a catheter in the femoral artery and supplemental fluids[90] were supplied to the pig via the femoral vein to maintain adequate hydration. The pressure-rate product was calculated as (1/3*SP + 2/3*DP)*HR.[91] Lidocaine was also added via the venous cannula whenever necessary to

---

[88] In this chapter, "spectroscopic images" are used to assess blood and tissue oxygenation, whereas "image sequences" monitor relative ICG concentrations.

[89] From the Greek *sternon* (meaning *chest*) and *tomē* (meaning *incision*).

[90] Previously prepared Ringer's solution was used, containing the following (in mM): Na^+ (147.5), K^+ (4), Ca^{++} (2.25), Cl^- (156).

[91] This calculation is different from that used in the isolated heart studies because in the previous study, an intraventricular balloon was able to measure the pressure difference directly. In this study, systolic and diastolic pressures were measured indirectly.

correct cardiac arrhythmias. The pericardium was opened and the left anterior descending (LAD) artery was isolated from the epicardium.

The animals were divided into two groups. For the first group (n=7), after a period of normal perfusion, the LAD was completely occluded to induce complete, regional ischemia. Following 90 min of ischemia, the occlusion was released, and reperfusion followed for 2 hrs. The second group of hearts (n=10) followed a similar protocol with partial, rather than complete, LAD occlusion. For some of these trials (n=6), LAD flow was reduced to 20% of its initial value (moderate ischemia); LAD flow was reduced to 50% of baseline (mild ischemia) for the other trials (n=4).

For the first group, a thread was positioned around the LAD (usually distal to the second diagonal branch), and ischemia was then induced by tightening the thread (no flow probe was applied to the artery). For the second group, an inflatable occluder (3-4 mm diameter, IVM, Headsburg, California) was positioned around the LAD,[92] and an ultrasonic flowmeter (Transonic Systems, Inc., Ithaca, NY) was placed on the LAD downstream of the occluder. For all trials, ECG electrodes were positioned in the right atrium and the apex to record changes in electrical activity and to supply an external trigger for image acquisition. The pigs lay in a supine position[93] atop a temperature-controlled blanket on the surgical table in order to maintain constant body temperature. Legs were fastened securely to prevent any movement.

---

[92] The LAD cannulation method used in the previous study could not be used because perfusion was not supplied by an external system.

[93] From the Latin *supinus*, it denotes the position of the body when lying on the back, facing upward.

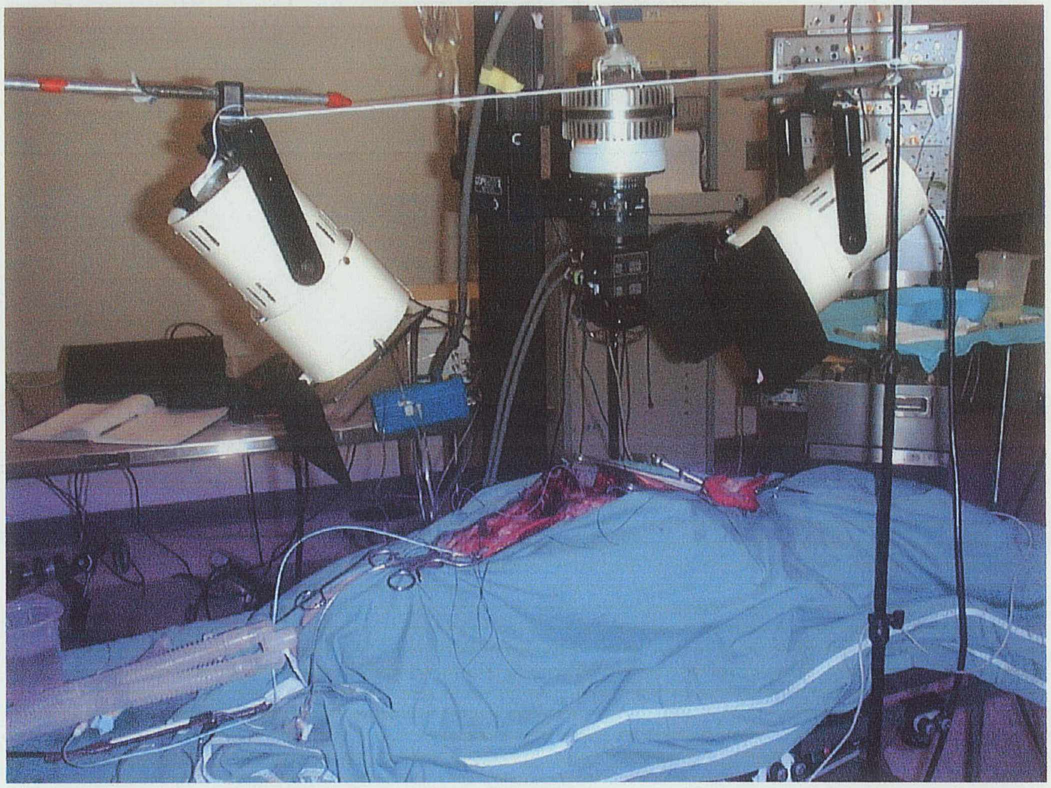

Figure 6.1. Photograph of experimental setup.

6.2.2. Spectroscopic Imaging

Spectroscopic imaging was performed with the same imaging and external triggering equipment as described in Chapter 5. Three images acquired at 10 nm intervals between 650 and 1050 nm (80 ms exposure time) were averaged to optimize signal-to-noise. The camera and LCTF were attached to a copystand above the chest, facing down (Figure 6.1). Lamps were placed along the midsagittal plane to illuminate both left and right sides of the heart uniformly.

In parallel with the blood/tissue oxygenation measurements, arterial clearance was monitored spectroscopically with indocyanine green (ICG). When a bolus of ICG is added to the blood, the rate at which it passes through a particular area is an indicator of coronary flow. To that end, a bolus of ICG was added to the perfusate (through a cannula in the jugular vein) during each stage of the protocol (normal perfusion, regional ischemia, and reperfusion).[94] For each bolus, a sequence of 60 images was acquired (80 ms exposure time) at a rate of 1 Hz during infusion, with the LCTF fixed at 800 nm. Each sequence included five or six images acquired before ICG infusion, to establish baseline absorbance values.

6.2.3. Experimental Design

Cardiac functional data and blood gas sample data were collected regularly throughout the experiment. All trials began with a period of normal perfusion lasting at least 30 minutes following placement of the occluder and flow probe (where applicable). Two spectroscopic images were acquired during this time. An ICG image sequence was acquired between the spectroscopic images, allowing at least five minutes between ICG infusion and spectroscopic image acquisition to allow clearance of the ICG bolus.

Spectroscopic images were then acquired at the 10, 30, 60, and 80 min time points following complete or partial LAD occlusion (Figure 6.2). In addition, at the 35 min time point, a second bolus of ICG was added and an image sequence was acquired. Following release of the LAD occlusion (after 90 min ischemia), the perfusion bed was reperfused for two hours, and spectroscopic images acquired approximately every 30 minutes. Following the first 40 min of reperfusion, a third bolus of ICG was added and a final image sequence was acquired. At the end of each trial, hearts were removed, stained with Evans Blue and TTC, and dissected as before.

---

[94] Since spectroscopic images were not acquired until after ICG had passed out of the system, this study of arterial clearance did not interfere with oxygenation studies.

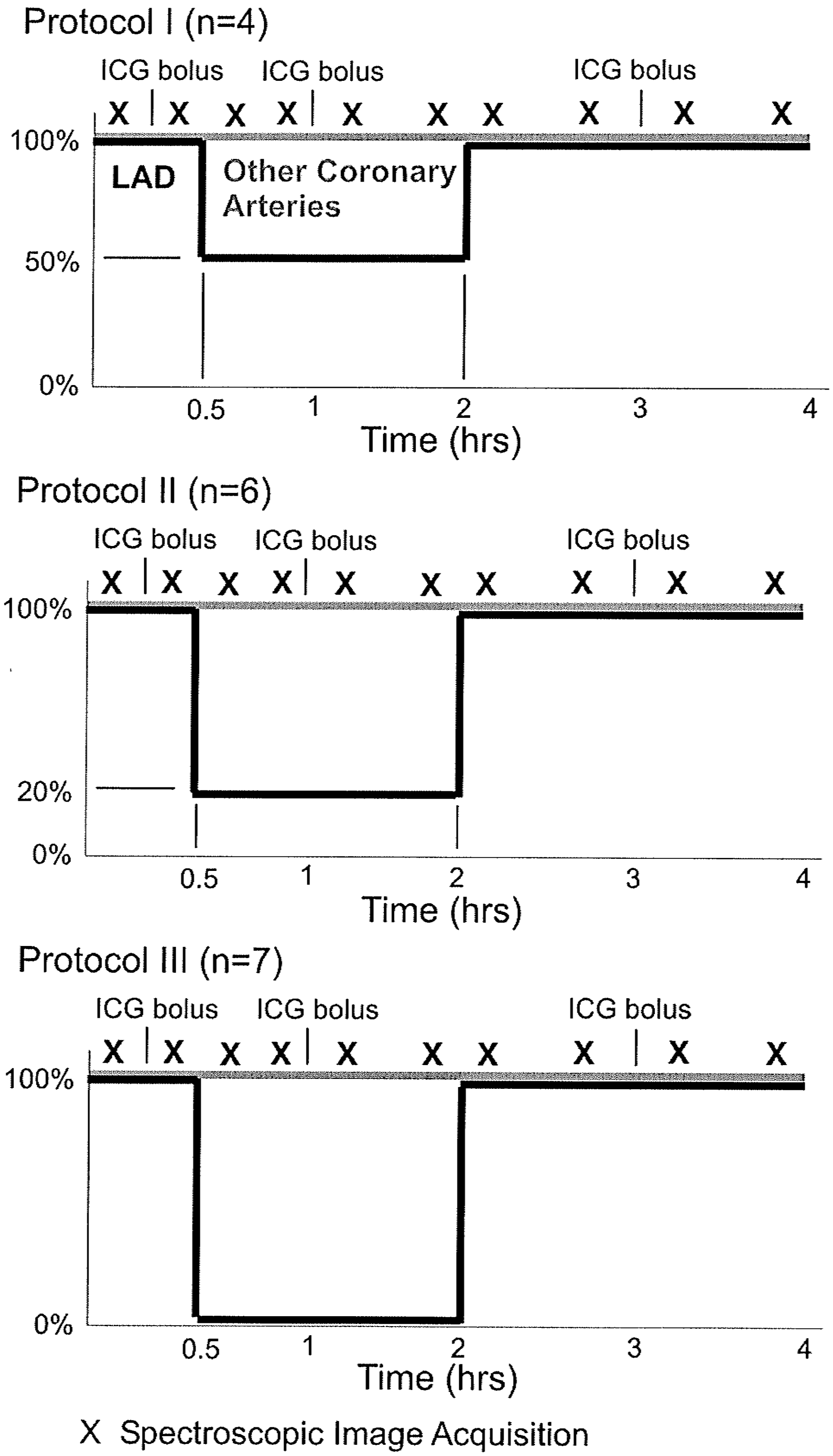

Figure 6.2. Experimental protocols for the three groups of trials.

6.3. Results and Discussion

6.3.1. Functional Results

The areas at risk in Group I trials comprised 17.3 ± 4.0% of the left ventricular mass (14.3 ± 3.5 g), as determined by Evans Blue staining (see Section 2.1.3). The areas at risk in Group II trials were comparable at 16.6 ± 3.6% of the left ventricular mass (15.3 ± 3.1 g). Both potassium and hemoglobin levels showed a mild increase relative to baseline levels during regional ischemia (Table 6.1). The rise in blood potassium might be explained

Table 6.1. Blood Component Data

Timepoint	**K^+ (mM)**		**Lactate (mM)**		**Hb (g/dL)**	
	Group I (complete)	Group II (partial)	Group I (complete)	Group II (partial)	Group I (complete)	Group II (partial)
Baseline	3.8 ± 0.3	4.0 ± 0.2	1.6 ± 0.3	1.2 ± 0.5	8.4 ± 1.0	9.3 ± 0.6
15 min. Ischemia	4.2 ± 0.3	4.1 ± 0.5	1.6 ± 0.3	1.4 ± 0.7	8.4 ± 0.6	9.2 ± 1.2
P value	*0.01*	NS	*NS*	*NS*	*NS*	*NS*
75 min. Ischemia	4.3 ± 0.4	4.2 ± 0.5	1.6 ± 0.4	1.5 ± 0.8	8.8 ± 1.1	9.2 ± 1.0
P value	*0.05*	*NS*	*NS*	*NS*	*0.01*	*NS*
15 min. Reperfusion	4.7 ± 0.6	4.4 ± 0.5	1.6 ± 0.2	1.4 ± 0.9	9.2 ± 1.0	9.6 ± 0.8
P value	*0.01*	*0.05*	*NS*	*NS*	*0.001*	*NS*
75 min. Reperfusion	5.3 ± 1.0	4.8 ± 0.6	1.5 ± 0.2	1.2 ± 0.8	9.4 ± 1.1	10.1 ± 0.6
P value	*0.01*	*0.001*	*NS*	*NS*	*0.01*	*0.001*

P values were calculated from comparisons with baseline
NS = not significant

Table 6.2. Cardiac Functional Parameters

Timepoint	**Heart Rate (bpm)**		**LV Systolic Pressure (mm Hg)**		**Pressure Rate Product (mm Hg / min)**	
	Group 1	Group 2	Group 1	Group 2	Group 1	Group 2
Baseline	113 ± 18	103 ± 16	80 ± 4	86 ± 7	6990 ± 1280	6530 ± 1560
15 min Ischemia	112 ± 16	107 ± 13	76 ± 10	83 ± 9	6510 ± 1360	6380 ± 1450
P value	*NS*	*0.05*	*NS*	*0.01*	*NS*	*NS*
75 min Ischemia	113 ± 10	109 ± 20	74 ± 4	85 ± 7	6340 ± 920	6620 ± 1640
P value	*NS*	*0.01*	*0.001*	*0.05*	*0.05*	*NS*
15 min. Reperfusion	118 ± 15	110 ± 22	73 ± 6	85 ± 8	6710 ± 1220	6770 ± 1790
P value	*NS*	*0.01*	*0.01*	*0.05*	*NS*	*NS*
75 min. Reperfusion	119 ± 12	114 ± 20	75 ± 6	84 ± 6	6720 ± 1390	7020 ± 1370
P value	*NS*	*0.01*	*0.05*	*NS*	*NS*	*0.01*

P values were calculated from comparisons with baseline
NS = Not Significant

in part by some cell membrane damage leading to leakage of potassium from the cellular space, but such membrane damage would also to lead to increases in blood lactate levels, which were not observed. Simultaneous increases in K^+ and Hb could also result from dehydration via respiration and urine formation, which may not have been completely compensated for by fluid infusion.

Despite changes in potassium and hemoglobin levels, no substantial changes were observed in cardiac functional parameters (Table 6.2). Changes in heart rate and systolic pressure of the Group II trials were physiologically inconsequential (despite statistical

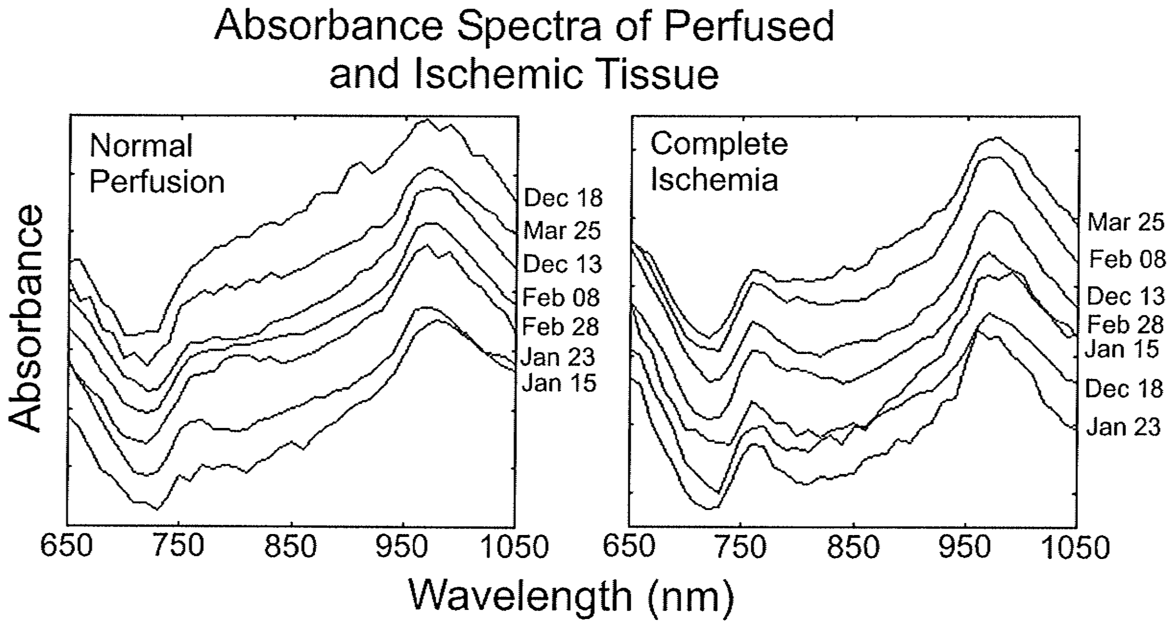

Figure 6.3. Sample spectra from Group I trials, acquired during normal perfusion and total ischemia.

significance according to Sandler's A-test). Since venous blood samples could not be acquired from the coronary sinus, oxygen consumption could not be calculated as it was for the isolated heart experiments.

6.3.2. Spectroscopic Imaging

6.3.2.1. Heart Motion

Sample spectra extracted from spectroscopic images exhibited good spectral signal-to-noise (Figure 6.3). For the previous study, the only cardiac motion was due to cardiac contraction, and ECG triggering ensured that images were consistently acquired at the same point in the cardiac cycle. For the present study, lung inflation and deflation also contributed to cardiac movement, not only moving the heart in and out of focus, but also contorting it so that the shape of the heart in successive images was not constant for a given phase in the cardiac cycle. Since the respiration cycle period (5 s) is much longer

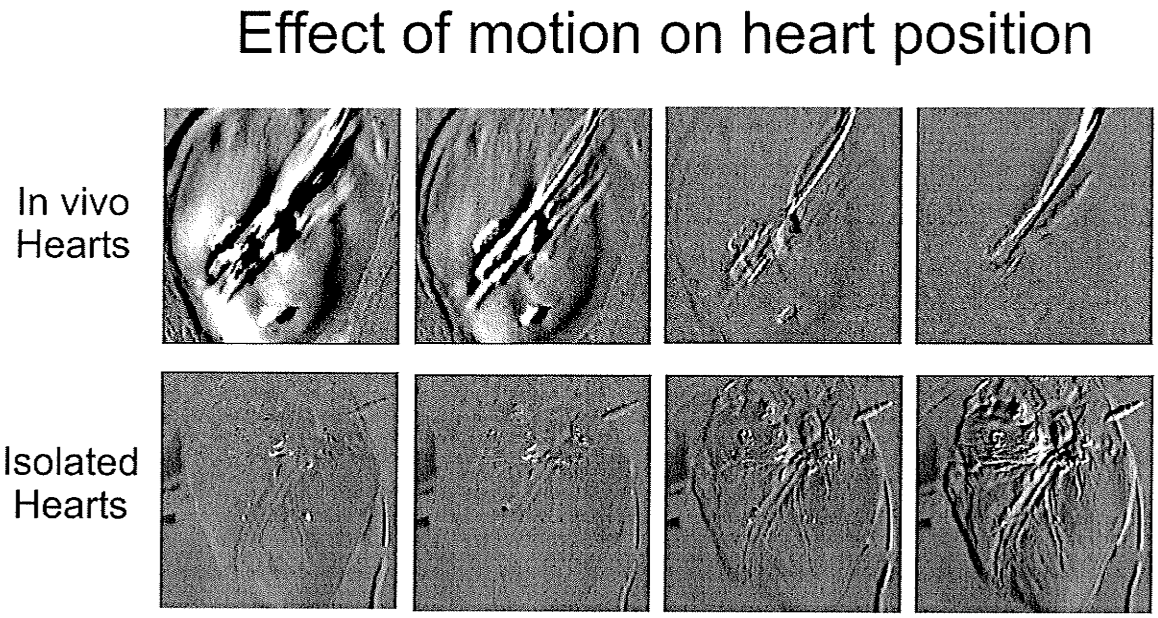

Figure 6.4. (top) Difference images showing the effect of lung motion due to breathing on heart position. (bottom) Difference images from previous (isolated heart) study, shown on the same scale.

than that of the cardiac cycle (600 ms), ECG triggering alone could not ensure that the heart will have the same shape and position in each image.

The effect of breathing on heart shape and position is demonstrated in Figure 6.4. These images show the differences between an initial image and four images acquired sequentially at the same wavelength and point in the cardiac cycle. White and black areas signify large differences in intensity (positive and negative, respectively), while areas of minimal difference are shown as grey.

The first two images of the *in vivo* sequence show substantial differences, not only around the tubes that laid atop the heart (connected to the occluder and flow probe) but also around the edges. By the time the last two images of the sequence had been acquired, the lungs (and heart) had returned to approximately the same position they had occupied for the initial image. By comparison, corresponding difference images for the isolated heart indicate that the heart's position and shape in this image sequence were very reproducible for a given phase of the cardiac cycle. It may also be relevant to note that the left ventricular volume was fixed for the isolated hearts, due to the balloon placed inside the cavity. For the present study, greater ventricular wall motion was permitted over the course of the cardiac cycle (as no balloon was in place).

While it is theoretically possible to gate image acquisition to both the respiration and the cardiac cycles, this was impractical for two reasons. The first is a technical point; while the Grass recorder (to which the ECG leads were connected) was able to send an output voltage signal to the gating box, the respiration monitor had no such output. A more fundamental problem is that it would have made the total acquisition time of each spectroscopic image prohibitively long. With the use of two external triggers, image acquisition would not occur until both cycles reached their respective threshold values simultaneously. While the period of the respiration cycle is only five seconds, the time between points where both cycles reached the required phase simultaneously would be much longer.

6.3.2.2. Fitting Coefficients

Deoxy-(Hb+Mb), oxy-(Hb+Mb) coefficients and oxygenation were calculated as before. Representative oxygenation maps are displayed in Figure 6.5. For regional ischemia, the ischemic region is easily distinguished from the normally-perfused region. Moreover, the ischemic region is clearly distal to the LAD occlusion in all images; the area downstream of the occlusion shows obvious deoxygenation whereas the area upstream remains well-oxygenated.

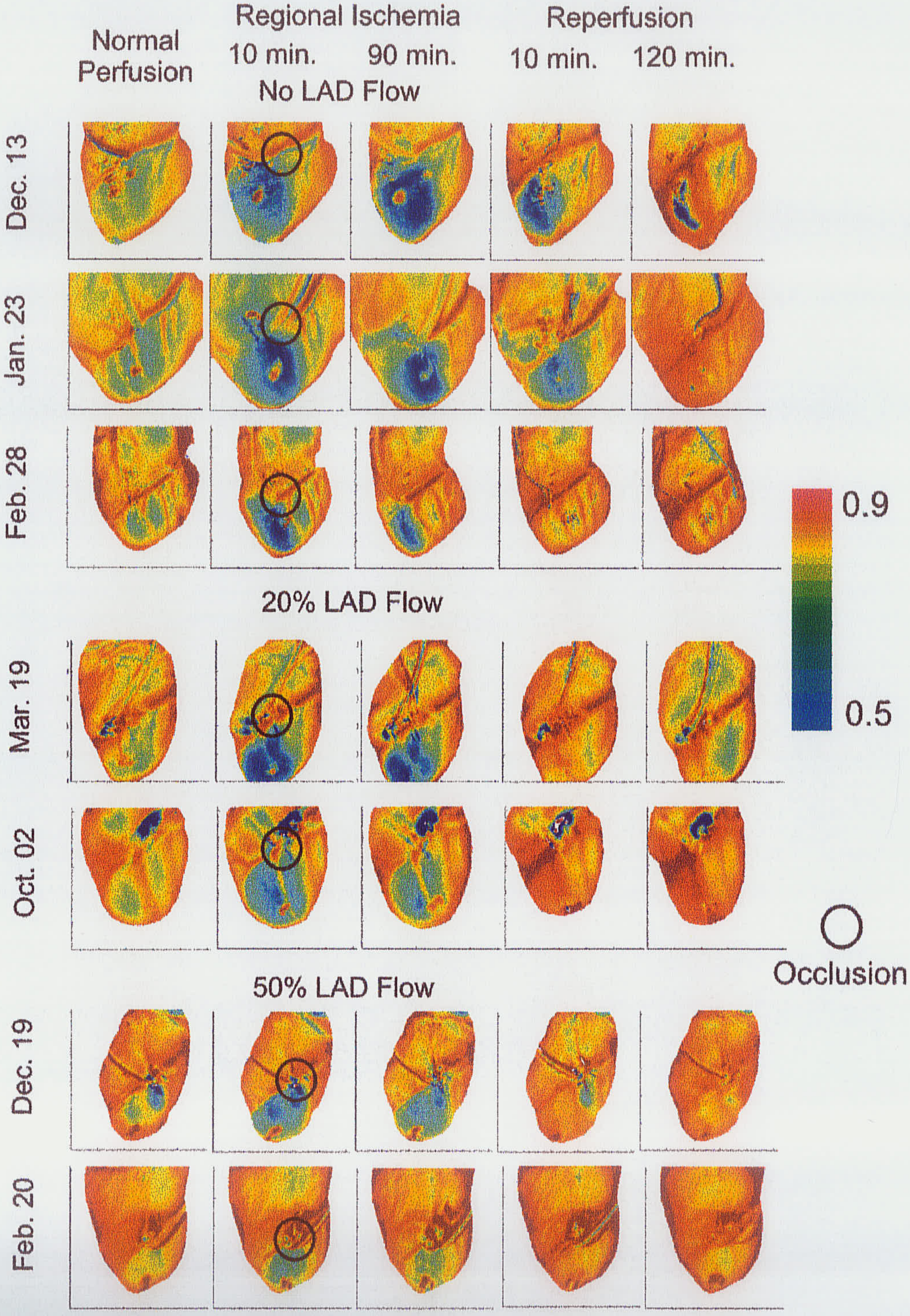

Figure 6.5. Representative oxygenation maps. The position of the occlusion on the LAD artery is highlighted. Note tissue deoxygenation downstream of occlusion.

Two differences between hearts suffering from mild and severe ischemia are evident. First, moderate or severe ischemia triggered visibly poorer oxygenation than mild ischemia. Second, reoxygenation was substantially slower upon reperfusion in some complete ischemia trials than in any partial ischemia trials. This was true for about half of the complete ischemia trials and was most notable for the Dec. 13 and Jan. 23 trials. In contrast, for isolated hearts, tissue oxygenation was restored immediately upon reperfusion after complete regional ischemia. This difference might be due to the fact that ischemia lasted longer in this study than in the previous study (90 min vs. 45 min), and the prolonged ischemia may therefore have resulted in greater vascular damage. Indeed, for the total occlusion group, infarcts developed (TTC revealed that 29 ± 16% of the area at risk was necrotic). The oxygenation of heme proteins did return to normal levels after two hours of reperfusion.

Mean oxygenation values were evaluated for representative tissue regions within and outside the area at risk at each time point (Figure 6.6). The effect of the occluder and flow probe during otherwise normal perfusion is demonstrated by the reduced oxygenation in the areas at risk of the partial ischemia trials (in which they were used). Oxygenation in the at-risk regions was therefore significantly lower than that for control tissue during nominally normal perfusion for the partial ischemia trials ($p < 0.05$).

The differences between mild and severe ischemia (noted above) are further illustrated by Figure 6.6. Tissue oxygenation levels are lower during moderate and severe

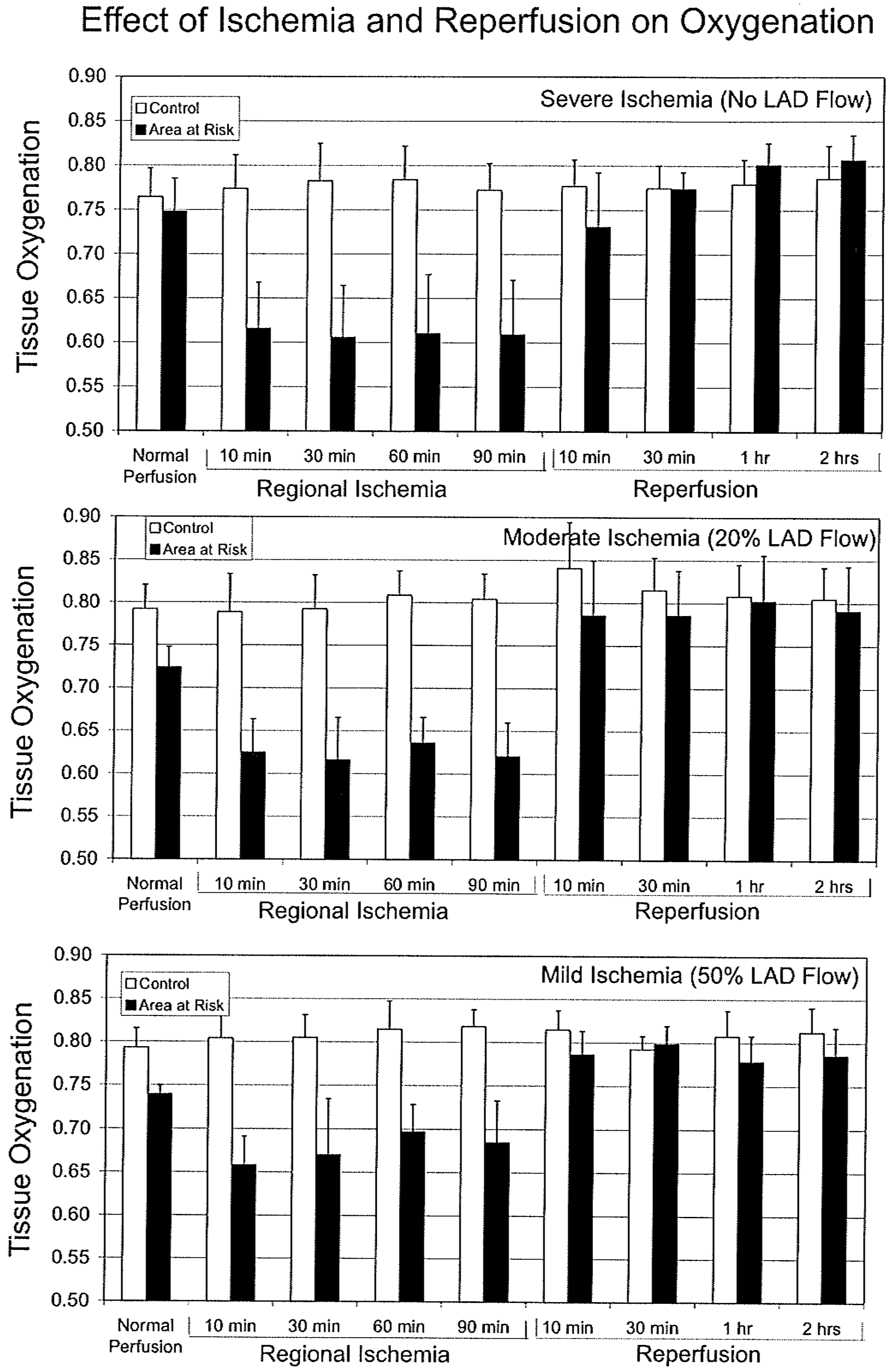

Figure 6.6. Oxygenation within areas of normally perfused tissue (white) and areas at risk (black) for each time point and each degree of regional ischemia.

ischemia than during mild ischemia (although there was no significant difference between the effects of moderate and severe ischemia). Moreoever, oxygenation remained constant throughout the ischemic period. It was also noted above that even after 10 min reperfusion, oxygenation maps still exhibited below-normal oxygenation in half of the complete ischemia trials. Figure 6.6 demonstrates that when all complete ischemia trials are considered, there was no significant difference in oxygenation between 10 min reperfusion and normal perfusion in complete ischemia trials. Moreover, after 10 min reperfusion in partial ischemia trials, oxygenation in the area at risk was restored to levels exhibited by control tissue during normal perfusion. Finally, in contrast to partial ischemia trials, oxygenation in the area at risk in complete ischemia trials continued to increase with prolonged reperfusion. Between 10 min and 30 min, and again between 30 min and 1 hr of reperfusion, oxygenation rose significantly ($p < 0.05$ in each case).

A final observation regarding these data (Figure 6.5) is that in the Dec. 13 trial, a small region of tissue was not reoxygenated even after two hours of reperfusion (spectra acquired from this region showed strong deoxy-(Hb+Mb) absorption bands at 760 nm). This was not observed in any other trial. It is possible that this area became necrotic as a result of the ischemic period and thus, heme proteins in the region were trapped and not reoxygenated. However, TTC-staining demonstrated that hearts of nearly all complete occlusion trials exhibited some necrosis (29 ± 16% of the area at risk; no necrosis was detected in partial occlusion trials) and no corresponding deoxygenation was observed in the other trials.

6.3.3. Coronary Flow Analysis

Images acquired during passage of ICG boli provided useful qualitative data regarding coronary flow rates. Figure 6.7 shows the three ICG image sequences for one of the complete ischemia trials, acquired during normal perfusion, regional ischemia, and reperfusion. As each sequence progresses, ICG first enters the major vessels and then fills the intermediary space. Since ICG binds to blood albumin and is therefore confined to the vascular space, these maps demonstrate the extent to which capillaries permeate the cardiac muscle tissue. As the sequence continues, the ICG drains from the capillary space, into the veins and on to the coronary sinus on the posterior side of the heart.

ICG washin and washout was seen to occur at roughly the same rate during regional ischemia as during normal perfusion. As expected, during total regional ischemia, ICG permeated the area at risk only very slowly; ICG is initially kept out and only gradually penetrates the area at risk. The ICG that did gradually penetrate the area at risk reflects the presence (and the relative inefficiency) of the collateral vasculature that serves as the only blood supply to the area during LAD occlusion. Since the occlusion remained in place and flow was negligible, the ICG that did enter the area at risk remained there until the occlusion was released. During the reperfusion period, the spatial distribution of ICG was slightly altered. ICG accumulated in the area that had been ischemic (the area at risk) more rapidly than in those areas that had been perfused continuously, likely due to coronary vasodilation in response to ischemia.

Sample ICG washin/washout time courses comparing the area at risk to a continuously perfused area (control) are displayed for each group in Figure 6.8. The periodic fluctuation in the absorbance values with a period of approximately 5 s is due to

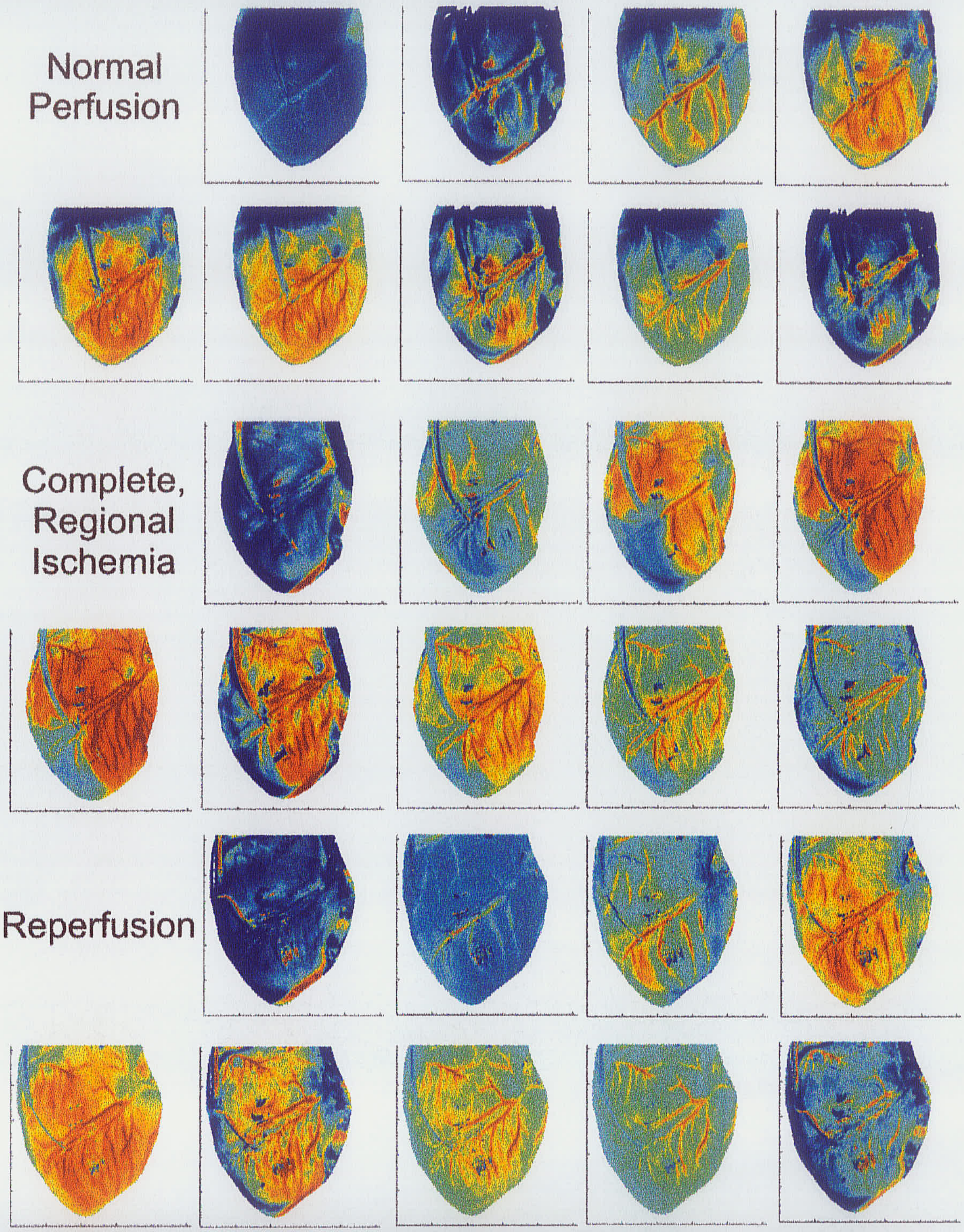

Figure 6.7. Images showing washin and washout of ICG in the Feb. 28 trial. Each image depicts the difference in absorbance (800nm) between the initial image (of each sequence) and subsequent images (acquired at 2 s intervals), High ICG content is marked in red and low ICG content in blue. In each sequence, the first image shown was acquired prior to entrance of ICG into the heart and serves as a baseline. Each sequence spans a period of 16 s.

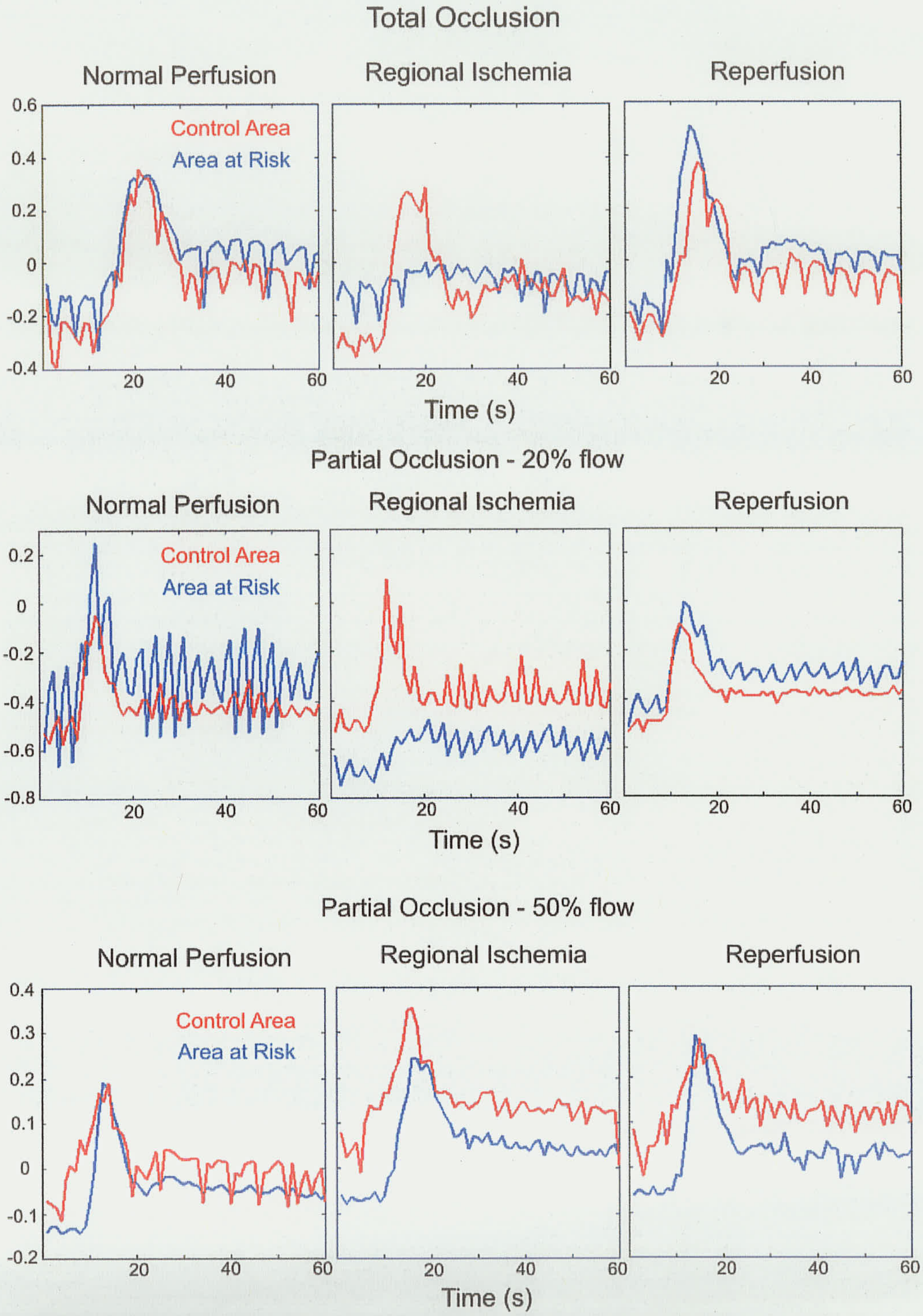

Figure 6.8. Representative time courses showing extent and rate of ICG washin and washout through perfused and ischemic tissue.

motion of the heart resulting from breathing. If the area under study is away from major vessels, areas in which CCD detector saturation might occur, or boundaries of ICG perfusion; then the absorbance values of neighbouring pixels are similar to those of the pixel under study and the periodic fluctuations will be small. Otherwise, the fluctuations can be quite intense.

These time courses depict both the extent of ICG accumulation and the rate of washin/washout, and those for the complete occlusion trial complement the observations noted above for the corresponding image sets. During normal perfusion, ICG flow through both areas is comparable. Regional ischemia virtually eliminates ICG accumulation within the area at risk. During reperfusion, ICG accumulates to higher levels within the area at risk than observed during normal perfusion, but the transit profile through the control area is unchanged.

Two other observations stand out. First, while the initial rise and fall in absorbance, reflecting passage of the bolus through the vasculature, is extremely pronounced (and of primary interest), a second, very weak rise and fall in absorbance can also be detected, as ICG reenters the coronary arteries after passing through the coronary sinus. Upon reentry, the ICG is much more diluted due to mixing with the venous return (hence the low intensity), and the peak is much broader since the ICG bolus is dispersed in the bloodstream. Secondly, the steady state absorbance value at the end of the minute is higher than the baseline absorbance value in nearly all cases. This indicates that ICG equilibrated with the blood pool and remained in the vasculature during the short time course probed by the image sequences. The ICG half-life is approximately 5 min, and hepatic clearance over a one-minute period should be low (~13%).

To place the analysis of ICG washin/washout on a more quantitative footing, three derived parameters were compared among the three experimental groups. These were peak ICG concentrations (measured by the peak absorbance value at 800 nm), the rate of ICG uptake (the rate of increase in absorbance), and the residual ICG concentration (the absorbance difference between the equilibrium value 1 min after infusion and the pre-infusion value). The mean values for each of these three parameters were determined within both the area at risk and the continuously perfused region.

Average ICG transit profiles were calculated for severe, moderate, and mild ischemia at each time point for both ischemic and control ROI's. Baseline absorbance values for each time course were determined as the average of the first five (pre-infusion) absorbance values within that time course (t=1 to 5 s). The four or five time points nearest the peak maximum were averaged and the baseline value subtracted to gauge the peak ICG concentration (ΔA).[95] The rate of increase was defined as $\Delta A/\Delta t$, i.e. the ratio of the peak absorbance to the time difference between the start of the rise in absorbance and the peak. Finally, the residual ICG concentration was gauged by the difference between the mean absorbance over the final ten time points (t=50 to 60 s) and the corresponding pre-infusion value.

---

[95] Averages were used to account for periodic fluctuations in absorbance.

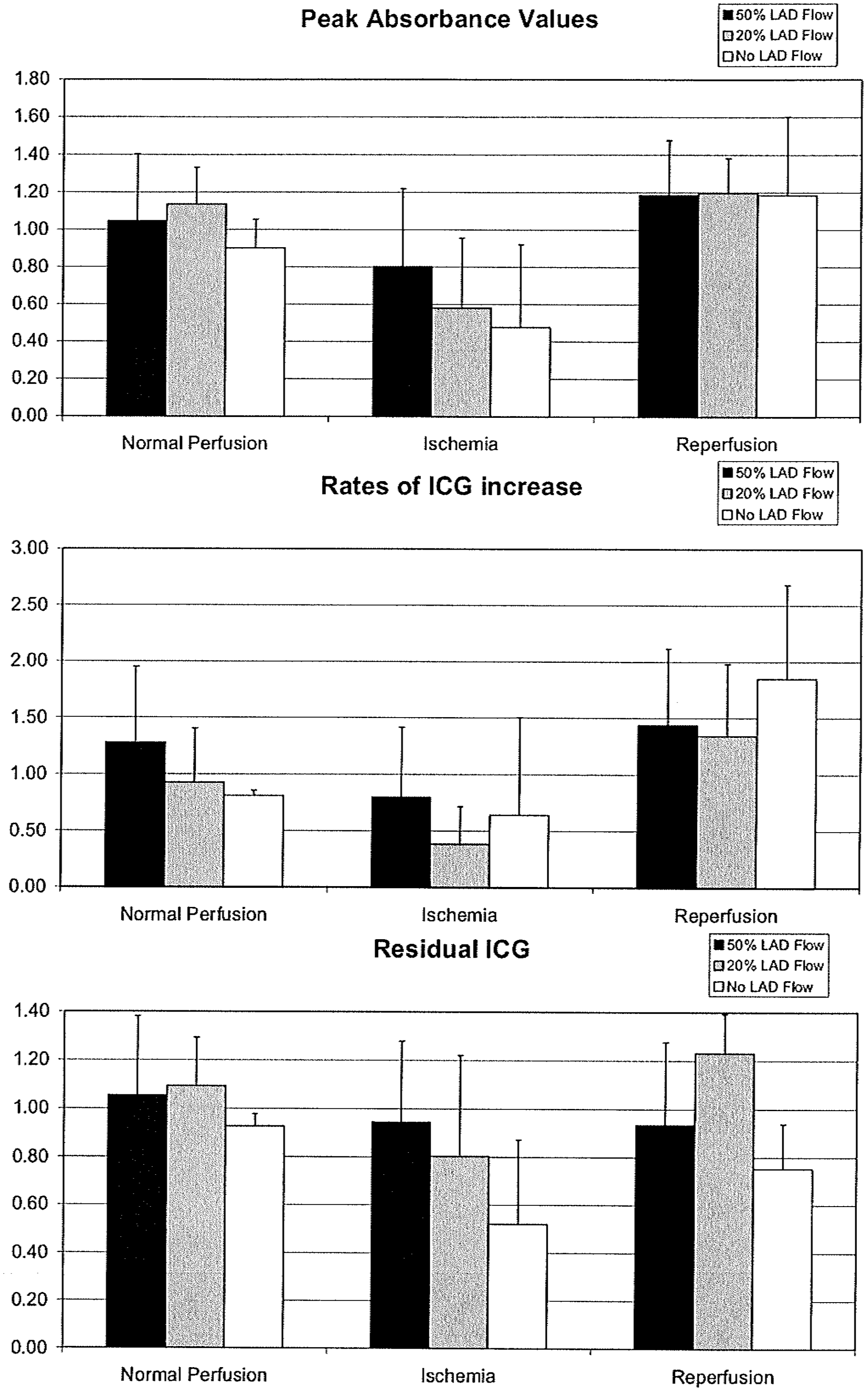

Figure 6.9. Effect of LAD occlusion severity on peak and residual ICG levels, and on the rate of ICG accumulation.

Each parameter derived for the area at risk was divided by the corresponding control value, and mean ratio values are presented in Figure 6.9. As expected, peak ICG levels in the area at risk (relative to the control area) were reduced during ischemia and restored upon reperfusion. Furthermore, the decline in peak ICG levels was more substantial during complete occlusion than during partial occlusion. It is also worthy of note that mean peak ICG levels were slightly higher during reperfusion than during normal perfusion for all three groups. This reflects vasodilation in the area at risk during ischemia (as suggested above) resulting in less dispersion of the ICG bolus in the vasculature during transit.

However, these comparisons should be interpreted with caution. The number of trials within each group is small (four with 50% flow, six with 20% flow, and ICG was used in only three of the no flow trials) and the variance within each group is high. For example, peak ICG levels during ischemia were only significantly different from the corresponding values during normal perfusion for the 20% flow trials ($p < 0.01$), despite the apparent differences in mean values for all groups. The corresponding differences between ischemia and reperfusion are significant only for 50% flow ($p < 0.05$) and 20% flow ($p < 0.01$). Nevertheless, significance (as determined by Sandler's A-test or Student's t-test) is difficult to attain for low sample sizes (indeed, the 20% flow group had more samples than the other groups).

The rate of ICG uptake decreased in parallel with the peak ICG concentration during ischemia. Although the differences (between normal perfusion and ischemia) were not statistically significant for any of the three groups, the uptake rate was significantly higher during reperfusion for both the 20% flow trials ($p < 0.05$) and the no flow trials ($p < 0.01$).

Finally, residual ICG levels for boli administered during ischemia were lower than corresponding values during normal perfusion, but the difference was again only significant for the 20% flow group ($p < 0.05$). Similarly, comparison of these values during ischemia and reperfusion also yielded a significant increase only for the 20% flow group ($p < 0.01$).

6.4. Conclusions

This study demonstrated the ability of spectroscopic imaging to detect regional myocardial ischemia in an intraoperative setting. The primary objective was to determine whether spectroscopic imaging could detect ischemic regions of tissue in a pseudo-surgical setting as effectively as in the isolated heart studies. This proved to be the case, and diagnosis of cardiac ischemia was nearly as straightforward here as in isolated hearts (although motion due to breathing made image analysis more complicated), and pooling of blood in the chest cavity also occasionally obscured imaging of tissue near the periphery of the heart. This study also sought to confirm the ability of spectroscopic imaging to differentiate between partial and total occlusion. While spectroscopic images were able to distinguish partial from complete occlusion clearly in isolated hearts, results were less clear-cut in the *in vivo* model.

The other main aim of this study was to visualize regional coronary flow using the intravascular contrast agent, indocyanine green (ICG). Capitalizing on the strong absorption band of ICG at 800 nm, ICG distribution was tracked with 1 s temporal resolution, This single-wavelength imaging approach was very effective in monitoring the wash-in and wash-out of ICG through the larger blood vessels and the capillaries. It proved more challenging to distinguish among the ICG transit rates observed for different degrees of arterial occlusion, and there was high variance in both peak ICG concentrations and in the rates of ICG accumulation among the hearts of each group. Overall, this study confirmed the value of spectroscopic imaging and the need for further studies in surgical settings.

7. Conclusions and Future Directions

7.1. Summary of Conclusions

The studies presented in this thesis have demonstrated the ability of near-infrared spectroscopic imaging (NIRSI) to identify and quantitatively assess regional ischemia in cardiac tissue by monitoring regional hemoglobin and myoglobin oxygenation. Two specific hypotheses were stated: first, that NIRSI can identify ischemic regions of cardiac tissue under surgical conditions; and second, that the technique can quantify the degree of ischemia. The results supported these hypotheses. However, in order for this technique to emerge as a clinically viable imaging modality, more work remains.

The first hypothesis was clearly validated. In arrested and beating, isolated hearts, NIRSI revealed oxygenation in regionally ischemic areas to be consistently and significantly lower than both pre-ischemia values (within the same region) and oxygenation in perfused tissue (adjacent to the ischemic region). The sensitivity of the method was maintained when time-saving protocols were implemented. For example, reduction of the number of sampled wavelengths did not impair the sensitivity of NIRSI, even to mild regional ischemia. The reduced data sets provided shorter acquisition times (1 min rather than 5 min) and hence more rapid detection of changes in blood and tissue oxygenation – a potentially critical factor for routine intraoperative use. These successes led to application of the technique under surgical conditions, and NIRSI continued to identify ischemic areas clearly, even with only a mild reduction in arterial flow.

Analysis of beating hearts was made possible by triggering image acquisition to the electrocardiogram (ECG), hence ensuring that the images were acquired at the same phase of the cardiac cycle. Spectra extracted from the spectroscopic images exhibited excellent signal-to-noise. While lung motion due to breathing caused some added heart motion in the *in vivo* study, this did not substantially reduce the spectral quality. Most significant in this context was the early finding that even in the presence of significant spectral noise, the fitting procedure used for data analysis still provided blood and tissue oxygenation with excellent precision.

While identification of the ischemic regions was clearly and readily achieved, accurate quantification was more challenging. For example, spectrally-derived tissue oxygenation values correlated well with the coronary flow rate within each group of isolated hearts independently, but oxygenation values in the two groups (at a particular flow rate) were not consistent with each other. For the *in vivo* study, oxygenation values clearly distinguished between tissue suffering from 50% vs. 20% normal perfusion, but no difference was found between oxygenation during 20% vs. 0% flow rates.

Oxygenation values under severely ischemic conditions were inconsistent with our expectations in that they did not fall to values near zero (in the last two studies). While the source of this apparent anomaly is not completely understood, it may reflect differences in Mb vs. Hb oxygenation, insufficient duration of ischemic episodes, problems in our assumptions underlying the spectral fitting algorithm, or a combination of the above. Repetition of the experiments with larger sample sizes (e.g. 10 per group) would help to clarify the sensitivity of the method in resolving degrees of ischemia severity and resolve the question of whether the observed variability reflects measurement noise or genuine variability among hearts in their response to ischemia.

Finally, the use of indocyanine green (ICG) as an intravascular contrast agent for assessment of coronary flow rates (capitalizing on its absorption band at 800 nm) was partially successful. Overall, passage of the ICG bolus through the vasculature was easily monitored with spectroscopic imaging, and arterial occlusion was clearly identified by the prevention of ICG transmission past the occlusion. The very slow penetration of ICG into the area at risk demonstrated the existence of small numbers of collateral vessels that connect the ischemic region with the normally perfused region. However, variation in the local flow rate did not consistently produce similar quantitative changes in the ICG distribution.

7.2. Future Directions

These studies show clear promise for the future of near-infrared spectroscopic cardiac imaging, and it is exciting to consider possible innovations that might improve the accuracy, precision, reliability, and applicability of spectroscopic imaging with the aim of implementing it in clinical settings. These advances are categorized here as technical improvements (both measurement and analysis), potential comparative studies of spectroscopic imaging to other imaging techniques, and long-term potential developments.

7.2.1. Improvements to Technique

While the studies described here show promising results, there are many ways in which the equipment, experimental methods, and analytical techniques might be improved. For instance, recent advances in optical equipment and computing hardware have made it possible to acquire complete spectroscopic images in one minute with the same image and spectral quality that previously required four. A number of further improvements to the analytical methods and experimental protocols are possible, as outlined below.

7.2.1.1. Experimental Methods

The studies reported in this thesis were conceived as proof-of-concept studies, deliberately designed to estimate the applicability of NIRSI to a variety of experimental conditions. Small trial sizes were deliberately used within each group, so as to increase the number of unique experiments. However, the small sizes of each group also limited the strength of the conclusions which could be drawn. The successes presented here suggest that further studies with larger groups are warranted, and provide the basis to estimate the appropriate group sizes.

To determine the group sizes required to achieve statistical significance, statistical power analysis may be applied.(46) Within this approach, the number of samples required is calculated from the desired power, p-value, and effect size.[96] For example, in the isolated, beating heart study, mean oxygenation values (Group I) within the area at risk during normal perfusion and 50% LAD flow were 0.90 and 0.85, respectively, and the standard deviations were approximately 0.04. Thus, the effect size is approximately 1.3. Given this effect size, the number of trials necessary for a power of 80% and a p-

---

[96] The power of the statistical test (given as a number between 0 and 1) is the probability that the test will detect the effect under study. Thus, the complement (1-power) is the rate of false negatives. In contrast, the p-value is the probability of detecting the effect where none exists (the rate of false positives). By convention, power and p-values of at least 0.8 and 0.05 are used as measures of significance. The effect size in a 2-group study (e.g. ischemic and control tissue) is defined as the ratio of the difference in means of the two groups to the standard deviation within each group.

value of 0.05 would be 9. A larger effect size (greater difference between means or smaller standard deviation within the groups) would also increase the power of the statistical analysis (for the same number of measurements). While groups of this size were not used, the effect sizes observed between the groups were still sufficiently large to provide p-values at or below 0.05 with a power of 0.8, demonstrating significance of these results.

Even given the sample sizes used here, the results provide the basis to suggest a number of experimental modifications. For example, analysis of deoxygenation kinetics in the isolated, beating heart study (Chapter 5) demonstrated that further information would have been gained from longer periods of total ischemia and reperfusion. Oxygenation of myoglobin and hemoglobin had not yet reached equilibrium after 10 min of total ischemia, and it remained unclear how low the oxygenation would have fallen had the period been extended. During the calibration tests of oxygenation values against blood sample data during global hypoxia (Section 5.4.4), the periods of hypoxia were also insufficient for oxygenation to reach equilibrium. These results may reflect differences in the responses of Hb and Mb to ischemia or hypoxia, and future studies may investigate this further.

For the study of oxygenation during partial ischemia (Chapter 5), LAD flow rates were decreased monotonically. While parallel trials with intermediate reperfusion established that oxygenation values associated with increasingly severe ischemia were not artificially depressed due to prolonged ischemia, changing the flow rate in a random fashion would have strengthened the case further. This would have been especially useful with larger groups.

In addition to monitoring heme protein oxygenation, it may also have been useful to monitor water content throughout each trial. Tissue water content could be obtained by exploiting the water absorption band at 970 nm and would allow assessment of edema. Spectroscopic imaging of water distribution in skin has been reported previously,(11,236) and application of this method to cardiac tissue would be straightforward. Hemoglobin/myoglobin measurements could also be normalized to water measurements (acquired spectroscopically) as a means of accounting for random variations in optical pathlength.

Finally, while this thesis has focused on application of spectroscopic imaging to the diagnosis of ischemia in heart tissue, the same approach might also prove useful for detection of cell death (necrosis) resulting from prolonged ischemia. One of the hallmarks of necrosis is disruption of the cellular membrane, allowing unrestricted transfer of both large and small molecules between the intracellular space and the extracellular space. For example, while myoglobin is normally confined to the intracellular space of muscle tissue, cell membrane disruption results in washout of myoglobin from the cellular space into the perfusate and hence a loss in the intensity of spectroscopic absorption bands of myoglobin. At the same time, it would be expected that an extracellular contrast agent such as Nd-DTPA (as used in Chapter 3) would accumulate in necrotic areas. Indeed, a recent study has demonstrated exactly these effects in isolated rat hearts, following both the accumulation of Nd and reduction of Mb resulting from cell membrane disruption.(177) We are currently investigating the possibility of applying this approach to spectroscopic imaging of regional cell membrane disruption in isolated pig hearts. This would provide a powerful complement to the detection of ischemia.

7.2.1.2. Analytical Methods

With regard to spectral interpretation, the acquired absorbance spectra were not perfectly fit by the algorithm used in this study. This residual error may have translated into errors in the fitting coefficient values, and hence in the tissue oxygenation values. The errors in the fit are likely due to problems in the assumptions underlying the algorithm. The Beer-Lambert Law is strictly valid only for non-interacting analytes in a non-scattering fluid. In these experiments, the tissue is highly scattering and there are multiple chromophores present. The highly scattering nature of tissue complicates the issue of optical pathlength, as discussed in Chapter 3. Although the wavelength-dependence of optical pathlength was considered, and attempts were made to account for it, the relative pathlength function that was used was strictly valid only for the optode geometry employed in deriving them.

In order to assess the wavelength-dependence as it influences the studies presented in Chapters 4-6, a similar study to that described in Chapter 3 but using the same experimental geometry employed in the subsequent imaging studies would be very useful. This would require perfusion of pig hearts with a hemoglobin-free blood substitute in which neodymium (Nd) was present at a sufficiently high concentration that the absorption bands appeared in the spectroscopic images.

Another factor complicating spectral analysis is chemical interaction of chromophores with the physiological environments. The most notable example is water, whose 970 nm absorption band appears substantially broader in *in vivo* spectra than in its absorptivity spectrum. This spectral broadening increases the error implicit in assuming that measured absorbance spectra can be expressed as weighted sums of the chromophore absorptivity spectra, and this effect may be comparable to variability of optical pathlength as a source of error.

Refinements to the spectral fitting algorithm taking the above factors into account might increase the accuracy of the derived fitting coefficients. Another possible refinement is placement of constraints on concentration values, based on physiological considerations. For instance, in well-oxygenated tissue, the algorithm occasionally returned negative values for the deoxy-Hb concentration. In this case, restriction of concentrations to non-negative values might increase the accuracy of values assigned to the other chromophores. Restriction of other coefficient values, such as that of water, to known concentration ranges in cardiac tissue might also improve the accuracy of the results.

7.2.2. Comparison with Other Techniques

The reliability of our quantitative analysis was limited by the lack of any accurate gold standard against which to compare the oxygenation estimates. Although results of calibration to blood sample data were promising (Section 5.4.4), these are of limited value. Because hemoglobin and myoglobin have substantially different p_{50} values (oxygen pressures at which they are half saturated), blood samples reflect neither the oxygenation of myoglobin nor the regional variations in hemoglobin and myoglobin oxygen saturation.

Techniques that have been used previously to highlight regional oxygenation in exposed cardiac tissue include phosphorescence quenching,(221,267) and nicotinamide adenine dinucleotide (NADH) fluorescence.(12,34,213) While phosphorescence quenching requires the addition of phosphorescent probes, NADH fluorescence gauges oxygenation by monitoring intracellular NADH levels[97].(12,34,213) Although observation of NADH fluorescence relies on visible light (limiting its penetration depth to the scale of millimetres), an interesting possibility does present itself. Since NADH fluorescence may be detected with similar equipment to that used in spectroscopic imaging, simultaneous application of both techniques may be straightforward. If the two imaging modalities were combined to investigate the kinetics of changes following ischemia and reperfusion, these studies might shed new light on the relative rates of change in heme protein oxygenation and NADH oxidation states.

As mentioned in the introduction, echocardiography is used routinely during coronary bypass operations to monitor heart wall thickness and motion. Thus, to establish the clinical relevance of regional oxygenation, a comparative study of the diagnostic and prognostic strengths and weaknesses of spectroscopic imaging and echocardiography would also be useful and interesting. Such a study might entail image acquisition with both modalities immediately after opening of the chest cavity (prior to any intervention on cardiac perfusion) and after completion of the bypass graft. Patients could be monitored following the operation, and both oxygenation and wall motion data

---

[97] Under normal conditions, the mitochondrial electron transport chain oxidizes NADH into NAD$^+$. When oxygen supply is low, the electron transport chain stops and NADH levels increase. See Sections 2.1.1.3 and 2.1.1.4.

subsequently compared against the stability of the graft and the patient's health following the surgery.

Since time is critical in coronary bypass operations, this type of study would require imaging equipment and software that allow for immediate data analysis and presentation of oxygenation maps shortly after image acquisition. Since images do not need to be acquired at every 10 nm, the number of acquired images can be reduced to nine or perhaps fewer.[98] The analysis involved in creating oxygenation maps is straightforward, and the total processing time for creation and display of oxygenation maps should not need to exceed one minute following image acquisition.

7.2.3. Long-Term Developments

While consideration of studies that may be performed in the near future is exciting, it is equally intriguing to speculate on longer term paths along which this technology might find itself in 10-20 years. Perhaps the most alluring is the possibility that spectroscopic imaging might not require exposure of the heart. Two possibilities are discussed here.

The first involves imaging through the ribcage and lung tissue. It is well-recognized that solid tissues such as the skull and ribcage are relatively transparent to near-infrared and visible light,(255)(p. 5 and cited references) and it has been argued that in near-IR spectroscopic studies of cerebral oxygenation, the skull contributes little to light absorption band and scattering *in vivo*.(54)(p. 1440) Since near-infrared point

---

[98] Another potential future study would be determination of the required number (and choice) of wavelengths at which images must be acquired, for effective monitoring of tissue oxygenation. It should also be recognized that as the number of sampling wavelengths decreases, the sensitivity to spectral noise also increases.

spectroscopy has been successfully applied to monitor cerebral oxygenation through the skull for many years,(58,160) it may prove possible to monitor cardiac blood and tissue oxygenation through the ribcage. A significant complication is the presence of the lungs; while the lung tissue and air sacs would not significantly absorb or scatter the light, the tissue is richly permeated with small blood vessels, which would absorb and scatter light significantly. However, intense light sources such as lasers may overcome this problem.

The second possibility piggybacks on the avalanche of minimally invasive techniques that have been developed over the last 10 years. For example, a recent report demonstrates the near-IR spectroscopic assessment of myocardial perfusion with a fibre optic catheter.(14) As cameras become smaller, it may prove possible to perform *in vivo* endoscopic imaging of myocardial oxygenation.

One final prospect that will be suggested here is that of three-dimensional imaging. Since near-infrared light penetrates several centimetres into tissue, the detected signals carry information regarding tissue oxygenation at various depths. With point spectroscopy, it is possible to probe varying tissue depths by making use of multiple light sources and/or detectors at varying distances from one another on the tissue surface (Figure 2.14); increased probe separation yields information from deeper tissue. It may be possible to implement an analogous approach with spectroscopic imaging. If a point source of light, for example, is placed against cardiac tissue, then absorbance data for tissue further from the source will reflect contributions of heme proteins deeper in the tissue than data for tissue nearer to the source. Expansion of this approach might allow for true, three-dimensional spectroscopic imaging.

It is an exhilerating venture to study a field in its infancy. It is a challenge to be sure, as the body of research and reference material upon which one might draw is limited; but there is also an increased degree of freedom, as the expanse of uncharted territory is vast. I sincerely hope that the work presented in this thesis represents only the first steps of a longer journey – that more research will be done to further expand the capabilities of NIRS imaging, that more development will improve its resolution and efficiency, and most importantly, that this technique will not stay in the research lab but rather become a clinically useful tool that will make a positive contribution to the state of health care around the world.

References

1. The changing face of heart disease and stroke in Canada. (Health Canada, Statistics Canada, Canadian Institute for Health Information, Canadian Cardiovascular Society, Canadian Stroke Society, Heart and Stroke Foundation of Canada, 1999).

2. Canada at a glance. (Statistics Canada, 2002).

3. Al-Saadi, N., Nagel, E., Gross, M., Bornstedt, A., Schnackenburg, B., Klein, C., Klimek, W., Oswald, H. & Fleck, E. Noninvasive detection of myocardial ischemia from perfusion reserve based on cardiovascular magnetic resonance. *Circulation* **101**, 1379-83 (2000).

4. Antonini, E. & Brunori, M. *Hemoglobin and myoglobin in their reactions with ligands* (North-Holland, Amsterdam, The Netherlands, 1971).

5. Arai, A. E., Kasserra, C. E., Territo, P. R., Gandjbakhche, A. H. & Balaban, R. S. Myocardial oxygenation in vivo: Optical spectroscopy of cytoplasmic myoglobin and mitochondrial cytochromes. *American Journal of Physiology* **277**, H683-97 (1999).

6. Arakaki, L. S. L. & Burns, D. H. Multispectral analysis for quantitative measurements of myoglobin oxygen fractional saturation in the presence of hemoglobin interference. *Applied Spectroscopy* **46**, 1919-1928 (1992).

7. Arridge, S. R., Schweiger, M., Hiraoka, M. & Delpy, D. T. A finite element approach for modeling photon transport in tissue. *Medical Physics* **20**, 299-309 (1993).

8. Arturson, G., Garby, L., Robert, M. & Zaar, B. The oxygen dissociation curve of normal human blood with special reference to the influence of physiological effector ligands. *Scandinavian Journal of Clinical Laboratory Investigations* **34**, 9-13 (1974).

9. Ashraf, M. & Sybers, H. D. Scanning electron microscopy of the heart after coronary occlusion. *Laboratory Investigations* **32**, 157-162 (1975).

10. Atkins, P. W. *Physical chemistry* (Freeman and Co., New York, 1994).

11. Attas, M., Hewko, M., Payette, J., Posthumus, T., Sowa, M. & Mantsch, H. Visualization of cutaneous hemoglobin oxygenation and skin hydration using near-infrared spectroscopic imaging. *Skin Research and Technology* **7**, 238-245 (2001).

12. Barlow, C. H., Rorvik, D. A. & Kelly, J. J. Imaging epicardial oxygen. *Annals of Biomedical Engineering* **26**, 76-85 (1998).

13. Bassingthwaighte, J. B. The myocardial cell. In *Cardiology: Fundamentals and practice* (eds. Giuliani, E. R., Fuster, V., Gersh, B. J., McGoon, M. D. & McGoon, D. C.) 113-149 (Mosby, St. Louis, 1991).

14. Baykut, D., Gebhard, M. M., Bolukoglu, H., Kadipasaoglu, K., Hennes, S., Frazier, O. H. & Krian, A. Online detection of myocardial ischemia by near infrared spectroscopy with a fiberoptic catheter. *Thoracic and Cardiovascular Surgery* **49**, 162-166 (2001).

15. Beer, A. *Annalen der Physik und Chemie* **163**, 78 (1852).

16. Beinert, H., Shaw, R. W., Hansen, R. E. & Hartzell, C. R. Studies on the origin of the near-infrared (800-900 nm) absorption of cytochrome c oxidase. *Biochimica Biophysica Acta* **591**, 458-70 (1980).

17. Benaron, D. A., Kurth, C. D., Steven, J., Wagerle, L. C., Chance, B. & Delivoria-Papadopoulos, M. Non-invasive estimation of cerebral oxygenation and oxygen consumption using phase-shift spectroscopy. *IEEE Engineering in Medicine and Biology Society* **12**, 2004-2006 (1990).

18. Benaron, D. A., Kurth, C. D., Steven, J. M., Delivoria-Papadopoulos, M. & Chance, B. Transcranial optical path length in infants by near-infrared phase-shift spectroscopy. *Journal of Clinical Monitoring* **11**, 109-17 (1995).

19. Benaron, D. A. & Stevenson, D. K. Optical time-of-flight and absorbance imaging of biologic media. *Science* **259**, 1463-6 (1993).

20. Benaron, D. A. & Stevenson, D. K. Resolution of near infrared time-of-flight brain oxygenation imaging. In *Oxygen transport to tissue xv* (ed. Vaupel, P. e. a.) 609-617 (Plenum Press, New York, 1994).

21. Benesch, R. & Benesch, R. E. The effect of organic phosphates from the human erythrocyte on the allosteric properties of hemoglobin. *Biochemical and Biophysical Research Communications* **26**, 162-167 (1967).

22. Bert, P. La pression barométrique. *Recherches de Physiologie Expérimentale*, 691 (1878).

23. Bichat, X. *Allgemeine anatomie, angewandt auf die physiologie und arzneywissenshaft. Ii.* (J.L.Crusius, Leipzig, 1803).

24. Bjure, J. & Nilsson, N. J. Spectrophotometric determination of oxygen saturation of hemoglobin in the presence of carboxyhemoglobin. *Scandinavian Journal of Clinical Laboratory Investigations* **17**, 491-500 (1965).

25. Bloor, C. M., White, F. C. & Roth, D. M. The pig as a model of myocardial ischemia and gradual coronary artery occlusion. In *Swine as models in biomedical research* (eds. Swindle, M. M., Moody, D. C. & Philips, L. D.) 163-175 (Iowa State University Press, Ames, 1992).

26. Bohr, C. Theoretische behandlung der quantitativen verhältnis bei der sauerstoffaufnahme des hämoglobins. *Zentralblatt für Physiologie* **17**, 682 (1904).

27. Bohr, C., Hasselbalch, K. & Krogh, A. Ueber einen in biologischer beziehung wichtigen einfluss, den die kohlensäurespannung des blutes auf dessen sauerstoffbindung übt. *Skandinavische Archiven der Physiologie* **16**, 402 (1904).

28. Bohren, C. F. & Huffman, D. R. *Absorption and scattering of light by small particles* (Wiley, New York, 1983).

29. Bolli, R., Patel, B. S., Jeroudi, M. O., Lai, E. K. & McCay, P. B. Demonstration of free radical generation in "stunned" myocardium of intact dogs with the use of the spin trap alpha-phenyl n-tert-butyl nitrone. *Journal of Clinical Investigations* **82**, 476-85 (1988).

30. Braasch, W., Gudbjarnason, S., Puri, P. S., Ravens, K. G. & Bing, R. J. Early changes in energy metabolism in the myocardium following acute coronary artery occlusion in anesthetized dogs. *Circulation Research* **23**, 429-438 (1968).

31. Braun, C. L. & Smirnov, S. N. Why is water blue? *Journal of Chemical Education* **70**, 612 (1993).

32. Braun, C. L. & Smirnov, S. N. Why is water blue? Retrieved 6 March, 2003 from http://www.dartmouth.edu/~etrnsfer/water.htm. (Updated 9 April 1997).

33. Braunwald, E., Ross, J. J. & Sonnenblick, E. H. Mechanisms of contraction of the normal and failing heart. *New England Journal of Medicine* **277**, 794-799 (1967).

34. Bruining, H. A., Pierik, G. J., Ince, C. & Ashruf, F. Optical spectroscopic imaging for non-invasive evaluation of tissue oxygenation. *Chirurgie Memoires de l'Academie de Chirurgie* **118**, 317-322 (1992).

35. Brunori, M., Noble, R. W., Antonini, E. & Wyman, J. The reactions of the isolated alpha and beta chains of human hemoglobin with oxygen and carbon monoxide. *Journal of Biological Chemistry* **241**, 5238-5243 (1966).

36. Bunn, H. F., Forget, B. G. & Ranney, H. M. *Human hemoglobins* (Saunders, Philadelphia, 1977).

37. Care, Canadian Council on Animal. *Guide to the care and use of experimental animals* (ed. McWilliam, A. A.) (Bradda Printing Services, Ottawa, 1993).

38. Caro, C. G., Doorly, D. J., Tarnawski, M., Scott, K. T., Long, Q. & Dumoulin, C. L. Non-planar geometry and non-planar-type flow at sites of arterial curvature and branching. In *Biological flow* (eds. Jaffrin, M. & Caro, C.) 69-81 (Plenum, New York, 1995).

39. Chance, B. & Leigh, J. S., Jr. Oxygen intermediates and mixed valence states of cytochrome oxidase: Infrared absorption difference spectra of compounds a, b, and c of cytochrome oxidase and oxygen. *Proceedings of the National Academy of Sciences of the United States of America* **74**, 4777-4780 (1977).

40. Chanutin, A. & Curnish, R. R. Effect of organic and inorganic phosphates on the oxygen equilibrium of human erythrocytes. *Archives of Biochemistry and Biophysics* **121**, 96-102 (1967).

41. Cheng, Y., Li, Y., Li, R. C., Lu, J. F. & Wang, K. Orally administrated cerium chloride induces the conformational changes of rat hemoglobin, the hydrolysis of 2,3-dpg and the oxidation of heme-fe(ii), leading to changes of oxygen affinity. *Chemico Biological Interactions* **125**, 191-208 (2000).

42. Chien, K. R., Han, A., Sen, A., Buja, L. M. & Willerson, J. T. Accumulation of unesterified arachidonic acid in ischemic canine myocardium. Relationship to a phosphatidylcholine deacylation-reacylation cycle and the depletion of membrane phospholipids. *Circulation Research* **54**, 313-322 (1984).

43. Christiansen, J., Douglas, C. G. & Haldane, J. S. *Journal of Physiology* **48**, 244 (1914).

44. Clore, G. M. & Chance, E. M. Low-temperature kinetics of the reactions of fully reduced membrane-bound cytochrome oxidase with oxygen in the soret, alpha and near-infrared regions. *Biochemistry Journal* **177**, 613-21 (1979).

45. Cobbe, S. M. & Poole-Wilson, P. A. The time of onset and severity of acidosis in myocardial ischaemia. *Journal of Molecular and Cellular Cardiology* **12**, 745-760 (1980).

46. Cohen, J. *Statistical power analysis for the behavioral sciences* (L. Erlbaum Associates, Hillsdale, N.J., 1988).

47. Cohen, M. V. *Coronary collaterals: Clinical and experimental observations* (Futura, New York, 1985).

48. Coin, J. T. & Olson, J. S. The rate of oxygen uptake by human red blood cells. *Journal of Biological Chemistry* **254**, 1178-90 (1979).

49. Collan, Y., McDowell, E. & Trump, B. F. Studies on the pathogenesis of ischemic cell injury. Vi. Mitochondrial flocculent densities in autolysis. *Virchows Archiv B, Cell Pathology including Molecular Pathology* **35**, 189-99 (1981).

50. Conn, H. L. J., Wood, J. C. & Morales, G. S. Rate of change in myocardial glycogen and lactic acid following arrest of coronary circulation. *Circulation Research* **7**, 721-727 (1959).

51. Cotton, F. A. & Wilkinson, G. *Advanced inorganic chemistry: A comprehensive text* (Interscience Publishers, New York, 1972).

52. de Groot, B., Zuurbier, C. J. & van Beek, J. H. Dynamics of tissue oxygenation in isolated rabbit heart as measured with near-infrared spectroscopy. *American Journal of Physiology* **276**, H1616-H1624 (1999).

53. Delpy, D. T. & Cope, M. Quantification in tissue near-infrared spectroscopy. *Philosophical Transactions of the Royal Society of London B Biological Sciences* **352**, 649-659 (1997).

54. Delpy, D. T., Cope, M., van der Zee, P., Arridge, S., Wray, S. & Wyatt, J. Estimation of optical pathlength through tissue from direct time of flight measurement. *Physics in Medicine and Biology* **33**, 1433-1442 (1988).

55. Dodge, H. T. & Sheehan, F. H. Quantitative angiographic techniques. In *The heart and cardiovascular system* (eds. Fozzard, H. A., Haber, E., Jennings, R. B., Katz, A. M. & Morgan, H. E.) 725-744 (Raven, New York, 1992).

56. Douglas, J. F., Gasiorek, J. M. & Swaffield, J. A. *Fluid mechanics* (Pitman Pub., London, 1985).

57. Duhm, J. Dual effect of 2,3-diphosphoglycerate on the bohr effects of human blood. *Pflügers Archiv European Journal of Physiology* **363**, 55-60 (1976).

58. Duncan, A., Meek, J. H., Clemence, M., Elwell, C. E., Fallon, P., Tyszczuk, L., Cope, M. & Delpy, D. T. Measurement of cranial optical path length as a function of age using phase resolved near infrared spectroscopy. *Pediatric Research* **39**, 889-94 (1996).

59. Duncan, A., Meek, J. H., Clemence, M., Elwell, C. E., Tyszczuk, L., Cope, M. & Delpy, D. T. Optical pathlength measurements on adult head, calf and forearm and the head of the newborn infant using phase resolved optical spectroscopy. *Physics in Medicine and Biology* **40**, 295-304 (1995).

60. Eaton, W. A., Hanson, L. K., Stephens, P. J., Sutherland, J. C. & Dunn, J. B. R. Optical spectra of oxy- and deoxyhemoglobin. *Journal of the American Chemical Society* **100**, 4991-5003 (1978).

61. Edwards, W. D. Applied anatomy of the heart. In *Cardiology: Fundamentals and practice* (eds. Giuliani, E. R., Fuster, V., Gersh, B. J., McGoon, M. D. & McGoon, D. C.) 47-112 (Mosby, St. Louis, 1991).

62. Eicher, H. & Trautwein, A. Electronic structure and quadupole splittings of ferrous iron in hemoglobin. *Journal of Chemical Physics* **50**, 2540-2551 (1969).

63. Elbeery, J. R., Brown, P. M. & Chitwood, W. R., Jr. Intraoperative midcabg arteriography via the left radial artery: A comparison with doppler ultrasound for assessment of graft patency. *Annals of Thoracic Surgery* **66**, 51-55 (1998).

64. Engelmann, M. G., Knez, A., von Smekal, A., Wintersperger, B. J., Huehns, T. Y., Hofling, B., Reiser, M. F. & Steinbeck, G. Non-invasive coronary bypass graft imaging after multivessel revascularisation. *International Journal of Cardiology* **76**, 65-74 (2000).

65. Essenpreis, M., Elwell, C. E., Cope, M., van der Zee, P., Arridge, S. & Delpy, D. T. Spectral dependence of temporal point spread functions in human tissues. *Applied Optics* **32**, 418-425 (1993).

66. Farrell, T. J., Patterson, M. S. & Wilson, B. A diffusion theory model of spatially resolved, steady-state diffuse reflectance for the noninvasive determination of tissue optical properties in vivo. *Medical Physics* **19**, 879-888 (1992).

67. Fawcett, D. W. & McNutt, N. S. The ultrastructure of the cat myocardium. I. Ventricular papillary muscle. *Journal of Cell Biology* **42**, 1-45 (1969).

68. Federspiel, W. J. & Popel, A. S. A theoretical analysis of the effect of the particulate nature of blood on oxygen release in capillaries. *Microvascular Research* **32**, 164-189 (1986).

69. Fishbein, M. C., Meerbaum, S., Rit, J., Lando, U., Kanmatsuse, K., Mercier, J. C., Corday, E. & Ganz, W. Early phase acute myocardial infarct size quantification: Validation of the triphenyl tetrazolium chloride tissue enzyme staining technique. *American Heart Journal* **101**, 593-600 (1981).

70. Forbes, M. S. & Sperelakis, N. Ultrastructure of mammalian cardiac muscle. In *Physiology and pathophysiology of the heart* (ed. Sperelakis, N.) 3-41 (Kluwer, Boston, 1989).

71. Foundation, Heart and Stroke. Coronary artery disease. Retrieved Feb 6, 2003 from http://ww1.heartandstroke.ca/Page.asp?PageID=1613&ContentID=175&ContentTypeID=1. (Updated Sept 20, 2001).

72. Frackowiak, D., Planner, A. & Wiktorowicz, K. Near-infrared applications in medicine. In *Near-infrared applications in biotechnology* (ed. Raghavachari, R.) 151-183 (Marcel Dekker, New York, 2001).

73. Franceschini, M. A., Toronov, V., Filiaci, M. E., Gratton, E. & Fantini, S. On-line optical imaging of the human brain with 160-ms temporal resolution. *Optics Express* **6**, 49-57 (2000).

74. Frederiks, W. M., Schellens, J. P., Marx, F., Bosch, K. S. & Vreeling-Sindelarova, H. Histochemical detection of glycogen phosphorylase activity as parameter for early ischemic damage in rat heart. *Basic Research in Cardiology* **88**, 130-40 (1993).

75. Freeman, B. A. & Crapo, J. D. Biology of disease: Free radicals and tissue injury. *Laboratory Investigations* **47**, 412-426 (1982).

76. Freund, J. E. *Mathematical statistics* (Prentice-Hall, Englewood Cliffs, NJ, 1992).

77. Fridovich, I. Biological effects of the superoxide radical. *Archives of Biochemistry and Biophysics* **240**, 500-508 (1985).

78. Fuller, W., Parmar, V., Eaton, P., Bell, J. R. & Shattock, M. J. Cardiac ischemia causes inhibition of the na/k atpase by a labile cytosolic compound whose production is linked to oxidant stress. *Cardiovascular Research* **57**, 1044-1051 (2003).

79. Fung, Y. C. *Biomechanics: Circulation* (Springer, New York, 1997).

80. Gandjbakhche, A. H., Bonner, R. F., Arai, A. E. & Balaban, R. S. Visible-light photon migration through myocardium in vivo. *American Journal of Physiology* **277**, H698-704 (1999).

81. Ganote, C. E. & Vander Heide, R. S. Irreversible injury of isolated adult rat myocytes. Osmotic fragility during metabolic inhibition. *American Journal of Pathology* **132**, 212-222 (1988).

82. Garratt, K. N. & Morgan, J. P. Coronary circulation: Pathophysiology of myocardial ischemia and reperfusion. In *Cardiology: Fundamentals and practice* (eds. Giuliani, E. R., Fuster, V., Gersh, B. J., McGoon, M. D. & McGoon, D. C.) 1150-1158 (Mosby, St. Louis, 1991).

83. Gayeski, T. E. & Honig, C. R. Intracellular po2 in individual cardiac myocytes in dogs, cats, rabbits, ferrets, and rats. *American Journal of Physiology* **260**, H522-H531 (1991).

84. Giannini, I., Ferrari, M., Carpi, A. & Fasella, P. Rat brain monitoring by near-infrared spectroscopy: An assessment of possible clinical significance. *Physiological Chemistry and Physics* **14**, 295-305 (1982).

85. Goldin, J. G., Ratib, O. & Aberle, D. R. Contemporary cardiac imaging: An overview. *Journal of Thoracic Imaging* **15**, 218-229 (2000).

86. Goldstein, M. A. & Murphy, D. L. A morphometric analysis of ischemic canine myocardium with and without reperfusion. *Journal of Molecular and Cellular Cardiology* **15**, 325-334 (1983).

87. Gouterman, M. Study of the effects of substitution on the absorption spectra of porphin. *Journal of Chemical Physics* **30**, 1139-1161 (1959).

88. Gratton, G., Goodman Wood, M. R. & Fabiani, M. Comparison of neuronal and hemodynamic measures of the brain response to visual stimulation: An optical imaging study. *Human Brain Mapping* **13**, 13-25 (2001).

89. Griffith, J. S. On the magnetic properties of some haemoglobin complexes. *Proceedings of the Royal Society (London)* **235A**, 23-36 (1956).

90. Grinwald, P. M. Calcium uptake during post-ischemic reperfusion in the isolated rat heart: Influence of extracellular sodium. *Journal of Molecular and Cellular Cardiology* **14**, 359-365 (1982).

91. Gründeman, R., de Beer, E. & Schiereck, P. Contraction mechanism in striated muscle. In *The physics of heart and circulation* (eds. Strackee, J. & Westerhof, N.) 121-152 (Institute of Physics, Bristol, 1993).

92. Guyton, A. C. *Textbook of medical physiology* (W.B. Saunders, Philadelphia, 1971).

93. Hale, G. M. & Querry, M. R. Optical constants of water in the 200 nm to 200 μm wavelength region. *Applied Optics* **12**, 555-563 (1973).

94. Harden, W. R., 3rd, Barlow, C. H., Simson, M. B. & Harken, A. H. Temporal relation between onset of cell anoxia and ischemic contractile failure. Myocardial ischemia and left ventricular failure in the isolated, perfused rabbit heart. *American Journal of Cardiology* **44**, 741-746 (1979).

95. Harris, C. R. S. *The heart and the vascular system in ancient greek medicine* (Clarendon, Oxford, 1973).

96. Harvey, W. *Exercitatio anatomica. De motu cordis et sanguinis in animalibus* (Charles C. Thomas, Springfield, IL, 1928).

97. Hastings, A. B., White, F. C., Sanders, T. M. & Bloor, C. M. Comparative physiological responses to exercise stress. *Journal of Applied Physiology* **52**, 1077-1083 (1982).

98. Hellums, J. D. The resistance to oxygen transport in the capillaries relative to that in the surrounding tissue. *Microvascular Research* **13**, 131-136 (1977).

99. Herschel, W. Experiments on the refrangibility of the invisible rays of the sun. *Philosophical Transactions of the Royal Society of London A* **90**, 284-292 (1800).

100. Hill, A. V. The possible effects of the aggregation of the molecules of haemoglobin on its dissociation current. *Journal of Physiology* **40**, iv-vii (1910).

101. Hill, J. L. & Gettes, L. S. Effect of acute coronary artery occlusion on local myocardial extracellular k+ activity in swine. *Circulation* **61**, 768-778 (1980).

102. Honig, C. R., Gayeski, T. E., Federspiel, W., Clark, A., Jr. & Clark, P. Muscle o2 gradients from hemoglobin to cytochrome: New concepts, new complexities. *Advances in Experimental Medicine and Biology* **169**, 23-38 (1984).

103. Hoppe-Seyler, F. Ueber die chemischen und optischen eigenschaften des blutfarbstoffs. *Virchows Archiv für Pathologische Anatomie* **29**, 233 (1864).

104. Hüfner, G. Uber die tension des sauerstoffes im blute und in oxyhämoglobinlösungen. *Zeitung der Physikalische Chemie* **13**, 285-291 (1889).

105. Huntington, H. B. Diffusion. In *Encyclopedia of physics* (eds. Lerner, R. G. & Trigg, G. L.) 255-257 (VCH, New York, 1991).

106. Huxley, V. H. & Kutchai, H. The effect of the red cell membrane and a diffusion boundary layer on the rate of oxygen uptake by human erythrocytes. *Journal of Physiology* **316**, 75-83 (1981).

107. Huynh, B. H., Papaefthymiou, G. C., Yen, C. S., Groves, J. L. & Wu, C. S. Electronic structure of fe/sup 2+/ in normal human hemoglobin and its isolated subunits. *Journal of Chemical Physics* **61**, 3750-3758 (1974).

108. Isobe, K., Kusaka, T., Nagano, K., Okubo, K., Yasuda, S., Kondo, M., Itoh, S. & Onishi, S. Functional imaging of the brain in sedated newborn infants using near infrared topography during passive knee movement. *Neuroscience Letters* **299**, 221-224 (2001).

109. Jacobus, W. E., Pores, I. H., Lucas, S. K., Weisfeldt, M. L. & Flaherty, J. T. Intracellular acidosis and contractility in the normal and ischemic heart as examined by 31p nmr. *Journal of Molecular and Cellular Cardiology* **14 Suppl 3**, 13-20 (1982).

110. Jenkins, F. A. & White, H. E. *Fundamentals of optics* (McGraw-Hill, New York, 1976).

111. Jennings, R. B., Hawkins, H. K., Lowe, J. E., Hill, M. L., Klotman, S. & Reimer, K. A. Relation between high energy phosphate and lethal injury in myocardial ischemia in the dog. *American Journal of Pathology* **92**, 187-214 (1978).

112. Jennings, R. B. & Morgan, H. E. Strategy of experiment design in metabolic experiments. In *The heart and cardiovascular system* (eds. Fozzard, H. A., Haber, E., Jennings, R. B., Katz, A. M. & Morgan, H. E.) 367-383 (Raven, New York, 1992).

113. Jennings, R. B., Murry, C. E., Steenbergen, C. & Reimer, K. A. The acute phase of regional ischemia. In *Acute myocardial infarction: Emerging concepts of pathogenesis and treatment* (ed. Cox, R. H.) 67-84 (Praeger, New York, 1989).

114. Jennings, R. B., Reimer, K. A., Hill, M. L. & Mayer, S. E. Total ischemia in dog hearts, in vitro. 1. Comparison of high energy phosphate production, utilization, and depletion, and of adenine nucleotide catabolism in total ischemia in vitro vs. Severe ischemia in vivo. *Circulation Research* **49**, 892-900 (1981).

115. Jennings, R. B., Reimer, K. A. & Steenbergen, C. Myocardial ischemia revisited. The osmolar load, membrane damage, and reperfusion. *Journal of Molecular and Cellular Cardiology* **18**, 769-780 (1986).

116. Jennings, R. B., Reimer, K. A. & Steenbergen, C. Effect of inhibition of the mitochondrial atpase on net myocardial atp in total ischemia. *Journal of Molecular and Cellular Cardiology* **23**, 1383-1395 (1991).

117. Jennings, R. B., Schaper, J., Hill, M. L., Steenbergen, C., Jr. & Reimer, K. A. Effect of reperfusion late in the phase of reversible ischemic injury. Changes in cell volume, electrolytes, metabolites, and ultrastructure. *Circulation Research* **56**, 262-278 (1985).

118. Jöbsis, F. F. Noninvasive, infrared monitoring of cerebral and myocardial oxygen sufficiency and circulatory parameters. *Science* **198**, 1264-1267 (1977).

119. Jobsis vanderVliet, F. F. Discovery of the near-infrared window into the body and the early development of near-infrared spectroscopy. *Journal of Biomedical Optics* **4**, 392-396 (1999).

120. Jones, C. E., Thomas, J. X., Parker, J. C. & Parker, R. E. Acute changes in high energy phosphates, nucleotide derivatives, and contractile force in ischaemic and nonischaemic canine myocardium following coronary occlusion. *Cardiovascular Research* **10**, 275-282 (1976).

121. Jung, C., Friedrich, J. & Ristau, O. Quantum chemical interpretation of the spectral properties of the co and o_2 complexes of hemoglobin and cytochrome p-450. *Acta Biologica et Medica Germanica* **38**, 363-377 (1979).

122. Kagen, L. J. *Myoglobin: Biochemical, physiological and clinical aspects* (Columbia University Press, New York, 1973).

123. Kanaide, H., Yoshimura, R., Makino, N. & Nakamura, M. Regional myocardial function and metabolism during acute coronary artery occlusion. *American Journal of Physiology* **242**, H980-H989 (1982).

124. Kassab, L. R. P., Courrol, L. C., Wetter, N. U., Tatumi, S. H. & Mendes, C. M. S. P. Glasses of heavy metal and gallium oxides doped with neodymium. *Radiation Effects and Defects in Solids* **156**, 371-375 (2001).

125. Kawasuji, M., Tomita, S., Yasuda, T., Sakakibara, N., Takemura, H. & Watanabe, Y. Myocardial oxygenation during terminal warm blood cardioplegia. *Annals of Thoracic Surgery* **65**, 1260-1264 (1998).

126. Kemp, D. S. & Vellaccio, F. *Organic chemistry* (Worth, New York, 1980).

127. Kerker, M. *The scattering of light: And other electromagnetic radiation* (Academic Press, New York, 1969).

128. Kihara, Y., Grossman, W. & Morgan, J. P. Direct measurement of changes in intracellular calcium transients during hypoxia, ischemia, and reperfusion of the intact mammalian heart. *Circulation Research* **65**, 1029-1044 (1989).

129. Klassen, L. M., MacIntosh, B. J. & Menon, R. S. Influence of hypoxia on wavelength dependence of differential pathlength and near-infrared quantification. *Physics in Medicine and Biology* **47**, 1573-1589 (2002).

130. Kleber, A. G. Resting membrane potential, extracellular potassium activity, and intracellular sodium activity during acute global ischemia in isolated perfused guinea pig hearts. *Circulation Research* **52**, 442-450 (1983).

131. Kleber, A. G. Extracellular potassium accumulation in acute myocardial ischemia. *Journal of Molecular and Cellular Cardiology* **16**, 389-394 (1984).

132. Kohl, M., Nolte, C., Heekeren, H. R., Horst, S., Scholz, U., Obrig, H. & Villringer, A. Determination of the wavelength dependence of the differential pathlength factor from near-infrared pulse signals. *Physics in Medicine and Biology* **43**, 1771-1782 (1998).

133. Kopelovich, O. V. Optical properties of pure water in the 250 - 600nm range. *Optical Spectroscopy* **41**, 391-392 (1976).

134. Koretsune, Y. & Marban, E. Mechanism of ischemic contracture in ferret hearts: Relative roles of [ca2+]i elevation and atp depletion. *American Journal of Physiology* **258**, H9-H16 (1990).

135. Kou, L., Labrie, D. & Chylek, P. Refractive indices of water and ice in the 0.65 - 2.5 μm spectral range. *Applied Optics* **32**, 3531-3540 (1993).

136. Krogh, A. The number and distribution of capillaries in muscles with calculation of the oxygen pressure head necessary for supplying the tissue. *Journal of Physiology* **52**, 409-415 (1919).

137. Kubler, W. & Spieckermann, P. G. Regulation of glycolysis in the ischemic and the anoxic myocardium. *Journal of Molecular and Cellular Cardiology* **1**, 351-377 (1970).

138. Kühne, W. Ueber den farbstoff der muskeln. *Virchows Archiv für Pathologische Anatomie* **33**, 79 (1865).

139. Kupriyanov, V. V., Shaw, R. A., Xiang, B., Mantsch, H. & Deslauriers, R. Oxygen regulation of energy metabolism in isolated pig hearts: A near-ir spectroscopy study. *Journal of Molecular and Cellular Cardiology* **29**, 2431-2439 (1997).

140. Kupriyanov, V. V., Xiang, B., Butler, K. W., St Jean, M. & Deslauriers, R. Energy metabolism, intracellular na+ and contractile function in isolated pig and rat hearts during cardioplegic ischemia and reperfusion: 23na- and 31p-nmr studies. *Basic Research in Cardiology* **90**, 220-233 (1995).

141. Kusuoka, H., Porterfield, J. K., Weisman, H. F., Weisfeldt, M. L. & Marban, E. Pathophysiology and pathogenesis of stunned myocardium. Depressed ca2+ activation of contraction as a consequence of reperfusion-induced cellular calcium overload in ferret hearts. *Journal of Clinical Investigations* **79**, 950-961 (1987).

142. Lai, F. & Scheuer, J. Early changes in myocardial hypoxia: Relations between mechanical function, pH and intracellular compartmental metabolites. *Journal of Molecular and Cellular Cardiology* **7**, 289-303 (1975).

143. Landau, L. D. & Lifshitz, E. M. *Fluid mechanics* (ed. Landau, L. D.) (Pergamon Press, London, 1959).

144. Lange, R., Kloner, R. A., Zierler, M., Carlson, N., Seiler, M. & Khuri, S. F. Time course of ischemic alterations during normothermic and hypothermic arrest and its reflection by on-line monitoring of tissue pH. *Journal of Thoracic and Cardiovascular Surgery* **86**, 418-434 (1983).

145. Lazdunski, M., Frelin, C. & Vigne, P. The sodium/hydrogen exchange system in cardiac cells: Its biochemical and pharmacological properties and its role in regulating internal concentrations of sodium and internal pH. *Journal of Molecular and Cellular Cardiology* **17**, 1029-1042 (1985).

146. Lee, J. A. & Allen, D. G. Mechanisms of acute ischemic contractile failure of the heart. Role of intracellular calcium. *Journal of Clinical Investigations* **88**, 361-367 (1991).

147. Lemberg, R. & Legge, J. *Hematin compounds and bile pigments: Their constitution, metabolism, and function* (Interscience Publishers, New York, 1949).

148. Leonardi, L., Sowa, M. G., Payette, J. R. & Mantsch, H. H. Near-infrared spectroscopy and imaging: A new approach to assess burn injuries. *American Clinical Laboratory* **19**, 20-22 (2000).

149. Levine, I. N. *Quantum chemistry* (Prentice Hall, Upper Saddle River, N.J., 2000).

150. Lewandowski, E. D. & Ingwall, J. S. The physiological chemistry of energy production in the heart. In *Hurst's the heart* (eds. Schlant, R. C., Alexander, R. W., O'Rourke, R. A., Roberts, R. & Sonnenblick, E. H.) 153-164 (McGraw-Hill, New York, 1994).

151. Logan, S. E. On the fluid mechanics of human coronary artery stenosis. *IEEE Transactions on Biomedical Engineering* **22**, 327-334 (1975).

152. Longuet-Higgins, H. C., Rector, C. W. & Platt, J. R. Molecular orbital calculations on porphine and tetrahydroporphine. *Journal of Chemical Physics* **18**, 1174-1181 (1950).

153. Lothian, G. F. *Absorption spectrophotometry* (Hilger, London, 1969).

154. Lu, T.-H., Panneerselvam, K., Liaw, Y.-C., Kan, P. & Lee, C.-J. Structure determination of porcine hemoglobin. *Acta Crystallographica* **D56**, 304-312 (2000).

155. Maki, A., Yamashita, Y., Ito, Y., Watanabe, E., Mayanagi, Y. & Koizumi, H. Spatial and temporal analysis of human motor activity using noninvasive nir topography. *Medical Physics* **22**, 1997-2005 (1995).

156. Makino, N., Kanaide, H., Yoshimura, R. & Nakamura, M. Myoglobin oxygenation remains constant during the cardiac cycle. *American Journal of Physiology* **245**, H237-H243 (1983).

157. Mancini, D. M., Bolinger, L., Li, H., Kendrick, K., Chance, B. & Wilson, J. R. Validation of near-infrared spectroscopy in humans. *Journal of Applied Physiology* **77**, 2740-2747 (1994).

158. Mansfield, J. R., Sowa, M. G., Payette, J. R., Abdulrauf, B., Stranc, M. F. & Mantsch, H. H. Tissue viability by multispectral near infrared imaging: A fuzzy c-means clustering analysis. *IEEE Transactions on Medical Imaging* **17**, 1011-1018 (1998).

159. Marshall, S. A., Levine, R. A. & Weyman, A. F. Echocardiography in cardiac research. In *The heart and cardiovascular system* (eds. Fozzard, H. A., Haber, E., Jennings, R. B., Katz, A. M. & Morgan, H. E.) 745-837 (Raven, New York, 1992).

160. Matcher, S. J., Cope, M. & Delpy, D. T. Use of the water absorption spectrum to quantify tissue chromophore concentration changes in near-infrared spectroscopy. *Physics in Medicine and Biology* **38**, 177-196 (1993).

161. Matcher, S. J., Elwell, C. E., Cooper, C. E., Cope, M. & Delpy, D. T. Performance comparison of several published tissue near-infrared spectroscopy algorithms. *Analytical Biochemistry* **227**, 54-68 (1995).

162. Mather, P. P. & Case, R. B. Phosphate loss during reversible myocardial ischemia. *Journal of Molecular and Cellular Cardiology* **5**, 375-393 (1973).

163. Mercer, R. W. & Dunham, P. B. Membrane-bound atp fuels the na/k pump. Studies on membrane-bound glycolytic enzymes on inside-out vesicles from human red cell membranes. *Journal of General Physiology* **78**, 547-568 (1981).

164. Mie, G. *Annalen der Physik* **25**, 377 (1908).

165. Millikan, G. A. Muscle hemoglobin. *Physiological Review* **19**, 503-523 (1939).

166. Moaveni, M. K. A multiple scattering field theory applied to whole blood. (Ph.D. Thesis, University of Washington, 1970)

167. Mochizuki, S. & Neely, J. R. Control of glyceraldehyde-3-phosphate dehydrogenase in cardiac muscle. *Journal of Molecular and Cellular Cardiology* **11**, 221-36 (1979).

168. Momenteau, M. & Reed, C. Synthetic heme dioxygen complexes. *Chemical Review* **94**, 654-698 (1994).

169. Mook, P. H., Proctor, H. J., Jobsis, F. & Wildevuur, C. R. Assessment of brain oxygenation: A comparison between an oxygen electrode and near-infrared spectrophotometry. *Advances in Experimental Medicine and Biology* **169**, 841-847 (1984).

170. Moore, W. S. & Malone, J. M. Effect of flow rate and vessel calibre on critical arterial stenosis. *Journal of Surgical Research* **26**, 1-9 (1979).

171. Mörner, K. A. H. Beobachtungen über den muskelfarbstoff. *Nordiskt Medicinskt Arkiv* **30**, 1 (1897).

172. Murphy, J. G., Smith, T. W. & Marsh, J. D. Mechanisms of reoxygenation-induced calcium overload in cultured chick embryo heart cells. *American Journal of Physiology* **254**, H1133-H1141 (1988).

173. Murray, R. K., Granner, D. K., Mayes, P. A. & Rodwell, V. W. *Harper's biochemistry* (Appleton & Lange, Stamford, CT, 1996).

174. Nayler, W. G. The role of calcium in the ischemic myocardium. *American Journal of Pathology* **102**, 262-270 (1981).

175. Neely, J. R. & Morgan, H. E. Relationship between carbohydrate and lipid metabolism and the energy balance of heart muscle. *Annual Review of Physiology* **36**, 413-459 (1974).

176. Neely, J. R., Whitmer, J. T. & Rovetto, M. J. Effect of coronary blood flow on glycolytic flux and intracellular pH in isolated rat hearts. *Circulation Research* **37**, 733-741 (1975).

177. Nighswander-Rempel, S. P., Shaw, R. A., Kuzio, B. & Kupriyanov, V. V. Detection of myocardial cell damage in isolated rat hearts with near-infrared spectroscopy. *Journal of Biomedical Optics* **in press** (2003).

178. Nilsson, A. M., Heinrich, D., Olajos, J. & Andersson-Engels, S. Near infrared diffuse reflection and laser-induced fluorescence spectroscopy for myocardial tissue characterisation. *Spectrochimica Acta A Molecular and Biomolecular Spectroscopy* **53A**, 1901-1912 (1997).

179. Nishimura, R. A. The role of echocardiography. In *Atherosclerosis and coronary artery disease* (eds. Fuster, V., Ross, R. & Topol, E. J.) 855-876 (Lippincott-Raven, Philadelphia, 1996).

180. Olsson, R. A., Bünger, R. & Spaan, J. A. E. Coronary circulation. In *The heart and cardiovascular system* (eds. Fozzard, H. A., Haber, E., Jennings, R. B., Katz, A. M. & Morgan, H. E.) 1393-1425 (Raven, New York, 1992).

181. Opie, L. H. *The heart: Physiology and metabolism* (Raven, New York, 1991).

182. Ornac, J., Schmidt, M. C., Theissen, P. & Sechtem, U. Assessment of myocardial perfusion by magnetic resonance imaging. *Herz* **22**, 16-28 (1997).

183. Osborne, B. G., Fearn, T. & Hindle, P. T. *Practical nir spectroscopy with applications in food and beverage analysis* (Longman Scientific & Technical, Essex, 1993).

184. Palmer, K. F. & Williams, D. Optical properties of water in the near infrared. *Journal of the Optical Society of America* **64**, 1107-1110 (1974).

185. Parsons, T. R. *Journal of Physiology* **53**, 42, 340 (1919).

186. Parsons, W. J., Rembert, J. C., Bauman, R. P., Duhaylongsod, F. G., Greenfield, J. C., Jr. & Piantadosi, C. A. Myocardial oxygenation in dogs during partial and complete coronary artery occlusion. *Circulation Research* **73**, 458-464 (1993).

187. Parsons, W. J., Rembert, J. C., Bauman, R. P., Greenfield, J. C., Jr. & Piantadosi, C. A. Dynamic mechanisms of cardiac oxygenation during brief ischemia and reperfusion. *American Journal of Physiology* **259**, H1477-H1485 (1990).

188. Patterson, M. S., Chance, B. & Wilson, B. C. Time resolved reflectance and transmittance for the non-invasive measurement of tissue optical properties. *Applied Optics* **28**, 2331-2336 (1989).

189. Pauling, L. Nature of the iron-oxygen bond in oxyhaemoglobin. *Nature* **203**, 182-183 (1964).

190. Pedley, T. J. *The fluid mechanics of large blood vessels* (Cambridge University Press, Cambridge, 1980).

191. Perutz, M. F. Stereochemistry of cooperative effects in haemoglobin. *Nature* **228**, 726-739 (1970).

192. Perutz, M. F., Heidner, E. J., Ladner, J. E., Beetlestone, J. G., Ho, C. & Slade, E. F. Influence of globin structure on the state of the heme. 3. Changes in heme spectra accompanying allosteric transitions in methemoglobin and their implications for heme-heme interaction. *Biochemistry* **13**, 2187-2200 (1974).

193. Philipson, K. D., Bersohn, M. M. & Nishimoto, A. Y. Effects of pH on na+-ca2+ exchange in canine cardiac sarcolemmal vesicles. *Circulation Research* **50**, 287-93 (1982).

194. Pike, M. M., Luo, C. S., Clark, M. D., Kirk, K. A., Kitakaze, M., Madden, M. C., Cragoe, E. J., Jr. & Pohost, G. M. Nmr measurements of na+ and cellular energy in ischemic rat heart: Role of na(+)-h+ exchange. *American Journal of Physiology* **265**, H2017-H2026 (1993).

195. Pohost, G. M., Henzlova, M. J., Okada, R., Boucher, C. A. & Bourge, R. C. Radionuclide methods to assess cardiac perfusion, function, viability and necrosis. In *The heart and cardiovascular system* (eds. Fozzard, H. A., Haber, E., Jennings, R. B., Katz, A. M. & Morgan, H. E.) 669-691 (Raven, New York, 1992).

196. Poole-Wilson, P. A., Harding, D. P., Bourdillon, P. D. & Tones, M. A. Calcium out of control. *Journal of Molecular and Cellular Cardiology* **16**, 175-187 (1984).

197. Pope, R. M. & Fry, E. S. Absorption spectrum (380-700 nm) of pure water. Ii. Integrating cavity measurements. *Applied Optics* **36**, 8710-8723 (1997).

198. Prahl, S. Optical absorption of water compendium. Retrieved 6 March, 2003 from http://omlc.ogi.edu/spectra/water/abs/index.html. (Updated 11 May 1998).

199. Prahl, S. Tabulated molar extinction coefficient for hemoglobin in water. Retrieved 3 March, 2003 from http://omlc.ogi.edu/spectra/hemoglobin/summary.html. (Updated 4 March 1998).

200. Pringle, J., Roberts, C., Kohl, M. & Lekeux, P. Near infrared spectroscopy in large animals: Optical pathlength and influence of hair covering and epidermal pigmentation. *Veterinary Journal* **158**, 48-52 (1999).

201. Rapoport, S. & Lübering, J. The formation of 2,3-diphosphoglycerate in rabbit erythrocytes: The existence of a diphosphoglycerate mutase. *Journal of Biological Chemistry* **183**, 507-516 (1950).

202. Ray, G. B. & Paff, G. H. A spectrophotometric study of muscle hemoglobin. *American Journal of Physiology* **94**, 521 (1930).

203. Rayleigh, L. On the light from the sky, its polarization and colour. *Philosophical Magazine* **41**, 107-120 (1871).

204. Reed, C. A. & Cheung, S. K. On the bonding of feo2 in hemoglobin and related dioxygen complexes. *Proceedings of the National Academy of Sciences of the United States of America* **74**, 1780-1784 (1977).

205. Reeder, G. S., Smith, H. C. & Frye, R. L. Cardiac catheterization and angiography b. Coronary arteriography. In *Cardiology: Fundamentals and practice* (eds. Giuliani, E. R., Fuster, V., Gersh, B. J., McGoon, M. D. & McGoon, D. C.) 552-573 (Mosby, St. Louis, 1991).

206. Reimer, K. A., Hill, M. L. & Jennings, R. B. Prolonged depletion of atp and of the adenine nucleotide pool due to delayed resynthesis of adenine nucleotides following reversible myocardial ischemic injury in dogs. *Journal of Molecular and Cellular Cardiology* **13**, 229-239 (1981).

207. Reimer, K. A. & Jennings, R. B. Myocardial ischemia, hypoxia, and infarction. In *The heart and cardiovascular system* (eds. Fozzard, H. A., Haber, E., Jennings, R. B., Katz, A. M. & Morgan, H. E.) 1875-1973 (Raven, New York, 1992).

208. Reimer, K. A., Murry, C. E. & Richard, V. J. The role of neutrophils and free radicals in the ischemic-reperfused heart: Why the confusion and controversy? *Journal of Molecular and Cellular Cardiology* **21**, 1225-1239 (1989).

209. Rempel, S. P. & Mantsch, H. H. Biomedical applications of near-infrared spectroscopy: A review. *Canadian Journal of Analytical Sciences and Spectroscopy* **44**, 171-179 (1999).

210. Reuthebuch, O. T., Kadner, A., Lachat, M. L. & Turina, M. I. Graft occlusion after deployment of the symmetry bypass system. *Annals of Thoracic Surgery* **75**, 1626-1629 (2003).

211. Roberts, R. Introduction to the techniques of molecular biology and the molecular basis for cardiac growth. In *Hurst's the heart* (eds. Schlant, R. C., Alexander, R. W., O'Rourke, R. A., Roberts, R. & Sonnenblick, E. H.) 3-30 (McGraw-Hill, New York, 1994).

212. Roberts, R., Morris, D., Pratt, C. M. & Alexander, R. W. Pathophysiology, recognition, and treatment of acute myocardial infarction and its complications. In *Hurst's the heart* (eds. Schlant, R. C., Alexander, R. W., O'Rourke, R. A., Roberts, R. & Sonnenblick, E. H.) 1107-1184 (McGraw-Hill, New York, 1994).

213. Roesen, R., Panzner, B. & Klaus, W. Epicardial image analysis using a desk top computer. Comparison of epicardial flow distribution and nadh-fluorescence pattern. *Advances in Myocardiology* **6**, 217-231 (1985).

214. Ross, J., Jr. & Franklin, D. Analysis of regional myocardial function, dimensions, and wall thickness in the characterization of myocardial ischemia and infarction. *Circulation* **53**, I88-I92 (1976).

215. Ross, R. & Fuster, V. The pathogenesis of atherosclerosis. In *Atherosclerosis and coronary artery disease* (eds. Fuster, V., Ross, R. & Topol, E. J.) 441-460 (Lippincott-Raven, Philadelphia, 1996).

216. Rouslin, W., Erickson, J. L. & Solaro, R. J. Effects of oligomycin and acidosis on rates of atp depletion in ischemic heart muscle. *American Journal of Physiology* **250**, H503-H508 (1986).

217. Rovetto, M. J., Whitmer, J. T. & Neely, J. R. Comparison of the effects of anoxia and whole heart ischemia on carbohydrate utilization in isolated working rat hearts. *Circulation Research* **32**, 699-711 (1973).

218. Rovira, C., Ballone, P. & Parrinello, M. A density functional study of iron-porphyrin complexes. *Chemical Physics Letters* **271**, 247-250 (1997).

219. Rovira, C., Kunc, K., Hutter, J., Ballone, P. & Parrinello, M. Equilibrium geometries and electronic structure of iron-porphyrin complexes: A density functional study. *Journal of Physical Chemistry A* **101**, 8914-8925 (1997).

220. Rowe, G. T., Manson, N. H., Caplan, M. & Hess, M. L. Hydrogen peroxide and hydroxyl radical mediation of activated leukocyte depression of cardiac sarcoplasmic reticulum. Participation of the cyclooxygenase pathway. *Circulation Research* **53**, 584-591 (1983).

221. Rumsey, W. L., Pawlowski, M., Lejavardi, N. & Wilson, D. F. Measurement of oxygen pressure in the heart in vivo using phosphorescence quenching. *Advances in Experimental Medicine and Biology* **361**, 93-7 (1994).

222. Sandler, J. A test of the significance of the difference between the means of correlated measures, based upon a simplication of student's *t*. *British Journal of Psychology* **46**, 225-226 (1955).

223. Sayen, J. J., Peirce, G., Katcher, A. H. & Sheldon, W. F. Correlation of intramyocardial electrocardiograms with polarographic oxygen and contractility in the nonischemic and regionally ischemic left ventricle. *Circulation Research* **9**, 1268-1279 (1961).

224. Schaper, J., Meiser, E. & Stammler, G. Ultrastructural morphometric analysis of myocardium from dogs, rats, hamsters, mice, and from human hearts. *Circulation Research* **56**, 377-391 (1985).

225. Schlant, R. C. & Sonnenblick, E. H. Normal physiology of the cardiovascular system. In *Hurst's the heart* (eds. Schlant, R. C., Alexander, R. W., O'Rourke, R. A., Roberts, R. & Sonnenblick, E. H.) 113-151 (McGraw-Hill, New York, 1994).

226. Schuder, S., Wittenberg, J. B., Haseltine, B. & Wittenberg, B. A. Spectrophotometric determination of myoglobin in cardiac and skeletal muscle: Separation from hemoglobin by subunit-exchange chromatography. *Analytical Biochemistry* **92**, 473-481 (1979).

227. Seeley, R. R., Stephens, T. D. & Tate, P. *Anatomy & physiology* (Mosby, St. Louis, 1998).

228. Seiyama, A., Hazeki, O. & Tamura, M. Noninvasive quantitative analysis of blood oxygenation in rat skeletal muscle. *Journal of Biochemistry Tokyo* **103**, 419-424 (1988).

229. Seno, Y., Kameda, N. & Otsuka, J. The electronic structure of ferrous heme with imidazole as the fifth ligand. I. Scf-lcao-asmo and cl calculation on the low-lying multiplets and optically allowed excited states. *Journal of Chemical Physics* **72**, 6048-6058 (1980).

230. Seshadri, V., Hochmuth, R. M., Croce, P. A. & Sutera, S. P. Capillary blood flow. 3. Deformable model cells compared to erythrocytes in vitro. *Microvascular Research* **2**, 434-42 (1970).

231. Severinghaus, J. W. Blood gas calculator. *Journal of Applied Physiology* **21**, 1108-1116 (1966).

232. Shaw, R. A., Mansfield, J. R., Kupriyanov, V. V. & Mantsch, H. H. In vivo optical/near-infrared spectroscopy and imaging of metalloproteins. *Journal of Inorganic Biochemistry* **79**, 285-293 (2000).

233. Shikama, K. Nature of the feo2 bonding in myoglobin: An overview from physical to clinical biochemistry. *Experientia* **41**, 701-706 (1985).

234. Simpson, W. T. On the theory of the pi-electron systemin porphyrins. *Journal of Chemical Physics* **17**, 1218-1221 (1949).

235. Smielewski, P., Kirkpatrick, P., Minhas, P., Pickard, J. D. & Czosnyka, M. Can cerebrovascular reactivity be measured with near-infrared spectroscopy? *Stroke* **26**, 2285-2292 (1995).

236. Sowa, M. G., Payette, J. R. & Mantsch, H. H. Near-infrared spectroscopic assessment of tissue hydration following surgery. *Journal of Surgical Research* **86**, 62-69 (1999).

237. Stedman, T. L. *Stedman's medical dictionary* (Williams & Wilkins, Baltimore, 1995).

238. Steenbergen, C., Deleeuw, G., Rich, T. & Williamson, J. R. Effects of acidosis and ischemia on contractility and intracellular pH of rat heart. *Circulation Research* **41**, 849-858 (1977).

239. Steenbergen, C., Hill, M. L. & Jennings, R. B. Volume regulation and plasma membrane injury in aerobic, anaerobic, and ischemic myocardium in vitro. Effects of osmotic cell swelling on plasma membrane integrity. *Circulation Research* **57**, 864-875 (1985).

240. Stein, P. D. & Sabbah, H. N. Turbulent blood flow in the ascending aorta of humans with normal and diseased aortic valves. *Circulation Research* **39**, 58-65 (1976).

241. Tada, M., Kuzuya, T., Hoshida, S. & Nishida, M. Arachidonate metabolism in myocardial ischemia and reperfusion. *Journal of Molecular and Cellular Cardiology* **20 Suppl 2**, 135-43 (1988).

242. Taggart, D. P. Biochemical assessment of myocardial injury after cardiac surgery: Effects of a platelet activating factor antagonist, bilateral internal thoracic artery grafts, and coronary endarterectomy. *Journal of Thoracic and Cardiovascular Surgery* **120**, 651-659 (2000).

243. Taggart, D. P., Choudhary, B., Anastasiadis, K., Abu Omar, Y., Balacumaraswami, L. & Pigott, D. W. Preliminary experience with a novel intraoperative fluorescence imaging technique to evaluate the patency of bypass grafts in total arterial revascularization. *Annals of Thoracic Surgery* **75**, 870-873 (2003).

244. Takahashi, K., Ogata, S., Atsumi, Y., Yamamoto, R., Shiotsuka, S., Maki, A., Yamashita, Y., Yamamoto, T., Koizumi, H., Hirasawa, H. & Igawa, M. Activation of the visual cortex imaged by 24-channel near-infrared spectroscopy. *Journal of Biomedical Optics* **5**, 93-96 (2000).

245. Takatani, S. & Graham, M. D. Theoretical analysis of diffuse reflectance from a two-layer tissue model. *IEEE Transactions on Biomedical Engineering* **BME-26**, 656-664 (1987).

246. Tamura, M., Hoshi, Y. & Okada, F. Localized near-infrared spectroscopy and functional optical imaging of brain activity. *Philosophical Transactions of the Royal Society of London B Biological Sciences* **352**, 737-742 (1997).

247. Tani, M. & Neely, J. R. Role of intracellular na+ in ca2+ overload and depressed recovery of ventricular function of reperfused ischemic rat hearts. Possible involvement of h+-na+ and na+-ca2+ exchange. *Circulation Research* **65**, 1045-1056 (1989).

248. Taylor, C. R., Karas, R. H., Weibel, E. R. & Hoppeler, H. Adaptive variation in the mammalian respiratory system in relation to energetic demand: Ii. Reaching the limits to oxygen flow. *Respiration Physiology* **69**, 7-26 (1987).

249. Teisseire, B., Loisance, D., Soulard, C., Herigault, R., Teisseire, L. & Laurent, D. In vitro and in vivo studies of a stroma free hemoglobin solution as a potential blood substitute. *Bulletin of European Physiopathological Respiration* **13**, 261-79 (1977).

250. Tennant, R. & Wiggers, C. J. The effect of coronary occlusion on myocardial contraction. *American Journal of Physiology* **112**, 351-361 (1935).

251. Theorell, H. Kristallinisches myoglobin. I. Kristallisieren und reinigung des myoglobins sowie vorläufige mitteilung über sein molekulargewicht. *Biochemische Zeitung* **252**, 1 (1932).

252. Thorniley, M. S., Houston, R., Wickramasinghe, Y. A. & Rolfe, P. Application of near-infrared spectroscopy for the assessment of the oxygenation level of myoglobin and haemoglobin in cardiac muscle in vivo. *Biochemical Society Transactions* **18**, 1195-6 (1990).

253. Tkachuk, A. M., Ivanova, S. E., Isaenko, L. I., Yelisseyev, A. P., Payne, S., Solarz, R., Page, R. & Nostrand, M. Spectroscopic study of neodymium-doped potassium-lead double chloride nd^{+3}:Kpb$_2$cl$_5$ crystals. *Optics and Spectroscopy* **92**, 83-94 (2002).

254. Topulos, G. P., Lipsky, N. R., Lehr, J. L., Rogers, R. A. & Butler, J. P. Fractional changes in lung capillary blood volume and oxygen saturation during the cardiac cycle in rabbits. *Journal of Applied Physiology Bethesda* **82**, 1668-1676 (1997).

255. Tuchin, V. *Tissue optics* (ed. O'Shea, D. C.) (SPIE, Bellingham, WA, 2000).

256. Vander Heide, R. S. & Ganote, C. E. Increased myocyte fragility following anoxic injury. *Journal of Molecular and Cellular Cardiology* **19**, 1085-1103 (1987).

257. Voet, D. & Voet, J. G. *Biochemistry* (John Wiley & Sons, New York, 1995).

258. Webb, S. C., Canepa-Anson, R., Rickards, A. F. & Poole-Wilson, P. A. Myocardial potassium loss after acute coronary occlusion in humans. *Journal of American College of Cardiology* **9**, 1230-1234 (1987).

259. Weiss, J. J. Nature of the iron-oxygen bond in oxyhaemoglobin. *Nature* **202**, 83-84 (1964).

260. Weiss, S. J. Oxygen, ischemia and inflammation. *Acta Physiol Scand Suppl* **548**, 9-37 (1986).

261. Weissbluth, M. *Hemoglobin: Cooperativity and electronic properties* (Chapman and Hall, London, 1974).

262. White, F. C. & Bloor, C. M. Coronary collateral circulation in the pig: Correlation of collateral flow with coronary bed size. *Basic Research in Cardiology* **76**, 189-96 (1981).

263. White, F. C., Roth, D. M. & Bloor, C. M. The pig as a model for myocardial ischemia and exercise. *Laboratory Animal Science* **36**, 351-356 (1986).

264. Whitman, G., Kieval, R., Wetstein, L., Seeholzer, S., McDonald, G. & Harken, A. The relationship between global myocardial ischemia, left ventricular function, myocardial redox state, and high energy phosphate profile. A phosphorous-31 nuclear magnetic resonance study. *Journal of Surgical Research* **35**, 332-339 (1983).

265. Wiedeman, M. P. Lengths and diameters of peripheral arterial vessels in the living animal. *Circulation Research* **10**, 686-690 (1962).

266. Williams, A. Mitochondria. In *Cardiac metabolism* (eds. Drake-Holland, A. J. & Noble, M. I. M.) (Wiley, Chichester, 1983).

267. Wilson, D. F. & Vinogradov, S. A. Recent advances in oxygen measurements using phosphorescence quenching. *Advances in Experimental Medicine and Biology* **361**, 61-66 (1994).

268. Wittenberg, B. A. & Wittenberg, J. B. Transport of oxygen in muscle. *Annual Review of Physiology* **51**, 857-878 (1989).

269. Wood, N. B. Aspects of fluid dynamics applied to the larger arteries. *Journal of Theoretical Biology* **199**, 137-161 (1999).

270. Wright, K. B., Klocke, F. J., Deshpande, V. S., Zheng, J., Harris, K. R., Tang, R., Finn, J. P. & Li, D. Assessment of regional differences in myocardial blood flow using t2-weighted 3d bold imaging. *Magnetic Resonance in Medicine* **46**, 573-8 (2001).

271. Yasuda, T., Ushijima, T., Kawasuji, M. & Watanabe, Y. [continuous measurement of myocardial oxygen saturation using near-infrared spectroscopy during warm blood cardioplegia]. *Kyobu Geka* **48**, 915-918 (1995).

272. Young, A. T. Rayleigh scattering. *Physics Today* **35**, 42-48 (1982).

273. Zerner, M., Gouterman, M. & Kobayashi, H. Porphyrins viii. Extended huckel calculations on iron complexes. *Theoretica Chimica Acta* **6**, 363-400 (1966).

274. Zijlstra, W. G., Buursma, A. & van Assendelft, O. W. *Visible and near infrared absorption spectra of human and animal haemoglobin: Determination and application* (Vsp, Utrecht ; Boston, 2000).

275. Zimmer, H. G. & Gerlach, E. Stimulation of myocardial adenine nucleotide biosynthesis by pentoses and pentitols. *Pflügers Archiv* **376**, 223-227 (1978).

276. Zwart, A., Kwant, G., Oeseburg, B. & Zijlstra, W. G. Human whole-blood oxygen affinity: Effect of temperature. *Journal of Applied Physiology* **57**, 429-434 (1984).

277. Zweier, J. L., Thompson Gorman, S. & Kuppusamy, P. Measurement of oxygen concentrations in the intact beating heart using electron paramagnetic resonance spectroscopy: A technique for measuring oxygen concentrations in situ. *Journal of Bioenergetics and Biomembranes* **23**, 855-871 (1991).